Dissertation zur Erlangung des Doktorgrades
der Fakultät für Chemie und Pharmazie
der Ludwig-Maximilians-Universität München

Enhancing Fluorophore Performance for Single-Molecule Applications and Super-Resolution Imaging

Cindy Mara Close

2025

Dissertation zur Erlangung des Doktorgrades
der Fakultät für Chemie und Pharmazie
der Ludwig-Maximilians-Universität München

Enhancing Fluorophore Performance for Single-Molecule Applications and Super-Resolution Imaging

Cindy Mara Close
aus
München, Deutschland

2025

Erklärung

Diese Dissertation wurde im Sinne von §7 der Promotionsordnung vom 28. November 2011 von Herr Prof. Dr. Philip Tinnefeld betreut.

Eidesstattliche Versicherung

Diese Dissertation wurde eigenständig und ohne unerlaubte Hilfe erarbeitet.

Generative KI

Diese Dissertation wurde ohne Verwendung generativer künstlicher Intelligenz erarbeitet.

Cindy Close
München, den 19.02.2025

Dissertation eingereicht am 19.02.2025
1. Gutachter: Prof. Dr. Philip Tinnefeld
2. Gutachter: Prof. Dr. Achim Hartschuh
Mündliche Prüfung am 11.04.2025

Abstract

To see the world, we need to see the small things. And so, science has made great efforts to observe the details of biological systems. Sophisticated microscopes have been developed to visualize structures and interactions at the dimension of proteins and other biomolecules. In fluorescence microscopy these nanometer-sized features are revealed through photon-emitting labels, attached to the molecule of interest. High performance of these dyes in terms of stability, specificity and brightness is a prerequisite for any successful experiment. At the same time, in order to observe the system in its innate state, interference of the observation method with the specimen should be minimal. Once this is ensured, it can be applied to observe biomolecules in their inherently complex environment and detect disease markers reliably.

The first section of this thesis is focused on increasing fluorophore photostability. To improve the signal-to-background ratio, fluorescence microscopy is often performed at the highest possible illumination power and for as long as possible before sample and fluorescent labels degrade (photobleaching). Aside from desired cycling between singlet excited and ground state (fluorescence), fluorophores can also enter other states such as the triplet state from where photobleaching is likely to originate. Systems to prevent this pathway commonly employ oxygen removing enzymes in combination with triplet state quenchers (TSQ), which ensure a fast return to the singlet state. Sensitive biological systems, however, can be disrupted by these additives and the required concentrations. In this work a minimally-invasive strategy that adresses this issue by attaching the TSQ to single stranded DNA (ssDNA) is introduced. An extended sequence (docking site) on the molecule of interest enables the hybridization and exchange of both the label and the photostabilization strand. This approach improves the TSQ soluability and increases the local concentration near the label. By performing hour-long measurements of an otherwise photolabile dye without oxygen removal, we demonstrate enhanced fluorophore performance at 10^7 less additive concentration. This DNA-mediated stabilization is not restricted to one type of TSQ. The modularity of the technique allows for exploration of several stabilizers to match other fluorophores. Due to its adaptability and efficacy at low concentrations, our method can be applied to challenging imaging modalities such as multi-target visualization in complex biological systems.

The next section explores key factors for fluorescence-based disease detection, namely specificity and brightness of fluorescent labels. Reliable diagnosis of Malaria tropica in early stages of infection is necessary to begin treatment as soon as possible.

While healthy red blood cells (RBC) do not contain cellular organelles, the *Plasmodium falciparum* parasite introduces them upon invasion. A silicon rhodamine dye equipped with a glibenclamide moiety is first used in this study to specifically target the endoplasmic reticulum. This allows for detection and distinction of infected over uninfected RBC in two different strains. The potential for application in the field is demonstrated by experiments on a low-cost portable smartphone microscope.

State-of-the-art methods for DNA detection rely on up-concentration of low-abundance target sequences over the background. A promising alternative is the detection of individual dye-labeled DNA molecules, which can be achieved through signal amplification using DNA origami nanoantennas. These plasmonic nanostructures bind two metallic nanoparticles (NP) and enhance fluorescence signal in the plamonic hotspot between. Fluorescently labeled disease markers can be directed towards this position by including ssDNA capture strands in the DNA origami. Two design generations for disease detection are included in this work. The chosen target sequence is responsible for an antibiotic resistant *Klebsiella pneumoniae* infection.

The first generation introduces a cleared region in the hotspot of the DNA nanostructure to provide space for the DNA detection element and two NPs. By optimizing the target DNA hybridization with label and capture strand (sandwich assay), efficient detection and amplification is achieved and a home-built smartphone microscope can be used to detect individual disease markers.

The second design (Trident) includes a more accessible hotspot to host even larger biomolecules. In comparison to the previous generation, detection speed of a 151 nucleotide ssDNA is tripled and the fraction of multiple captured molecules is doubled. Simultaneously, high fluorescence amplification is ensured.

This thesis demonstrates how photostabilization improves the performance of fluorophores in state-of-the art fluorescence microscopy. Through specific labeling and fluorescence enhancement, disease detection can be performed even on low-tech microscopes.

Table of Contents

List of Figures

1 Introduction

Microscopy enables us to see objects and details that are not visible to the naked eye. One initial use of lenses was the refraction and focusing of light for magnification in eyeglasses.[1] Early optical microscopes consisted of an objective lens close to the sample, often combined with an ocular lens, which allowed the user to see the magnified real image.[2] Since its invention, the optical microscope has been used to observe countless biological structures, revealing ever smaller details.

First reports of red blood cells and microorganisms are dated in the 17th century (Figure 1a).[3–5] Later, the sample was additionally illuminated using a condensor lens to achieve higher resolution. The observation of processes inside cells at sub-micrometer dimensions is, however, limited by the wavelength of the light source (λ) and numerical aperture (NA) of the objective or light source.[6] Ernst Abbe formulated this diffraction limit d: (refractive index n, opening angle α). For green excitation at 500 nm, this amounts to roughly d =250 nm.

$$d = \frac{\lambda}{2n\sin(\alpha)} = \frac{\lambda}{2NA} \tag{1}$$

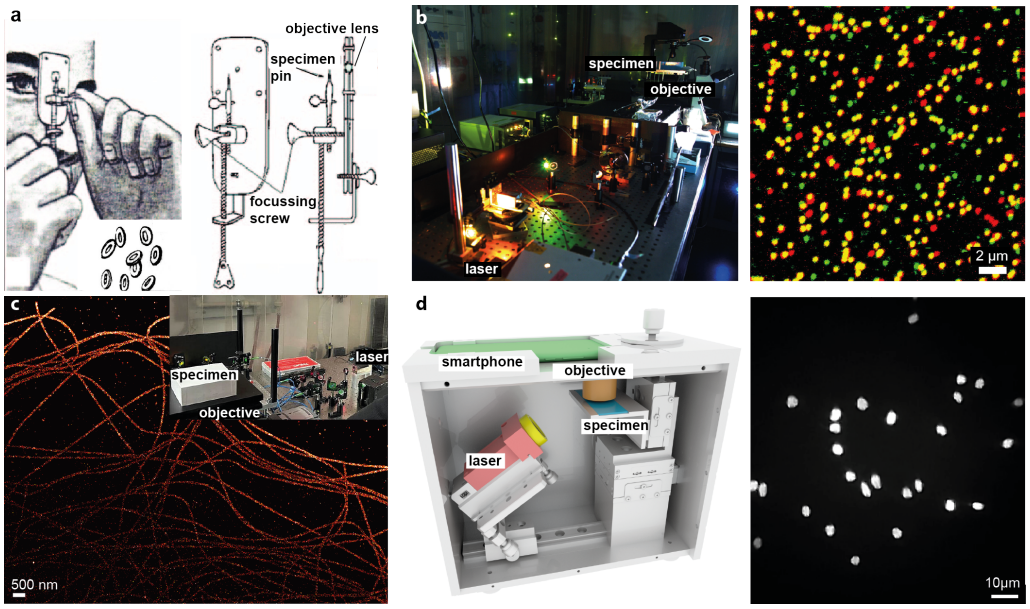

Figure 1: Microscope types and resolved structures. (**a**) Early microscope used by Leeuwenhoek and notes showing the structure of red blood cells.[3,4] (**b**) Confocal microscope and single fluorescent dye molecules emitting in red and green (overlap in yellow). (**c**) Super-resolution microscope and image of fluorescently labeled microtubules in cells. (**d**) Smartphone microscope[7] and fluorescently labeled cell nuclei.

As nanometer-sized features cannot be directly observed by eye, fluorescence microscopy relies on making proteins and other biomolecules visible with fluorescence markers. If excited at a distinct wavelength, fluorophores emit red-shifted light, thereby revealing the position of the labeled molecule. Three important features of fluorescent labels are their stability, labeling specificity and brightness. In this thesis, I aim to improve the performance of fluorophores in all of these aspects and apply this to advance state-of-the-art microscopy techniques and fluorescence-based disease detection.

In confocal microscopy the excitation beam size is constricted with a pinhole to reduce the number of simultaneously excited molecules.[8] This enables the observation of individual fluorophores at once (Figure 1b). So-called single-molecule spectroscopy is a powerful tool to study the state of the fluorophore and derive its molecular environment.[9,10] But in densely packed biological environments, such as cells, the emission profiles of objects in close proximity may overlap and the individual signals are blurred.[11–13]

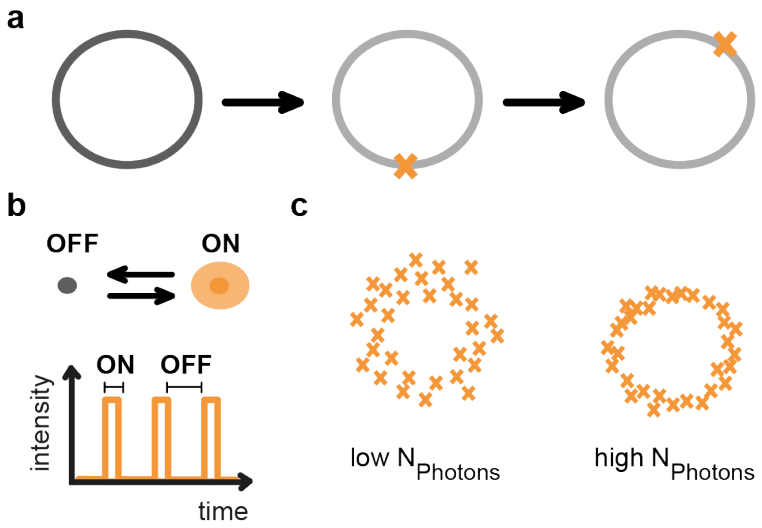

Figure 2: (**a**) Sequential turn-on of emitters at separate positions of a labeled object (grey circle). (**b**) Controlled turn-on of emitters leads to increased intensity (on-time), followed by periods where the molecule is dark (off). (**c**) Localized emitter positions in experiments with low and highly emissive fluorophores. Influence of photon number on localization accuracy and object reconstruction quality.

Super-resolution microscopy (Figure 1c) uses techniques to control the number of simultaneously emitting molecules (Figure 2a).[14–16] This can be done by modifying either the excitation or imaging buffer conditions. Single-molecule localization microscopy (SMLM) methods achieve stochastical on/off switching of emitters and

separate the signals of close-by molecules in time (Figure 2b). Transiently binding labels[17,18] that produce a signal once bound and no signal when detached have been employed to resolve molecules at distances below ∼1 nm.[19–21]

The accuracy (σ_{SMLM}) with which the emitter position can be determined depends on microscope optics, the localization algorithms detection efficacy and also the properties of the fluorescent label. To improve the σ_{SMLM} of the experiment and thereby the achievable resolution, it is desirable to minimze the size of the emitters point spread function (σ_{PSF}) and increase their intensity (photon number $N_{Photons}$).[22–26] Figure 2c shows how low photon numbers can obscure the shape of a labeled structure.

$$\sigma_{SMLM} \propto \frac{\sigma_{PSF}}{\sqrt{N_{Photons}}} \tag{2}$$

1.1 Improving fluorophore stability

Fluorophore performance is limited by photochemical processes that lead to permanent loss of emission (photobleaching). In single-molecule fluorescence experiments, the observation window closes as soon as the label no longer emits photons. The aforementioned transient binding in SMLM overcomes the limit posed by single dye photobleaching through continuous label exchange. However, even if the photobleached fluorophore is replaced, (by)products that form at the label binding site can also compromise sample integrity.[27]

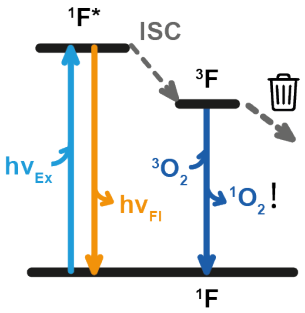

Figure 3: Simplified Jabłoński diagram of electronic states and transitions of a fluorophore. After excitation (cyan) from the singlet ground state to the singlet excited state ^{1}F*, the fluorophore can return to the ground state ^{1}F by fluorescence (orange). From ^{1}F* inter system crossing (ISC) to the triplet state ^{3}F can also occur. From here, the molecule is susceptible to photobleaching pathways (trash). $^3O_2$ can quench the triplet state efficiently (blue), but produces the reactive $^1O_2$.

For example, oxygen, ubiquitous in aqueous solutions in its quantum triplet state ($^3O_2$), may react with a fluorophore that has entered the triplet state (^{3}F, Fig-

ure 3). This leads to formation of singlet state oxygen ($^1O_2$), a strong oxidant that can damage the surrounding environment. Chemical photostabilization additives (triplet state quenchers, TSQ) that compete with this reaction can reduce the formation of $^1O_2$ and recover the fluorophore from the triplet to the singlet ground state.[28,29] So-called physical TSQ act via energy transfer, while others work based on electron transfer and redox reactions (chemical). Fluorescence does not occur from the ^3F state, but once the dye is in its ground state, it can undergo excitation and subsequent emission again. Therefore, photostabilizer molecules not only enhance fluorophore performance by minimizing $^1O_2$ formation and thereby damage to the sample. They also increase the observation time and mean photon number by returning the dye to a state from which fluorescence occurs.

Up until now, most photostabilization strategies are, however, hardly compatible with sensitive biological samples. The solubility of the stabilizing additives and required concentrations have been shown to perturb the innate state of samples.[30–33] Alternatively, in self-healing dyes, the photostabilizers are covalently attached to the fluorophore.[34–37] While this eliminates the need for additives in solution, it requires tedious synthesis and multiple purification steps. Furthermore, in some cases such as high excitation intensities, the stabilizing entity can degrade, leaving the fluorophore unprotected.[38] Enzymatic oxygen scavenging systems like glucose oxidase catalase are used to reduce the generation of $^1O_2$ and other reactive oxygen species directly. However, acidic byproducts are formed in the process of oxygen removal and accumulate over time. Other enzymes, such as protocatechuate-3,4-dioxygenase maintain stable pH values. Still, their use is limited to biological systems that are not negatively affected by enzyme, substrate and products. Lastly, delivery to the imaging site needs to be ensured and may be hindered by the polarity and size of the enzyme, as well as molecular crowding inside the specimen.[33,39,40] Less invasive photostabilization agents are needed that can reach the labeled biomolecules and act at low concentrations.

Inspired by the use of DNA hybridization for transient binding of labels in DNA-PAINT (point accumulation for imaging for nanoscale topography), chapter 4.1 introduces DNA-mediated photostabilization.

In standard DNA-PAINT SMLM experiments, molecules of interest are equipped with a synthetic single-stranded DNA (ssDNA) sequence - the docking site (Figure 4a). Complementary, dye-labeled ssDNA (imager strands) are added to the imaging solution. DNA base-pairing interactions between docking site and imager are designed by sequence and length to result in frequent events of hybridization and dissociation during the measurement. A camera captures the fluorophore sig-

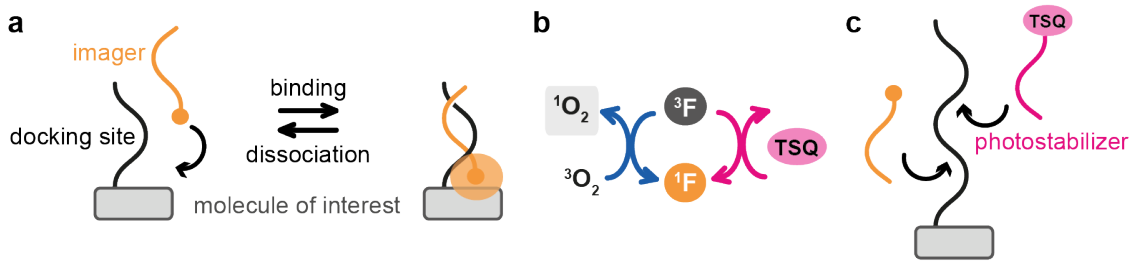

Figure 4: (**a**) DNA-PAINT experiment with transient binding of dye-labeled imager strands to single stranded DNA docking sites on a molecule of interest. (**b**) Alternative mechanism to triplet state quenching through of oxygen (blue): Introducing a photostabilizing TSQ (magenta). (**c**) Delivery of TSQ to an extended docking site by the photostabilizer strand.

nals once the imager is bound (on-time Figure 2b). Quickly diffusing strands are not detected (off-time).

In chapter 4.1 I discuss how - analogous to how the imager strand attaching the label - a ssDNA-bound photostabilizer can deliver a TSQ (Figure 4b and c). We therefore link physical TSQs to ssDNA which also increases their solubility and permeability. The standard docking site for imager binding is extended to also host a photostabilizer strand. Binding of the stabilizer to the docking site close to the label increases the local concentration and thereby reduces the necessary amount in solution. Additionally, the biomolecule and docking site are directly protected at the labeling site. This way, DNA-mediated photostabilization adresses the shortcomings of disruptive solution additives. In comparison to self-healing dyes, the close proximity of fluorophore and stabilizer is ensured, but the moieties are not coupled. Instead, both the label and stabilizer are delivered by designated ssDNA strands. As various different moieties can be attached to DNA, this approach is a modular and cost-effective alternative to test and use several fluorophore/stabilizer combinations. To showcase these advantages, chapter 4.1 includes DNA-PAINT measurements with a fluorophore prone to quick photobleaching. The minimally invasive photostabilization strategy protects fluorophores from degradation, facilitating their use even under harsh illumination conditions and hour-long imaging periods.

1.2 Target-specific fluorescent labels in point-of-care application

Other than resolving structures, fluorescence microscopy can also serve as a tool to report on the presence or absence of biomolecules.[41–46] This can be be applied to diagnostic settings (point-of-care) where disease markers need to be detected reliably.[47] A prerequisite for this is the target-specific attachment of the fluorescent label.

The *Plasmodium falciparum* parasite invades red blood cells (RBC) and causes the most common and dangerous type of Malaria in humans (Figure 5). While healthy RBC do not contain cellular organelles such as the endoplasmic reticulum, they are inserted upon invasion with the parasite (iRBC). A reliable way to determine the degree of infection is therefore the staining of organelles and detection in a blood smear.

The most common technique is labeling the parasites' nucleus with Giemsa (a mixture of methylene blue, eosin, and Azure B) and detection with light microscopy.[48,49] However, this requires incubation for at least 15 minutes and trained personnel. The fluorescent dye DAPI labels DNA and has been used to determine amount of infected RBC (parasitemia), but does not permeate the cell *in vivo*.[50] Other rapid diagnostic tests are based on immunochromatography but may require storage at 4 °C.[51] As local healthcare providers often lack access to electricity or specialized treatment facilities, a simple diagnostic test (assay) and portable detection device are essential. For starting treatment as soon as possible, sensitive detection reagents that report on early stages in the asexual reproduction cycle (ring stage Figure 5) are needed.

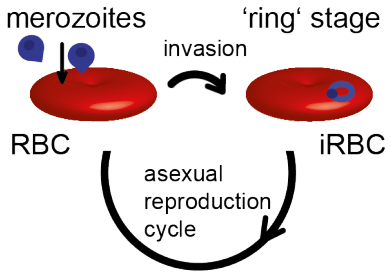

Figure 5: Invasion of red blood cells by the merozoit stage of the *Plasmodium falciparum* parasite. Inside the RBC, the parasite cycles through several stages. The ring stage is the earliest one.

In chapter 5.1 I describe how a fluorescent probe (SiR-glib), specifically designed

for this study, is used to develop a diagnostic test for detecting Malaria-infected RBC on a low-cost microscope. The dye targets a receptor of the endoplasmatic reticulum and emits in a spectrally separate window to hemoglobin to minimize signal overlap. We test the specificity of the assay by comparing cells infected with one of two distinct parasite strains to non-infected RBCs. In combination with a portable smartphone microscope[52] (Figure 1d), we explore the potential for applying the Malaria detection assay at the point of care (POC).

1.3 Amplifying the signal of individual fluorophores

Oftentimes, diagnostically relevant molecules are only present at low quantities. The state-of-the-art protocol for nucleic acid detection is molecular amplification of the target sequence using the polymerase chain reaction (PCR).[53–56] In most settings, well-trained staff is necessary to perform the test. Robustness and reproducibility are limited by contamination.[57] False positive signals are generated when incorrect sequences are up-concentrated instead of the target DNA. If the concentration is too low to be sufficiently amplified for subsequent detection, this can generate a false negative result.

Ultimate sensitivity can be achieved by directly detecting single molecules such as fluorescently labeled markers.[41] However, the signal of individual fluorophores is too weak to be observed with low-tech microscopes.[52] In chapters 6.1 and 6.2 I discuss our work on enhancing the fluorescence signals of individual fluorophores and the application of this technology to diagnostic settings.

One characteristic which determines the brighntess (equation 3) of organic fluorophores is the molar extinction coefficient ϵ. It is an intrinsic property and defines how strongly light of a given wavelength is absorbed. The fluorescence quantum yield ϕ relates the number of emitted photons to absorbed photons (equation 4). It is also defined as the fraction of molecules that transition from $^1F^*$ to ^1F through fluorescence (rate k_f), compared to all non-radiative relaxation processes (rate k_{nr} and k_{ISC}, equation 5).

$$Brightness = \epsilon \cdot \phi \tag{3}$$

$$\phi = \frac{\text{number of emitted photons}}{\text{number of absorbed photons}} \tag{4}$$

$$\phi = \frac{k_F}{k_F + k_{nr} + k_{isc}} \tag{5}$$

For low quantum yield emitters, increasing the radiative rate k_F can enhance emission.[58] Metallic nanoparticles (NPs) have been shown to increase both emission and excitation rates by concentrating electromagnetic fields into subdiffraction-sized volumes.[59] Upon irradiation with wavelengths larger than the particle size, localized surface plasmon resonance occurs.[60] Between two NPs the combined effect of excitation and emission enhancement is especially large (plasmonic hotspot), but strongly dependent on the distance between fluorophore and NPs. To optimally position a dye molecule in the hotspot, spherical NPs have been elevated above a surface using DNA nanotechnology.[61–63] For this, the DNA origami method was employed which uses DNA as a building material to create three-dimensional structures at the nanometer scale. Through modifications at the single nucleotide level, NPs are precisely positioned to create a plasmonic hotspot. The DNA origami is further equipped with binding sites for a fluorophore to enable signal amplification inside this region.[64–66] The emitter can either be a built-in element of the DNA nanostructure, or it includes a DNA protrusion that allows for sequence-specific binding of a dye-labeled probe (Figure 6).

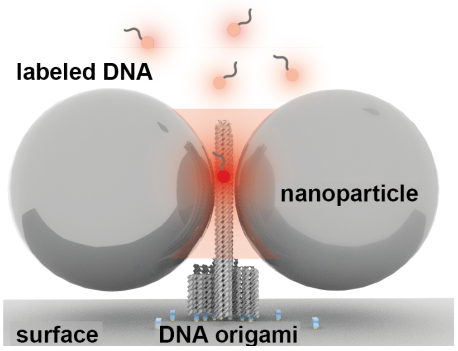

Figure 6: DNA origami nanoantenna with two silver nanoparticles increases the fluorescence signal of a labeled probe.

In diagnostic practice, patient samples often contain a mix of biomolecules, leading to pronounced background signals, e.g., due to autofluorescence. For the detection of low-abundance disease markers over this background, assays with high specificity and sensitivity are required.[42,43,46] The physical amplification mechanism of DNA origami nanoantennas is a promising alternative to PCR, as fluorescence is only amplified inside the confined hotspot region.[43–46]

To minimize false positive signals, previous configurations of DNA origami plasmonic nanostructures included a spectrally separate reference dye.[66,67] Specific interaction of the target with the detection element inside DNA origami was ensured by counting only target-reporting probes that colocalize with the reference dye as positive signals. The construct, however, only included attachment sites for one NP

next to the detection assay, limiting the signal amplification. This calls for a structurally redesigned DNA origami nanoantenna that provides space for two NPs and the target-specific assay. The small hotspot region needs to be efficiently used for the capture of analytes and placing them in the hotspot for fluorescence enhancement.

Distinct from the discussed earlier plasmonic nanostructures, the design in chapter 6.1 includes a hotspot region cleared from DNA origami. To achieve efficient target binding and improve sensitivity, we place multiple capture strands in the hotspot. Each strand can form a duplex with a segment of a short target DNA (Figure 7). The chosen target sequence is part of the Oxa-48 gene, used to diagnose patients with an antibiotic resistant infection of *Klebsiella pneumoniae*.[68,69] A dye-labeled probe can then hybridize with the target DNA overhang (sandwich assay) and remains in the hotspot region where fluorescence is enhanced. The amplification mechanism allows us to use a home-built smartphone microscope to observe the fluorescence signal of the individual fluorophores, labeling the target DNA.

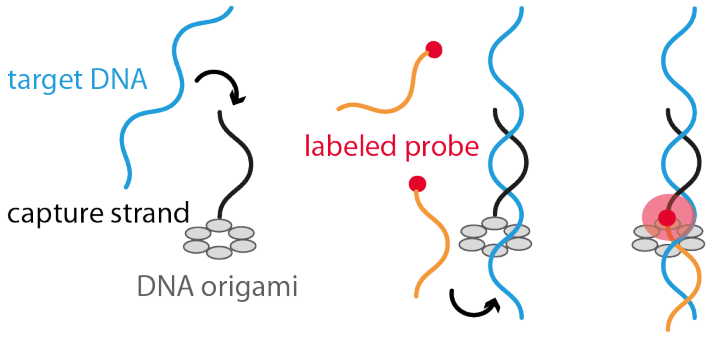

Figure 7: Scheme depicting the sandwich hybridization assay for sequence-specific detection of target DNA (cyan). Capture strands (black) protrude from DNA origami and bind the target. By attaching to the created single stranded overhang of target DNA, the reporting probe is bound to and the fluorophore fixed at a defined position in the DNA nanostructure.

The DNA origami nanoantenna introduced in chapter 6.1 was used in a subsequent study to incorporate a DNA nanoswitch which generates signal upon antibody binding.[70,71] While this assay performed well on a sterically accessible, two-dimensional DNA origami, placement into the nanoantenna led to decreased sensitivity. Because the test also suffered from unwanted photophysical effects in the hotspot of two NPs, again a monomer nanoantenna configuration was used, resulting in weaker fluorescence enhancement.

In chapter 6.2 of this thesis, I therefore further advance the DNA origami nanoantenna design to accomodate larger biomolecules. For the optimal use of the hotspot region, we adapt the DNA nanostructure to include a larger clearing. The Trident design introduced in this work consists of three pillars. The orientation on the bottom of the DNA origami is adjusted to allow NP binding close to the DNA structure. These new features aim to increase the accessibility to the hotspot while maintaining the rigid NP positioning which ensures high fluorescence enhancement. To verify that fluorescence enhancement is not compromised by the larger transversal gap, the NP attachment and incubation conditions are optimized and compared to previous designs. The interplay of more efficient target capture and strong fluorescence enhancement in the Trident DNA origami nanoantenna expands its use from single-molecule diagnostics of small nucleic acids to even larger biomarkers such as proteins or antibodies.

2 Theoretical Background

2.1 Single-molecule detection

Cells are a crowded place for biomolecules. And observing dynamic processes in such complex environments is a challenging task for scientists. Localizing *all* biomolecules at once and measuring their interactions is not feasible. Instead, one is commonly limited to observing the behaviour of only a subsection, e.g., several types of proteins. Specific labels such as fluorophores can be attached, making it possible to observe where the molecules of interest are, how they interact and how their function and state are influenced. But even one protein species can exist during several stages of a cell cycle and appears in different environments within the cell (Figure 8). When averaging over all proteins of the same kind, rare events and subpopulations are likely to be overlooked. Only when observing the individual molecules, the dynamics of stochastic and unsynchronized processes are revealed, from which time-dependent molecular properties can be determined.[72,73]

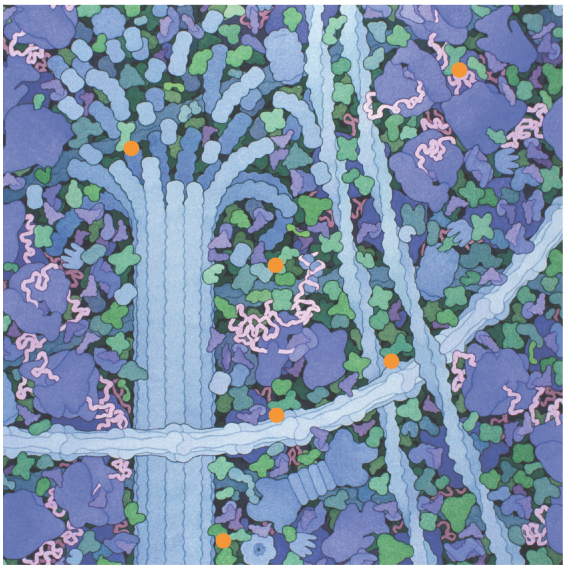

Figure 8: Artistic view of the cells cytoplasm filled with microtubules, actin and various other proteins, demonstrating the multitude of environments they exist in.[74] Proteins of one kind are labeled with fluorophores in orange.

Visualization of individual molecules is only rarely possible by eye. In fluorescence-based single-molecule spectroscopy and microscopy, the photons emitted by the fluorescent label are detected. A sufficient signal-to-noise ratio needs to be ensured to distinguish the individual molecule from its surroundings. Monitoring the photophysical behaviour of the fluorophore can also give detailed information about the biomolecular environment.

2.2 Single-molecule fluorescence

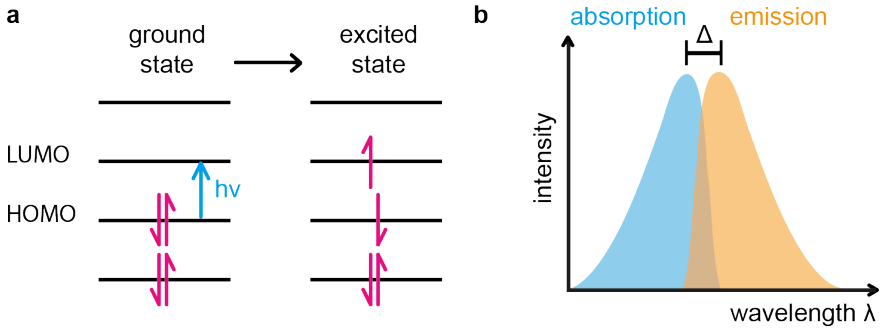

Figure 9: (**a**) Electronic transition upon absorption from highest occupied molecular orbital (HOMO) to lowest unoccupied molecular orbital (LUMO). (**b**) Absorption and emission spectra of fluorophores illustrate the Stokes shift.

Fluorphores can absorb light energy of a certain wavelength and re-emit light of a slightly lower energy. Commonly, fluorescent molecules feature conjugated systems of p-orbitals such as alternating single and double bonds or aromatic groups where π electrons are delocalized. Electrons in these systems can be excited from the highest occupied molecular obital (HOMO) into a higher energy state such as the lowest unoccupied molecular oribtal (LUMO) (Figure 9a). The spin of the electron in the singlet excited state (S_1) is paired with an electron in the ground state (S_0). The return to the ground state is spin-allowed and occurs rapidly on a timescale of $10^8\,\mathrm{s}^{-1}$.[75]

$$\Delta E = h \cdot \nu = h \cdot \frac{c}{\lambda} \tag{6}$$

The phenomenon of fluorescence emission occuring at a discrete, slightly longer wavelength (lower energy) is known as the Stokes Shift (Figure 9b and equation 6: Energy E of the photon, frequency ν, wavelength λ, speed of light c and Planck's constant h.).[76,77] It is commonly caused by rapid decay to the lowest vibrational level of the excited S_1 state ($10^{12}\,\mathrm{s}^{-1}$), but it may also be due to solvent effects, excited-state reactions, complex formation or energy transfer mechanisms.[78] Figure 10a shows a typical Jabłoński diagram, including some of the involved radiative and non-radiative relaxation processes.[79]

Due to the general occurence of fluorescence after relaxation to the lowest vibrational S_1 level, the emission spectrum is commonly observed to be independent of the excitation wavelength (Kasha's rule).[80]

Because of their significantly smaller mass in relation to an atoms nucleus, electronic transitions occur on a much faster timescales, while the nuclei remain at the

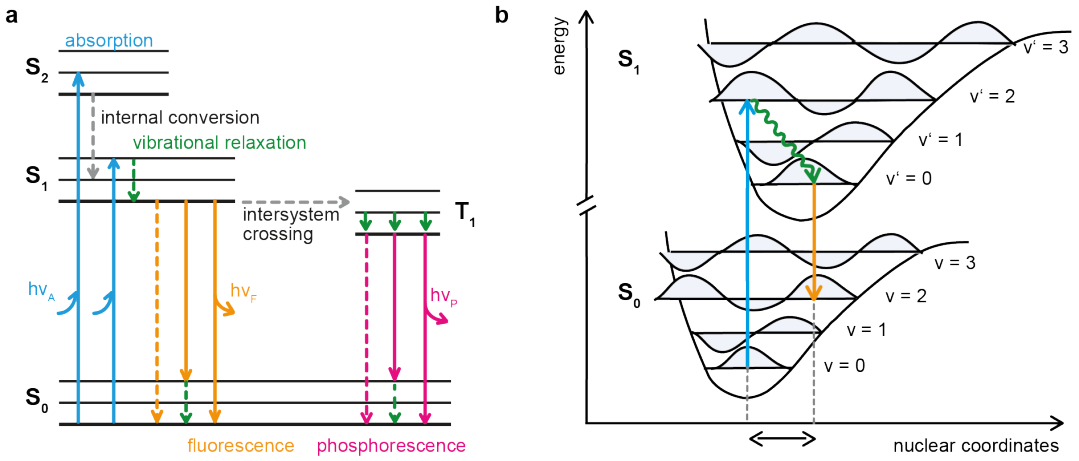

Figure 10: (**a**) Jabłoński diagram of the electronic states of a molecule and possible transitions between them. The electronic ground state is noted as S_0, different vibrational states are indicated by numbers. Radiative transitions are represented by solid vertical arrows, dashed arrows indicate non-radiative transitions such as vibrational, solvent relaxation and the process of internal conversion. (**b**) Favoured vibrational transitions according to the Franck-Condon principle.[81]

same position.[82] Figure 10b shows the vertical, instantaneous transition between two electronic states (Franck-Condon principle). For transition to a different vibrational level, their wavefunctions must overlap. Correspondingly, if the transition probability betwen two vibrational levels ($v = 0 \rightarrow v' = 2$) is largest for absorption, the same is true for the reciprocal transition during emission (mirror-image rule). Exceptions to this rule occur when molecules react in between absorption and emission.[81,83]

How bright a fluorophore is depends on its extinction coefficient ϵ (how strongly the molecule absorbs) and the ratio of photons emitted to the number of photons absorbed (ϕ, equation 7). The fluorescence quantum yield ϕ can also be described by relating the excited state decay through fluorescence k_F to other relaxation processes (equation 8, k_{isc} rate of intersystem crossing and k_{nr} all other non-radiative processes). Intersystem crossing as shown in Figure 10 is the non-radiative transition from an singlet excited state S_1 to a triplet state T_1 without energy loss.[84] Against quantum mechanical selection rules, this transition between states of different spin multiplicity involves the spin flip of the excited electron. The probability of this process is highest for overlapping vibrational wavefunctions. The slow decay of the electron from the triplet to the ground can either occur non-radiatively or radiatively through phosphorescence.

$$\phi = \frac{\text{number of emitted photons}}{\text{number of absorbed photons}} \tag{7}$$

$$\phi = \frac{k_F}{k_F + k_{nr} + k_{isc}} \tag{8}$$

$$\tau_D = \frac{1}{k_F + k_{nr} + k_{isc}} \tag{9}$$

Fluorescence lifetime τ_D is defined as the average time of the molecule in its excited state before returning to the ground state (equation 9).[85] However, additional deexcitation pathways such as intersystem crossing or energy transfer mechanisms greatly influence τ_D. Since fluorescence lifetime is sensitive to changes in the environment it is an important parameter to monitor when performing single-molecule measurements.[75]

2.3 Molecular control with DNA nanotechnology

Desoxyribonucleic acid (DNA) is biologically relevant for storing and transporting information. The four nucleotides adenine (A), guanine (G), thymine (T) and cytosine (C) comprise of the three components: phosphate group, pentose and a nucleobase. Base stacking interactions between the aromatic bases and two hydrogen bonds between A and T - three among G and C - lead to formation and stabilization of a helical structure. Together, this creates the DNA polymer with its sugar-phosphate backbone. The Watson-Crick-Franklin base-pairing rule implies predictable complementarity of any given DNA sequence. In cells DNA is predominantly in its helical B-form which features a major and minor groove of 2.2 nm and 1.2 nm wide spacing between the glycosidic bonds of two pairing strands. The $\sim$ 2 nm diameter of the right-handed double helix and $\sim$ 3.4 nm per helix turn allow precise structural engineering at the nanometer scale.[86,87]

By introducing the structural motif of the immobile Holliday junction Ned Seeman opened up the field DNA nanotechnology.[62,88] While two branched and connected double helices occur naturally as a key intermediate in genetic recombination and repair mechanisms, branch point migration is undesirable for creating stable building blocks.[89] In the Holliday junction Seeman created the necessary immobility by minimizing sequence symmetry. Three-dimensional (3D) nucleic acids networks were now feasible through rational design of sticky end associations. However, predicting the conformation of highly branched multiarm junctions remained difficult due to their flexibility which limited their use as a basic building block.[90] For higher-order structures, two 4-way DNA junctions were joined into one motif, constructing the double crossover (DX) motif with increased structural rigidity (Figure 11).[91] Aligning the double helices in parallel or antiparallel alignment enabled the formation of

4 x 4 tiles or six-helix bundles.[92,93]

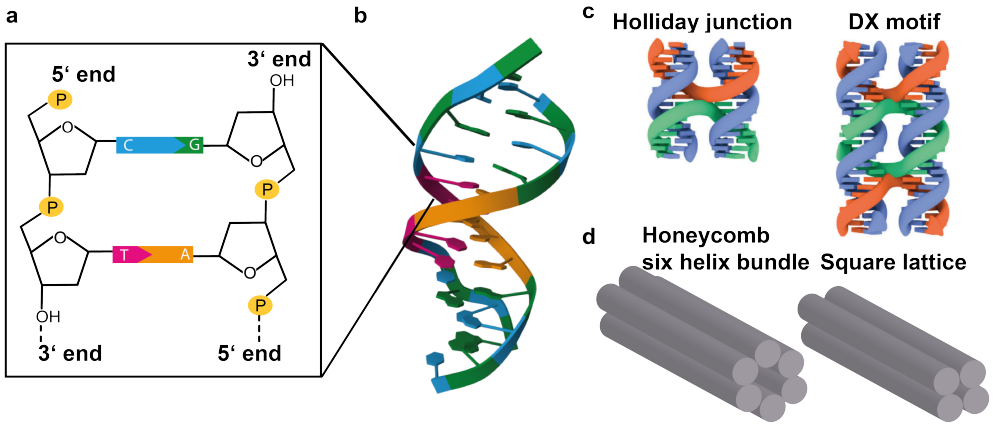

Figure 11: (**a**) Structure of deoxyribonucleic acid with sugar-phosphate backbone and base pairing. (**b**) Structure of B-DNA. (**c**) DX motif, Holliday junction and six helix bundle. Cylinder elements indicate double-helices. Figure adapted from reference and reprinted with permission from RSC.[94]

Paul Rothemund first reported the formation of DNA nanostructures via bottom-up self-assembly, coining the term "DNA origami".[61] The technique includes a long single-stranded DNA scaffold strand ($\sim$ 8 nucleobases) which is continuously routed through adjacent helices with crossovers every 1.5 helical turns. The shape of the DNA origami is defined by how the strand is routed. Sequences of the short complementary strands (15 to 60 oligonucleotide) are designed to connect selected domains within the long scaffold strand, thereby folding the DNA origami (see Figure 12). The long DNA sequence can be extracted from bacteriophage viruses (e.g., M13mp18) for which the DNA sequence is known. Shorter staple strands are produced via synthesis and added in large excess. Both components are then combined in a salted buffer and exposed to a temperature gradient. In the beginning secondary structures are resolved at high temeperatures, making all domains accessible for staple strand hybridization. During successive cooling steps, the short staples find their uniquely designed position through base complementarity and fold the desired DNA origami structure.[95]

Formation of aperiodic and three-dimensional (3D) structures was achieved shortly afterwards.[96] Bending of helices was realized by varying the distance of crossovers along the outer helices.[97] Multilayered 3D structures with the six-helix bundle as the basic unit were introduced by Douglas et al.[98,99] Twists and turns in multilayered origami designs were first reported by Dietz et al., expanding the technique to even more complicated structures.[97] However, to produce sufficient yields of the compact strucutures, the scaffold pathway and staple breaks need to be carefully designed.[100]

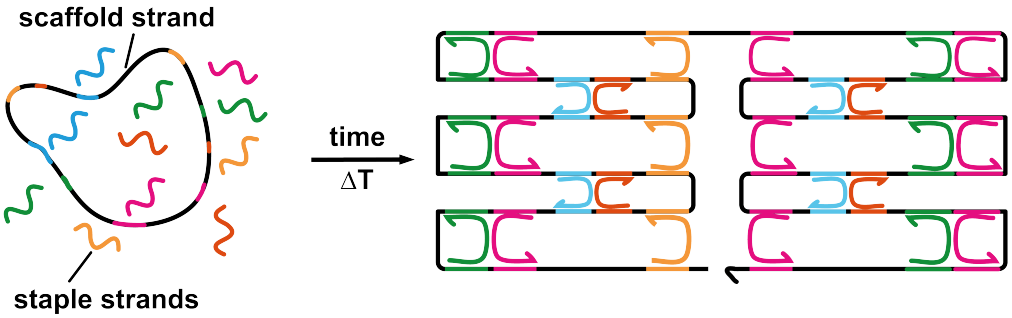

Figure 12: Schematic representation of DNA scaffold and staple strands forming a designed DNA origami shape.

Functional groups such as amines, thiols, click-chemistry functionalities etc. can be attatched to specific nucleotides of the staple strands to incorporate the desired modifications into the DNA origami. It is an unique feature of DNA nanotechnology to faciliatate the poistioning of single molecules such as fluorophores with nanometer precision.

2.4 Enhancing fluorescence with plasmonics

Metallic nanoparticles (NP) made of gold or silver can enhance fluorescence intensity based on the principle of surface plasmon resonance.[60] When light of a longer wavelength than the size of spherical metallic NPs hits, electrons in the conduction band are displaced from their nuclei (see Figure 13). In line with the Drude-Sommerfeld model, these electrons are treated as free particles.

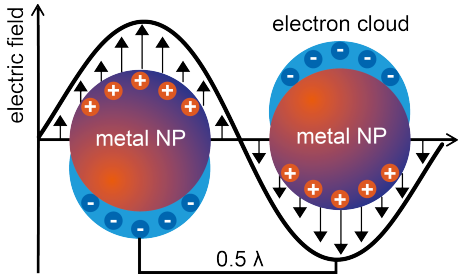

Figure 13: Visualization of incident electric field and resulting electron displacement upon illumination of metallic NP.

The electron clouds begin to oscillate coherently with the incident electric field ($\mathbf{E}(t) = \mathbf{E}_0 e^{-i\omega t}$, angular frequency ω). These so-called surface plasmons are confined when the particle is smaller than the wavelength of light exciting the particle..[101,102] Collisions occur that dampen the electron motion (mass m and charge e, relaxation time of the free electron gas τ_r, collision frequency $\gamma = 1/\tau_r$) and their response to the electric field is described as:

$$m\ddot{\mathbf{x}} + m\gamma\dot{\mathbf{x}} = -e\mathbf{E} \tag{10}$$

The oscillation and displacement of the electrons is described by equation 11, assuming harmonic time dependence of the driving field.

$$\mathbf{x}(t) = \frac{e}{m(\omega^2 + i\gamma\omega)}\mathbf{E}(t) \tag{11}$$

The plasma frequency of the free electron gas ω_p^2 is given by equation 12 (vacuum permittivity ϵ_0).

$${\omega_p}^2 = \frac{ne^2}{\epsilon_0 m} \tag{12}$$

The dielectric displacement $\mathbf{D}$ with inserted macroscopic polarisation $\mathbf{P}(= -ne\mathbf{x})$ is:

$$\mathbf{D} = \epsilon_0(1 - \frac{\omega_p^2}{(\omega^2 + i\gamma\omega)})\mathbf{E} \tag{13}$$

Finally, the dielectric function of the free electrons comes down to:

$$\epsilon(\omega) = 1 - \frac{{\omega_p}^2}{\omega^2 + i\gamma\omega} \tag{14}$$

For high frequencies much larger than the collision rate γ, close to ω_p, damping is negligible and the the dielectric function of the medium is reduced to:

$$\epsilon(\omega) = 1 - \frac{{\omega_p}^2}{\omega^2} \tag{15}$$

Photons at visible frequencies can induce interband transitions in noble metals such as gold or silver (see Figure 10). This change in energy effects the dielectric function and the imaginary part of the complex dielectric function $\epsilon(\omega) = \epsilon_1(\omega) + i\epsilon_2(\omega)$ becomes more dominant. For the classical bound electron, these interband stransitions are described with the electron's resonance frequency ω_0. Equation 10 is expanded with $m\omega_0\mathbf{x}$. For excitation with light at the plasma frequency of noble metal electrons, the resonance frequency coupling is referred to as localized surface plasmon resonance (LSPR). The surface plasmon frequencies are:

$$\omega_{sp} = \frac{\omega_p}{\sqrt{1 + 2\epsilon_2}} \tag{16}$$

The resonance frequency can be effected by changes in the particle shape, type of metal and dielectric environment. In spherical NPs that are smaller than the excitation wavelength, Fröhlich's plasmonic resonance condition is $\epsilon_P(\omega_{sp}) = -2\epsilon_m$. The applied field induces a dipole moment inside the sphere. The polarizability is defined in α equation 17 (k= $2\pi/\lambda$, R radius of the NP).

$$\alpha(\lambda) = 4\pi R^3 |\frac{\epsilon_P - \epsilon_m}{\epsilon_P + 2\epsilon_m}| \tag{17}$$

Equation 18 gives the scattering cross-section, scaling with R^6. It follows, that the extinction of large particles is dominated by scattering. Equation 19 is the absorption cross-section. For particles $R \ll \lambda$, absorption is dominant.[102–107]

$$\sigma_{scatt} = \frac{k^4}{6\pi}|\alpha(\lambda)|^2 = \frac{8\pi}{3} k R^6 |\frac{\epsilon - \epsilon_m}{\epsilon + 2\epsilon_m}|^2 \tag{18}$$

$$\sigma_{abs} = kIm[\alpha(\lambda)] = 4\pi k R^3 Im|\frac{\epsilon - \epsilon_m}{\epsilon + 2\epsilon_m}| \tag{19}$$

A fluorophore in proximity to a NP is effected by the exciting electric field $\mathbf{E}$ (see equation 20). This and the balance between non-radiative and radiative decay affect emission. k_{exc} is the excitation rate, μ the transition dipole moment.

$$k_{exc} \propto |\mu \cdot \mathbf{E}|^2 \tag{20}$$

Close to the NP, the field is non-homogeneous, prohibiting the dipole approximation. To obtain sufficient values for emission, nonradiative decay rate and quantum yield of a fluorophore, the values are calculated using the multiple multipole method.[59] In experiments, a decrease of the dyes quantum yield is observed when the fluorophore is close to the NP. This effect dominates over the increase in excitation rate and the fluorophore is quenched (see Figure 14). Further away from the NP, the quantum yield increases and fluorescence is enhanced. This strong distance dependence creates an ideal region for fluorescence enhancement (hotspot) at which the effect of increased quantum yield dominates. For the practical use of plasmonic NPs techniques that allow precise positioning on the nanoscale are highly desirable (chapter 2.3).[59,104,108]

When a fluorophore is positioned in the hotspot between two plasmonic NPs even higher values of fluorescence enhancement occur due to coupling of LSPR modes.[106] In Figure 14 the theoretical electric field intensity is shown. The plasmonic hotspot with the maximum field enhancement is between the two NP.

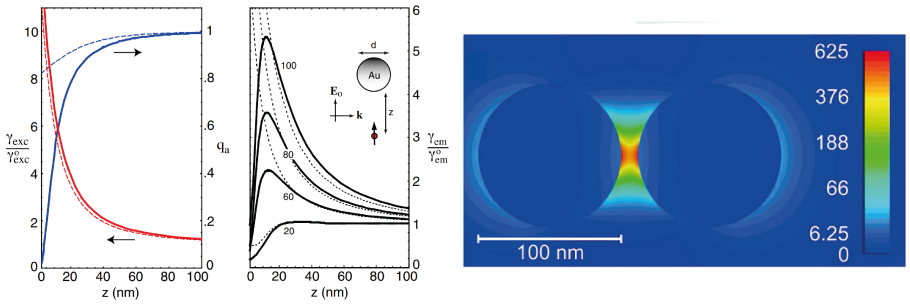

Figure 14: Two 100 nm Au NP, interparticle distance 12 nm and numerically simulated electric field intensity. Incident light is polarized parallel to the dimer at 640 nm. Figure adapted from reference and reprinted with permission.[64] Copyright 2015 American Chemical Society.

For experimental quantification of single-molecule fluorescence enhancement, the enhancement factor f_F is defined (fluorescence signal $I_{antenna}$, laser excitation power $P_{antenna}$, I_{un} and P_{un} respective reference without NP):

$$f_F = \frac{I_{antenna} P_{un}}{I_{un} P_{antenna}} \tag{21}$$

It has been reported that molecules with low intrinsic quantum efficiency η_0 lead to more strongly enhanced fluorescence than emitters with high quantum efficiency, due to their potential for improvement. It is enhanced by the factor f_η (f_{nr} non-radiative and f_r radiative decay factor).[109]

$$f_\eta = \frac{f_r}{[(1-\eta_0) + \eta_0(f_r + f_{nr})]} \tag{22}$$

The ideal fluorophore candidate for these studies has a low intrinsic quantum efficiency and overlaps in absorption and emission with the plasmon resonance of the NPs. Since the fluorescence lifetime depends on the non-radiative and radiative processes and both rates are increased in the presence of NPs, highly enhanced molecules exhibit shorter fluorescence lifetimes.[109–113]

2.5 Fluorescent labels

In single-molecule experiments the fluorophore acts as the reporter. Its sensitivity to the environment is its strength and weakness. To make sure that the observed signal in a measurement is not distorted by the label, the dyes properties need to be understood and matched to experimental conditions. Intrinsic fluorophores such as chlorophyll, aromatic amino acids and the enzyme cofactor NADH occur naturally in various organisms.[75] The discovery of the green fluorescent protein (GFP) in jellyfish enabled the attachment of fluorescent labels via genetic engineering.[114,115] The GFP-gene can be inserted at a specific position in the plasmid, so that fluorescently tagged proteins are expressed. Countless FPs have since been discovered and designed.[116] They share the structural components of a chromophore inside the protein surrounded by several amino acid residues and are commonly around $\sim 5nm$ large. Smaller, organic fluorophores have also been synthesized and can label molecules of interest by functionalization. Chemists have extensively studied and tweaked the molecular structure of fluorophores to meet the needs of microscopists.[28,117–120]

2.5.1 Tuning photochemical and photophysical parameters

The most important parameters to consider before selecting a fluorescent label are the molecules **color, brightness and stability**. But also sample compatibility such as soluability and permeability through biological membranes are crucial factors for application.

Several classes of fluorophores have been discovered, each tunable in their properties. For example, fluorescein can be shifted in its **color** from green to red by extending the electronic conjugated system. When the rigidifying oxygen is omitted, fluorescence is entirely lost (see Figure 15).

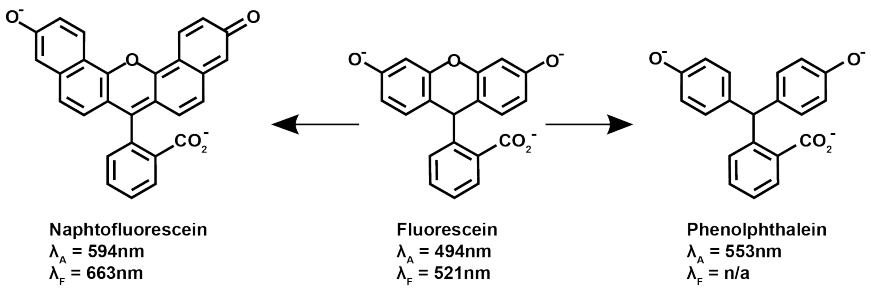

Figure 15: Chemical structures of Fluorescein (center) and derived molecules with red-shifted fluorescence (Naphtofluorescein) and no fluorescence (Phenolphtalein).

The xanthene core is common for all rhodamine dyes. Replacing the heteraoatom often induces large shifts in the emission wavelength (Rhodamine with oxygen:

565 nm emission maximum, with silicon: 666 nm). Other classes of small-molecule fluorophores include coumarins, BODIPY dyes, phenoxazines and cyanines.[37] **Brightness**, dependent on the intrinsic absorption extinction coefficient ϵ and quantum yield (ϕ, see chapter 2.2 equation 7), is another key feature determining the applicability in single-molecule fluorescence experiments. The classic dye tetramethylrhodamine (TMR) undergoes a drastic increase of ϕ when replacing an N,N-dimethyl group with a four-membered azetidine ring (see Figure 16). This method to create the brighter Janelia Fluor 549 dye is one example of how to tune the dye features and is quite broadly applicable.[121]

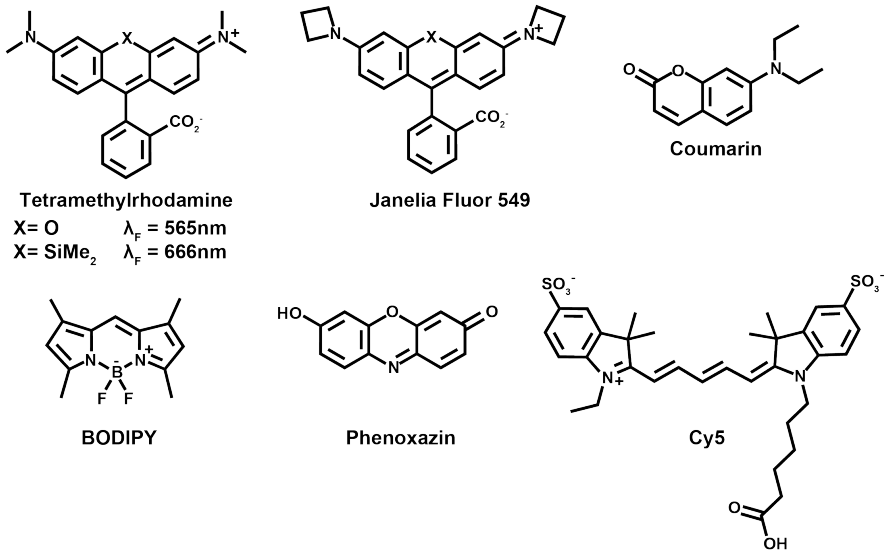

Figure 16: Chemical structures of common small-molecule fluorophore classes.

Any single-molecule experiment ends when the reporting fluorophore stops emitting. It is therefore necessary to use **stable** fluorophores that remain emissive for long enough to gather the required amount of information. The way in which a fluorophore turns non-emissive is, however, not always clear. Two examples are shown in Figure 17. One way to create fluorophores with higher photostability is modifying their structure to minimize their oxidation potential. This can be done by introducing electron withdrawing groups or by introducing shielding moieties. Since the triplet state is often the source of photobleaching, reducing its lifetime is a general strategy to increase stability. For this purpose, small-molecule triplet state quenchers (TSQ) can be covalently attached to the fluorophore.[37] Since standard fluorophores are more accessible to most experimentalists, photostabilization in single-molecule experiments is often rather achieved via solution additives.

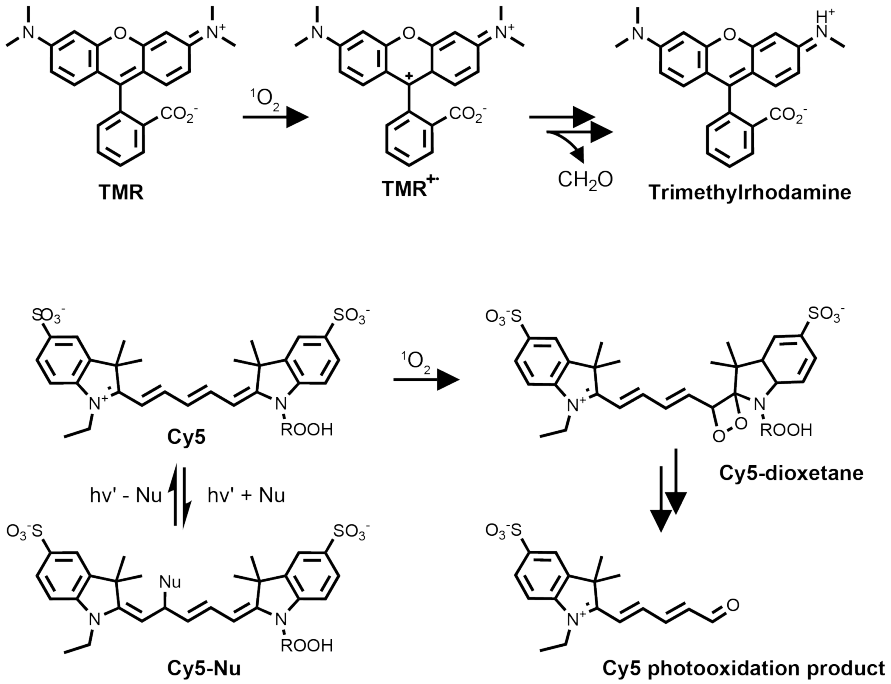

Figure 17: Chemical reactions leading to photobleached products. TMR reacting with singlet oxygen, resulting in blue-shifted trimethylrhodamine. Cy5 undergoing light-induced addition of a Nucleophile (Nu) or addition of singlet oxygen.

Apart from cycling between ground state (S_0) and singlet excited state (S_1), transitions to other electronic states can also occur (Figure 18). One pathway to photobleaching is intersystem crossing from the S_1 to a triplet state (either directly to T_1 or to higher T_n, from which internal conversion to T_1 occurs). The T_1 lifetime is in the range of µs to ms. During this time the molecule is subject to further reactions that lead to photobleaching. Molecular oxygen $^3O_2$, ubiquitous in aqueous solution (∼0.3 mmol), can undergo energy transfer with the triplet state fluorophore.[122] From here, the fluorophore again enters the ground sate, however the highly reactive oxidant $^1O_2$ is released in the process. Consequently, also other reactive oxygen species (ROS) may form.[118]

Fluorescent dyes may also photobleach when photoinduced electron transfer (P*e*T) with redox active molecules takes place. These molecules can be present either in solution or in the biomolecular surroundings (e.g. guanosine, tryptophan). P*e*T can occur both from higher singlet and triplet states, but due to longer triplet state lifetimes it is more likely to take place from the latter. From there, geminate radical ion pairs (GRIP) form. In some instances, GRIP can reenter the singlet state *via* ISC and geminate recombination transfer can take place, returning the fluorophore back to the ground state. In most cases, however, the free radical ions escape from the GRIP. These highly reactive species have been reported to exhibit even longer

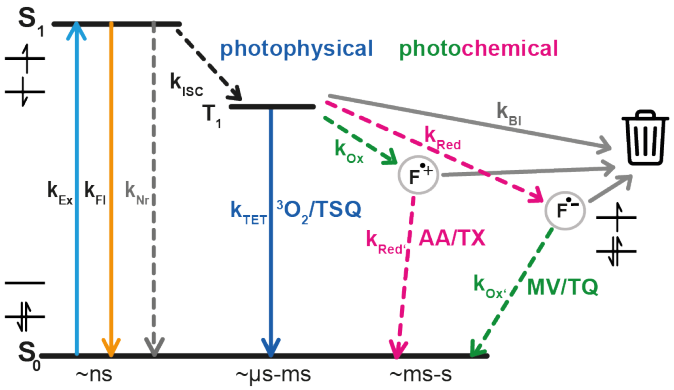

Figure 18: Jabłoński diagram of photobleaching pathways. From the ground state S_0, excitation (cyan) to singlet excited state S_1 occurs. HOMO and LUMO are shown for both. From here, either radiative decay via fluorescence (orange), non-radiative decay (dotted line) or intersystem crossing to triplet state T_1 takes place. Due to its long lifetime, photobleaching pathways (grey) are likely to originate from the triplet state. Energy transfer (blue) to oxygen or physical triplet state quenchers is possible. Photochemical pathways of oxidation (green) and reduction (magenta) lead to radical cations and anions (HOMO and LUMO included). The complementary reaction (reduction/oxidation) sends the fluorophore back to the ground state.

lifetimes than the triplet state. During that time further reactions can take place that lead to photobleaching.[122,123]

One way to circumvent $^1O_2$ related photobleaching pathways is the removal of oxygen, either by injecting argon into the imaging solution or, more commonly, by adding enzymatic oxygen scavengers. The combination of gluocose oxidase (GOD) and glucose converts oxygen to D-gluconic acid and H_2O_2. Catalase (CAT) helps reduce the build-up of H_2O_2. However, this combination (GODCAT) has been shown to lower the pH over longer imaging periods. As an alternative, pyranose oxidase converts glucose to a ketone instead. To recover the fluorophore from the long-lived triplet state, TSQ additives need to be added. They can either act in synergy with oxygen scavengers or individually (competing with $^3O_2$). Photophysical TSQ can recover the fluorophore from the triplet state via energy transfer.[124] For this process to be effective, the triplet energy of the TSQ needs to be lower than that of the fluorophore. Cyclooctatetraene has been demonstrated to effectively stabilize the dyes Atto647N and Cy5, due to its matched energy.[125–129] Also, Ni ions have been reported to photostabilize through this pathway.[130,131] Other TSQ molecules with matching energies may also be explored in the future.[132]

Going the photochemical pathway, redox active additives can induce oxidation or reduction, yielding the radical ions of the dye. The addition of both reducing (e.g., ascorbic acid, AA) and oxidizing (e.g., methyl viologen, MV) leads to consecutive

reactions that recover the fluorophore back to the ground state (Figure 18). However, it is important to note that some additives may also quench the singlet excited state, prohibiting relaxation *via* fluorescence.[133] Therefore, well matched concentrations and energies of the photostabilizers are crucial for getting the most out of every fluorescent dye.

2.5.2 Sensitive reporters on their environment

The responsiveness of fluorescent dyes is the reason why observing individual labels is so powerful. If not fully understood, however, the susceptibility of a fluorescent probe to changes in the environment can perturb the single-molecule experiment.

Once the dye photobleaches, information on the state and position of the molecule of interest is lost, which commonly terminates the experiment. Several approaches try to delay or avoid this process (see chapter 2.5.1). Nevertheless, since one-step photobleaching (Figure 19a) is a unique characteristic of single molecules, it can also help identify them. Single-molecule bleaching experiments report on how many labeled molecules were in the sample by counting the bleaching steps. This can be useful, e.g., to count protein numbers or detect disease biomarkers at extremely low concentrations.[7,134,135]

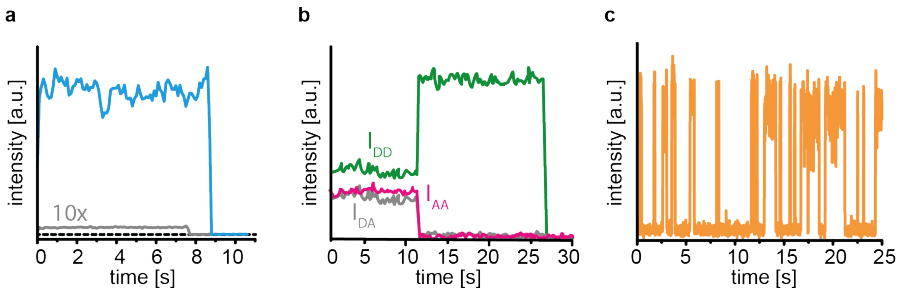

Figure 19: Examples of characteristic single-molecule behaviour. (**a**) Single-molecule digital bleaching down to background intensity. Increased fluorescence intensity due to localized surface plasmon resonance with gold nanoparticles (cyan), without NPs (grey). (**b**) Single-molecule FRET traces of donor excitation/emission (I_{DD}, green) and acceptor excitation/emission (I_{AA}, magenta) channel. Donor excitation acceptor emission channel (I_{DA}, grey). (**c**) single molecule showing blinking behaviour.

Fluorophore properties are also altered through interactions with other molecules. Often, the distinctiveness of these effects depends on intermolecular distance. The presence of (unlabeled) proteins and resulting changes in local viscosity have been shown to influence quantum yield and flourescence intensity (protein induced fluorescence enhancement, PIFE).[136–139] The effect of plasmonic nanostructures on fluorophores has been discussed in 2.4 (Figure 19a).

Fluorescence resonance energy transfer (FRET), a dipole-dipole interaction, is another distance-dependent phenomenon. It takes place when the absorption spectrum of an "acceptor" molecule overlaps with the emission spectrum of a "donor" fluorophore. Donor and acceptor transition dipoles are usually assumed to explore all possible orientations and therefore are held constant for dynamic random averaging. Importantly, the effect occurs in a range from 1 to 10 nm and its efficiency scales with distance. As an example of applying FRET to biosensing, a protein is equipped with fluorescent dyes at two positions (donor and acceptor). Conformational changes of the protein will change the distance between the two probes and thereby FRET efficiency. This can be registered in several ways: Due to the energy transfer to the acceptor, the donor will exhibit a lower emission intensity and slower photobleaching rate. Additionally, since energy transfer occurs from the donors excited state, the fluorescent lifetime decreases. The acceptor can release the energy recieved from the donor via increased photon emission. In single-molecule intensity time traces the photobleaching of the acceptor should be accompanied by an increase in donor emission if FRET has previously occured. Subsequently, donor photobleaching should be observed to prove the involvement of individual molecules (Figure 19b).

Since the energy transfer process is independent of absorption and emission of photons, the acceptor does not need to be fluorescent.[140] In this case, only the fluorescence of the donor is quenched, which can be used to create fluorogenic probes, emitting only upon separation of quencher and fluorophore (e.g. opening a DNA hairpin).[141] In some cases, dyes also undergo self-quenching (homo-FRET) or exciton diffusion which can prohibit close placement of dyes next to each other.[142,143] While all of these processes have the potential to disturb experiments, their specific signature can also be used purposefully for single-molecule sensing.

When a molecule transiently goes into a low or non-emissive state, the process is referred to as photoblinking (Figure 19c).[144] This can be caused by several photophysical effects such as excited triplet states, photoisomers or geminate radicals (chapter 2.5.1).[122,145–147] Discrete spectral shifts such as photoblueing[148] similarily affect the fluorescence intensity. Changes in emission wavelength or intensity can originate from local interactions or conformational changes such as molecular rotation.[149]

Super-resolution microscopy methods have used the reversible single-molecule blinking of dyes to resolve distances beyond the diffraction limit (see chapter 2.6.3). In stochastic optical reconstruction microscopy (STORM), the Cy5 fluorophore is driven to a dark state by formation of a thiol adduct and subsequently returned

to the fluorescent state.[150–152] To decide on an appropriate labeling and imaging modality for an experiment, careful consideration of the fluorophores properties and susceptability is required to fully exhaust the dyes performance.

2.6 Microscopy methods - Theory

When designing a single-molecule experiment, it is also vital to match the fluorescent label with the detection method. The accessible amount of information is determined by how many photons the fluorophore emits and how well the optical equipment detects them. The brightness of the fluorescent dye can be increased, as discussed in the previous chapters 2.4 and 2.5.2. This is especially important in highly concentrated samples where the signal of a single molecule needs to be distinguished from the background.[43] This signal-to-noise ratio can be described as in equation (23).[153] D is the overall detection efficiency factor, depending on the instruments material-dependent collection and quantum efficiency. ϕ_f is the fluorescence quantum yield, σ_P the peak absorption cross-section, P_0 the laser power and T the integration time. A is the laser beam area in the sample and hν the photon energy. C_b is the background count rate per watt excitation power and N_d the dark count rate. The three summands in the denominator correspond to shot-noise from the emission path, background and the dark counts.

$$SNR = \frac{D\phi_f\sigma_P P_0 T}{\sqrt{(D\phi_f\sigma_P P_0/Ah\nu) + C_b P_0 T + N_d T}} \tag{23}$$

2.6.1 Confocal Microscopy

In confocal microscopy point illumination is achieved by reducing the beam shape to a diffraction-limited spot.[8,75] The minimal spot size is determined by Abbe's diffraction limit d (wavelength λ, refractive index n, opening angle α).

$$d = \frac{\lambda}{2n\sin(\alpha)} \tag{24}$$

This is achieved by using a collimator and pinhole in the excitation path and another pinhole in the emission path where fluorescence originating from the excited sample is guided towards the detector (see Figure 20). Only a small region of the microscope slide is illuminated but several areas in up to three dimensions can be probed using a scanning stage. Fluorophores within the excitation volume emit photons that travel back through the objective. The dichroic mirror filters out the photons of the excitation beam (separated by wavelength, see chapter 2.2). Photons are detected on sensitive avalanche photodetectors for each wavelength and guided

towards a time correlated single photon counting (TCSPC) unit. This allows for single-molecule fluorescence lifetime measurements.

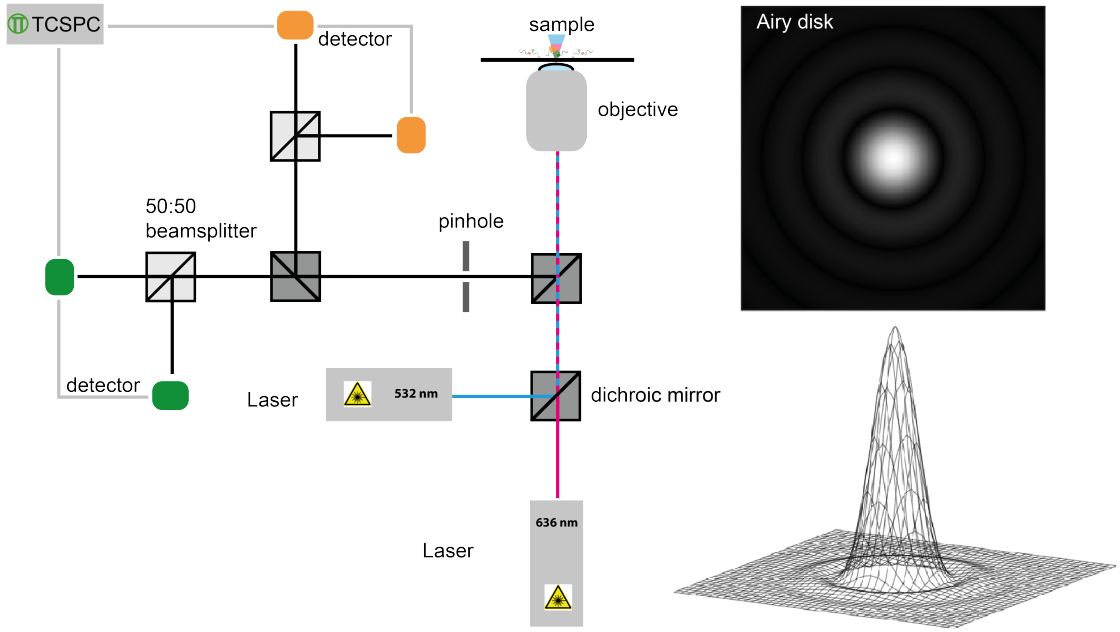

Figure 20: Left: Schematic of the beam path in confocal microscopy. Right: Airy disk and surface plot. Figure reproduced from reference and reprinted with permission. Copyright 2010 College of American Pathologists

The point-spread function (PSF) is the intensity distribution of the photons emitted by a point source. In confocal microscopy it is affected by the excitation and emission pinholes. It has the shape of an Airy disk (Figure 20) which is described with the following formula:

$$PSF_{confocal} \approx PSF_{excitation} \cdot PSF_{detection} \tag{25}$$

$$d(x,y) = \frac{0.37\bar{\lambda}}{NA} \tag{26}$$

$$d(z) = \frac{0.64\bar{\lambda}}{n - \sqrt{n^2 - NA^2}} \tag{27}$$

$$\bar{\lambda} = \sqrt{2}\frac{\lambda_{excitation}\lambda_{emission}}{\sqrt{\lambda^2_{excitation} + \lambda^2_{emission}}} \tag{28}$$

The first minimum r of the Airy pattern in the series of concentric rings from the emission source defines the smallest angular separation (d) of two objects. While the resolution in the widefield microscope is diffraction limited,the confocal microscope achieves smaller values for d:

$$d_{Confocal} = \frac{1}{\sqrt{2}} d_{Widefield} \tag{29}$$

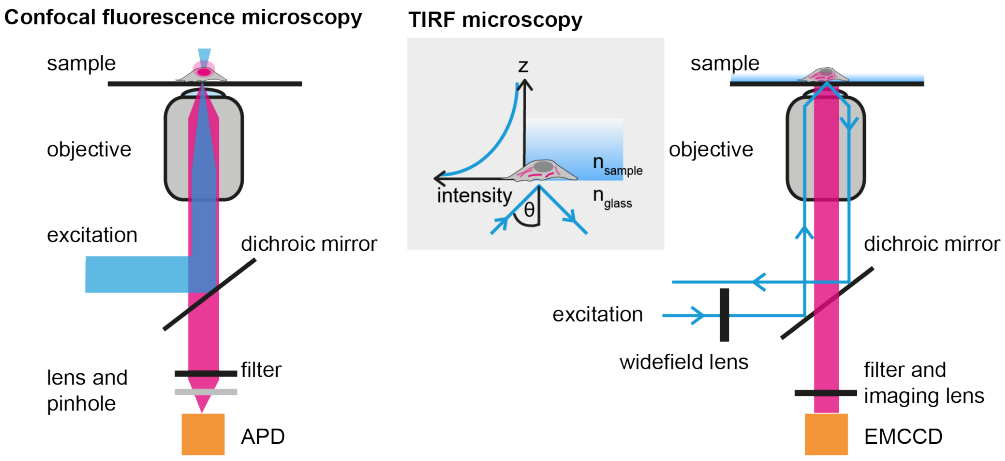

Figure 21: Comparison of two fluorescence microscope configurations: Confocal and total internal reflection configuration.

2.6.2 Total internal reflection

For imaging of biological samples, microscopists require means to reduce the inherent background of the sample. By positioning the excitation laser at a critical angle, total internal reflection (TIRF) occurs at the sample surface.[154] Above the glass, refracted wavefronts align perpendicularly and the field intensity exponentially decreases (equation 30). As a result, penentration depth and thereby excited volume are limited to ∼100 nm. In contrast to epifluorescence, where the laser beam travels perpendicularly through the sample (0°), TIRF illumination significantly minimizes the background that originates from out-of-focus emitters deeper inside (z) the sample.

$$I(z) = I_0 e^{-z/d} \tag{30}$$

2.6.3 Super-resolution microscopy

For detailed studies of biomolecules microscopy needs to resolve structures beyond the diffraction limit. Super-resolution techniques provide insight into nanometer dimensions by either physically reducing the size of excitation PSF or influencing the transition between the fluorophores states (e.g., on and off-state).

Point-spread function engineering

Reversible saturable (or switchable) optical fluorescence transitions (RESOLFT) methods improve resolution by modifying the PSF.[12,155,156] Fluorescent probes in their on-state (S_1) are switched off (to S_0, triplet states, isomers) in a spatially controlled manner.

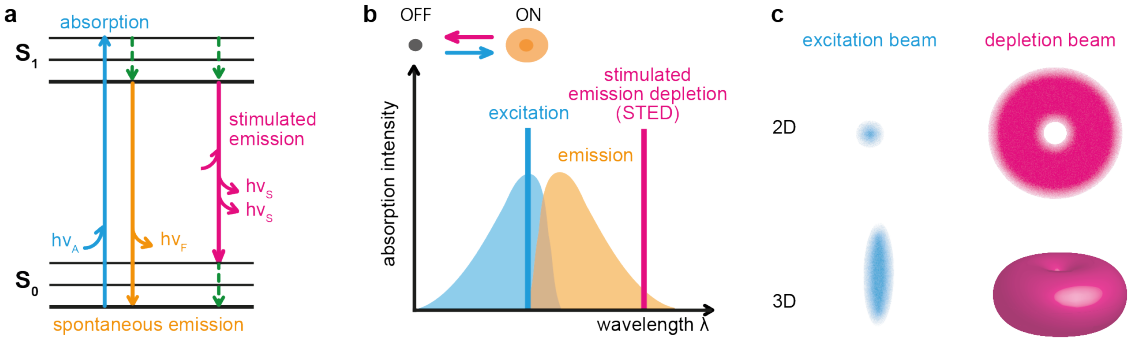

Figure 22: Principle of STED microscopy. (**a**) Jabłoński diagram comparing spontaneous to stimulated emission. (**b**) Excitation and emission spetrum of fluorophores for STED. (**c**) Point spread functions of beams generated by phase plates in the excitation path in two and three dimensions.

The saturation intensity at which the switching transition occurs is inversely proportional to the off and on-state lifetime. Stimulated emission depletion (STED) uses extremely high intensities of the so-called depletion laser (Figure 22). As it exceeds the saturation intensity, each incoming photon has a greatly increased probability to lead to photoswitching. The region in which a fluorophore is able to remain in the on-state is held small to increase the lateral resolution (Figure 22c). This way, only few molecules in a defined region fluoresce and the majority remains non-emissive. Similar to confocal microscopy, the STED lasers are raster-scanned to image the entire sample. The resolution in full width at half maximum (FWHM) of the PSF is approximated as: (λ: excitation wavelength, NA: numerical aperture, I_{max}: peak depletion laser intensity, I_S: fluorophore saturation intensity)

$$FWHM \approx \frac{\lambda}{2NA\sqrt{1 + a(I_{max}/I_S)}} \tag{31}$$

Other super-resolution techniques that use specific excitation beam shapes such as patterns, include structured illumination microscopy (SIM).[157,158] In lattice light-sheet microscopy[159,160] (LSS) the excitation laser illuminates perpendicular to detection and creates succesive planes through the specimen.

Single-molecule localization microscopy

Single-molecule-based super-resolution techniques improve resolution without the need for modification of the optical properties of the microscope or scanning across the sample. In densely labeled samples where emission profiles of fluorescent labels overlap, it is advantageous to observe individual molecules instead of imaging the ensemble (Figure 23a and b). Super-resolution radial fluctuation (SRRF) microscopy[161] approaches this issue by analyzing fluctuations in the radial symmetry of the emitter PSF during the measurement. Super-resolution optical fluctuation imaging (SOFI)[162] makes use of fluorophores cycling between distinguishable intensity states and derives their cumulants. By sequentially turning only a subsection of fluorophores on, their emission profiles no longer overlap and their positions can be determined at distances smaller than the diffraction limit (Figure 23 a and b).

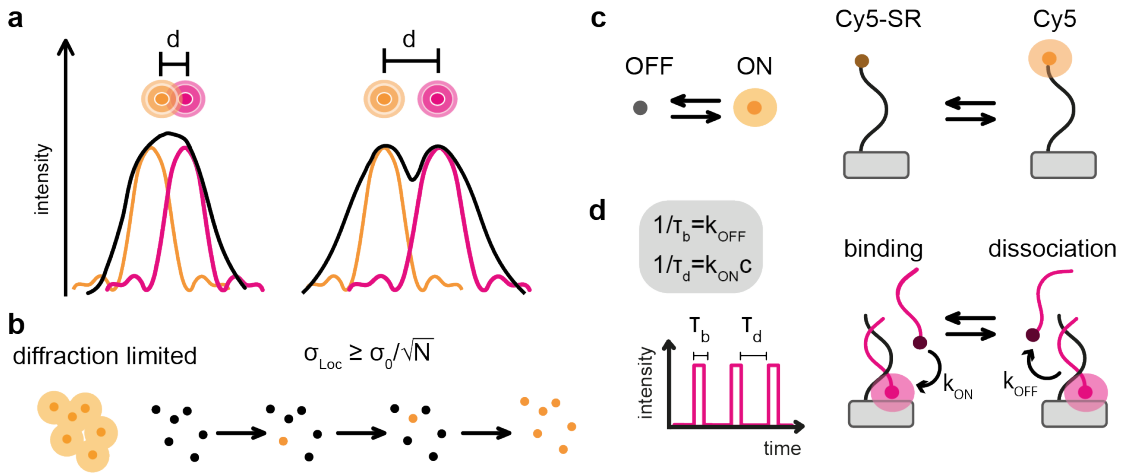

Figure 23: Principle of single-molecule localization microscopy. (**a**) Rayleigh criterion that defines the smallest resolvable distance d. (**b**) Diffraction limited imaging with all emitters on. Switching on only a subsection of emitters, allows precise localization. (**c**) Principle of dSTORM with reversible photoswitches. (**d**) DNA-PAINT dissociation rate (k_{OFF}) and association rate (k_{ON}). Binding and dissociation of the dye-labeled imager strand leads to apparent blinking traces.

Labels for single-molecule localization microscopy (SMLM) can be spontanously blinking probes (hydroxymethyl silicon-rhodamine HMSiR) or fluorophores that are converted, activated or photoswitched in a controlled manner.[163] Specific fluorescent proteins such as mEos can undergo photoconversion from green to red fluorescence when illuminated with UV light. Other FPs such as PAmCherry are reversibly photoactivated upon UV irradation to turn from non-emissive to emitting at 595 nm and return to their dark state when quenched by blue light. Photoactivation lo-

calization microscopy (PALM)[14,164] uses this particular feature of FPs for acquiring super-resolution images.

In stochastic optical reconstruction microscopy (STORM)[15] photoswitching is realized with organic fluorophores such as the pair Cy5 and Cy3. After illumination, Cy5 forms a dark state from which it can be recovered when illuminated with green light in proximity to Cy3. Photoswitching between dark and emissive state of one fluorophore instead of the pair can also be realized[165,166] such as in dSTORM[167,168] (Figure 23c). For this, carbocyanines such as Cy5 or Alexa Fluor 647 are reversibly driven towards formation of non-emissive states such as thiol-adducts.[151,152]

Instead of controlling photophysical processes such as photoactivation or chemically induced photoswitching, PAINT (point accumulation for imaging nanoscale topography) microscopy relies on dynamic labeling (Figure 23d).[17] In an imaging solution with freely diffusing labels their signals appear blurred. However, upon binding to the targets of interest, the emission of a label can efficiently be detected as a PSF and localized. This imaging method relies on the continous exchange of fluorophores and is therefore less compromised by the photobleaching of individual labels.

DNA-PAINT

In DNA-PAINT, biomolecules are tagged with a ssDNA docking strand, so that a complementary dye-labeled DNA sequence (imager strand) can transiently bind with an association rate (k_{ON}).[18] The duration of the on-event (bright or bound time, τ_b) therefore depends on the energy released upon duplex formation and can be tuned by adjusting sequence and length of the DNA. Binding events should be long enough to allow sufficient detection of photons but short enough to ensure quick acquisition of many localizations. Several other factors also influence the hybridization kinetics in a DNA-PAINT experiment (see Figure 24): The dissociation rate k_{OFF} was shown to be tunable through addition of the solvent ethylene carbonate.[169] The dark time (or dissociated time τ_d) can be adjusted by optimizing the buffer composition or concentration of the imager. Hybridization kinetics are dependent on the concentration of Mg^{2+} or Na^{+} cations that influence duplex stability. Preventing the formation of secondary structures in the imager strand also improves its accessibility for duplex formation.[170] This can be achieved either by directed sequence design or with the help of proteins. The Ago protein has been shown to preorder the DNA and RNA into a helical conformation, leading to higher imaging speed.[171] By designing a docking site with a repetitive sequences that partially overlap, the

binding frequency of one imager can be further increased.[172]

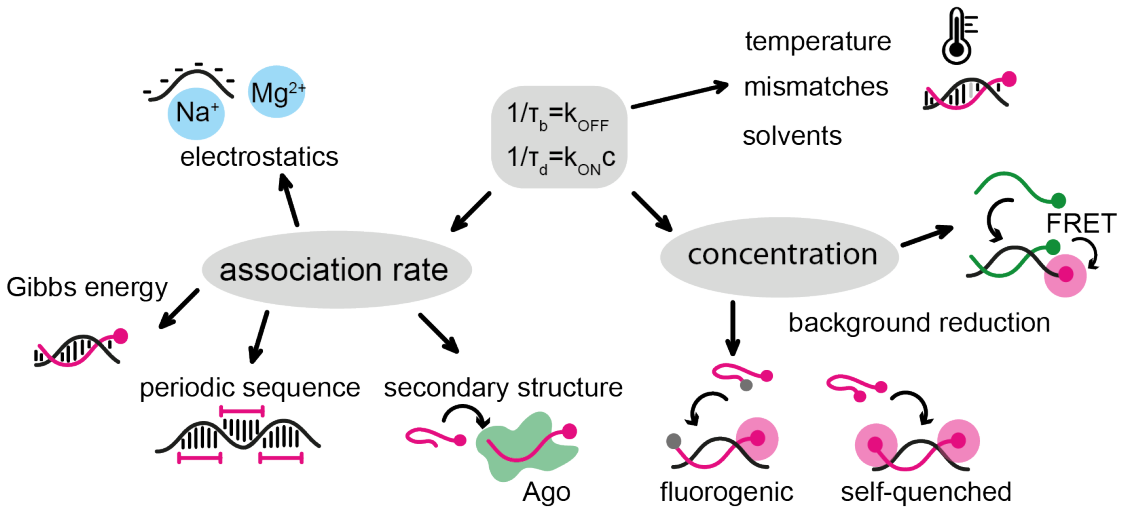

Figure 24: Influences on DNA-PAINT hybridization kinetics. k_{OFF} is affected by temperature, base-pair mismatches and solvents such as ethylen carbonate. The dark time is governed by k_{ON} and imager concentration. The association rate is adjustable through salt concentration and duplex stability. Periodic motifs in the docking site increase the binding frequency. The minimization of secondary structures reduces the entropic barrier of hybridization. To increase concentration without increasing background, fluorogenic probes or a donor/acceptor FRET-PAINT scheme are employed.

The concentration of dye-labeled strands in solution is limited by the increased background that is created by the diffusing probe. A variety of methods exist to circumvent this issue. Labeling docking strand and imager strand with a FRET pair allows the detection of fluorescence in the FRET acceptor channel only.[173] However, spectral cross-talk of the donor to the acceptor channel may limit the advantage. Another approach is the photoactivation of reductively caged labels that turn emissive upon UV illumination.[174] The Cy3B dye used in this study may, however also recover spontaneously, decreasing the fluorogenicity. Other methods involve a more complex imager strand design, such that fluorescence is entirely quenched in solution due to secondary structure formation (e.g., DNA hairpins).[175] Only upon binding to the DNA docking site, fluorescence occurs due to an increased distance between fluorophore and quencher. This also enables adding the probe at high concentrations (10 µM) without significant background.[176] For fast k_{ON}, sequence length and secondary structure formation are carefully optimized and matched with an fluorophore/quencher pair that produces high contrast. Self-quenching probes, doubly labeled with fluorophores on both ends, can also be implemented to improve signal increase upon binding.[177,178] When separated, both dyes emit which leads to a higher photon output and also improves the effective photostability.

Analysis of the acquired image stacks involves finding the center of the localization by curve-fitting the emission profile. The standard deviation of errors in the estimated coordinates (localization precision σ_{loc}) has beed defined as:[23,25] (σ_0: standard deviation of the emitter PSF, N: number of photons, a: pixel size of the camera, b: background intensity)

$$\sigma_{loc} \geq \sqrt{\left(\frac{\sigma_0^2 + a^2/12}{N}\right)\left(\frac{16}{9} + \frac{8\pi(\sigma_0^2 + a^2/12)b^2}{Na^2}\right)} \tag{32}$$

To fit the localization, the maximum likelihood estimation is the state-of-the-art algorithm. For this, a so-called gradient ascent is used to iteratively determine the likelihood at a position.

The achievable resolution of DNA-PAINT was further improved down to Ångström distances by implementation of sequential imaging (RESI).[20] If target molecules in close proximity (sub 10 nm) are reliably equipped with orthogonal labeling sequences, they can be probed in separate, subsequent imaging rounds to generate two distinct PSFs.

Crucial for all super-resolution techniques is the collection of a sufficient number of photons during imaging. The photon budget determines spatial resolution, imaging depth, acquisition speed and the amount of photodamage.[24,163,179]

2.6.4 Accessible Microscopy for Diagnostics

Advanced fluorescence microscopes used in reasearch are often self-built and require trained personal for operation. Together with the high cost of the equipment, they are poorly accessible. One key component is the photon detector such as an avalanche photodiodes (APD), charge coupled devices (CCD), or a complementary metal oxide semiconductor (CMOS) camera. The technology of cameras in ubiquitously available smartphones has developed rapidly, making them a suitable alternative for a low-cost component for a portable microscope.[180] Current models include electron-multiplying CCDs, sCMOS or back-illuminated CMOS as detectors.[181] Often, multiple cameras are included to correlate and reduce noise. In addition to serving as the camera, the smartphone can store, compute and transmit acquired data making its use largely independent of local infrastructure. Together with sensitive and specific diagnostic assays that report on the presence of biomarkers, smartphone-based detection devices can be realized for the use at the point of care (POC). Similar to fluorescence microsocpy in research, the method benefits of detection reagents and labels having high photostability and brightness.[182]

3 Materials and Methods

3.1 Sample preparation

Cell culture

Cos-7 cells (ATCC) were cultured in DMEM (Gibco, No. 11965084) medium supplemented with 10% FBS (Gibco, No. 10500064). Cells were passaged twice a week using 0.05% trypsin EDTA (Gibco, No. 25300054).

Cos-7 cells were seeded on Ibidi eight-well glass-bottom chambers (No. 80827) at a density of 25 000 cm^{-2}. Before imaging, cells were fixed using the protocol described by Whelan and Bell,[183] using 0.4% Glutaraldehyde (Sigma Aldrich, USA) and 0.25% Triton X-100 (Sigma Aldrich, USA) in CSB (1M NaCl, 100 mM PIPES, 30 mM $MgCl_2$, 10 mM EGTA, 10 mM Sucrose; pH = 6.2) for 90s. After twice with 37°C PBS, cells were incubated with 3% Glutaraldehyde in CSB for 15 min, followed by washing with PBS (30s, 1min, 5min, 10min, 15min). To quench residual aldehyde, the reductant $NaBH_4$ was added at 0.5% (w/v), followed by PBS washing steps (30s, 1min, 5min, 10min, 15min). To avoid unspecific binding of antibodies, a 45 minutes blocking step in antibody incubation buffer (Massive Photonics) was included. Primary rat anti-tubulin antibody (Massive Photonics) was incubated overnight at 1:100 dilution. After washing twice with washing buffer (WB, MP), secondary anti-rat Ab (MP) was added at a 1:100 dilution and incubated overnight. Afterwards, the sample was washed three times and stored in washing buffer before imaging.

For in vivo measurements of red blood cells, microscope cover slides (22mm × 22 mm and 76 x 26 mm, Carl Roth GmbH, Germany) were cleaned using Ethanol 70% and dried with Kimtech Wipes (Merck KgaA, Germany). Then the slides were treated for 30 min at 100 °C in a UV-Ozone cleaner (PSD-UV4, Novascan Technologies, USA). Dust was removed with compressed air. Two stripes of double-sided tape (3M, Germany) were then glued onto the long edges of the large slide and a small cover slip laid on top to create a flow chamber. 200 µL of purified iRBC were centrifuged for 30 seconds at 1800 rpm at RT. The supernatant was discarded and the sediment was washed twice with 500 µL cell culture medium. After each washing step, the sample was placed in the centrifuge for 30s at 1800 rpm RT. To stain the parasite organelles, 200 µL of 2 µM SiR-glib in medium were added to the sediment and incubated for 1h at 37 °C. The sample was then washed twice with 500 µL cell medium, performing centrifugation steps after each wash (30 s at 1800 rpm RT). The sediment was diluted individually in medium to yield samples with

similar blood cell concentration. Diluted blood samples were added to the chamber, which was sealed from one side with one Tough-Tag (Diversified Biotech) and closed with another from the other side.

DNA Origami design and production

The structural design of DNA origami was created with the open-source software package with graphical user interface for 3D origami shapes *caDNAno* version 2.3.0.[184] Structural rigidity and flexibility was simulated using the online tool *CanDo*.[185,186]

Table 1: Parameters used for *CanDo* simulation. Values provided by the developers.

Parameter	Value
Axial rise per bp [nm]	0.34
Helix diameter [nm]	2.25
Crossover spacing [bp]	10.5
Axial stiffness [pN]	1100
Bending stiffness [pN x nm^2]	230
Torsional stiffness [pN x nm^2]	460
Nick stiffness factor	0.01

Trident NACHOS were assembled using 25 µL of 100 nM p8064 scaffold and 18 µL unmodified staple strands (Integrated DNA Technologies Europe GmbH, Germany). After pooling together the staples at 100 nM initial concentration, an excess of modified staple strands was added at a volume of 2 µL (Eurofins Genomics GmbH, biomers.net GmbH, Germany). 5 µL of folding buffer were added and thermal annealing was performed using the respective temperature ramp.

Table 2: Recipe for the folding of the Fork DNA origami.

Name	Volume [µL]
scaffold	25
unmodified staples	18
modified staples	2
buffer	5
total volume	50

Purification of the reaction mixture and upconcentration of the DNA origami were performed using 100kDa membrane MWCO Amicon Ultra filters (Merck KGaA, Germany). Lower ionic strength FoB5 buffer (refer to supplementary information

of 6.2 for buffer compositions) was added, then the mixture was centrifuged five times for 5 min at 20 °C and a speed of 10 000 g. DNA origami concentration was determined with UV-vis spectroscopy (NanoDrop, Fischer Scientific, USA).

Nanoparticle functionalization

Plasmonic nanoparticles were functionalized using a modified version of a protocol by Mirkin et al..[66,187] 2 mL of the particle solution (BioPure Silver Nanospheres (Citrate), nanoComposix, USA; gold particles from BBI solutions, UK) were continously stirred at 550 rpm at 40 °C. 20 µL of Tween20 10% (Sigma Aldrich, USA), as well as 20 µL potassium phosphate buffer (1 M solutions of each mono- and dibasic potassium phosphate in a 4:5 mixture, Sigma Aldrich, USA) and 10 µL of a 2 nM thiol–modified single stranded DNA solution (5'-thiol-25T-3' or 5'-thiol-20T-3' Ella Biotech GmbH) were added succesively. The solution was then incubated at 40 °C for 1 h. A final concentration of 750 mM of NaCl was achieved by gradually adding portions of salt buffer (PBS3300) over a period of 45 min (refer to supplementary information of 6.2 for buffer compositions). The solution was then diluted 1:1 with PBS10 buffer. Unbound thiolated ssDNA was removed by centrifuging the solution for 10 min at 2800 g and 20 °C. The supernatant was discarded and the pellet dissolved in PBS10 buffer. This washing procedure was repeated four times. The nanoparticles were then diluted in 1xTE containing 750 mM NaCl to reach an approximate value of 0.1 absorption maximum on the UV-Vis spectrometer (Nanodrop 2000, Thermo Fisher, USA). To study differences between DNA origami structures, the same batch of functionalized particles was used to ensure similar ssDNA density.

Surface immobilization of DNA origami and nanoantenna preparation

To prepare glass surfaces for immobilization of DNA origami, microscope coverslips of 24 mm x 60 mm size and 170 µm thickness were UV-Ozone cleaned (PSD-UV4, Novascan Technologies, USA). SecureSeal Hybridization Chambers (2.6 mm depth, Grace Bio-Labs, USA) were then glued to the cleaned coverslips and washed three times with 1xPBS buffer. To passivate the surface, bovine serum albumin (BSA)-biotin (1 mg/mL, Sigma Aldrich) was incubated for 15 min. After washing the chambers three times with 1xPBS, NeutrAvidin (for trial measurements, 0.25 mg/mL) or StreptAvidin (for DNA-PAINT measurements, 0.2 mg/mL) (Sigma-Aldrich) were added and incubated for 15 min. After cleaning the surfaces with 1xPBS three times, DNA Origami was added to the prepared chamber in TE 750 mM NaCl at

an approximate concentration of 50 pM to 250 pM. Sufficient single-molecule surface density was confirmed on the microscope (see chapter 3.2). After three washing steps with immobilization buffer, the nanoparticle solution was added and incubated in different buffers depending on the experiment, including 0.01% Tween20 (Sigma Aldrich, USA). Saples were then incubated at (21 °C) or 37 °C for 3 h to 18 h. The sample was then washed three times with 150 µL the nanoparticle incubation buffer. The surface was stored in incubation buffer to avoid drying and sample degration. Samples containing AF647 were imaged in a reducing and oxidizing buffer system for enzymatic oxygen removal (ROXS).

Sandwich Assay

To avoid unspecific binding of imager strand on the surface, the prepared nanoantenna sample was passivated by incubating BSA in 1 x PBS for 15 min at 1 mg/mL and 12.5 mM $MgCl_2$. Target DNA specific to the Oxa-48 gene was diluted to 4 nM concentration. Alexa Fluor 647 imager was diluted to 12 nM, both in 1xTE containing 2 M NaCl. A 1:3 ratio of target to imager solution was added with target concentration of 2 nM.To achieve higher binding yields, the concentration was raised to 4 nM target, while maintaining the 1:3 target/imager ratio, adding 0.01% Tween20 (Sigma Aldrich, USA) to the buffer. The sample was incubated for 2 h at 37 °C. Unbound target and imager strands were removed after incubation by washing three times with 1xTE buffer containing 2 M NaCl. Afterwards, the sample was imaged on the confocal microscope.

3.2 Microscopes and imaging conditions

Confocal microscope 1

To detect the fluorescence of single molecules in DNA origami structures, a custom-built confocal setup based on an Olympus IX-83 inverted microscope (Olympus Corporation, Japan) with a 78 MHz pulsed supercontinuum white-light laser (SuperK Extreme, NKT Photonics A/S, Denmark) was used. An acoustooptically tunable filter (AOTF, SuperK Dual AOTF, NKT Photonics, Denmark) and a digital controller (AODS 20160 8R, Crystal Technology, Inc., USA) allowed for wavelength selection between 532 and 639 nm via software (AODS 20160 Control Panel, Crystal Technology, Inc. USA). To alternate between the two wavelenghts, a second AOTF (AA.AOTF.ns : TN AA-Opto-Electronic, France) was used. Using a LabVIEW software, the laser intensity was set via the second AOTF and the laser

beam spectrally cleaned. To manually regulate the laser intensity, a neutral density filter (ndF, OD 0-2, Thorlabs, Germany) was used, followed by a linear polarizer (LPVISE100-A, Thorlabs, Germany) and lambda quarter plate (AQWP05M-600, Thorlabs, Germany) for circular polarized excitation. The laser was coupled into a polarization maintaining fiber (PM-Faser, P1-488PM-FC-2, Thorlabs, Germany) to overcome the height difference between excitation path and microscope body. The laser was then focused onto the sample with an oil-immersion objective (UPlanSApo100x, NA = 1.4, WD = 0.12 mm, Olympus Corporation, Japan). A piezo stage (P-517.3CL, E-501.00, Physik Instrumente GmbH & Co. KG, Germany) positioned the sample. The excitation light was separated from emission through the dichroic beam splitter and focused on a 50 µm pinhole (Linos AG, Germany). Red and green emission channels were spectrally separated (red: RazorEdge 647, Semrock Inc., USA and green: Brightline HC582/75, Semrock Inc, USA). Photons were detected by a Single-Photon Avalanche Diode (SPCM, AQR 14, PerkinElmer Inc., USA) and registered by a TCSPC system (HydraHarp 400, PicoQuant GmbH, Germany). Scans of the sample were performed at powers of 2 µW before the objective, 50 nW for transients of samples with NPs, 200 nW for samples without NPs.

Confocal microscope 2

Another confocal setup, based on an Olympus IX-71 microscope body was also used for single molecule data acquisition. For this a LDH-D-C-640 laser (636 nm) or LDH-P-FA-530B laser (532 nm) (PicoQuant, Germany) were collimated and passed a linear polarizer (LPVISE100-A, Thorlabs GmbH) and a lamda quarter plate (AQWP05M-600, Thorlabs GmbH) to generate circularly polarized light. The excitation beam was focused on the sample with an oil-immersion objective (UPLSAPO100XO, NA1.40, Olympus Deutschland GmbH). A piezo stage (P-517.3CD, Physik Instrumente GmbH & Co. KG) and piezo controller (E-727.3CDA, Physik Instrumente GmbH & Co. KG) were used to scan the sample. A dichroic beam splitter (zt488/543/ 635/730rpc or zt532/640rpc, Chroma Technologies) separated the fluorescence emission from excitation light. The beam was then focused on a pinhole (50 µm diameter, Thorlabs GmbH). A beam splitter (HC BS 749 SP or 640 LPXR, Chroma Technologies) separated the red and green emission channel. Subsequently, red fluorescence was directed towards an APD (SPCM-AQRH-14-TR, Excelitas Technologies GmbH & Co. KG, Germany). For correlation studies a nonpolarizing 50:50 beam splitter (CCM1-BS013/M, Thorlabs GmbH) directed the beam to another APD (SPCM-AQRH-14-TR and SPCM-AQR-15, Excelitas Tech-

nologies GmbH & Co. KG, Germany). Green emission was directed towards another APD (SPCM-AQRH-14-TR, Excelitas Technologies GmbH & Co. KG, Germany) or distributed between 2 APDs (SPCM-AQRH-14-TR and SPCMAQR- 15, Excelitas Technologies GmbH & Co. KG, Germany) using another nonpolarizing 50:50 beam splitter (CCM1-BS014/M, Thorlabs GmbH). A multichannel picosecond event timer registered incoming photons (HydraHarp 400, PicoQuant GmbH). All hardware was controlled using a commercial software (SymPhoTime 64, PicoQuant GmbH).

Widefield microscope

A custom-built total internal reflection fluorescence (TIRF) microscope, based on an inverted microscope (IX71, Olympus) was used to perform DNA-PAINT measurements in fixed cells. A nosepiece (IX2-NPS, Olympus) was implemented for drift suppression. Red excitation at 644 nm was realized with a 150 mW laser (iBeam smart, Toptica Photonics) and spectrally filtered with a clean-up filter (Brightline HC 650/13, Semrock). The excitation beam was coupled into a polarization maintaining single mode fiber (P3-488PM-FC-2 for 560 nm, P3-630PM-FC-2 for 644 nm) to achieve a gaussian beam shape. Behind the fibers, excitation beam paths were combined with a dichroic mirror (T612lpxr, Chroma). A homogenous excitation profile across the whole detection plane was achieved by guiding the laser light through a diffractive beam shaper (piShaper 6_6_ VIS, AdlOptica) to change the Gaussian beam profile to a flat-top beam profile. Coupling into the microscope body was done with a triple-color beam splitter (Chroma z476-488/568/647, AHF Analysentechnik). Light was focused on the back focal plane of an oil-immersion objective (100x, NA = 1.45, UPlanXApo, Olympus) with a telescope, that can be aligned for TIRF illumination. An additional x1.6 optical magnification lens was included in the detection path to achieve an effective pixel size of 92.6 nm. Fluorescence emission was spectrally cleaned (ET 700/75, Chroma for red excitation or ET 605/70m, Chroma for yellow excitation) and recorded using an electron multiplying charge-coupled device camera (Ixon X3 DU-897, Andor). The camera was controlled with the Micro-Manager 1.4 software.[188,189] Cos-7 samples, without andwith pCOT/rCOT were measured using an excitation power density of ca. 0.6 kW/cm^2 for 36000 frames at 100 m sec exposure time and EM gain set to 150.

Smartphone microscope

Inside the portable box (LMU Munich chemistry department workshop) the 638 nm

laser diode with output power 180 mW (0638L-11A, Integrated Optics, UAB, Lithuania, driven by a portable power bank) was focused onto the sample at a $\sim 45°$ angle. After passing spectral filtering (BrightLine HC 731/137, Semrock Inc., USA), the fluorescent signal was collected using an objective lens (NA = 0.25, LS-40166, UCTRONICS, USA) that guides the light to the monochrome camera of the smartphone (P20, Huawei, China).

3.3 Data analysis

Smartphone data

The FreeDCam application (Troopii) was used to acquire movies. These were analyzed with ImageJ 1.54f (Fiji, Java 1.8.0_322) after file conversion with the FFMPEG plugin to .tif (32-bit). A home-written macro crops a defined region of interest in the video and calculates the area of pixels above a defined threshold. This threshold is individually set to the intensity value that is above the highest pixel intensities detected in the uninfected sample (100 for samples without dye, 120 with dye). The extracted data was analyzed using OriginPro2019. Significance was determined using an ANOVA test.

Confocal data

A custom LabVIEW software (National Instruments, USA) was used to process the data acquired on the confocal microscope 1. Background correction was performed for each transient. Fluorescence lifetime decays were extracted and monoexponentially fitted for the shortest lifetime component and deconvolved from the instrument response function using FluoFit (PicoQuant GmbH, Germany). The extracted data were analyzed in OriginPro2019.

Data acquired on the confocal microscope 2 was analyzed using a commercial software (SymPhoTime 64, PicoQuant GmbH). Extracted data in the .fifo format was converted and further analyzed with custom Python codes.

DNA-PAINT

X/y coordinates and photon counts were extracted from raw data using the "Localize" feature of the software Picasso.[190] PSF fitting was performed using MLE with minimal net gradient 12000 and box size 5. To correct for drift, RCC was applied in Picasso "Render". Drift-corrected data was subjected to filtering using a

custom written software.[191] First and last frame were excluded to factor out photon count errors due to incompletely acquired binding events. Only localizations that were detected for more than three frames within half a camera pixel size (93 nm size, distance threshold 50 nm) were included in the filtered data. Rendered images were extracted at the same zoom and contrast settings with individual localization precision blur. Rendered images with color coding according to photon count (32 colors) were extracted setting the maximum photon number to 10000. 3D cross sections of microtubules were generated by picking localizations perpendicular to the microtubules' length using the rectangular tool in Render. The custom-built SIMPLER software in MATLAB was used to extract the axial positions.[191] Following parameters were set: N_0 (photons expected for z = 0) = 7000, Θ_i (incident angle) = 66°, α (evanescent component) = 0.9, NA = 1.45, λ_0 (excitation wavelength) = 644 nm and λ_d (mean detection wavelength) = 700 nm. The ThunderStorm plugin for Image-J was used to create the z-color coded image rendering, as reported in the SIMPLER publication, using a pixel size of 3.5 nm in the super-resolved image, where every localization is rendered as a Gaussian blurred spot with a width of 7 nm. A custom software was used to calculate the localization precision, analyzing individual ON-events. A minimum ON-time of 3 frames is set as a prerequisite for calculating standard deviation in x/y and average number of photons from an event.

4 Fluorophore photostabilization for single molecule imaging and SMLM

4.1 Associated Publication 1

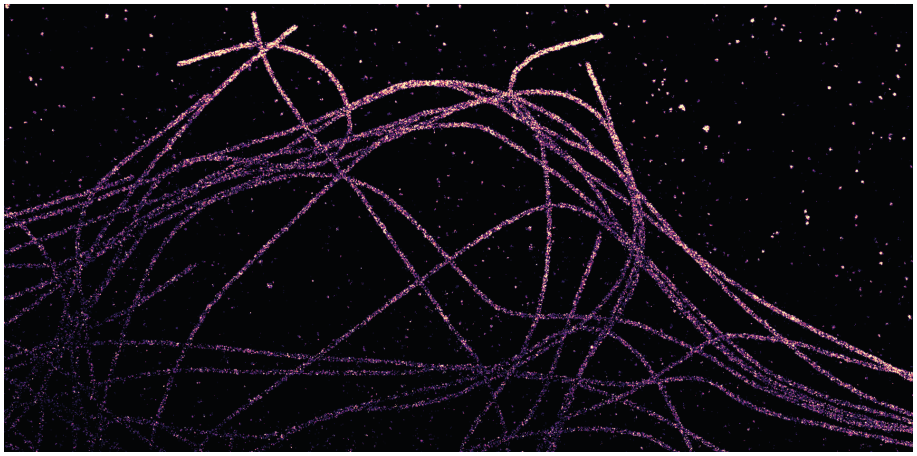

Minimally Invasive DNA-Mediated Photostabilization for Extended Single-Molecule and Super-resolution Imaging

Michael Scheckenbach,* Cindy Close,* Julian Bauer, Lennart Grabenhorst, Fiona Cole, Jens Köhler, Siddharth S. Matikonda, Lei Zhang, Thorben Cordes, Martin J. Schnermann, Andreas Hermann, Philip Tinnefeld, Alan Szalai and Viktorija Glembockyte

*equal contribution

Preprint on bioRxiv 2025/631860 (2025).
doi: https://doi.org/10.1101/2025.01.08.631860

Single-molecule and super-resolution experiments are limited by premature photobleaching of fluorescent dyes. To prolong imaging and improve photostability, imaging solutions commonly contain enzymes for oxygen removal, their substrates and triplet state quenchers. This approach is not universally applicable since the composition of the solution needs to be carefully matched with the fluorophores in use and additives at high concentrations may disrupt the biomolecular environment.

To address these limitations, we developed a modular and minimally invasive photostabilization strategy which relies on the DNA-mediated delivery of a photostabilizer directly to the imaging site. We found an improved photon budget

of permanent dye labels at low excitations intensities outperforming the solution additives. At increased excitation intensities, we identified the stability of the photostabilizer itself as a bottleneck. A recovering photostabilization scheme where the photostabilizer is continuously exchanged but still acts locally at the imaging site significantly slowed down the loss of DNA-PAINT localizations, even under high excitation intensities and ambient oxygen. We further demonstrated the applicability of our approach to complex biological environments by imaging microtubules in cells and observed an improved localization rate and precision, even without oxygen removal.

Our DNA-mediated photostabilization approach offers a promising strategy for challenging biological samples where the delivery of high concentrations of additives is difficult or harmful. Its modularity enables the adaptation to various imaging schemes, simplifies photostabilizer screening and expands the pool of applicable fluorophores for super-resolution microscopy and single molecule imaging.

Author contributions

VG and MS conceived the idea. MS and VG designed and the experiments on DNA origami nanostructures. CC, MS and VG designed DNA-PAINT experiments in fixed cos-7 cells. MS synthesized and characterized DNA origami nanostructures. MS performed bleaching experiments and DNA-PAINT imaging on DNA nanostructures and subsequent data analysis. CC performed DNA-PAINT imaging in fixed cos-7 cells and subsequent data analysis with help of AS. MS and VG performed single-molecule fluorescence correlation studies. AS provided custom written software and support for filtering and analysis of DNA-PAINT microtubule data. JB built the flat-top TIRF setup to enable DNA-PAINT cell measurements. FC provided custom-written software for the analysis of single-molecule bleaching data. LG provided custom-written software for fluorescence autocorrelation studies. AS and JB provided custom written software for filtering and analysis of obtained DNA-PAINT data. SSM and MJS synthesized and provided Cy5-NHS ester. JK and AH synthesized the COT-maleimide NHS ester compound, LZ and TC provided the molecule. VG, AS and PT supervised the study. MS and CC visualized the data. VG, MS, CC and AS wrote the manuscript with additional input from PT, JB, and LG. All authors reviewed and approved the manuscript.

5 Target-specific fluorescent labels for Malaria detection

5.1 Associated Publication 2

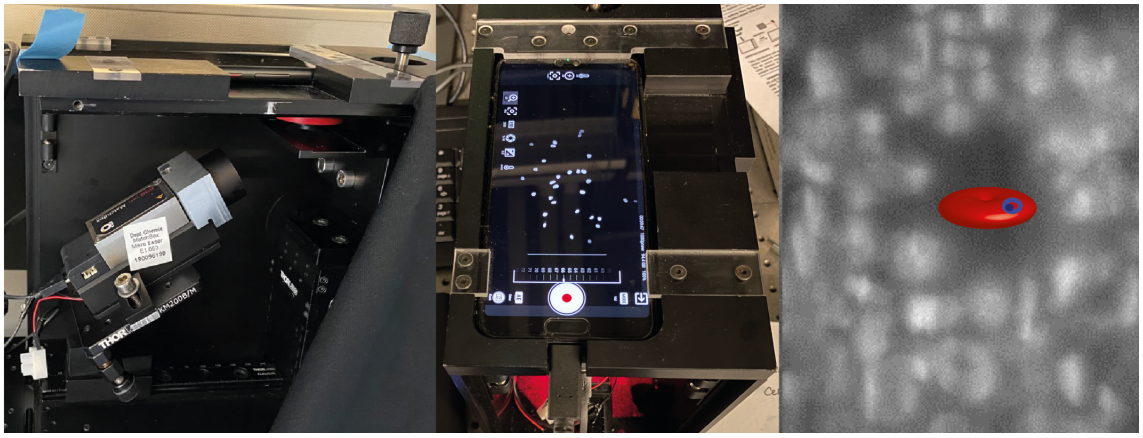

A silicon rhodamine-fused glibenclamide to label and detect Malaria-infected red blood cells

Claudia Bastl*, Cindy Close*, Ingo Holtz*, Blaise Gatin-Fraudet, Mareike Eis, Michelle Werum, Smilla Konrad, Kilian Roßmann, Christiane Huhn, Souvik Ghosh, Julia Ast, Dorien A. Roosen, Martin Lehmann, Volker Haucke, Luc Reymond, David J. Hodson, Philip Tinnefeld, Kai Johnsson, Viktorija Glembockyte, Nicole Kilian, Johannes Broichhagen

*equal contribution

Preprint on bioRxiv 2025/637098 (2025).
doi: https://doi.org/10.1101/2025.02.07.637098

Plasmodium falciparum (*P. falciparum*) is the protozoan parasite responsible for Malaria tropica, the most common and dangerous type of Malaria infection for humans. Its reliable detection is essential to begin treatment of patients as soon as possible. However, regional healthcare providers often have only limited access to electricity or designated diagnostic or treatment facilities.

During the asexual reproduction of the parasite (erythrocytic schizogony), mature human red blood cells (RBCs) act as the host cell. *P. falciparum* invades the RBC and processes nutrients to mature from ring to trophozoite and finally schizont stage.

As organelles are only present in the infected cells (iRBC), uninfected RBCs can be distinguished from ones that have been invaded by the parasite. In this publication, we make use of this unique property by labeling cell organelles with fluorescent probes.

To achieve spectrally well separated fluorescence signals from hemoglobin in its oxygenated or deoxygenated form, a new label was designed. Therefore, a silicon rhodamine (SiR) was chemically fused with glibenclamide (glib) moiety which targets the sulfonylurea receptor 1 of the endoplasmatic reticulum. The probe (SiR-glib) was characterized and tested for specificity by performing live cell confocal imaging of mammalian cells and tissue. RBC infected with the *P. falciparum* strains 3D7 and FCR3 were labeled at all three stages of maturation using a confocal microscope.

To showcase the synergy of the specific, bright and photostable SiR-glib with accessible microscopy, a smartphone-based microscope was used for detection of iRBC. Using the low-cost portable device, cells infected by the 3D7 strain could be clearly differentiated from uninfected RBCs.

Author contributions

LR, KJ, VG, NK and JB were responsible for conceptualization and methodology. CB, CC, IH, BG-F, ME, MW, SK, KR, CH, SG, JA, DR, ML, DJH, VG, NK and JB performed formal analysis and investigation. DJH, NK, and JB wrote the original draft. All authors reviewed and edited the manuscript. Visualization was done by NK and JB with help from CC on Figure 4. VH, PT, KJ, VG, NK and JB supervised the project. Funding was acquired by DJH, PT, VG, and JB.

6 Development and application of DNA origami nanoantennas

Chapters 2.4 and 2.5.2 have established that plasmonic nanostructures influence the fluorescence intensity of dye molecules. Early adaptations of so-called nanoantennas that position the fluorophores in this environment relied on random orientation of the dye.[59,109,192] The dyes were either diffusing in solution or embedded in a polymer. The metal nanostructure was produced using top-down lithography methods. While nanophotonic structures, like the zero-mode-waveguide have been commercially applied for biosensing, such as single-molecule real-time sequencing[193] (Figure 25a), the potential of fluorescence enhancement is not exhausted. Emitters will pass through the hotspot region but not remain fixed at this optimal position for fluorescence enhancement. Approaches using DNA strands as spacers suffered from high flexibility on short length scales.[194–196]

The bottom-up self-assembly approach of DNA-origami finally allowed the arrangement of fluorescent dyes and functionalized nanoparticles with nanometer precision.[197–201] Using a two-dimensional rectangular DNA origami platform, Acuna et al. studied the distance-dependent interaction of the ATTO 647N fluorophore with a gold NP.[63] For this, a dye-labeled staple strand was included in the structure at varying positions. The NP was attached using three protruding binding strands (NPs covered in complementary thiolated DNA) and held at a constant position on the nanostructure. In line with previous reports that used near-field fluorescence imaging of polymer embedded dyes,[59] quenched fluorescence intensity and reduced fluorescence lifetime were observed at dye-particle distances smaller than 15 nm.

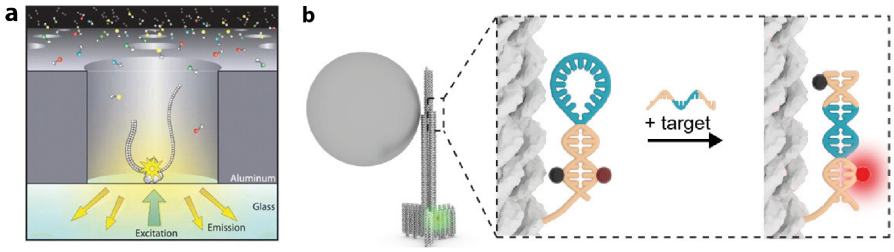

Figure 25: Nanophotonic structures for biosensing.(**a**) Zero-mode-waveguide for single molecule real-time DNA sequencing.[202](**b**) DNA origami nanoantenna pillar including the fluroescence quenched hairpin assay for DNA detection.[66,203] Figure adapted and reprinted with permission. Copyright 2009 AAAS and 2021 American Chemical Society.

To achieve high fluorescence enhancement, a three dimensional DNA origami pillar

was implemented to provide binding sites for two NP and a fluorophore in between.[63] The bottom of the pillar was equipped with biotinylated DNA such that interaction with a glass surface (covered in biotinylated BSA) allowed vertial placement of the structure. Inside the 23 nm gap between NPs, fluorophores and biomolecular assays such as the Holliday junction could be kept at a designated position. For gold NPs of 100 nm diameter fluorescence enhancement up to 60-fold was observed. Holzmeister et al. studied the influence of the particle size on the radiative, non-radiative and excitation rate of dyes in a DNA origami structure.[110] All three rates increased with particle size at fixed interparticle distance. In addition to the particle size, optimized interparticle distance was made possible by adjusting the binding geometry of the NP attachment strands to the zipper approach.[204] Fluorophores in the green and blue spectral range were enhanced by using NPs made of silver.[65]

Application of the DNA self-assembled nanoantennas for single-molecule sensing was implemented in 2017 by incoroprating a fluorescence quenched DNA hairpin (FQH) into the DNA origami (Figure 25b).[66,205] Upon hybridization with a partially complementary nucleic acid sequence that is specific for the Zika virus, quencher and fluorophore of the FQH are separated and fluorescence signal increase is detected. The FQH element was placed at 12 nm distance to a silver NP, further amplifying of the optical signal.[67] However, under the enhanced electric field in the plasmonic hotspot photobleaching of the dark quencher was observed which led to false-positive signals.[206] To ensure a high contrast between structures with and without target DNA, an alternative nucleic acid sensing element was needed. Another drawback of the pillar structure, was the insufficient formation of dimer nanoantennas, as the FQH blocked the binding site for a second NP. To achieve greater fluorescence enhancement, the attachement of two particles to a structure with an incorporated bioassay was therefore highly desirable.

6.1 Associated Publication 3

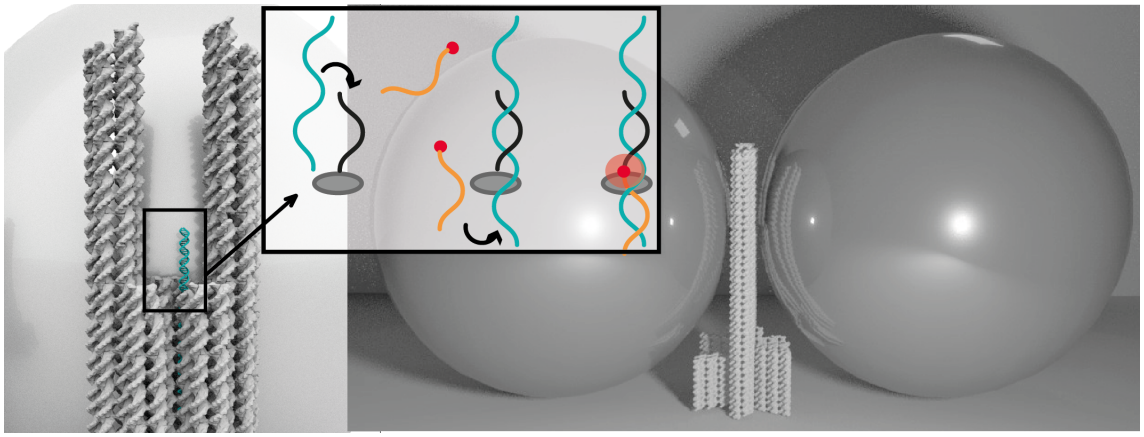

Addressable nanoantennas with cleared hotspots for single-molecule detection on a portable smartphone microscope

Kateryna Trofymchuk*, Viktorija Glembockyte*, Lennart Grabenhorst, Florian Steiner, Carolin Vietz, Cindy Close, Martina Pfeiffer, Lars Richter, Max L. Schütte, Florian Selbach, Renukka Yaadav, Jonas Zähringer, Qingshan Wei, Aydogan Ozcan, Birka Lalkens, Guillermo P. Acuna, Philip Tinnefeld

*equal contribution

Nature Communications 12, 950 (2021). doi: 10.1038/s41467-021-21238-9

In this publication the DNA origami nanoantenna design was adapted for optimal signal enhancement while providing a binding site for a biomolecular assay. The DNA origami included binding regions for the attachment of two nanoparticles and an addressable site for capturing analytes inside the plasmonic hotspot. A nucleic acid detection assay was incorporated in the rigid gap between the NPs, which is cleared from DNA origami (NanoAntennas with Cleared Hotspots, NACHOS). The so-called sandwich assay is designed such that a DNA sequence, specific to *Klebsiella pneumoniae*,[68,69] hybridizes to the region and creates a single-stranded overhang. Here, a dye-labeled imaging strand can permanently attach. This way the fluorescent label only remains inside the hotspot if the biomolecular target is also bound. The plasmonic nanoparticles increased the fluorescence signal of single molecules up to 461-fold (average of 89 ± 7-fold). Single-molecule sensitivity was achieved by intensifying only the fluorescence of the molecules bound in the zeptoliter volume of the DNA nanoantenna hotspot. Through fluorescence enhancement,

molecular amplification is no longer required to detect biomarkers at low concentrations. In combination, the DNA origami design with a DNA detection element and the strong signal enhancement enabled the detection of single biomolecules on the smartphone microscope.

Author contributions

PT, AO and GPA conceived the project, LG and BL developed the DNA origami structure, KT, VG and MP optimized the solution synthesis procedure, FSe performed the TEM measurements, KT, VG, CC, MP and RY developed the sandwich assay and prepared samples, performed and analyzed the measurements on the confocal microscope, CV, LR, MLS, QW, AO and GPA worked on an earlier version of the smartphone microscope, KT, VG, FSt and JZ constructed the portable smartphone microscope, KT, VG and FSt performed and analyzed the measurements on the smartphone microscope, KT, VG, LG, FSt and PT wrote the manuscript.

6.2 Associated Publication 4

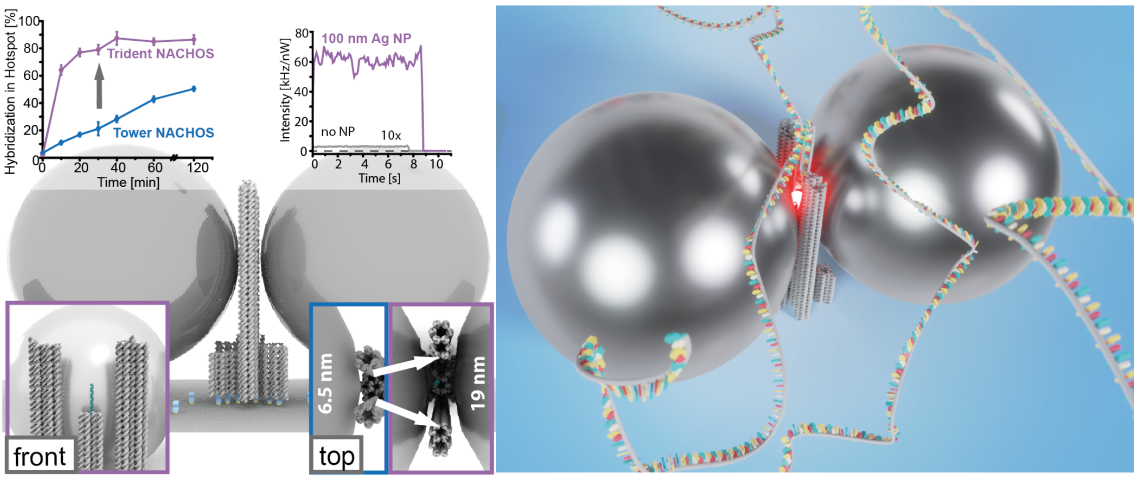

Maximizing the Accessibility in DNA Origami Nanoantenna Plasmonic Hotspots

Cindy Close, Kateryna Trofymchuk, Lennart Grabenhorst, Birka Lalkens, Viktorija Glembockyte, Philip Tinnefeld

Advanced Materials Interfaces 9, 24 (2022). doi: 10.1002/admi.202200255

To expand the applicability of the DNA origami nanoantenna, we focussed on designing nanoantennas specifically for detection of larger biomolecules. While the previous publication showed efficient capture of a 34 nucleotide DNA target molecule inside NACHOS, the space for binding two NPs and larger biomolecules was limited. To improve the hotspot accessibility, another design (Trident NACHOS) was developed as part of this work. The structure provided an even larger cleared hotspot region for biomolecules to be captured while ensuring rigid binding of nanoparticles at a defined distance. For this, the structure included three pillars. The outer two were designed for NP attachment and included up to six binding strands each. The central pillar served as a spacer between the NP, ensuring an interparticle distance of 12 nm. Most importantly, this provided a platform for placing a biomolecular sensing assay in the plasmonic hotspot. The transversal space between the NP attachment pillars was increased from 6.5 nm in previous NACHOS to 19 nm, creating a larger accessible hotspot volume. Trident NACHOS were optimized with respect to NP binding, fluorescence enhancement and compared to previous nanoantenna generations. The biomolecule capture region was used to bind a large 151 nucleotide DNA sequence, specific to *Klebsiella pneumoniae*. Overall, the more accessible hotspot in

Trident NACHOS significantly improved the target capturing efficiency. Compared to previous NACHOS, delivery of target DNA into the hotspot and thereby detection speed were increased threefold. While both NACHOS generations were equipped with three capture strands to bind DNA in the hotspot, two or more binding events were more frequently observed in the Trident hotspot. Even upon NP binding to the DNA origami, kinetics of target capture were not reduced significantly. Together with the achieved high fluorescence enhancement values, Trident NACHOS mark a step forward in single-molecule-based plasmonic biosensing.

Author contributions

PT, VG, KT and BL concieved and supervised the project. LG and CC developed the DNA origami structure. KT helped delevop Figure 5. CC performed the single molecule measurements, analyzed and visualized the data. CC wrote the original draft and finalized the manuscript with help of KT, LG, VG and PT. All authors reviewed and edited the manuscript.

7 Conclusions and Outlook

Since the observation of cells and microorganisms through the lens of the first microscope, humans have discovered smaller and smaller details by improving the method. While the use of super-resolution fluorescence microscopy now enables us to discern sub-nanometer distances, it is important to study biomolecules in their macromolecular context as well. This not only requires advanced microscopes, but also well performing labels and detection platforms.

7.1 Minimally-invasive and modular photostabilization for single-molecule and super-resolution microscopy

Complex organisms such as eukaryotic cells are able to sense and adapt to changes in their environment. Observing them close to their innate state requires non-invasive visualization methods. For fluorescence microscopy this means that the label should not perturb the system, e.g. by inducing photodamage. To ensure a sufficient number of emitted photons and the endurance of fluorophores over long experiments, photostabilization strategies are necessary. When adding stabilizing compounds, their compatibility with the system, however, needs to be ensured.

Chapter 4.1 introduced the DNA-mediated photostabilization mechanism as a minimally invasive strategy. By delivering the DNA-linked photostabilizer directly to the site where the biomolecule is labeled, the increased local concentration enabled stabilization at much lower concentrations (Figure 26a). Using this approach, the performance of a dye, previously not used for super-resolution imaging due to its photolability, was improved greatly. Many more localizations were detected, even after hour-long experiments. The improved localization precision enabled three-dimensional reconstruction of microtubules at similar quality to routinely used fluorophores.[207,208] Furthermore, the binding time of the stabilizer strand can be tailored to the imaging modality. Our studies showed that a bound photostabilization strand increases the photon budget of permanent labels significantly at low excitation intensities.

However, under harsh illumination conditions the degradation of the photostabilizer becomes limiting. This effect was hinted at in publications in which the cyclooctatetraene (COT) molecule was covalently attached to the fluorophore.[38] To circumvent this, we switched to a transiently hybridizing photostabilizer scheme. Similar to the concept of constant label exchange, continous replacement of the photostabilizers reduces the effect of individual damaged molecules. Nevertheless, it

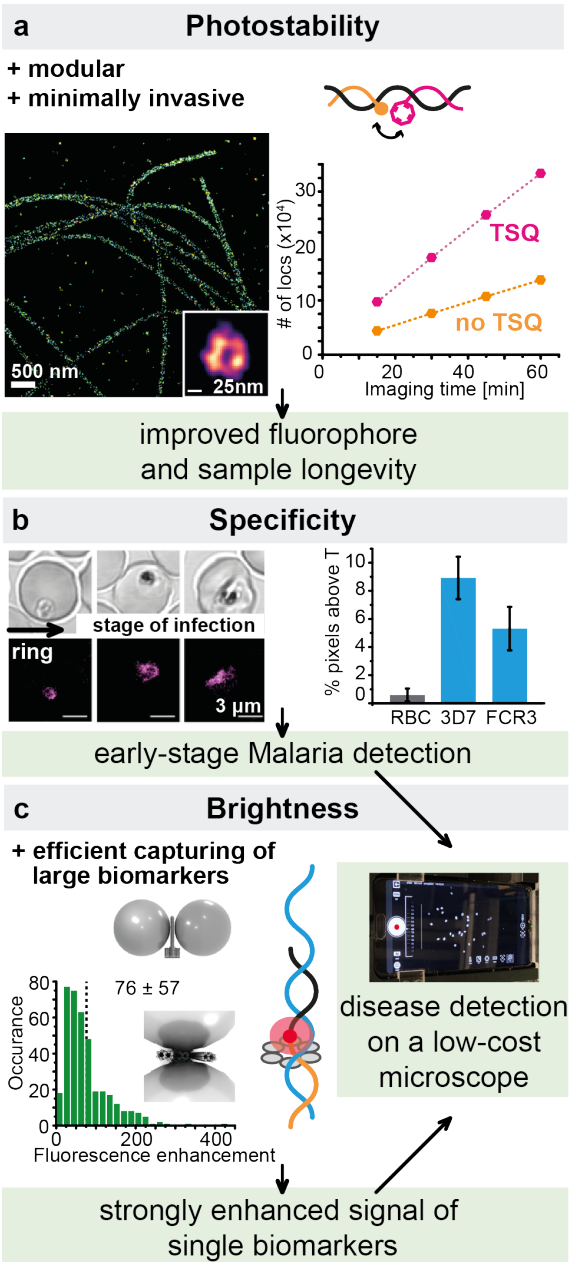

Figure 26: Summary of how this thesis enhances fluorophore performance in the aspects of photostability, specificity and brightness. (**a**) DNA-mediated photostabilization is a modular and minimally invasive photostabilization approach to improve longevity in single-molecule and super-resolution imaging. Even under aerobic conditions the reconstruction of the microtubule shape is significantly improved. Hour-long measurements benefit in terms of localization precision and number of localizations. Inset microtubule scale bar 25 nm. (**b**) The specificity of the SiR-glib probe allows for reliable detection of an early-stage Malaria infection (ring stage). Scale bar 3 µm. Measurements on a portable smartphone microscope of two different strains of the parasite (3D7 and FCR3) bring the detection assay close to application in the field. (**c**) DNA origami nanoantennas with cleared hotspots enable the efficient capturing and enhancement of single biomarkers and their label. Due to the strong signal amplification single molecules can be detected with a smartphone camera. The Trident structure improves the hotspot accessibility and enables the detection of a wider range of analytes.

would be interesting to study the mechansim of photostabilizer degradation. While it has been shown that the COT molecule itself may react with generated oxygen species,[209] we observed this effect even when removing oxygen enzymatically. This points towards an oxygen-independent degradation pathway of COT. Due to the relatively long triplet state lifetime of COT (100 µs),[210] photoinduced electron transfer and radical formation, e.g., with the excited state fluorophore become probable, as proposed for self-healing dyes.[211] Electron withdrawing groups attached to cyclooctatetraene may slow down its degradation.[38,212]

In addition, the coupling strategy of COT to DNA and its influence on the nearby fluorophore could be reconsidered. The linker molecule used in this study was initially designed for attaching three moieties: A photostabilizer (COT), a biomolecule (*via* maleimide-thiol coupling) and a fluorophore (*via* alkyne).[34,213] As only two of the functionalities were needed to create the photostabilizer strand, the alkyne was not used and could be omitted. Commonly, the maleimide-thiol coupling to biomolecules is employed to ensure site-specific labeling of proteins to cystein-tags in otherwise cystein-deprived proteins. However, Zhang et al. showed that directly attached maleimide-thiol linkers on cyanine dyes accelearated photobleaching through formation of a thioether adduct.[214] Even if our approach explicitly avoids the covalent binding of the fluorophore to the photostabilizer, the close proximity of the linker could still affect the dye, particularly if placed on the blunt end. Therefore, alternative strategies such as NHS-amine coupling or the use of electron-deficient aryl thioethers like phenyloxadiazole could be explored.

DNA-mediated photostabilization with TSQ molecules other than COT is also an obvious next step. Especially when correlating several molecules at once, multiplexed imaging with spectrally separate labels may be required (Figure 27a). To improve photostability, efficient recovery of fluorophores from the triplet state is needed. On the one hand this depends on the triplet state energy of the TSQ, which must have a well matched overlap with the fluorophore triplet state. For COT, the relatively low energy[210] prohibits efficient energy transfer with fluorophores such as Cy3 that have higher triplet state energies. Another important feature would be the quick recovery from the triplet state, so that energy transfer can occur frequently.[132] The modular DNA-mediated approach presents a universal photostabilization strategy. By including different photostabilizers, each matched with spectrally separated dyes, long multicolor measurements such as FRET will be possible.

When imaging more complex or sensitive biological environments, the DNA-mediated photostabilization approach could be of great advantage. The strategy involves a well-soluble DNA strand which does not have to be diluted in organic

solvents and can be added at a factor of up to 10^7 lower concentration, depending on the labeling density of the sample. Systems for which enzymatic oxygen scavengers[31,32] or TSQ[30] have been shown to disrupt the native state of the system could benefit from this. For example, delivering probes into bacteria is often difficult because of the limited diffusion through the cell wall and the high concentration of macromolecules inside the cells.[33,39,40] Electroporation has been used to efficiently deliver DNA for the purpose of genetic modification through transformation. Instead of bulky, enzymatic oxygen scavengers, the smaller, negatively charged DNA-linked photostabilizers could enter the cell more easily (Figure 27a).[215,216] Similar to the delivery of dye-labeled DNA or RNA, additional protection, e.g., via chemical linking might be necessary. Finally, this local photostabilization method could also be used for a correlative live-cell and super-resolution imaging scheme.[217] For example, STED imaging could be performed *in vivo* under high excitation intensites. During this, photostabilization could help reduce the damage that ROS not only inflicts on the fluorophore but also the labeled sample. Afterwards, the specimen could be permeabilized to allow, e.g., DNA-PAINT with even higher resolution.

7.2 Target-specific labels and fluorescence enhancement for disease detection

The application of fluorescence microscopy as a diagnostic tool requires accessible and robust equipment such as stable and target-specific detection reagents and easy-to-use imaging devices. Chapter 5.1 focused on the use of a novel probe for Malaria detection based on the fact that red blood cells only contain cellular organelles after infection (Figure 26b). Routinely used stains for determining the fraction of infected RBC (parasitemia) include Giemsa which targets the parasites nucleus.[48,49] Rapid diagnostic tests that employ immunochromatography can be performed in 20 minutes, but may require storage at 4 °C.[51] The SiR-glib synthesized by our collaborators specifically labels the endoplasmatic reticulum and can be stored and applied above room temperature over long periods. The high stability, labeling efficiency and brightness of the fluorescent probe enabled the detection of Malaria-infected RBC on our portable smartphone microscope (Figure 26b).[52]

Li et al. developed a more specialized and portable fluorescence microscope to deduce parasitemia.[50] Instead of a smartphone module, their microscope contained a CMOS sensor and Raspberry Pi for control and computation. The large field-of-view allowed high-throughput measurements. In that study, plateles were stained using DAPI, which exhibits an emission maximum at 461 nm. The dye does not permeate the cell membrane at low concentrations and therefore requires an addi-

tional permeabilization step with methanol which prohibits *in vivo* measurements. The spectral window of SiR-glib lies above 600 nm, where background fluorescence originating from hemoglobin should be less pronounced. The excitation wavelength is also well matched with the 639 nm laser inside our device. In combination, the permeable probe and our low-cost imaging device, enabled the clear distinction of Malaria-infected RBCs *in vivo*.

Initially, the portable microscope was developed for the publication discussed in chapter 6.1. The scope of the work was the demonstration of single-molecule detection on a smartphone camera (Figure 26c). For this, DNA origami nanoantennas were used to enhance the fluorescence signal of analytes. The NACHOS DNA origami enabled attachment of two NPs and a bioassay in the hotspot, which had not been possible in previous designs. The diagnostic target molecule was a 34 nucleotide DNA sequence, specific to an antibiotic resistant strain of the *Klebsiella pneumoniae* bacterium.[68,69] The DNA sandwich hybridization assay ensured specific binding to the hotspot. The incorporation of three capture strands led to a high detection efficiency. Partial complementarity of the Alexa Fluor 647-labeled DNA probe to the target DNA ensured that the label would only remain bound in the hotspot region when target DNA was captured. To demonstrate the feasibility of the assay in diagnostically relevant solutions which contain a multitude of biomolecules, the work includes measurements in blood serum.

Subsequent studies involved the detection of anti-digoxigenin antibodies inside NACHOS using a DNA nanoswitch.[70,71] This detection element consists of a fluorophore/quencher pair that is separated upon target molecule binding. Although antibody concentrations of 129 pM where reliably detected on a flat DNA origami, incorporation of the assay into NACHOS reduced its sensitivity. Further, the binding of two nanoparticles induced undesired photophysical effects on the quencher molecule, possibly due to the increased excitation rate in the hotspot.[206] By carefully selecting a FRET pair that does not form dim states in NACHOS, Grabenhorst et al. achieved count rates in the MHz regime.[218] This increased emission intensity enabled the observation of biomolecular interactions at the microsecond timescale such as transcription factor binding.

To accomodate and detect even larger biomolecules in NACHOS, chapter 6.2 focused on developing a new DNA origami structure (Trident). NP binding was optimized to match the strong fluorescence enhancement of the previous design. The larger cleared hotspot region enabled efficient capturing of a 151 nucleotide

DNA sequence. In comparison with the more confined environment in the previous generation, the detection speed in the Trident was tripled.

Based on the NACHOS Trident design, Yaadav et al. implemented nanopatterning and microfluidics in a follow-up study to further improve the detection sensitivity and usability.[135] Among other strategies, this entailed placing more capturing strands inside the cleared hotspot. Since false-positive signals from unspecific binding become increasingly disruptive at lower concentrations, blocking strands were introduced which are only displaced upon target binding. To further improve target capturing, the density of DNA structures on the surface was increased through nanopatterning[219,220] of nanoantennas every 300 nm. To withstand changes in temperature, pH or ionic concentration, DNA origami were coated with silica. For reusability, a strand-displacement reaction removed target and imager after the assay. High throughput experiments were performed on an imaging device with large FOV while flowing the sample through a microchip. After counting the number of detected spots, the limit of detection was determined to $\sim$ 5 aM (10 aM in blood plasma).

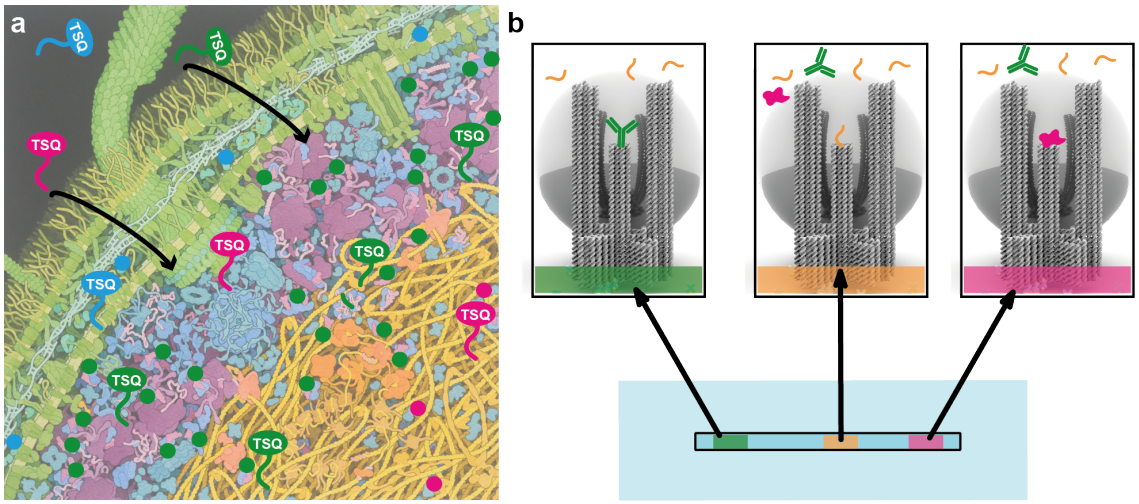

Figure 27: Fluorescent labels with enhanced performance allow us to see the complexity of biological systems. (**a**) Super-resolution imaging of multiple proteins in *E. coli*[221] with DNA-mediated photostabilization. Several molecules of interest are labeled and for each an optimally matched stabilizer is included. The photostabilizer strand is less bulky and invasive than common stabilization approaches and acts locally. (**b**) Multiplexed detection platform for several biomolecular targets. Sections of the chip are equipped with designated Trident DNA origami nanoantennas that capture and enhance the fluorescence signal upon binding of antibodies (green), nucleic acids (orange) or proteins (magenta).

Single-molecule-based biosensing methods are especially promising for the detection of low-abundance biomarkers,[41–46] as they do not require a pre-concentration

step.[53–57,222,223] Any patient sample contains a multitude of biomolecules and its composition holds valuable information. By placing the according detection elements in the hotsptot, Trident NACHOS can be modified for sensing of micro RNA[224] or low abundant proteins.[225–227] Similar to DNA microaarrays,[228] a microfluidic chip can be designed such that specialized DNA origami nanoantennas are placed at designated positions (Figure 27b), each of which reports on the presence of a different analyte.[229] This parallelized diagnostic testing scheme could be especially useful for precision medicine, e.g., in early-stage cancer diagnosis[230] where practitioners not only require information on one, but several biomarkers.

8 Bibliography

[1] David Bardell. "The invention of the microscope". In: *Bios* 75.2 (2004), pp. 78–84.

[2] Adam JM Wollman et al. "From Animaculum to single molecules: 300 years of the light microscope". In: *Open biology* 5.4 (2015), p. 150019. DOI: 10.1098/rsob.150019.

[3] Ahmed Awad Adeel. "A relic of the Wellcome Tropical Research Laboratories in Khartoum (1903–34)". In: *Sudanese Journal of Paediatrics* 16.1 (2016), p. 67.

[4] Dieter Gerlach. *Geschichte der Mikroskopie*. Harry Deutsch Verlag, 2009. ISBN: 978-3-8171-1781-9.

[5] David Wootton. *Bad medicine: doctors doing harm since Hippocrates*. OUP Oxford, 2007. ISBN: 0199212791.

[6] Ernst Abbe. "Beiträge zur Theorie des Mikroskops und der mikroskopischen Wahrnehmung". In: *Archiv für mikroskopische Anatomie* 9.1 (1873), pp. 413–468. DOI: 10.1007/BF02956173.

[7] Kateryna Trofymchuk et al. "Addressable nanoantennas with cleared hotspots for single-molecule detection on a portable smartphone microscope". In: *Nature communications* 12.1 (2021), p. 950. DOI: 10.1038/s41467-021-21238-9.

[8] Minsky Marvin. *Microscopy apparatus*. US Patent US3013467. 1961.

[9] W. E. Moerner and L. Kador. "Optical detection and spectroscopy of single molecules in a solid". In: *Phys. Rev. Lett.* 62.21 (1989), pp. 2535–2538. DOI: 10.1103/PhysRevLett.62.2535.

[10] Michel Orrit and J Bernard. "Single pentacene molecules detected by fluorescence excitation in a p-terphenyl crystal". In: *Physical review letters* 65.21 (1990), p. 2716. DOI: 10.1103/PhysRevLett.65.2716.

[11] VA Okhonin. "Method of investigating specimen microstructure". In: *Patent SU* 1374992 (1986).

[12] Stefan W Hell and Jan Wichmann. "Breaking the diffraction resolution limit by stimulated emission: stimulated-emission-depletion fluorescence microscopy". In: *Optics letters* 19.11 (1994), pp. 780–782. DOI: 10.1364/ol.19.000780.

[13] Lexy von Diezmann, Yoav Shechtman, and WE Moerner. "Three-dimensional localization of single molecules for super-resolution imaging and single-particle tracking". In: *Chemical reviews* 117.11 (2017), pp. 7244–7275. DOI: 10.1021/acs.chemrev.6b00629.

[14] Eric Betzig et al. "Imaging intracellular fluorescent proteins at nanometer resolution". In: *Science* 313.5793 (2006), pp. 1642–1645. DOI: 10.1126/science.1127344.

[15] Michael J Rust, Mark Bates, and Xiaowei Zhuang. "Sub-diffraction-limit imaging by stochastic optical reconstruction microscopy (STORM)". In: *Nature methods* 3.10 (2006), pp. 793–796. DOI: 10.1038/nmeth929.

[16] Mike Heilemann et al. "Subdiffraction-resolution fluorescence imaging with conventional fluorescent probes". In: *Angewandte Chemie-International Edition* 47.33 (2008). DOI: 10.1002/anie.200802376.

[17] Alexey Sharonov and Robin M Hochstrasser. "Wide-field subdiffraction imaging by accumulated binding of diffusing probes". In: *Proceedings of the National Academy of Sciences* 103.50 (2006), pp. 18911–18916. DOI: 10.1073/pnas.0609643104.

[18] Ralf Jungmann et al. "Single-molecule kinetics and super-resolution microscopy by fluorescence imaging of transient binding on DNA origami". In: *Nano letters* 10.11 (2010), pp. 4756–4761. DOI: 10.1021/nl103427w.

[19] Roman Schmidt et al. "MINFLUX nanometer-scale 3D imaging and microsecond-range tracking on a common fluorescence microscope". In: *Nature communications* 12.1 (2021), p. 1478. DOI: 10.1038/s41467-021-21652-z.

[20] Susanne CM Reinhardt et al. "Ångström-resolution fluorescence microscopy". In: *Nature* 617.7962 (2023), pp. 711–716. DOI: 10.1038/s41586-023-05925-9.

[21] Ali H Shaib et al. "One-step nanoscale expansion microscopy reveals individual protein shapes". In: *Nature biotechnology* (2024), pp. 1–9. DOI: 10.1038/s41587-024-02431-9.

[22] Norman Bobroff. "Position measurement with a resolution and noise-limited instrument". In: *Review of Scientific Instruments* 57.6 (1986), pp. 1152–1157. DOI: 10.1063/1.1138619.

[23] Russell E Thompson, Daniel R Larson, and Watt W Webb. "Precise nanometer localization analysis for individual fluorescent probes". In: *Biophysical journal* 82.5 (2002), pp. 2775–2783. DOI: 10.1016/S0006-3495(02)75618-X.

[24] Raimund J Ober, Sripad Ram, and E Sally Ward. "Localization accuracy in single-molecule microscopy". In: *Biophysical journal* 86.2 (2004), pp. 1185–1200. DOI: 10.1016/S0006-3495(04)74193-4.

[25] Kim I Mortensen et al. "Optimized localization analysis for single-molecule tracking and super-resolution microscopy". In: *Nature methods* 7.5 (2010), pp. 377–381. DOI: 10.1038/nmeth.1447.

[26] Ulrike Endesfelder et al. "A simple method to estimate the average localization precision of a single-molecule localization microscopy experiment". In: *Histochemistry and cell biology* 141 (2014), pp. 629–638. DOI: 10.1007/s00418-014-1192-3.

[27] Philipp Blumhardt et al. "Photo-induced depletion of binding sites in DNA-PAINT microscopy". In: *Molecules* 23.12 (2018), p. 3165. DOI: 10.3390/molecules23123165.

[28] Taekjip Ha and Philip Tinnefeld. "Photophysics of fluorescent probes for single-molecule biophysics and super-resolution imaging". In: *Annual review of physical chemistry* 63.1 (2012), pp. 595–617. DOI: 10.1146/annurev-physchem-032210-103340.

[29] Hendrik Deschout et al. "Precisely and accurately localizing single emitters in fluorescence microscopy". In: *Nature methods* 11.3 (2014), pp. 253–266. DOI: 10.1038/nmeth.2843.

[30] Jose L Alejo, Scott C Blanchard, and Olaf S Andersen. "Small-molecule photostabilizing agents are modifiers of lipid bilayer properties". In: *Biophysical journal* 104.11 (2013), pp. 2410–2418. DOI: 10.1016/j.bpj.2013.04.039.

[31] Xinghua Shi, John Lim, and Taekjip Ha. "Acidification of the oxygen scavenging system in single-molecule fluorescence studies: in situ sensing with a ratiometric dual-emission probe". In: *Analytical chemistry* 82.14 (2010), pp. 6132–6138. DOI: 10.1021/ac1008749.

[32] Marko Swoboda et al. "Enzymatic oxygen scavenging for photostability without pH drop in single-molecule experiments". In: *ACS nano* 6.7 (2012), pp. 6364–6369. DOI: 10.1021/nn301895c.

[33] Steven B Zimmerman and Stefan O Trach. "Estimation of macromolecule concentrations and excluded volume effects for the cytoplasm of Escherichia coli". In: *Journal of molecular biology* 222.3 (1991), pp. 599–620. DOI: 10.1016/0022-2836(91)90499-v.

[34] Jasper HM Van Der Velde et al. "A simple and versatile design concept for fluorophore derivatives with intramolecular photostabilization". In: *Nature communications* 7.1 (2016), p. 10144. DOI: 10.1038/ncomms10144.

[35] Jasper HM Van Der Velde et al. "Self-healing dyes for super-resolution fluorescence microscopy". In: *Journal of Physics D: Applied Physics* 52.3 (2018), p. 034001. DOI: 10.1088/1361-6463/aae752.

[36] Michael Isselstein et al. "Self-healing dyes—keeping the promise?" In: *The journal of physical chemistry letters* 11.11 (2020), pp. 4462–4480. DOI: 10.1021/acs.jpclett.9b03833.

[37] Gangwei Jiang et al. "Chemical approaches to optimize the properties of organic fluorophores for imaging and sensing". In: *Angewandte Chemie* 136.11 (2024), e202315217. DOI: 10.1002/anie.202315217.

[38] Qinsi Zheng et al. "Electronic tuning of self-healing fluorophores for live-cell and single-molecule imaging". In: *Chemical science* 8.1 (2017), pp. 755–762. DOI: 10.1039/c6sc02976k.

[39] Christoph K Spahn et al. "A toolbox for multiplexed super-resolution imaging of the E. coli nucleoid and membrane using novel PAINT labels". In: *Scientific reports* 8.1 (2018), p. 14768. DOI: 10.1038/s41598-018-33052-3.

[40] Ulrike Endesfelder. "From single bacterial cell imaging towards in vivo single-molecule biochemistry studies". In: *Essays in Biochemistry* 63.2 (2019), pp. 187–196. DOI: 10.1042/EBC20190002.

[41] David R. Walt. "Optical Methods for Single Molecule Detection and Analysis". en. In: *Analytical Chemistry* 85.3 (Feb. 2013), pp. 1258–1263. DOI: 10.1021/ac3027178.

[42] Deep Punj et al. "A plasmonic 'antenna-in-box' platform for enhanced single-molecule analysis at micromolar concentrations". In: *Nature nanotechnology* 8.7 (2013), pp. 512–516. DOI: 10.1038/nnano.2013.98.

[43] Phil Holzmeister et al. "Breaking the concentration limit of optical single-molecule detection". In: *Chem. Soc. Rev.* 43.4 (2014), pp. 1014–1028. DOI: 10.1039/C3CS60207A.

[44] Sandeep Kumar Vashist et al. “Emerging technologies for next-generation point-of-care testing”. In: *Trends in biotechnology* 33.11 (2015), pp. 692–705. DOI: 10.1016/j.tibtech.2015.09.001.

[45] Adam B Taylor and Peter Zijlstra. “Single-molecule plasmon sensing: current status and future prospects”. In: *ACS Sensors* 2.8 (2017), pp. 1103–1122. DOI: 10.1021/acssensors.7b00382.

[46] Sijia Peng, Wenjuan Wang, and Chunlai Chen. “Breaking the Concentration Barrier for Single-Molecule Fluorescence Measurements”. In: *Chemistry–A European Journal* 24.5 (2018), pp. 1002–1009. DOI: 10.1002/chem.201704065.

[47] Günter Gauglitz. “Point-of-care platforms”. In: *Annual review of analytical chemistry* 7.1 (2014), pp. 297–315. DOI: 10.1146/annurev-anchem-071213-020332.

[48] E Zipfel et al. “Ueber Romanowsky-Farbstoffe und den Romanowsky-Giemsa-Effekt”. In: *Histochemistry (Berlin)* 81.4 (1984), pp. 337–351. DOI: 10.1007/BF00640605k.

[49] World Health Organization. *World malaria report 2023*. World Health Organization, 2023. ISBN: 978-92-4-008617-3.

[50] Hongquan Li et al. “Octopi: Open configurable high-throughput imaging platform for infectious disease diagnosis in the field”. In: *bioRxiv* (2019). DOI: 10.1101/684423.

[51] Jessica Maltha, Philippe Gillet, and J Jacobs. “Malaria rapid diagnostic tests in endemic settings”. In: *Clinical Microbiology and Infection* 19.5 (2013), pp. 399–407. DOI: 10.1111/1469-0691.12151.

[52] Carolin Vietz et al. “Benchmarking Smartphone Fluorescence-Based Microscopy with DNA Origami Nanobeads: Reducing the Gap toward Single-Molecule Sensitivity”. In: *ACS Omega* 4.1 (Jan. 31, 2019), pp. 637–642. DOI: 10.1021/acsomega.8b03136.

[53] Kary Mullis et al. “Specific enzymatic amplification of DNA in vitro: the polymerase chain reaction”. In: *Cold Spring Harbor symposia on quantitative biology*. Vol. 51. Cold Spring Harbor Laboratory Press. 1986, pp. 263–273. DOI: 10.1101/sqb.1986.051.01.032.

[54] Russell Higuchi et al. “Simultaneous amplification and detection of specific DNA sequences”. In: *Nature Biotechnology* 10.4 (1992), pp. 413–417. DOI: 10.1038/nbt0492-413.

[55] Benjamin J Hindson et al. “High-throughput droplet digital PCR system for absolute quantitation of DNA copy number”. In: *Analytical chemistry* 83.22 (2011), pp. 8604–8610. DOI: 10.1021/ac202028g.

[56] Willard M. Freeman, Stephen J. Walker, and Kent E. Vrana. “Quantitative RT-PCR: Pitfalls and Potential”. en. In: *BioTechniques* 26.1 (1999), pp. 112–125. DOI: 10.2144/99261rv01.

[57] Thomas R. Kozel and Amanda R. Burnham-Marusich. “Point-of-Care Testing for Infectious Diseases: Past, Present, and Future”. en. In: *Journal of Clinical Microbiology* 55.8 (Aug. 2017). Ed. by Colleen Suzanne Kraft, pp. 2313–2320. DOI: 10.1128/JCM.00476-17.

[58] Joseph R Lakowicz. “Radiative decay engineering: biophysical and biomedical applications”. In: *Analytical biochemistry* 298.1 (2001), pp. 1–24. DOI: 10.1006/abio.2001.5377.

[59] Pascal Anger, Palash Bharadwaj, and Lukas Novotny. “Enhancement and Quenching of Single-Molecule Fluorescence”. In: *Physical Review Letters* 96.11 (2006). DOI: 10.1103/PhysRevLett.96.113002.

[60] Stefan A. Maier. *Plasmonics: fundamentals and applications*. en. New York: Springer, 2007. ISBN: 978-0-387-33150-8. ISBN: 978-0-387-33150-8.

[61] Paul W. K. Rothemund. “Folding DNA to create nanoscale shapes and patterns”. In: *Nature* 440.7082 (Mar. 2006), pp. 297–302. DOI: 10.1038/nature04586.

[62] Nadrian C Seeman. “Nucleic acid junctions and lattices”. In: *Journal of Theoretical Biology* 99.2 (1982), pp. 237–247. DOI: 10.1016/0022-5193(82)90002-9.

[63] G. P. Acuna et al. “Fluorescence Enhancement at Docking Sites of DNA-Directed Self-Assembled Nanoantennas”. In: *Science* 338.6106 (Oct. 26, 2012), pp. 506–510. DOI: 10.1126/science.1228638. (Visited on 12/09/2018).

[64] Anastasiya Puchkova et al. “DNA Origami Nanoantennas with over 5000-fold Fluorescence Enhancement and Single-Molecule Detection at 25 uM”. In: *Nano Letters* 15.12 (Dec. 9, 2015), pp. 8354–8359. DOI: 10.1021/acs.nanolett.5b04045.

[65] Carolin Vietz et al. “Broadband Fluorescence Enhancement with Self-Assembled Silver Nanoparticle Optical Antennas”. In: *ACS Nano* 11.5 (May 23, 2017), pp. 4969–4975. DOI: 10.1021/acsnano.7b01621.

[66] Sarah E. Ochmann et al. “Optical Nanoantenna for Single Molecule-Based Detection of Zika Virus Nucleic Acids without Molecular Multiplication”. In: *Analytical Chemistry* 89.23 (Dec. 5, 2017), pp. 13000–13007. DOI: 10.1021/acs.analchem.7b04082.

[67] Carolin Vietz et al. “Synergistic Combination of Unquenching and Plasmonic Fluorescence Enhancement in Fluorogenic Nucleic Acid Hybridization Probes”. In: *Nano Letters* 17.10 (Oct. 11, 2017), pp. 6496–6500. DOI: 10.1021/acs.nanolett.7b03844.

[68] J Hrabák, E Chudáčková, and CC Papagiannitsis. “Detection of carbapenemases in Enterobacteriaceae: a challenge for diagnostic microbiological laboratories”. In: *Clinical Microbiology and Infection* 20.9 (2014), pp. 839–853. DOI: 10.1111/1469-0691.12678.

[69] Laurent Poirel et al. “Emergence of oxacillinase-mediated resistance to imipenem in Klebsiella pneumoniae”. In: *Antimicrobial agents and chemotherapy* 48.1 (2004), pp. 15–22. DOI: 10.1128/aac.48.1.15-22.2004.

[70] Martina Pfeiffer et al. “Single antibody detection in a DNA origami nanoantenna”. In: *Iscience* 24.9 (2021). DOI: 10.1016/j.isci.2021.103072.

[71] Alessandro Porchetta et al. “Programmable nucleic acid nanoswitches for the rapid, single-step detection of antibodies in bodily fluids”. In: *Journal of the American Chemical Society* 140.3 (2018), pp. 947–953. DOI: 10.1021/jacs.7b09347.

[72] Charles R. Cantor and Paul R. Schimmel. *Biophysical Chemistry: Part II: Techniques for the Study of Biological Structure and Function*. W. H. Freeman, Apr. 15, 1980. ISBN: 978-0-7167-1190-2.

[73] Achillefs N Kapanidis and Terence Strick. “Biology, one molecule at a time”. In: *Trends in biochemical sciences* 34.5 (2009), pp. 234–243. DOI: 10.1016/j.tibs.2009.01.008.

[74] David S. Goodsell. “Biosites: Illustration of the Cytoplasm”. In: *Molecular Landscapes* (2005). DOI: 10.2210/rcsb_pdb/goodsell-gallery-006.

[75] Joseph R. Lakowicz. *Principles of fluorescence spectroscopy*. 3rd edition. ISBN: 978-0-387-46312-4. New York, NY: Springer, 2010. ISBN: 978-0-387-46312-4 978-0-387-31278-1.

[76] Albert Einstein. “Über einen die Erzeugung und Verwandlung des Lichtes betreffenden heuristischen Gesichtspunkt”. In: *Annalen der Physik* 322.6 (1905), pp. 132–148. DOI: 10.1002/andp.19053220607.

[77] George Gabriel Stokes. "On the change of refrangibility of light". In: *Philosophical transactions of the Royal Society of London* 142 (1852), pp. 463–562. DOI: 10.1098/rstl.1852.0022.

[78] Michael Kasha. "Energy Transfer Mechanisms and the Molecular Exciton Model for Molecular Aggregates". In: *Radiation Research* 20.1 (Sept. 1, 1963), pp. 55–70. DOI: 10.2307/3571331.

[79] Aleksander Jablonski. "Efficiency of anti-Stokes fluorescence in dyes". In: *Nature* 131.3319 (1933), pp. 839–840. DOI: 10.1038/131839b0.

[80] Michael Kasha. "Characterization of electronic transitions in complex molecules". In: *Discussions of the Faraday Society* 9 (1950), pp. 14–19. DOI: 10.1039/DF9500900014.

[81] Edward Condon. "A theory of intensity distribution in band systems". In: *Physical Review* 28.6 (1926), p. 1182. DOI: 10.1103/PhysRev.28.1182.

[82] Max Born and Robert Oppenheimer. "Zur Quantentheorie der Moleküle". In: *Annalen der Physik* 389.20 (1927), pp. 457–484. DOI: 10.1002/andp.19273892002.

[83] James Franck and EG Dymond. "Elementary processes of photochemical reactions". In: *Transactions of the Faraday Society* 21.February (1926), pp. 536–542. DOI: 10.1039/TF9262100536.

[84] Wolfgang Pauli. "Über den Zusammenhang des Abschlusses der Elektronengruppen im Atom mit der Komplexstruktur der Spektren". In: *Zeitschrift für Physik* 31.1 (1925), pp. 765–783. DOI: 10.1007/BF02980631.

[85] Aleksander Jabłoński. "Über den Mechanismus der Photolumineszenz von Farbstoffphosphoren". In: *Zeitschrift für Physik* 94.1-2 (1935), pp. 38–46. DOI: 10.1007/BF01330795.

[86] Fan Hong et al. "DNA Origami: Scaffolds for Creating Higher Order Structures". en. In: *Chemical Reviews* 117.20 (2017), pp. 12584–12640. DOI: 10.1021/acs.chemrev.6b00825.

[87] Giuseppe Arrabito and Liqian Wang. *DNA Nanotechnology for Bioanalysis*. World Scientific, 2017. DOI: 10.1142/q0110.

[88] Neville R Kallenbach, Rong-Ine Ma, and Nadrian C Seeman. "An immobile nucleic acid junction constructed from oligonucleotides". In: *Nature* 305.5937 (1983), pp. 829–831. DOI: 10.1038/305829a0.

[89] J Thomas Holthausen, Claire Wyman, and Roland Kanaar. "Regulation of DNA strand exchange in homologous recombination". In: *DNA Repair* 9.12 (2010), pp. 1264–1272. DOI: 10.1016/j.dnarep.2010.09.014.

[90] Xing Wang and Nadrian C Seeman. "Assembly and characterization of 8-arm and 12-arm DNA branched junctions". In: *Journal of the American Chemical Society* 129.26 (2007), pp. 8169–8176. DOI: 10.1021/ja0693441.

[91] Tsu Ju Fu and Nadrian C Seeman. "DNA double-crossover molecules". In: *Biochemistry* 32.13 (1993), pp. 3211–3220. DOI: 10.1021/bi00064a003.

[92] Hao Yan et al. "DNA-templated self-assembly of protein arrays and highly conductive nanowires". In: *Science* 301.5641 (2003), pp. 1882–1884. DOI: 10.1126/science.1089389.

[93] Frederick Mathieu et al. "Six-helix bundles designed from DNA". In: *Nano Letters* 5.4 (2005), pp. 661–665. DOI: 10.1021/nl050084f.

[94] Thomas Tørring et al. "DNA origami: a quantum leap for self-assembly of complex structures". In: *Chemical Society Reviews* 40.12 (2011), pp. 5636–5646. DOI: 10.1039/c1cs15057j.

[95] Erik Winfree et al. "Design and self-assembly of two-dimensional DNA crystals". In: *Nature* 394.6693 (1998), pp. 539–544. DOI: 10.1038/28998.

[96] Dongran Han et al. "DNA origami with complex curvatures in three-dimensional space". In: *Science* 332.6027 (2011), pp. 342–346. DOI: 10.1126/science.1202998.

[97] Hendrik Dietz, Shawn M Douglas, and William M Shih. "Folding DNA into twisted and curved nanoscale shapes". In: *Science* 325.5941 (2009), pp. 725–730. DOI: 10.1126/science.1174251.

[98] Yonggang Ke et al. "Multilayer DNA origami packed on a square lattice". In: *Journal of the American Chemical Society* 131.43 (2009), pp. 15903–15908. DOI: 10.1021/ja906381y.

[99] Shawn M Douglas et al. "Self-assembly of DNA into nanoscale three-dimensional shapes". In: *Nature* 459.7245 (2009), pp. 414–418. DOI: 10.1038/nature08016.

[100] Yonggang Ke et al. "Two design strategies for enhancement of multilayer-DNA-origami folding: underwinding for specific intercalator rescue and staple-break positioning". In: *Chemical science* 3.8 (2012), pp. 2587–2597. DOI: 10.1039/C2SC20446K.

[101] Zhiqiang Liang et al. "Plasmonic Enhanced Optoelectronic Devices". In: *Plasmonics* 9.4 (Aug. 2014), pp. 859–866. DOI: 10.1007/s11468-014-9682-7.

[102] Mathieu L Juan, Maurizio Righini, and Romain Quidant. "Plasmon nano-optical tweezers". In: *Nature Photonics* 5.6 (June 2011), pp. 349–356. DOI: 10.1038/nphoton.2011.56.

[103] Lukas Novotny and Bert Hecht. *Principles of Nano-Optics*. 2nd ed. Cambridge: Cambridge University Press, 2012. ISBN: 978-0-511-79419-3. ISBN: 978-0-511-79419-3.

[104] Lukas Novotny and Niek van Hulst. "Antennas for light". In: *Nature Photonics* 5.2 (Feb. 2011), pp. 83–90. DOI: 10.1038/nphoton.2010.237.

[105] Jon A. Schuller et al. "Plasmonics for extreme light concentration and manipulation". In: *Nature Materials* 9.3 (Mar. 2010), pp. 193–204. DOI: 10.1038/nmat2630.

[106] Eduardo A. Coronado, Ezequiel R. Encina, and Fernando D. Stefani. "Optical properties of metallic nanoparticles: manipulating light, heat and forces at the nanoscale". In: *Nanoscale* 3.10 (2011), p. 4042. DOI: 10.1039/c1nr10788g.

[107] Vincenzo Giannini et al. "Plasmonic nanoantennas: fundamentals and their use in controlling the radiative properties of nanoemitters". In: *Chemical reviews* 111.6 (2011), pp. 3888–3912. DOI: 10.1021/cr1002672.

[108] Raju Regmi et al. "Nanoscale volume confinement and fluorescence enhancement with double nanohole aperture". In: *Scientific reports* 5.1 (2015), p. 15852. DOI: 10.1038/srep15852.

[109] Anika Kinkhabwala et al. "Large single-molecule fluorescence enhancements produced by a bowtie nanoantenna". In: *Nature Photonics* 3.11 (Nov. 2009), pp. 654–657. DOI: 10.1038/nphoton.2009.187.

[110] Phil Holzmeister et al. "Quantum yield and excitation rate of single molecules close to metallic nanostructures". In: *Nature Communications* 5.1 (Dec. 2014). DOI: 10.1038/ncomms6356.

[111] O. L. Muskens et al. "Strong Enhancement of the Radiative Decay Rate of Emitters by Single Plasmonic Nanoantennas". In: *Nano Letters* 7.9 (Sept. 1, 2007), pp. 2871–2875. DOI: 10.1021/nl0715847.

[112] J. B. Khurgin, G. Sun, and R. A. Soref. "Practical limits of absorption enhancement near metal nanoparticles". In: *Applied Physics Letters* 94.7 (Feb. 16, 2009), p. 071103. DOI: 10.1063/1.3081631.

[113] G. Sun, J. B. Khurgin, and R. A. Soref. "Practical enhancement of photoluminescence by metal nanoparticles". In: *Applied Physics Letters* 94.10 (Mar. 9, 2009), p. 101103. DOI: 10.1063/1.3097025.

[114] Osamu Shimomura, Frank H. Johnson, and Yo Saiga. "Extraction, Purification and Properties of Aequorin, a Bioluminescent Protein from the Luminous Hydromedusan, Aequorea". In: *Journal of Cellular and Comparative Physiology* 59.3 (1962), pp. 223–239. DOI: 10.1002/jcp.1030590302.

[115] Douglas C Prasher et al. "Primary structure of the Aequorea victoria green-fluorescent protein". In: *Gene* 111.2 (1992), pp. 229–233. DOI: 10.1016/0378-1119(92)90691-h.

[116] Roger Y Tsien. "The green fluorescent protein". In: *Annual review of biochemistry* 67.1 (1998), pp. 509–544. DOI: 10.1146/annurev.biochem.67.1.509.

[117] Luke D Lavis and Ronald T Raines. "Bright building blocks for chemical biology". In: *ACS chemical biology* 9.4 (2014), pp. 855–866. DOI: 10.1021/cb500078u.

[118] Qinsi Zheng and Luke D Lavis. "Development of photostable fluorophores for molecular imaging". In: *Current opinion in chemical biology* 39 (2017), pp. 32–38. DOI: 10.1016/j.cbpa.2017.04.017.

[119] Marcel Streit et al. "Fluorescent labeling strategies for molecular bioimaging". In: *Biophysical Reports* (2025). DOI: 10.1016/j.bpr.2025.100200.

[120] Jonathan B Grimm and Luke D Lavis. "Caveat fluorophore: an insiders' guide to small-molecule fluorescent labels". In: *Nature Methods* 19.2 (2022), pp. 149–158. DOI: 10.1038/s41592-021-01338-6.

[121] Jonathan B Grimm et al. "A general method to improve fluorophores for live-cell and single-molecule microscopy". In: *Nature methods* 12.3 (2015), pp. 244–250. DOI: 10.1038/nmeth.3256.

[122] Nicholas J Turro, Vaidhyanathan Ramamurthy, Juan C Scaiano, et al. *Modern molecular photochemistry of organic molecules*. Vol. 188. University Science Books Sausalito, CA, 2010. ISBN: 1891389254.

[123] Sebastian Van De Linde et al. "Photoinduced formation of reversible dye radicals and their impact on super-resolution imaging". In: *Photochemical & Photobiological Sciences* 10.4 (2011), pp. 499–506. DOI: 10.1039/C0PP00317D.

[124] JB Marling, DW Gregg, and L Wood. "Chemical quenching of the triplet state in flashlamp-excited liquid organic lasers". In: *Applied Physics Letters* 17.12 (1970), pp. 527–530. DOI: 10.1063/1.1653296.

[125] Paul G Wenthold et al. "Transition-state spectroscopy of cyclooctatetraene". In: *Science* 272.5267 (1996), pp. 1456–1459. DOI: 10.1126/science.272.5267.1456.

[126] Sarah Schols et al. *Organic Light Emitting Materials and Devices XIII: Triplet excitation scavenging as method to control the triplet concentration*. Vol. 7415. SPIE, 2009, pp. 43–51. DOI: 10.1117/12.826176.

[127] Ma Heupel et al. "Photophysical and photochemical properties of electronically excited fluorescent dyes: a new type of time-resolved laser-scanning spectroscopy". In: *International Journal of Photoenergy* 1.3 (1999), pp. 165–172. DOI: 10.1155/S1110662X9900029X.

[128] Richa Dave et al. "Mitigating unwanted photophysical processes for improved single-molecule fluorescence imaging". In: *Biophysical journal* 96.6 (2009), pp. 2371–2381. DOI: 10.1016/j.bpj.2008.11.061.

[129] Jerker Widengren et al. "Strategies to improve photostabilities in ultrasensitive fluorescence spectroscopy". In: *The journal of physical chemistry A* 111.3 (2007), pp. 429–440. DOI: 10.1021/jp0646325.

[130] Viktorija Glembockyte, Richard Lincoln, and Gonzalo Cosa. "Cy3 photoprotection mediated by Ni2+ for extended single-molecule imaging: old tricks for new techniques". In: *Journal of the American Chemical Society* 137.3 (2015), pp. 1116–1122. DOI: 10.1021/ja509923e.

[131] Viktorija Glembockyte, Junan Lin, and Gonzalo Cosa. "Improving the photostability of red-and green-emissive single-molecule fluorophores via Ni2+ mediated excited triplet-state quenching". In: *The Journal of Physical Chemistry B* 120.46 (2016), pp. 11923–11929. DOI: 10.1021/acs.jpcb.6b10725.

[132] Sandra Monti et al. "The triplet state of azobenzene". In: *Chemical Physics Letters* 77.1 (1981), pp. 115–119. DOI: 10.1016/0009-2614(81)85611-4.

[133] P Targowski, B Ziktek, and A Bkaczynski. "Luminescence quenching of rhodamines by cyclooctatetraene". In: *Zeitschrift Fuer Naturforschung A* 42.9 (1987), pp. 1009–1013. DOI: 10.1515/zna-1987-0914.

[134] Sang-Hyuk Lee et al. “Counting single photoactivatable fluorescent molecules by photoactivated localization microscopy (PALM)”. In: *Proceedings of the National Academy of Sciences* 109.43 (2012), pp. 17436–17441. DOI: 10.1073/pnas.1215175109.

[135] Renukka Yaadav et al. “Bringing Attomolar Detection to the Point-of-Care with Nanopatterned DNA Origami Nanoantennas”. In: *bioRxiv* (2024). DOI: 10.1101/2024.10.14.618183.

[136] Helen Hwang and Sua Myong. “Protein induced fluorescence enhancement (PIFE) for probing protein–nucleic acid interactions”. In: *Chemical Society Reviews* 43.4 (2014), pp. 1221–1229. DOI: 10.1039/c3cs60201j.

[137] Pedro F Aramendia, R Martin Negri, and Enrique San Roman. “Temperature dependence of fluorescence and photoisomerization in symmetric carbocyanines. Influence of medium viscosity and molecular structure”. In: *The Journal of Physical Chemistry* 98.12 (1994), pp. 3165–3173. DOI: 10.1021/j100063a020.

[138] Matthew E Sanborn et al. “Fluorescence properties and photophysics of the sulfoindocyanine Cy3 linked covalently to DNA”. In: *The Journal of Physical Chemistry B* 111.37 (2007), pp. 11064–11074. DOI: 10.1021/jp072912u.

[139] Marcia Levitus and Suman Ranjit. “Cyanine dyes in biophysical research: the photophysics of polymethine fluorescent dyes in biomolecular environments”. In: *Quarterly reviews of biophysics* 44.1 (2011), pp. 123–151. DOI: 10.1017/S0033583510000247.

[140] Ludovic Le Reste et al. “Characterization of dark quencher chromophores as nonfluorescent acceptors for single-molecule FRET”. In: *Biophysical journal* 102.11 (2012), pp. 2658–2668. DOI: 10.1016/j.bpj.2012.04.028.

[141] Sanjay Tyagi and Fred Russell Kramer. “Molecular Beacons: Probes that Fluoresce upon Hybridization”. In: *Nature Biotechnology* 14 (Mar. 1, 1996), p. 303. DOI: 10.1038/nbt0396-303.

[142] Tim Schröder et al. “Interchromophoric interactions determine the maximum brightness density in DNA origami structures”. In: *Nano letters* 19.2 (2019), pp. 1275–1281. DOI: 10.1021/acs.nanolett.8b04845.

[143] Gordon J Hedley et al. “Picosecond time-resolved photon antibunching measures nanoscale exciton motion and the true number of chromophores”. In: *Nature Communications* 12.1 (2021), p. 1327. DOI: 10.1038/s41467-021-21474-z.

[144] Thomas Gensch, Martin Böhmer, and Pedro F Aramendía. "Single molecule blinking and photobleaching separated by wide-field fluorescence microscopy". In: *The Journal of Physical Chemistry A* 109.30 (2005), pp. 6652–6658. DOI: 10.1021/jp0510847.

[145] Erwin JG Peterman, Sophie Brasselet, and WE Moerner. "The fluorescence dynamics of single molecules of green fluorescent protein". In: *The Journal of Physical Chemistry A* 103.49 (1999), pp. 10553–10560. DOI: 10.1021/jp991968o.

[146] Jerker Widengren and Petra Schwille. "Characterization of photoinduced isomerization and back-isomerization of the cyanine dye Cy5 by fluorescence correlation spectroscopy". In: *The Journal of Physical Chemistry A* 104.27 (2000), pp. 6416–6428. DOI: 10.1021/jp000059s.

[147] Rob Zondervan et al. "Photoblinking of rhodamine 6G in poly (vinyl alcohol): Radical dark state formed through the triplet". In: *The Journal of Physical Chemistry A* 107.35 (2003), pp. 6770–6776. DOI: 10.1021/jp034723r.

[148] Dominic A Helmerich et al. "Photoblueing of organic dyes can cause artifacts in super-resolution microscopy". In: *Nature Methods* 18.3 (2021), pp. 253–257. DOI: 10.1038/s41592-021-01061-2.

[149] NA Evans. "Photofading of rhodamine dyes: I—Identification of some rhodamine B photoproducts". In: *Journal of the Society of Dyers and Colourists* 86.4 (1970), pp. 174–177. DOI: 10.1111/j.1478-4408.1970.tb02946.x.

[150] Mark Bates, Timothy R Blosser, and Xiaowei Zhuang. "Short-range spectroscopic ruler based on a single-molecule optical switch". In: *Physical review letters* 94.10 (2005), p. 108101. DOI: 10.1103/PhysRevLett.94.108101.

[151] Graham T Dempsey et al. "Photoswitching mechanism of cyanine dyes". In: *Journal of the American Chemical Society* 131.51 (2009), pp. 18192–18193. DOI: 10.1021/ja904588g.

[152] Yasser Gidi et al. "Unifying mechanism for thiol-induced photoswitching and photostability of cyanine dyes". In: *Journal of the American Chemical Society* 142.29 (2020), pp. 12681–12689. DOI: 10.1021/jacs.0c03786.

[153] Th Basché, WP Ambrose, and WE Moerner. "Optical spectra and kinetics of single impurity molecules in a polymer: spectral diffusion and persistent spectral hole burning". In: *JOSA B* 9.5 (1992), pp. 829–836. DOI: 10.1364/JOSAB.9.000829.

[154] Daniel Axelrod, Thomas P Burghardt, and Nancy L Thompson. "Total internal reflection fluorescence". In: *Annual review of biophysics and bioengineering* 13.1 (1984), pp. 247–268. DOI: 10.1146/annurev.bb.13.060184.001335.

[155] Stefan W Hell and Matthias Kroug. "Ground-state-depletion fluorscence microscopy: A concept for breaking the diffraction resolution limit". In: *Applied Physics B* 60 (1995), pp. 495–497. DOI: 10.1007/BF01081333.

[156] Thomas A Klar and Stefan W Hell. "Subdiffraction resolution in far-field fluorescence microscopy". In: *Optics letters* 24.14 (1999), pp. 954–956. DOI: 10.1364/OL.24.000954.

[157] Rainer Heintzmann and Christoph G Cremer. "Laterally modulated excitation microscopy: improvement of resolution by using a diffraction grating". In: 3568 (1999), pp. 185–196. DOI: 10.1117/12.336833.

[158] Mats GL Gustafsson. "Surpassing the lateral resolution limit by a factor of two using structured illumination microscopy". In: *Journal of microscopy* 198.2 (2000), pp. 82–87. DOI: 10.1046/j.1365-2818.2000.00710.x.

[159] Arne H Voie, DH Burns, and FA Spelman. "Orthogonal-plane fluorescence optical sectioning: Three-dimensional imaging of macroscopic biological specimens". In: *Journal of microscopy* 170.3 (1993), pp. 229–236. DOI: 10.1111/j.1365-2818.1993.tb03346.x.

[160] Jan Huisken et al. "Optical sectioning deep inside live embryos by selective plane illumination microscopy". In: *Science* 305.5686 (2004), pp. 1007–1009. DOI: 10.1126/science.1100035.

[161] Siân Culley et al. "SRRF: Universal live-cell super-resolution microscopy". In: *The international journal of biochemistry & cell biology* 101 (2018), pp. 74–79. DOI: 10.1016/j.biocel.2018.05.014.

[162] Thomas Dertinger et al. "Fast, background-free, 3D super-resolution optical fluctuation imaging (SOFI)". In: *Proceedings of the National Academy of Sciences* 106.52 (2009), pp. 22287–22292. DOI: 10.1073/pnas.0907866106.

[163] Mickaël Lelek et al. "Single-molecule localization microscopy". In: *Nature reviews methods primers* 1.1 (2021), p. 39. DOI: 10.1038/s43586-021-00038-x.

[164] Samuel T Hess, Thanu PK Girirajan, and Michael D Mason. "Ultra-high resolution imaging by fluorescence photoactivation localization microscopy". In: *Biophysical journal* 91.11 (2006), pp. 4258–4272. DOI: 10.1529/biophysj.106.091116.

[165] Sebastian van de Linde et al. "Photoswitching microscopy with standard fluorophores". In: *Applied Physics B* 93 (2008), pp. 725–731. DOI: 10.1007/s00340-008-3250-9.

[166] Christian Steinhauer et al. "Superresolution microscopy on the basis of engineered dark states". In: *Journal of the American Chemical Society* 130.50 (2008), pp. 16840–16841. DOI: 10.1021/ja806590m.

[167] Sebastian Van de Linde et al. "Direct stochastic optical reconstruction microscopy with standard fluorescent probes". In: *Nature protocols* 6.7 (2011), pp. 991–1009. DOI: 10.1038/nprot.2011.336.

[168] Ulrike Endesfelder and Mike Heilemann. "Direct stochastic optical reconstruction microscopy (d STORM)". In: *Advanced Fluorescence Microscopy: Methods and Protocols* (2015), pp. 263–276. DOI: 10.1007/978-1-4939-2080-8_14.

[169] Fehmi Civitci et al. "Fast and multiplexed superresolution imaging with DNA-PAINT-ERS". In: *Nature communications* 11.1 (2020), p. 4339.

[170] Florian Schueder et al. "An order of magnitude faster DNA-PAINT imaging by optimized sequence design and buffer conditions". In: *Nature methods* 16.11 (2019), pp. 1101–1104. DOI: 10.1038/s41592-019-0584-7.

[171] Mike Filius et al. "High-speed super-resolution imaging using protein-assisted DNA-PAINT". In: *Nano letters* 20.4 (2020), pp. 2264–2270. DOI: 10.1021/acs.nanolett.9b04277.

[172] Sebastian Strauss and Ralf Jungmann. "Up to 100-fold speed-up and multiplexing in optimized DNA-PAINT". In: *Nature methods* 17.8 (2020), pp. 789–791. DOI: 10.1038/s41592-020-0869-x.

[173] Alexander Auer et al. "Fast, background-free DNA-PAINT imaging using FRET-based probes". In: *Nano letters* 17.10 (2017), pp. 6428–6434. DOI: 10.1021/acs.nanolett.7b03425.

[174] Soohyun Jang, Mingi Kim, and Sang-Hee Shim. "Reductively Caged, Photoactivatable DNA-PAINT for High-Throughput Super-resolution Microscopy". In: *Angewandte Chemie International Edition* 59.29 (2020), pp. 11758–11762. DOI: 10.1002/anie.201915377.

[175] Kenny KH Chung et al. “Fluorogenic DNA-PAINT for faster, low-background super-resolution imaging”. In: *Nature methods* 19.5 (2022), pp. 554–559. DOI: 10.1038/s41592-022-01464-9.

[176] Mirjam Kummerlin et al. “Tunable fluorogenic DNA probes drive fast and high-resolution single-molecule fluorescence imaging”. In: *bioRxiv* (2025), pp. 2025–01. DOI: 10.1101/2025.01.21.634148.

[177] Laurell F Kessler et al. “Self-quenched Fluorophore Dimers for DNA-PAINT and STED Microscopy”. In: *Angewandte Chemie International Edition* 62.39 (2023), e202307538. DOI: 10.1002/anie.202307538.

[178] Mirjam Kümmerlin, Abhishek Mazumder, and Achillefs N Kapanidis. “Bleaching-resistant, Near-continuous Single-molecule Fluorescence and FRET Based on Fluorogenic and Transient DNA Binding”. In: *ChemPhysChem* 24.12 (2023), e202300175. DOI: 10.1002/cphc.202300175.

[179] Lothar Schermelleh et al. “Super-resolution microscopy demystified”. In: *Nature cell biology* 21.1 (2019), pp. 72–84. DOI: 10.1038/s41556-018-0251-8.

[180] Peuli Nath, Kazi Ridita Mahtaba, and Aniruddha Ray. “Fluorescence-based portable assays for detection of biological and chemical analytes”. In: *Sensors* 23.11 (2023), p. 5053. DOI: 10.3390/s23115053.

[181] Haoran Wang, Rainer Heintzmann, and Benedict Diederich. “The power in your pocket–uncover smartphones for use as cutting-edge microscopic instruments in science and research”. In: *Advanced Optical Technologies* 10.2 (2021), pp. 89–108. DOI: 10.1515/aot-2021-0013.

[182] Daria Semeniak et al. “Plasmonic fluorescence enhancement in diagnostics for clinical tests at point-of-care: A review of recent technologies”. In: *Advanced Materials* 35.34 (2023), p. 2107986. DOI: 10.1002/adma.202107986.

[183] Donna R Whelan and Toby DM Bell. “Image artifacts in single molecule localization microscopy: why optimization of sample preparation protocols matters”. In: *Scientific reports* 5.1 (2015), p. 7924. DOI: 10.1038/srep07924.

[184] Shawn M Douglas et al. “Rapid prototyping of 3D DNA-origami shapes with caDNAno”. In: *Nucleic Acids Research* 37.15 (2009), pp. 5001–5006. DOI: 10.1093/nar/gkp436.

[185] Do-Nyun Kim et al. “Quantitative prediction of 3D solution shape and flexibility of nucleic acid nanostructures”. In: *Nucleic Acids Research* 40.7 (2012), pp. 2862–2868. DOI: 10.1093/nar/gkr1173.

[186] Carlos Ernesto Castro et al. "A primer to scaffolded DNA origami". en. In: *Nature Methods* 8.3 (2011), pp. 221–229. DOI: 10.1038/nmeth.1570.

[187] Chad A Mirkin et al. "A DNA-based method for rationally assembling nanoparticles into macroscopic materials". In: *Nature* 382.6592 (1996), p. 607. DOI: 10.1038/382607a0.

[188] Arthur Edelstein et al. "Computer control of microscopes using μManager". In: *Current protocols in molecular biology* 92.1 (2010), pp. 14–20.

[189] Arthur D Edelstein et al. "Advanced methods of microscope control using μManager software". In: *Journal of biological methods* 1.2 (2014). DOI: 10.1002/0471142727.mb1420s92.

[190] Joerg Schnitzbauer et al. "Super-resolution microscopy with DNA-PAINT". In: *Nature protocols* 12.6 (2017), pp. 1198–1228. DOI: 10.1038/nprot.2017.024.

[191] Alan M Szalai et al. "Three-dimensional total-internal reflection fluorescence nanoscopy with nanometric axial resolution by photometric localization of single molecules". In: *Nature communications* 12.1 (2021), pp. 1–13. DOI: 10.1038/s41467-020-20863-0.

[192] Sergei Kühn et al. "Enhancement of Single-Molecule Fluorescence Using a Gold Nanoparticle as an Optical Nanoantenna". In: *Physical review letters* 97.1 (2006), p. 017402. DOI: 10.1103/PhysRevLett.97.017402.

[193] M. J. Levene. "Zero-Mode Waveguides for Single-Molecule Analysis at High Concentrations". In: *Science* 299.5607 (Jan. 31, 2003), pp. 682–686. DOI: 10.1126/science.1079700.

[194] Rahul Chhabra et al. "Distance-dependent interactions between gold nanoparticles and fluorescent molecules with DNA as tunable spacers". In: *Nanotechnology* 20.48 (2009), p. 485201. DOI: 10.1088/0957-4484/20/48/485201.

[195] Paul A Wiggins et al. "High flexibility of DNA on short length scales probed by atomic force microscopy". In: *Nature Nanotechnology* 1.2 (2006), p. 137. DOI: 10.1038/nnano.2006.63.

[196] Mickaël P Busson et al. "Accelerated single photon emission from dye molecule-driven nanoantennas assembled on DNA". In: *Nature communications* 3.1 (2012), pp. 1–6. DOI: 10.1038/ncomms1964.

[197] Guillermo P Acuna et al. "Distance dependence of single-fluorophore quenching by gold nanoparticles studied on DNA origami". In: *ACS Nano* 6.4 (2012), pp. 3189–3195. DOI: 10.1021/nn2050483.

[198] Anton Kuzyk et al. “DNA-based self-assembly of chiral plasmonic nanostructures with tailored optical response”. In: *Nature* 483.7389 (2012), pp. 311–314. DOI: 10.1038/nature10889.

[199] Robert Schreiber et al. “Hierarchical assembly of metal nanoparticles, quantum dots and organic dyes using DNA origami scaffolds”. In: *Nature nanotechnology* 9.1 (2014), pp. 74–78. DOI: 10.1038/nnano.2013.253.

[200] Anton Kuzyk et al. “Reconfigurable 3D plasmonic metamolecules”. In: *Nature materials* 13.9 (2014), pp. 862–866. DOI: 10.1038/nmat4031.

[201] Julia Prinz et al. “DNA origami based Au–Ag-core–shell nanoparticle dimers with single-molecule SERS sensitivity”. In: *Nanoscale* 8.10 (2016), pp. 5612–5620. DOI: 10.1039/C5NR08674D.

[202] John Eid et al. “Real-Time DNA Sequencing from Single Polymerase Molecules”. In: *Science* 323.5910 (Jan. 2, 2009), pp. 133–138. DOI: 10.1126/science.1162986.

[203] Viktorija Glembockyte et al. “DNA Origami Nanoantennas for Fluorescence Enhancement”. In: *Accounts of Chemical Research* 54.17 (2021), pp. 3338–3348. DOI: 10.1021/acs.accounts.1c00307.

[204] Carolin Vietz et al. “Functionalizing large nanoparticles for small gaps in dimer nanoantennas”. In: *New Journal of Physics* 18.4 (Apr. 2016), p. 045012. DOI: 10.1088/1367-2630/18/4/045012.

[205] Sanjay Tyagi and Fred Russell Kramer. “Molecular beacons: probes that fluoresce upon hybridization”. In: *Nature Biotechnology* 14.3 (1996), pp. 303–308. DOI: 10.1038/nbt0396-303.

[206] Lennart Grabenhorst et al. “Fluorophore photostability and saturation in the hotspot of DNA origami nanoantennas”. In: *Methods and Applications in Fluorescence* (2020). DOI: 10.1088/2050-6120/ab6ac8.

[207] Jonas Ries et al. “A simple, versatile method for GFP-based super-resolution microscopy via nanobodies”. In: *Nature methods* 9.6 (2012), pp. 582–584. DOI: 10.1038/nmeth.1991.

[208] Philipp R Steen et al. “The DNA-PAINT palette: a comprehensive performance analysis of fluorescent dyes”. In: *Nature Methods* 21.9 (2024), pp. 1755–1762. DOI: 10.1038/s41592-024-02374-8.

[209] Waldemar Adam et al. “Synthesis of endoperoxides derived from cyclooctatetraenes via singlet oxygenation”. In: *Tetrahedron* 41.11 (1985), pp. 2045–2056. DOI: S0040-4020(01)96575-5.

[210] Tomi NathâDas and K IndiraáPriyadarshini. “Triplet of cyclooctatetraene: Reactivity and properties”. In: *Journal of the Chemical Society, Faraday Transactions* 90.7 (1994), pp. 963–968. DOI: 10.1039/FT9949000963.

[211] Supphachok Chanmungkalakul et al. “The dark side of cyclooctatetraene (COT): photophysics in the singlet states of “self-healing” dyes”. In: *Chinese Chemical Letters* 35.8 (2024), p. 109227. DOI: 10.1016/j.cclet.2023.109227.

[212] Avik K Pati et al. “Tuning the Baird aromatic triplet-state energy of cyclooctatetraene to maximize the self-healing mechanism in organic fluorophores”. In: *Proceedings of the National Academy of Sciences* 117.39 (2020), pp. 24305–24315. DOI: 10.1073/pnas.2006517117.

[213] Lei Zhang et al. “Linker Molecules Convert Commercial Fluorophores into Tailored Functional Probes during Biolabelling”. In: *Angewandte Chemie* 134.19 (2022), e202112959. DOI: 10.1002/ange.202112959.

[214] Yuan Zhang et al. “General strategy to improve the photon budget of thiol-conjugated cyanine dyes”. In: *Journal of the American Chemical Society* 145.7 (2023), pp. 4187–4198. DOI: 10.1021/jacs.2c12635.

[215] Robert Crawford et al. “Long-lived intracellular single-molecule fluorescence using electroporated molecules”. In: *Biophysical journal* 105.11 (2013), pp. 2439–2450. DOI: 10.1016/j.bpj.2013.09.057.

[216] A Plochowietz et al. “Stable end-sealed DNA as robust nano-rulers for in vivo single-molecule fluorescence”. In: *Chemical Science* 7.7 (2016), pp. 4418–4422. DOI: 10.1039/c6sc00639f.

[217] Christoph Spahn et al. “Correlative super-resolution imaging of RNA polymerase distribution and dynamics, bacterial membrane and chromosomal structure in Escherichia coli”. In: *Methods and applications in fluorescence* 3.1 (2015), p. 014005. DOI: 10.1088/2050-6120/3/1/014005.

[218] Lennart Grabenhorst et al. “Single-Molecule FRET at 10 MHz Count Rates”. In: *Journal of the American Chemical Society* 146.5 (2024), pp. 3539–3544. DOI: 10.1021/jacs.3c13757.

[219] Rishabh M Shetty et al. “Bench-top fabrication of single-molecule nanoarrays by DNA origami placement”. In: *ACS nano* 15.7 (2021), pp. 11441–11450. DOI: 10.1021/acsnano.1c01150.

[220] Irina V Martynenko et al. “DNA origami meets bottom-up nanopatterning”. In: *ACS nano* 15.7 (2021), pp. 10769–10774. DOI: 10.1021/acsnano.1c04297.

[221] David S. Goodsell. “Integrative illustration of Escherichia coli”. In: *Molecular Landscapes* (2022). DOI: 10.2210/rcsb_pdb/goodsell-gallery-028.

[222] Peter B Luppa et al. “Point-of-care testing (POCT): Current techniques and future perspectives”. In: *TrAC Trends in Analytical Chemistry* 30.6 (2011), pp. 887–898. DOI: 10.1016/j.trac.2011.01.019.

[223] Alpaslan Alp. “Advancement in POCT molecular testing: the multiplex PCR POCT devices for infectious diseases”. In: *EJIFCC* 29.3 (2018), p. 205. PMCID: PMC6247132.

[224] Yong Peng and Carlo M Croce. “The role of MicroRNAs in human cancer”. In: *Signal transduction and targeted therapy* 1.1 (2016), pp. 1–9. DOI: 10.1038/sigtrans.2015.4.

[225] David M Rissin et al. “Single-molecule enzyme-linked immunosorbent assay detects serum proteins at subfemtomolar concentrations”. In: *Nature Biotechnology* 28.6 (2010), p. 595. DOI: 10.1038/nbt.1641.

[226] Stephanie M Schubert et al. “Ultra-sensitive protein detection via Single Molecule Arrays towards early stage cancer monitoring”. In: *Scientific Reports* 5 (2015), p. 11034. DOI: 10.1038/srep11034.

[227] Egisto Boschetti and Pier Giorgio Righetti. “Low-Abundance Protein Enrichment for Medical Applications: The Involvement of Combinatorial Peptide Library Technique”. In: *International Journal of Molecular Sciences* 24.12 (2023), p. 10329. DOI: 10.3390/ijms241210329.

[228] Floyd E Taub, James M DeLeo, and E Brad Thompson. “Sequential comparative hybridizations analyzed by computerized image processing can identify and quantitate regulated RNAs”. In: *Dna* 2.4 (1983), pp. 309–327. DOI: 10.1089/dna.1983.2.309.

[229] M Kursad Araz, Augusto M Tentori, and Amy E Herr. “Microfluidic multiplexing in bioanalyses”. In: *Journal of Laboratory Automation* 18.5 (2013), pp. 350–366. DOI: 10.1177/2211068213491408.

[230] James F Rusling. “Multiplexed electrochemical protein detection and translation to personalized cancer diagnostics”. In: *Analytical chemistry* 85.11 (2013), pp. 5304–5310. DOI: 10.1021/ac401058v.

9 Publications and conference contributions

Preprints

Claudia Bastl*, Cindy Close*, Ingo Holtz*, Blaise Gatin-Fraudet, Mareike Eis, Michelle Werum1, Smilla Konrad, Kilian Roßmann, Christiane Huhn, Souvik Ghosh, Julia Ast, Dorien A. Roosen, Martin Lehmann, Volker Haucke, Luc Reymond, David J. Hodson, Philip Tinnefeld, Kai Johnsson, Viktorija Glembockyte, Nicole Kilian, Johannes Broichhagen. A silicon rhodamine-fused glibenclamide to label and detect malaria-infected red blood cells. bioRxiv 2025/637098 (2025). doi: https://doi.org/10.1101/2025.02.07.637098

Michael Scheckenbach,* Cindy Close,* Alan Szalai, Julian Bauer, Lennart Grabenhorst, Fiona Cole, Lei Zhang, Thorben Cordes, Philip Tinnefeld, and Viktorija Glembockyte. Minimally Invasive DNA-Mediated Photostabilization for Extended Single-Molecule and Super-resolution Imaging. bioRxiv 2025/631860 (2025). doi: https://doi.org/10.1101/2025.01.08.631860

Renukka Yaadav, Kateryna Trofymchuk, Mihir Dass, Vivien Behrendt, Benedikt Hauer, Jan Schütz, Cindy Close, Michael Scheckenbach, Giovanni Ferrari, Leoni Maeurer, Sophia Sebina, Viktorija Glembockyte, Tim Liedl, Philip Tinnefeld. Bringing Attomolar Detection to the Point-of-Care with Nanopatterned DNA Origami Nanoantennas. bioRxiv, 2024/618183 (2024). doi: 10.1101/2024.10.14.618183

* equal contribution

Peer reviewed publications

Kateryna Trofymchuk*, Viktorija Glembockyte*, Lennart Grabenhorst, Florian Steiner, Carolin Vietz, Cindy Close, Martina Pfeiffer, Lars Richter, Max L. Schütte, Florian Selbach, Renukka Yaadav, Jonas Zähringer, Qingshan Wei, Aydogan Ozcan, Birka Lalkens, Guillermo P. Acuna, Philip Tinnefeld. Addressable nanoantennas with cleared hotspots for single-molecule detection on a portable smartphone microscope. *Nature Communications* **12**(1):950 (2021). doi: 10.1038/s41467-021-21238-9

Cindy Close, Kateryna Trofymchuk, Lennart Grabenhorst, Birka Lalkens, Viktorija Glembockyte, Philip Tinnefeld. Maximizing the Accessibility in DNA Origami Nanoantenna Plasmonic Hotspots. *Advanced Materials Interfaces* **9**, 24 (2022). doi: 10.1002/admi.202200255

* equal contribution

Invited Talks

Cindy Close, Michael Scheckenbach, Alan Szalai, Julian Bauer, Giovanni Ferrari, Lennart Grabenhorst, Fiona Cole, Lei Zhang, Thorben Cordes, Javier Periz, Philip Tinnefeld, and Viktorija Glembockyte. Photostabilization in single-molecule and super-resolution measurements. Invited talk presented at the Biophysics Seminar 3 TT5 of the Oxford Biophysics Department (Physics) **2024** (Oxford, UK)

Cindy Close, Kateryna Trofymchuk, Lennart Grabenhorst, Birka Lalkens, Viktorija Glembockyte, Philip Tinnefeld. NACHOS for Biosensing: Maximizing the Accessibility in DNA Origami Nanoantenna Plasmonic Hotspots. Invited talk presented at the webinar DNA Nanotech for Medicine and Biology of the University of Edinburgh **2022** (virtual)

Awards

Best oral presentation award in chemistry and chemical physics at the 67th international Open Readings conference **2024** (Vilnius, Lithuania)

Best student talk award at the 27th international PicoQuant workshop on single molecule spectroscopy and super-resolution microscopy **2022** (Berlin, Germany)

CeNS publication award scientific breakthrough for *Nature Communications* **12**(1):950 **2021**. (Munich, Germany)

Conference contributions

Cindy Close, Michael Scheckenbach, Alan Szalai, Julian Bauer, Lennart Grabenhorst, Fiona Cole, Thorben Cordes, Philip Tinnefeld, Viktorija Glembockyte. Docking-site mediated photostabilization for single-molecule and super-resolution Imaging. Poster presented at the 13th international single molecule localization microscopy symposium (SLMLS) **2024** (Lisbon, Portugal)

Cindy Close, Michael Scheckenbach, Alan Szalai, Julian Bauer, Lennart Grabenhorst, Fiona Cole, Thorben Cordes, Philip Tinnefeld, Viktorija Glembockyte. Docking-site mediated photostabilization for single-molecule and super-resolution imaging. Talk presented at the 67th international Open Readings conference for students of physics and natural sciences **2024** (Vilnius, Lithuania)

Cindy Close, Michael Scheckenbach, Lei Zhang, Michael Isselstein, Thorben Cordes, Philip Tinnefeld, Viktorija Glembockyte. Docking site-mediated photostabilization for single-molecule and super-resolution imaging. Talk and poster presented at the international physics of living systems (iPoLS) network annual meeting **2023** (Atlanta, USA)

Cindy Close, Michael Scheckenbach, Lei Zhang, Michael Isselstein, Thorben Cordes, Philip Tinnefeld, Viktorija Glembockyte. Docking-site mediated photostabilization for super-resolution Imaging. Talk presented at the 12th international single molecule localization microscopy symposium (SLMLS) **2023** (Vienna, Austria)

Cindy Close, Michael Scheckenbach, Alan Szalai, Julian Bauer, Giovanni Ferrari, Lennart Grabenhorst, Fiona Cole, Lei Zhang, Thorben Cordes, Javier Periz, Philip Tinnefeld, Viktorija Glembockyte. Docking-Site-Mediated Photostabilization for Super-Resolution Imaging. Talk presented at the 27th international PicoQuant workshop on single molecule spectroscopy and super-resolution microscopy **2022** (Berlin, Germany)

Cindy Close, Michael Scheckenbach, Viktorija Glembockyte, Lei Zhang, Pheng Zhou, Thorben Cordes, Philip Tinnefeld. Self-regenerating photostabilization mechanism for DNA-PAINT using cyclooctatetraene. Poster presented at the winter school for fluorescence markers and advanced microscopies **2022** (Les Houches, France)

10 Acknowledgements

I want to thank Philip for introducing me to his group and making me feel welcome in the scientific community. Thank you for providing us with great facilities and equipment to play around with and for financial support to go to conferences. I am very grateful for your support when pursuing projects and collaborations I was interested in. You always acknowledged the effort it takes to do experiments and I could always count on your scientific integrity. Working in this supportive athmosphere made it easier to navigate the scientific and personal challenges of a PhD and I am incredibly grateful for this experience.

I sincerely thank Achim Hartschuh for agreeing to be the co-examiner of this thesis. His lecture for the first semester chemistry lab was my first contact with the physical chemistry department and I remember it fondly.

Thank you to Tim Liedl, Lukas Milles and Silvija Markic for being part of my committee.

I want to thank Viktorija for being an inspiring role model and mentor for the past seven years. Through you I will always regain my excitement for science and remember why it is all worth it. I'm looking forward to see all of the cool projects you and your new students will realize!

Kateryna, I was so lucky to join you on the nanoantenna project! You were a patient and supportive teacher and helped me so much, from my beginnings in the group, to my first manuscript and beyond. I am very grateful to have worked with you.

Alan, thank you for being my guide on microtubule imaging and for supporting the quencher project. I hope it continues!

Giovanni: It was great fun to work with you and Javier on the Toxoplasm project. Even when Alan got scared and left the room because something moved in the fixed sample, we kept measuring.

Thank you to JB and Nicole for involving me in the Malaria detection project. It was so fun to work in the lab with you (especially on Koawach at midnight).

Dear Angelika: You are a huge support to all of us, particularly for me in the cell culture. Thank you for giong to cool concerts with us!

Herr Ehrl, aside from supporting us in contract and ordering-related matters, thank you for taking care we work in an organized and safe environment.

Thank you Tim for supporting all of us. Specifically, thank you for teaching Patrick and me at the confocal and for actually taking notes and following up with ideas after meetings.

Kalys, thank you for helping us with all things administrative. You have made our life in the group alot easier and fun when you joined.

Thank you to my three office amigos, for always being there to talk and vent on science and everything else:

Michi, after working alone on my cells, you asking me to join on the COT project really lifted me up. I really enjoy working with someone as conscientious and understanding as you are.

Renu, I am so happy to have worked with you on the nanoantennas. I continue to be amazed with your endurance and success in optimizing the assay and wish you good luck for all future endeavors in science and life.

Ece, you were an inspiration to me for being so well organized and getting through the hard parts of a project without losing motivation. I am sure many exciting new projects in science and life lie in your future.

Thank you Lennart for helping me with the Fork design and DNA simulations. I'm very grateful you designed such an amazing cover figure for the project!

Julian, thank you for keeping me company in the Widefield lab, for spending the time building in the flat-top beam shaper, being interested in my projects and sparking my interest in yours.

Karina, thank you for dancing with me! Merve, thank you for investing some long days at the ÄKTA and making kazakh Mantisi with us.

My students Dominik, Maximilian and Christoph I thank for their interest, hard work and persistence on their projects. I am especially lucky to have had Jakob join early on in my PhD and return again later. Jakob, thank you for help and discussions on our latest cell-related project.

I thank every single member that has joined the Tinnefeld group during the past years. You all have contributed to a supportive and fun environment.

Mama, thank you for always being interested in my work and studies and for reassuring me during difficult times.

Daddy, thank you for studying physics with me in school. You showed me how

fun it is to futz around with things to find out how they work.

Evelyn, thank you for being a wonderful and supportive sister. I hope to visit you often in your new home and make dessert together.

Thank you Jericho Fischer for meeting me in Moosach and serenading me ever since.

I thank Patrick, Benald and Lennart for their long-standing support and all the fun times. Its very special that all of us are finding their own way in life, but still remain connected.

My ensemble members Lilly, Vincent and Andi I thank for the joyous times playing music together and making people listen.

I thank the entire StOrch, in particular the first violin section for all of the fun reheasals and cool concerts we got to experience together.

I thank Mirjam, one of my first friends in our studies, for always staying by my side and supporting me all the way until now.

11 Appendix

11.1 Associated Publication 1

Minimally Invasive DNA-Mediated Photostabilization for Extended Single-Molecule and Super-resolution Imaging

Michael Scheckenbach,* Cindy Close,* Julian Bauer, Lennart Grabenhorst, Fiona Cole, Jens Köhler, Siddharth S. Matikonda, Lei Zhang, Thorben Cordes, Martin J. Schnermann, Andreas Hermann, Philip Tinnefeld, Alan Szalai and Viktorija Glembockyte

*equal contribution

Preprint on bioRxiv 2025/631860 (2025).
doi: https://doi.org/10.1101/2025.01.08.631860

Minimally Invasive DNA-Mediated Photostabilization for Extended Single-Molecule and Super-resolution Imaging

Michael Scheckenbach,[1‡] Cindy Close,[1‡] Julian Bauer,[1] Lennart Grabenhorst,[1] Fiona Cole,[1] Jens Köhler,[2,3] Siddharth S. Matikonda,[4] Lei Zhang,[5] Thorben Cordes,[5,6] Martin J. Schnermann,[4] Andreas Herrmann,[3,4] Philip Tinnefeld,[1] Alan Szalai,[1,7] and Viktorija Glembockyte*[1,8]

[1] Department of Chemistry and Center for NanoScience, Ludwig-Maximilians-Universität München, Butenandtstr. 5-13, 81377 München, Germany

[2] DWI – Leibniz Institute for Interactive Materials, Forckenbeckstr. 50, 52056 Aachen, Germany

[3] Institute of Technical and Macromolecular Chemistry, RWTH Aachen University, Worringerweg 2, 52074 Aachen, Germany

[4] Laboratory of Chemical Biology, Center for Cancer Research, National Cancer Institute, Frederick, MD 21702 (USA)

[5] Physical and Synthetic Biology, Faculty of Biology, Ludwig-Maximilians-Universität München, Großhadernerstr. 2-4, 82152 Planegg-Martinsried, Germany

[6] Biophysical Chemistry, Department of Chemistry and Chemical Biology, Technische Universität Dortmund, Otto-Hahn-Str. 4a, 44227 Dortmund, Germany

[7] Centro de Investigaciones en Bionanociencias, Consejo Nacional de Investigaciones Científicas y Técnicas; Ciudad Autónoma de Buenos Aires, C1425FQD, Argentina

[8] Max Planck Institute for Medical Research, Jahnstr. 29, 69120 Heidelberg, Germany

E-mail: viktorija.glembockyte@mr.mpg.de

‡ These authors contributed equally

Abstract:

Photobleaching of fluorescence labels poses a major limitation in single-molecule and super-resolution microscopy. Conventional photostabilization methods, such as oxygen removal and addition of high concentrations of photostabilization additives, often require careful fluorophore selection and can disrupt the biological environment. To address these limitations, we developed a modular and minimally invasive photostabilization approach that utilizes DNA-mediated delivery of a photostabilizer directly to the imaging site. Under lower excitation intensities, the DNA-mediated strategy outperformed solution-based approaches, achieving efficient photostabilization at significantly lower additive concentrations. However, at higher excitation intensities, the stability of a single photostabilizer molecule became the limiting factor. To overcome this and reduce the loss of localizations in DNA-PAINT experiments we have also implemented a recovery scheme where the photostabilizer is continuously replenished at the imaging site. We further extended the approach to cell imaging, demonstrating improved localization rate and precision in 3D-DNA PAINT measurements. DNA-mediated photostabilization offers a promising solution for imaging applications where high additive concentrations are prohibited. Its modularity enables adaptation

to various imaging schemes and ultimately expands the repertoire of fluorophores suitable for single-molecule and super-resolution imaging.

Introduction

Single-molecule fluorescence imaging methods have expanded tremendously since the very first observation of single molecules at ultra-low temperatures[1] and led to many exciting experiments investigating biomolecular interactions, tracking them inside of live cells[2-6] and even breaking the diffraction barrier to resolve nanoscale features[7], interactions, or dynamics. Meanwhile one of the main bottlenecks in most of fluorescence imaging experiments remains the premature photobleaching of fluorescent labels[8]. When tracking and monitoring the interactions between individual molecules (e.g. via fluorescence resonance energy transfer (FRET)), the total number of photons that can be collected from a fluorescent label determines the end of the observation window, while in localization-based super resolution imaging techniques it is tightly linked to the localization precision one can achieve[9].

To extend the total photon budget of fluorescence labels used for these imaging applications one relies on photostabilization strategies that act on the photochemical bleaching pathways (Figure 1a). This typically includes removing molecular oxygen (which can undergo triplet-triplet energy transfer with triplet excited states of fluorescent labels) to prevent the sensitization of singlet oxygen and downstream reactive oxygen species (ROS)[10, 11]. However, removal of oxygen leads to long-lived and reactive triplet dark states, therefore, oxygen removal is typically supplemented by addition of triplet state quenchers (TSQs). [8, 12] TSQs can quench the triplet excited states via photophysical mechanisms (k_{TET} in Figure 1a), such as energy transfer (e.g., as is observed for cyclooctatetraene[13-17] or Ni^{2+} ions[18, 19]) or photochemical mechanisms that rely on reduction (or oxidation) of the triplet excited state with an appropriate reducing (or oxidizing) additive to generate the radical anion (or cation) species[20-23]. The long-lived radical intermediates are subsequently rescued by the addition of a complementary oxidizing (or reducing) partner, an approach that is commonly known as ROXS for **r**educing and **ox**idizing **s**ystem (k_{red} and k_{ox} in Figure 1a)[12]. To circumvent the need for high concentrations of solution-based additives, the photostabilizers can alternatively be directly coupled to the fluorophore core to obtain "self-healing" dyes, however, at the price of additional synthesis and optimization steps.[24-29] The strategies outlined above have helped to improve the photon budgets by over hundreds of folds in specific instances. Nonetheless, even with the most photostable fluorescent labels paired with the most efficient stabilization approaches the total number of photons is limited to a few millions of photons.

One of the imaging "tricks" used to fundamentally overcome the limits posed by the finite photon budget of single fluorescent labels involves the continuous replacement of bleached labels via transient binding. This is nicely exemplified by super-resolution imaging with DNA-PAINT.[30] DNA-PAINT relies on transient binding of short fluorescently labelled DNA oligonucleotides (imager strands) to the target of interest labelled with a complementary DNA sequence (docking sites) to achieve apparent blinking at the imaging site which is, in turn, used for stochastic super-resolution imaging. Here, each docking site can bind multiple imager strands over time and the imaging quality and efficiency are no longer limited by the photobleaching of the single-fluorescent label in contrast to other localization-based super-resolution imaging methods (e.g., PALM or STORM)[31-33].

In recent years, several other approaches that exploit DNA-mediated dynamic exchange of fluorescent labels to generate a long lasting and photostable fluorescence signal have been put forward. For example, in our previous work we have used the dynamic exchange of bleached fluorophore strands with intact ones from solution to generate self-regenerating DNA origami-based brightness rulers.[34] Repetitive DNA

binding motives to continuously exchange labels in solution have also been successfully exploited to design a long-lasting fluorescence label for tracking single biological molecules for hours.[35] Introduction of DNA-PAINT imager strands into STED microscopy has overcome the photobleaching of permanent fluorescent labels.[36] The more recent "REFRESH" and "Dye cycling" approaches used analogous strategies to continuously exchange both, donor and acceptor labels enabling near-continuous observation of single-molecules for more than an hour and extending these ideas to FRET imaging studies.[37, 38] New imaging schemes going beyond DNA-mediated transient binding have also been realized, e.g. by engineering exchangeable HaloTag ligands that can be used for super-resolution imaging.[39, 40]

These dynamic labelling strategies elegantly overcome the problem of bleaching of single fluorescent labels. However, they are still limited by the photochemical processes in the excited states. When imaging is performed in the absence of photostabilization additives, every time the fluorophore enters the triplet excited state it has a probability to generate singlet oxygen and other ROS. While the ROS-induced photodamage to the fluorescent label is addressed by recovering it over time, the damage to the target molecule or binding site is not mitigated (Figure 1b). For example, in DNA-PAINT imaging studies it has been shown that the photoinduced damage of docking sites leads to loss of localizations over time, setting a limit on the total number of localizations that can be achieved.[41] Not surprisingly, removal of oxygen and use of common photostabilization cocktails, such as ROXS, has also been essential in the above-mentioned studies using DNA-mediated label exchange[34, 35, 37, 38], emphasizing the importance of photostabilization even if the experiment is no longer limited by the bleaching of the label itself. [34, 35, 37, 38, 41]

Nevertheless, the need for oxygen removal and addition of photostabilizing agents also limits their use to applications compatible with the required conditions. On one hand, photostabilization additives at millimolar concentrations can influence the biomolecular system under study[42] and the removal of oxygen by enzymatic scavenging systems can result in acidification of the sample solution[43, 44]. On the other hand, efficient removal of oxygen and solution-based photostabilization, which depend on efficient diffusional collision, simply might not be possible (e.g. crowded and inaccessible cellular compartments[45, 46], correlative measurements[47]). Additionally, in applications that rely on the exchange of fluorescent labels in solution such as DNA-PAINT or dynamic labelling, solution-based photostabilization can lead to an undesirably high background (unspecific photostabilization). In multicolor imaging schemes, it can also be difficult to identify one photostabilization additive that allows for optimal performance of multiple fluorophores.[19]

With these limitations in mind, we developed a modular and minimally invasive photostabilization strategy which relies on the DNA-mediated delivery of a photostabilizer, i.e. a TSQ, directly to the imaging site, circumventing the need for high concentrations of additives. We first characterize and benchmark this strategy by comparing it to solution-based photostabilization and then show that it can be successfully applied to slow down photoinduced depletion of docking sites in DNA-PAINT imaging as well as utilized for long term imaging studies based on continuous exchange of labels. Finally, we use this photostabilization strategy to enable 3D DNA-PAINT imaging in cells in the presence of oxygen to mimic imaging in biological samples, where oxygen removal is not feasible. To illustrate the future modularity of this approach, we also outline how it can be extended to different imaging schemes.

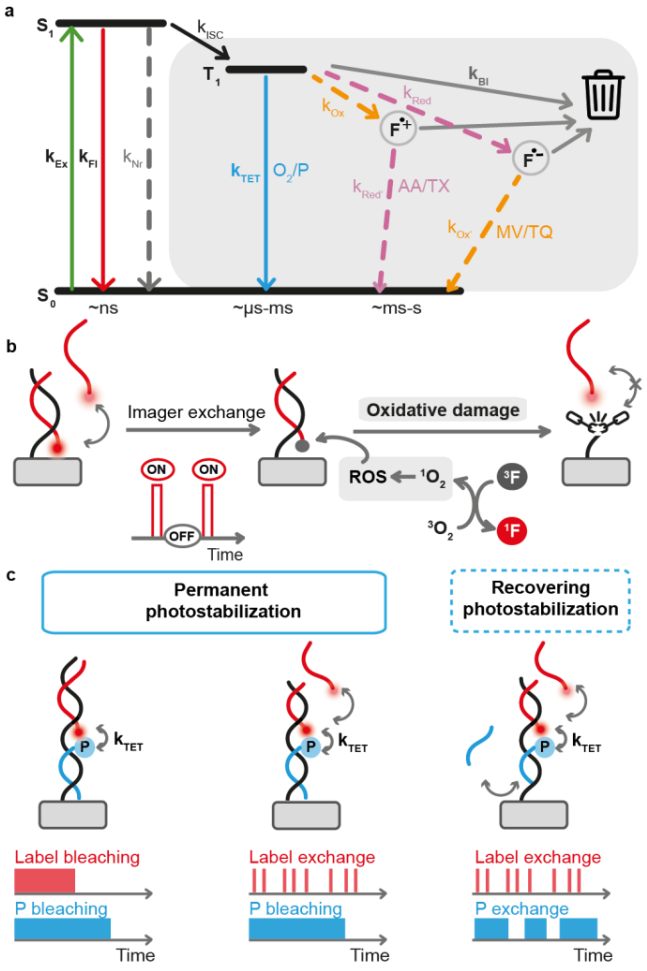

Figure 1. a) Jablonski diagram illustrating the photophysical processes involved in photobleaching pathways of fluorescent labels and common strategies to mitigate them by depopulating the non-emissive and reactive triplet and radical states. Here one can utilize photophysical triplet state quenchers that operate via triplet energy transfer (TET, k_{TET}) or photochemical quenchers that rely on ping-pong redox reactions (ROXS, k_{red}, k_{ox}); **b)** Illustration of oxidative damage that limits the performance of imaging methods based on continuous label exchange: although the photobleached label is exchanged the photostabilization is necessary to ensure the depopulation of the reactive triplet states and generation of ROS and consecutive photodamage of the docking site; **c)** Minimally invasive photostabilization introduced in this work that relies on DNA-mediated delivery of the photostabilizer directly to the imaging site. The photostabilizer can be attached to the imaging/docking site permanently (left and middle panels) via stable DNA-DNA interaction or exchanged continuously using transient DNA-DNA interaction (right panel). Lower panel illustrates time course of the experiment and residence time of the fluorescent label (red) as well as the photostabilizer (blue) on the docking site.

Results

In DNA-PAINT, the target structure is chemically modified with a nucleic acid sequence. To not only direct the imager strand but also the photostabilizer to the imaging site, we extended the DNA docking site sequence. The additional binding site for the photostabilizer strand allows it to locally act at the imaging site, where most of the photoinduced damage occurs (Figure 1c). By changing the sequence length one can design the photostabilizer strand to either permanently bind at the imaging site (Figure 1c, left and middle

panels) or continuously exchange analogously to fluorescent labels (Figure 1c, right panel). Differently from a "self-healing" approach which requires direct coupling of the photostabilizer to the fluorophore, our strategy relies on coupling the photostabilizer to a DNA oligonucleotide which can later be modularly reused for different fluorescent labels or imaging schemes. To avoid potential radical intermediates, in this work, we used cyclooctatetraene (COT) as physical TSQ due to its ability to depopulate the triplet excited states via a photophysical pathway circumventing possible radical intermediates at the imaging site. COT-functionalized oligonucleotide photostabilizers were prepared using a previously reported universal linker molecule by coupling maleimide functionalized COT linker molecules to thiolated DNA oligonucleotides (Scheme S1, Table S4).[48]

We first performed single-molecule fluorescence studies to test whether DNA-mediated photostabilization can be as efficient as solution-based photostabilization. Common additives work at millimolar concentrations, thereby proving a virtually unlimited pool of photostabilizer molecules. To show the strength of our photostabilization approach we chose the otherwise photolabile Cy5 dye. As it has been demonstrated that COT significantly improves photostability of Cy5[27], we expected a distinct contrast between the bare and photostabilized fluorophore. For this, Cy5-labelled twelve helix bundle DNA origamis (12HB) were immobilized on a BSA-biotin passivated glass coverslip using neutravidin-biotin interactions (Figure S2, Figure 2) and imaged on a total internal reflection (TIRF) microscope. The COT photostabilizer strand (17 nucleotides long) was permanently attached to the imaging site via DNA-hybridization (pCOT, Figure 2c). Control samples included a construct carrying an analogous oligonucleotide without the COT moiety (Figures 2a and 2b). In the absence of oxygen (scavenged with glucose oxidase/ catalase) and photostabilization additives, single-molecule imaging of Cy5 resulted in a characteristic fluorescence blinking behavior due to the formation of long-lived triplet-born dark states (Figure 2a).[12, 17, 19, 23] This dark state formation also leads to early saturation of fluorescence signal at excitation intensities as low as 0.3 kW/cm^2 (Figure 2a and 2d). Subsequent addition of 2 mM of triplet state quencher COT[49, 50] allowed for efficient collisional quenching of triplet excited states, consequently leading to a much more stable and bright fluorescence signal (Figure 2b and 2d).

Aiming for efficient collisional quenching between the photostabilizer (COT) and the fluorophore (Cy5) in the DNA-mediated strategy[14], we designed the DNA docking site in a manner that leads to a head-to-head placement of the two (Figure 2c)[17]. As illustrated in the single-molecule fluorescence trajectories (Figure 2c), a single photostabilizer delivered to the imaging site via DNA hybridization was sufficient to achieve a stable fluorescence signal, as bright as the one obtained in the presence of 2 mM COT as a solution additive (Figure 2d). In fact, further characterization of total photon budget (average number of photons collected before the photobleaching event) demonstrated that at low illumination intensities (0.3 kW/cm^2, typical for single-molecule studies) a DNA-mediated approach is more efficient leading to an almost two-fold higher photon budget when compared to the solution-based approach (Figure 2e). This suggests that the direct delivery of photostabilizers to the imaging site with the help of DNA hybridization, resulting in higher local concentration, can be even more efficient than collisional quenching by solution additives.

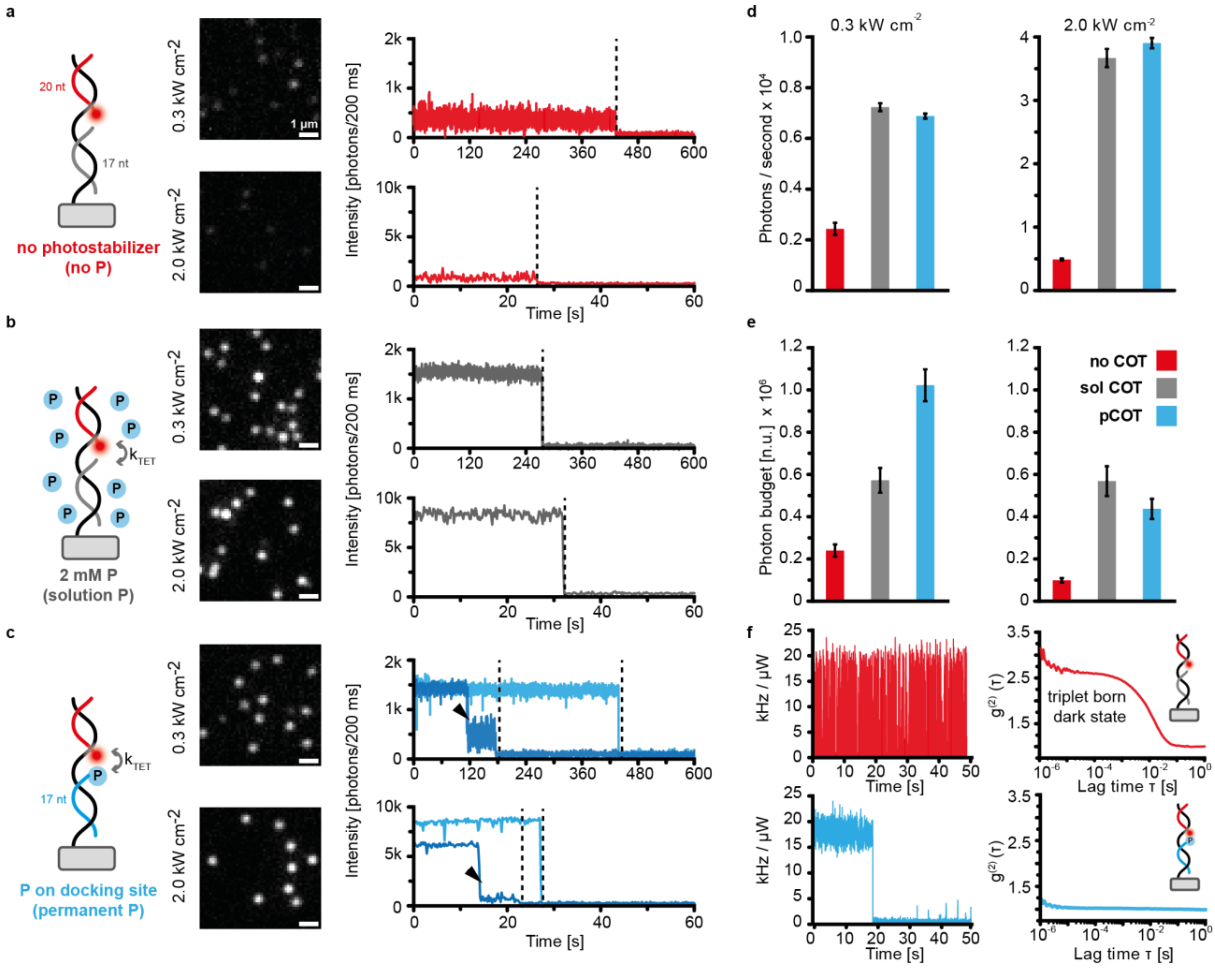

Figure 2. Photophysical characterization of the DNA-mediated photostabilization strategy. Single molecule TIRF images (middle panel) and representative single-molecule trajectories (right panel) obtained for Cy5-labelled DNA origami in the absence of oxygen and (**a**) no photostabilization additives, (**b**) 2 mM COT as a photostabilizer, and (**c**) DNA-labelled COT photostabilizer attached directly at the imaging site; **d)** Average brightness of single-molecule fluorescence signal and (**e**) average total photon budget obtained at two different illumination intensities; **f)** representative single-molecule trajectories obtained imaging the Cy5B-labelled DNA origami in the absence of oxygen and no photostabilization additives (top) or in the presence of DNA-mediated photostabilization by COT (bottom). The corresponding average fluorescence autocorrelation functions obtained analyzing single molecule trajectories are shown on the right and indicate efficient DNA-COT mediated depopulation of the dark states.

To investigate the effectiveness of the DNA-mediated photostabilization approach for applications that require higher illumination intensities (e.g., single-molecule localization microscopy (SMLM)) we also carried out single molecule studies at 2.0 kW/cm^2. Under these conditions, however, the photostabilization with a single COT moiety resulted in lower overall photon budget when compared to 2 mM COT in solution. We hypothesize that this reduced performance could be related to photoinduced degradation of the COT moiety at increased excitation intensities. In par with this observation, single-molecule fluorescence trajectories for both a low and a high excitation power density revealed instances of Cy5 fluorescence blinking before bleaching (9% of the traces for 0.3 kW/cm^2, 15% of the traces for 2.0 kW/cm^2, Figures S3 and S4). This observation additionally illustrates that the stability of the photostabilizer itself

can present a bottle-neck in the performance, especially in the photostabilization schemes that rely on only one photostabilizer moiety, i.e. as in the one studied here or in self-healing dyes. [27]

To confirm that the improved photostability stems from efficient depopulation of the triplet excited states and shed light on efficiency of triplet state quenching via the DNA-mediated approach, we performed analogous single-molecule imaging studies with the rigidified Cy5 analogue Cy5B.[51, 52] For this dye, a dark state originating from photoisomerization can be excluded. Autocorrelation analysis of single-molecule fluorescence trajectories of Cy5B in the absence of oxygen revealed analogous blinking due to the formation of triplet-born dark states (Figure 2f, upper panel). Photostabilization via DNA-mediated strategy with pCOT, on the other hand, led to a stable and bright fluorescence signal with significant quenching of the triplet-born dark state intermediates, confirming an efficient collision between the fluorophore and the photostabilizer.

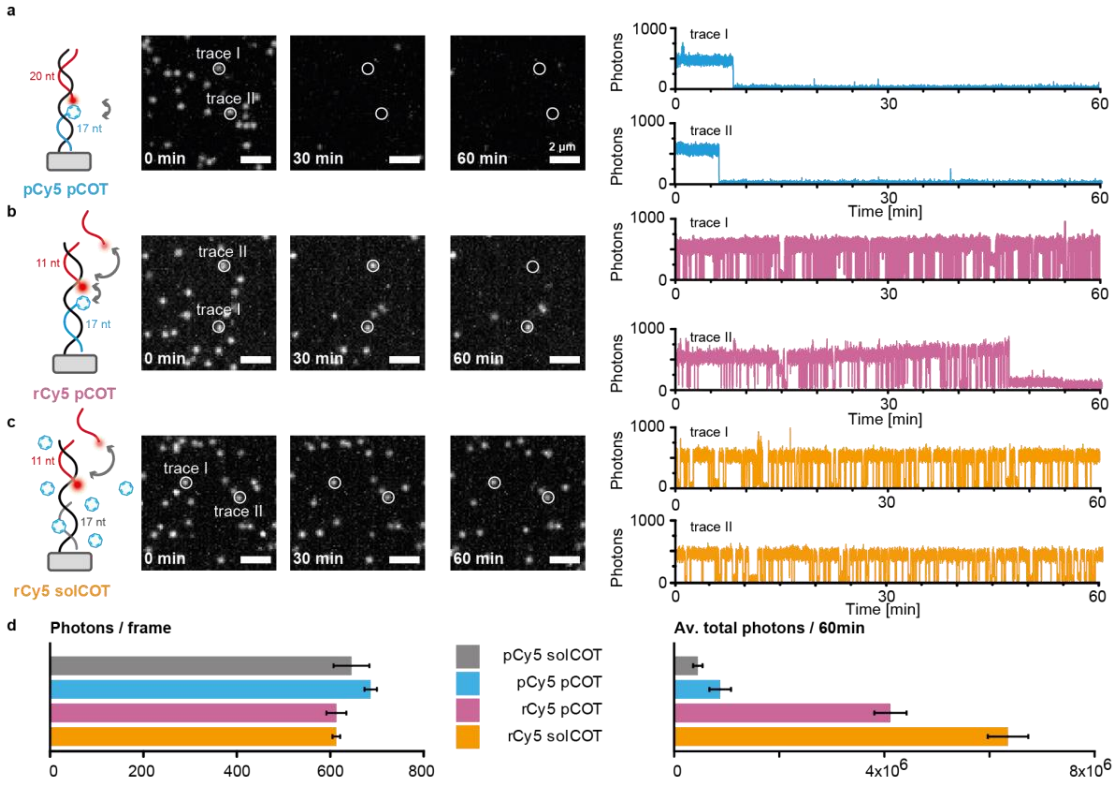

Figure 3. DNA-mediated photostabilization for recovering Cy5 imager labels in the absence of oxygen over a long observation time (60 min) and under low illumination intensity (ca 0.1 kW/cm^2). Single molecule TIRF images at 0, 30, and 60 min as well as representative single-molecule trajectories obtained for (**a**) a permanent Cy5 and a pCOT on the DNA docking site, (**b**) a recovering Cy5 and a permanent COT on the DNA docking site, and (**c**) a recovering Cy5 label with 2 mM COT as a photostabilizer in solution, respectively; **d**) Average brightness of single-molecule fluorescence signals and average total photon budget obtained for different imaging conditions. Bar plots in (**d**) represent average of three measurements, errors represent the standard deviation.

The limitation posed by having only a single photostabilizer that can eventually photodegrade is even more pronounced in imaging applications that rely on the continuous exchange of fluorescent labels under continuous illumination, such as DNA-PAINT[27, 30, 41] and recovering labeling.[34, 35, 37, 38] Over the course of an experiment, the single photostabilizer molecule has to stabilize multiple fluorophores binding transiently over time, favorably under a high excitation illumination to ensure a high photon count rate. To investigate

the applicability and performance of DNA-mediated photostabilization under these conditions, we implemented a shorter binding sequence (11 nucleotides) for the transient, recovering binding of Cy5 imagers and compared it to the permanent labeling approach (Figures 3, S8-10).[37] We performed long-term single molecule studies over an observation time of 60 min at low illumination intensities of 0.1 kW/cm^2 to ensure that photobleaching is slow and not outcompeting transient binding kinetics. Even though efficiently photostabilized by a single COT moiety on the DNA docking site, the permanent Cy5 label (Figure 3a) was still limited by irreversible photobleaching yielding an average total photon budget of around 1×10^6 photons (Figure 3d) comparable to the one obtained for slightly higher illumination intensity used before (0.3 kW/cm^2, Figure 2e). Nevertheless, as observed earlier, the DNA mediated photostabilization approach with pCOT again outperformed the commonly used solution photostabilization with 2 mM COT by a factor of ca. 2, while yielding similar photon count rates (Figure 3d blue vs. grey bars, more data in Figures S8 and S9).

Switching to a dynamic imaging scheme and using 10 nM of the recovering Cy5 imager (Figure 3b and S10) came at the cost of a slightly increased background but resulted in blinking, pseudo-continuous trajectories (as observed in previous studies[37, 38]) with comparable brightness values, but a highly improved imaging time, surpassing the total photon budget of a single Cy5 molecule by approximately four-fold (Figure 3d and S10). However, we still observed slow photo-induced degradation of the DNA docking site over time, leading to a loss of around 60% of imaging trajectories after 60 min (Figure S11). Recovering imaging with solution based photostabilization (Figure 3c), resulted in an even higher photon budget (ca. $6x10^6$ photons over 60 min) and almost no label bleaching over the entire duration of the experiment (Figures 3d, and S11). On one hand, these findings highlight that DNA mediated photostabilization can be applied to recovering labels resulting in long-lasting single-molecule observation times breaking the photobleaching limit of a single fluorophore. On the other hand, they also underscore that even under very low illumination intensities, photoinduced damage to the photostabilizer remains the bottleneck, especially when the experiment is no longer limited by the bleaching of the fluorescence label and requires long-observation times.

After successfully applying DNA mediated photostabilization to recovering imager labels under low illumination intensities applicable for single-molecule imaging routines such as single-particle tracking or SM-FRET studies, we next aimed to extend our approach to DNA-PAINT super-resolution imaging. In SMLM techniques such as STORM, PALM or DNA-PAINT, the achieved resolution in the super-resolved image relies on the photon count rate of the detected blinking events. SMLM experiments are, hence, commonly performed under high illumination intensities (typically $\geq$ 1.0 kW/cm^2) to obtain a high spatiotemporal resolution. To test the performance and stability of DNA mediated photostabilization under these conditions, we equipped a 12HB DNA origami with three DNA docking sites placed at 90 nm distances (Figure 4). Each docking site consisted of a short DNA-PAINT imager binding sequence (8 nucleotides) and a neighbouring photostabilizer binding sequence of different lengths in order to investigate permanent (17 nt for pCOT) as well as recovering (10 nt for recovering COT (rCOT)) photostabilization schemes (Figure 1).

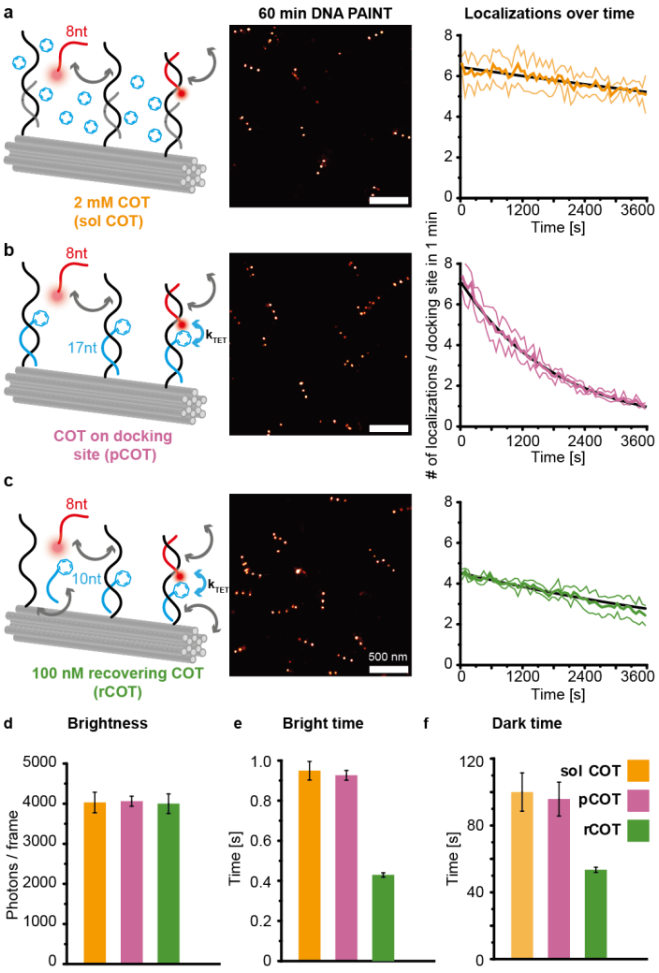

Figure 4: DNA-mediated photostabilization for DNA-PAINT imaging with Cy5 in the absence of oxygen and under high illumination intensity (ca 1.0 kW/cm^2). Exemplary reconstructed DNA-PAINT images of 12HB nanostructures with three docking sites and detected localizations per docking site over time obtained with (**a**) 2 mM COT solution-based photostabilization, (**b**) a permanent DNA mediated photostabilization (pCOT, 17 nt binding sequence) and (**c**) a recovering DNA mediated photostabilization (rCOT, 10 nt binding sequence). Brightness values (**d**), and DNA-PAINT bright times (**e**) and dark times (**f**) extracted for single DNA docking sites. Coloured curves in (**a**) to (**c**) represent the average of three measurements, errors represent the standard deviation, dark lines represent exponential fits. Bar plots in (**d**) to (**f**) represent the average of three measurements, errors represent the standard deviations.

For this purpose, we performed DNA-PAINT imaging on a total internal reflection (TIRF) microscope with 1 nM of a Cy5 imager strand in an oxygen depleted imaging buffer at a typical SMLM illumination intensity of 1.0 kW/cm^2. DNA-PAINT imaging in oxygen-depleted buffer without any photostabilization additives resulted in a poorly resolved image and localizations bearing low photon counts (660 photons/ 100 ms) at a generally low localization rate over time indicating that the presence of TSQ is crucial for successful super-resolution measurement (Figure S12). DNA-PAINT measurements with the classical solution-based stabilization (2 mM COT, Figure 4a), on the other hand, allowed for the successful reconstruction of the designed three-spot pattern enabling the selection and examination of individual docking sites. To investigate the stability of the DNA docking sites against triplet state mediated and ROS-induced photodamage, we extracted the number of localizations of individual docking sites for a defined time unit (i.e., 1 min). As reported previously, the addition of an unlimited pool of photostabilizer molecules in solution resulted in an almost constant average localization rate per single docking site over the whole

observation time indicating a high stability of the DNA docking sites (Figure 4a, right).[41] Next, we performed DNA-PAINT imaging on the 12HB nanostructures with a COT functionalized photostabilizer strand permanently bound to the docking site (pCOT, Figure 4b). While the reconstructed DNA-PAINT images revealed the designed three-spot pattern accurately and photon count rates similar to solution-based photostabilization, we also observed a rapid decay of localizations over time and almost complete loss of docking sites by the end of the 60 min measurement (Figure 4b, right). Due to the high turnover of imager strands and high illumination intensity, the limited stability of the COT photostabilizer became even more relevant limiting the meaningful observation times to less than 60 min and potentially preventing a complete reconstruction of the sample.

Although the intrinsic instability of COT towards photoinduced electron transfer reactions with oxygen can be improved by the introduction of electron withdrawing groups, this strategy only slows down the irreversible degradation of the photostabilizing molecule and does not overcome it entirely.[27, 53] To circumvent the inevitable loss of docking sites due to limited stability of the COT moiety, we introduced an imaging scheme that allows for the recovery of the photostabilizer strand as well (rCOT, Figure 1c), analogously to the recovery of bleached fluorescent labels. To this end, we shortened the binding sequence of the photostabilizer strand on the DNA docking to 10 nt to ensure a shorter binding time and dynamic exchange. After determining the concentration of the recovering COT strand needed to saturate the binding to the DNA docking site (Figure S13), we then carried out the recovering DNA-PAINT photostabilization with 100 nM rCOT photostabilizer over 60 min (Figure 4c). Photon count rates comparable to pCOT and solution-based photostabilization (Figure 4d) and reconstruction of the DNA-PAINT images revealing the designed three-spot pattern suggested an efficient photostabilization for the rCOT strategy despite its dynamic nature. Moreover, the average localization rates per single docking site showed a significantly improved stability of the DNA docking sites when compared to pCOT photostabilization which relies on a single photostabilizer. Therefore, by relying on this recovering exchange of photostabilizer molecules with the help of DNA, we could achieve photostabilization comparable to the solution-based approach, however, at seven orders of magnitude lower concentration of additives (Figure 4c, right), also in an oxygenated environment (Figure S14).

To determine if the binding kinetics of the DNA-PAINT imager are affected by the COT functionalization on the docking site, we also extracted the average dark- and bright-times of selected docking sites for each photostabilization approach (Figures 4e, 4f and S15). While we found comparable binding kinetics for the solution-based approach and the pCOT photostabilization, the dynamic rCOT photostabilization surprisingly resulted in the decrease of both, bright-times and dark-times, by ca. 50%, in turn, doubling both the association and dissociation rates of the imager strand to the DNA docking site. The faster blinking for the sample in the rCOT imaging scheme was also clearly visible in fluorescence time traces (Figure S16), highlighting the increased binding and dissociation rates.

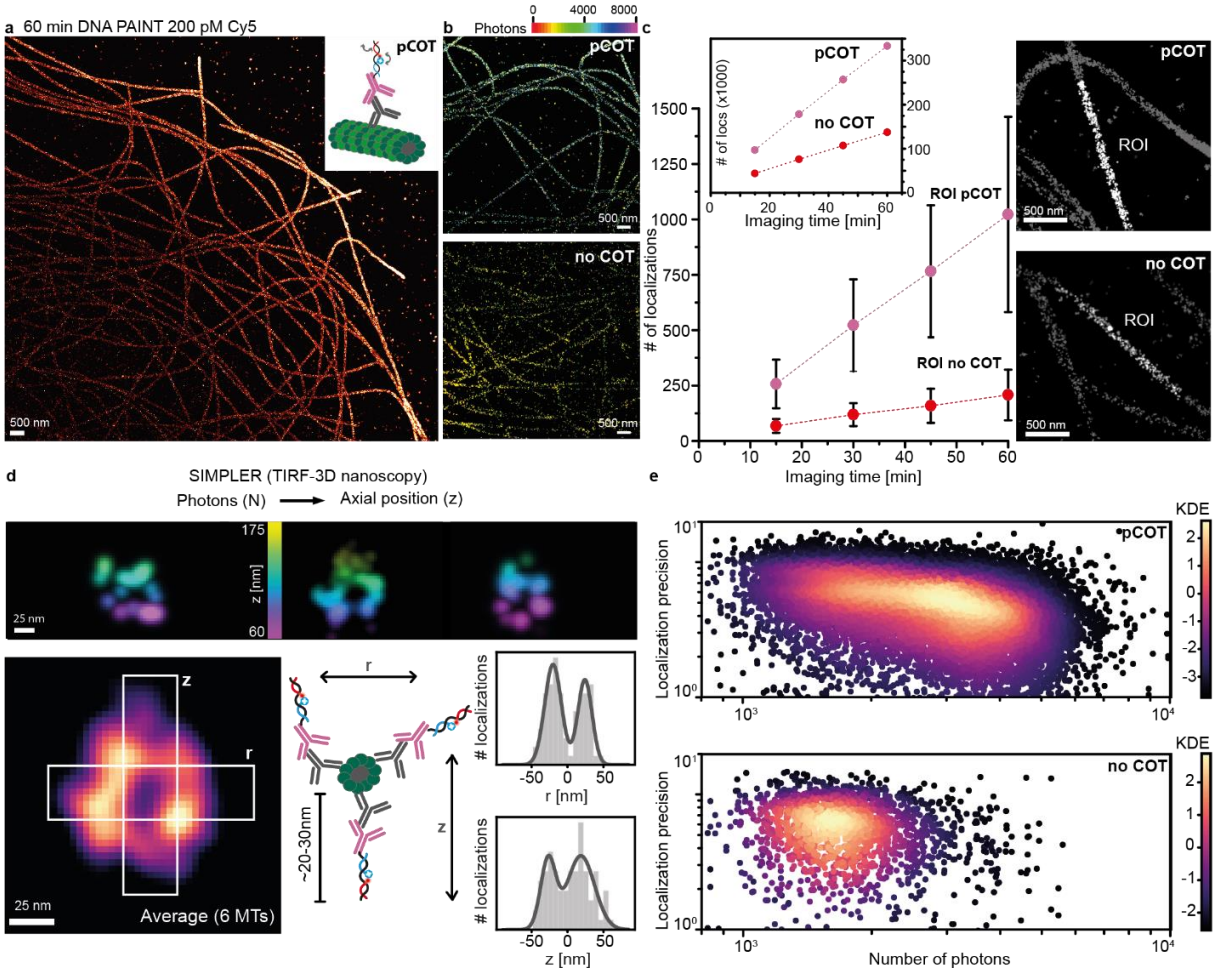

Figure 5. Application of DNA-mediated photostabilization to DNA-PAINT imaging in cells. 60-minute DNA-PAINT experiment under low illumination intensities (ca 0.6 kW/cm^2) and with ambient oxygen. **a)** Overview image of the sample where the permanent photostabilizer was added at 200 pM (inset shows the labelling strategy); **b)** Exemplary zoom-ins on regions in the samples with no photostabilization or pCOT photostabilization (color coded by photon number); **c)** Accumulation of localizations over the course of the experiment within comparable selected regions (example highlighted in ROI in white) for pCOT and no photostabilization control. Inset shows localizations over time for the entire imaged region (isolated region of interest (ROI) at a similar position in the field of view for both samples). **d)** Cross-sections of microtubules extracted using the SIMPLER (supercritical illumination microscopy photometric z-localization with enhanced resolution) algorithm.[54] Three exemplary reconstructed images of microtubules, color coded by position in z-dimension, (top), average of six cross-sections (bottom left), linkage-errors due to labelling reported in literature, histogram of localizations in dimension r and z of the average microtubule (bottom right). **e)** Number of photons plotted against the corresponding localization precision for pCOT and no photostabilization (color coded by kernel density estimation).

To explore whether DNA-mediated photostabilization could be used for imaging applications with more complex biological samples, we performed DNA-PAINT measurements in fixed fibroblast cells (COS-7) using the pCOT photostabilization strategy. We chose to image microtubules, as they are an established model system in the super-resolution microscopy community, allowing for an intuitive and fair comparison to different labeling and photostabilization techniques. Experiments were performed in ambient oxygen conditions, to mimic applications where the use of oxygen scavenging systems is prohibited. This way, COT bound to the docking site directly competes with the high concentrations of oxygen in solution

(typically ca. 0.3 mM).[11] To observe the effect of pCOT stabilization on the performance of Cy5, we imaged the microtubules for 60 minutes (Figure 5a). Figure 5b shows zoom-ins of reconstructed images from both conditions with and without DNA mediated photostabilization. Homogenous illumination of the sample was ensured by including a flat-top beam shaper in the excitation path.[55] The photon number per localization is color coded, illustrating the increased number of photons for DNA-PAINT imaging with pCOT photostabilization. To quantify this further, we plotted the binned number of localizations over the course of the experiment (Figure 5c). The inset of Figure 5c shows how, during the experiment, localizations continuously increase in the entire field of view, while the pCOT sample has an overall higher number of localizations to begin with and accumulates them more quickly. This trend is confirmed when comparing selected regions of interest (ROIs) of fixed dimensions within several individual microtubules. We hypothesize that the lower number of localizations is either due to the loss of docking sites when Cy5 is not photostabilized or an effect of Cy5 bleaching within the binding time leading to an insufficient number of photons per localization to be detected. With COT, an increased fraction of docking sites is preserved, leading to the higher number of localizations.

To test whether DNA-PAINT measurements with the photostabilized Cy5 can be used to reconstruct the three-dimensional position of localizations, we applied the SIMPLER (supercritical illumination microscopy photometric z-localization with enhanced resolution) algorithm.[54] The method by Szalai *et al.* converts the number of detected photons to the axial position (z) of single molecules when acquisitions are performed under total internal reflection (TIR) conditions. SIMPLER strongly relies on the use of stably emitting dyes, since fluctuations in brightness significantly reduce axial localization precision. Given that a binding event needs to last at least three camera frames to be considered in the SIMPLER algorithm, it is crucial that the dye does not undergo fast photobleaching once the imager strand binds to the docking site. Figure 5d shows cross-sections of three exemplary microtubules, as well as an average over six microtubules. Considering the size of the primary and secondary antibodies (adding approximately 20-30 nm[56]) the achieved peak-to-peak distance of the hollow microtubule (44 nm in r and 45 nm in z) is in good agreement with literature.[57, 58] Inherently, the localization precision in DNA-PAINT measurements is a function of the photon number N (Figure 5e). Additional to yielding overall more localizations, the introduction of DNA-mediated photostabilization increases the number of localizations with higher photon count. The mean photon count for pCOT amounts to 3082, while without COT this value drops to 1897. As a result, the ratio of localization precision pCOT/no COT (σ_x = 5.6 nm/6.0 nm) is 0.91 (ratio of $\sqrt{N}$ = 0.76).

To investigate whether even better performance can be achieved we also performed experiments with the recovering rCOT strand in the imaging solution (Figure S18). However, no substantial improvement of brightness or number of localizations was observed when compared to the pCOT stabilization shown in Figure 5. Since super-resolution experiments in cells were performed at lower excitation intensities (0.6 kW/cm^2), we hypothesize that under this regime we were not limited by bleaching of the photostabilizer as observed previously (Figure 4). Together, this illustrates, that the choice between permanent or recovering modality can be based either on sample requirements (e.g., when pCOT would be the least invasive choice) or imaging conditions (e.g., when higher illumination intensity is necessary, rCOT can potentially help to circumvent photostabilizer bleaching).

Discussion

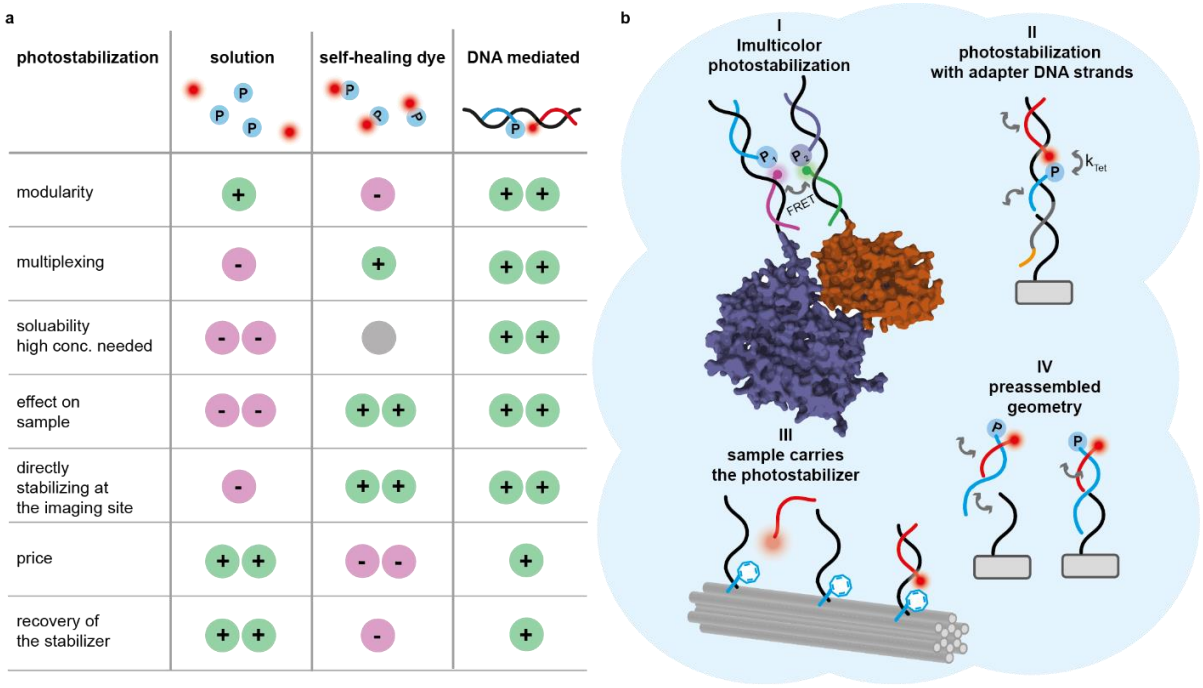

Figure 6. Comparison of conventional solution based photostabilization, self-healing dyes and DNA mediated photostabilization and further single-molecule imaging assays. **a)** Table stating advantages and disadvantages of common photostabilization techniques compared to the DNA-mediated photostabilization approach introduced here; **b)** Schemes showing how DNA-mediated photostabilization could be implemented in different imaging approaches: I: "mix and match" use of DNA-mediated photostabilization in multicolor imaging when two dyes need different photostabilizer molecules; II: introducing the photostabilizer molecule via the adapter strand (orange: toehold for displacement, gray: complementary to ssDNA on the target, black: for imager and stabilizer binding) used in multiplexed DNA-PAINT measurements[59, 60]; III: functionalization of biomolecule itself with the photostabilizer to place it directly at the imaging site (e.g. via DNA origami staple strand); IV: preassembly of photostabilizer and imager strands to create modular self-healing constructs.

Using DNA interactions to direct the photostabilizer to the imaging site enables the modular combination of a photostabilizer with different fluorophores (Figure 6a, first row). Within this work, we attached COT to oligonucleotides of two different lengths (10 and 17 nt) and applied them to various fluorophores and imager strands on the DNA docking site. While we could show highly efficient photostabilization for permanent and recovering imager strands with the red-emissive dyes Cy5, Cy5B and Atto647N (Figure S7), we observed no photostabilization for permanent Cy3 (Figure S5) and Cy3B (Figure S6) imager strands consistent to inefficient triplet state depopulation of these dyes by COT[27, 28].

The sequence specificity and modularity of our DNA mediated design enables multicolor or multiplex imaging while circumventing undesired cross-interactions (Figure 6a, second row). Especially when using multiple fluorophores simultaneously, one is confronted with challenges in choosing the right photostabilization approach. The DNA-mediated approach, however, is not limited to one TSQ molecule type. Any photostabilizing moiety that can be coupled to DNA, or to any other site-specific binders (e.g. in peptide-PAINT[61]), can be implemented in this approach. Since the individual photostabilizer is directed only to the specific imaging site, different fluorophores can be optimally stabilized within the same imaging solution, enabling multicolor measurements optimized for all dyes in the experiment (Figure 6a, 6bI).

To further increase multiplexing capabilities for imaging several targets in complex biological samples, our DNA-mediated photostabilization approach can also easily be combined with current adapter-mediated techniques, that use transient secondary labels for imager binding[59, 60] (Figure 6bII). It is even conceivable to incorporate the photostabilizer molecule directly into the sample itself, e.g., by functionalizing a protruding staple strand in a DNA origami (Figure 6bIII) or coupling a short photostabilizer strand to an antibody. When designed smartly, the added linkage error can be minimal[56, 58]. Since the photostabilizer acts only locally and specifically at the imaging site of the reporting fluorophore (Figure 6a, fifth row), the contrast when compared to unspecific signal is additionally enhanced given that the directed photostabilization approach does not act on non-specifically bound labels.[62]

Coupling the photostabilizer to DNA not only allows to direct it to the specific imaging site, but also brings the additional advantage of increasing the solubility of the TSQ entity (Figure 6a, third row). Many TSQs, like COT, are poorly water-soluble organic molecules, calling for pre-dissolvement in organic solvents like DMSO[16] or methanol[23]. This often leads to precipitation of the organic TSQs in the imaging buffer at high concentrations (typically mM range of TSQ and ca. 1% organic solvent). In our DNA mediated approach, TSQs without pre-dissolvement in an organic solvent still resulted in successful photostabilization of the fluorophore (Figure 5), highlighting the advantage of exploiting DNA as the carrier scaffold of the photostabilizer molecule and potential platform to test even less water-soluble TSQs.

These findings make the DNA mediated approach an attractive tool for minimally invasive imaging in a biological context, where the addition of high concentrations of TSQs such as COT[42] and of organic co-solvents like DMSO[63] can influence the sample of interest (Figure 6a, fourth row). Additionally, carefully prepared cell samples often undergo multiple imaging rounds under prolonged exposure, either for the sake of higher resolution or to deduce the interplay of several components. This makes photostabilization mandatory in most cases, but not always straightforward to implement. In our DNA-mediated approach the soluble photostabilizer can be added at a fraction (10^7 less as in Figure 5) of the concentration needed for the solution-based technique. The stabilizing entity can also bind permanently, reducing the amount of additive in solution to zero (Figure 2 and 3). While exploiting DNA interactions allows to specifically direct the photostabilizer to the imaging site (Figure 6a, fifth row), it comes at the cost of increasing the linkage error of the fluorescent label on the object of interest. Nevertheless, the achieved 3D resolution (Figure 5) indicates, that the introduced additional linkage error does not affect the achievable resolution of the applied secondary antibody labeling[56, 58]. Additionally, for imaging applications such as DNA-PAINT based kinetic referencing[64] or quantitative DNA-PAINT (qPAINT)[65], a slightly increased linkage error is irrelevant to the measure outcome but a high stability of the DNA docking site is a prerequisite. The specificity of DNA-mediated photostabilization, hence, makes it an attractive tool for these super-resolution imaging applications requiring a large statistic of binding events over time for a reliable quantification.

In comparison to self-healing dyes that require multistep synthesis steps or come with high associated costs when obtained commercially, coupling of the photostabilizer to DNA is relatively simple and affordable (Figure 6a, sixth row) and the same TSQ-coupled oligonucleotide can be reused in multiple imaging schemes. As it has been shown in our experiments with pCOT (and is also the case for self-healing dyes[28]), a single photostabilizing moiety is not sufficient when higher excitation intensities are needed. In such situations the performance of the self-healing dyes would be limited by the stability of the photostabilizer. In contrast, as demonstrated in Figure 4, the DNA-mediated approach can overcome this bottleneck by photostabilizer recovery (Figure 6a, seventh row). Analogous to self-healing dyes, it is, however, also conceivable to pre-assemble the photostabilizer and imager strands (Figure 6bIV) in a stable DNA duplex[66, 67], that binds to the imaging site via a single-stranded overhang. As has been recently reported, using partially double-stranded DNA could also additionally help reduce non-specific binding and, therefore, undesired background in DNA-PAINT imaging applications[62]. The pre-assembled geometry could hence serve as a cost-effective approach to emulate the self-healing dye strategy.

Currently, the performance of our DNA mediated photostabilization strategy is both restricted by DNA as the mediating agent, making it susceptible to DNA degrading conditions (e.g., DNAses), and by the imperfect photostabilizer COT. The rather low energy of its triplet state (ca. 0.8 eV[68]) only allows for photostabilization of dyes with low triplet state energies. Quenching a dye's triplet state via energy transfer, leads to the formation of the triplet excited state of COT which has a lifetime of up to 100 µs[68] introducing a potentially reactive long-lived intermediate and reducing the duty cycle of triplet state depopulation. An improved performance, thus, requires a TSQ entity with 1) tunable triplet state energy to extend the approach to broader range of fluorescence labels; 2) a shorter triplet state lifetime to preclude the formation of long-lived intermediates and to improve the stability of TSQ itself. We are currently exploring both avenues to create a library of DNA-mediated photostabilizers that could be applied to broad range of fluorescence labels in multicolor imaging applications.

Conclusion and Outlook

In conclusion, we have developed a modular DNA-mediated photostabilization approach that relies on delivery of photostabilizers directly to the imaging site. We demonstrated that the approach allows to improve photon budgets of permanent dye labels at lower excitation intensities outperforming solution additives which are used at several orders of magnitude larger concentrations (Figure 2). Nevertheless, at increased excitation intensities or repetitive binding of multiple fluorophores (Figure 3), the stability of the photostabilizer itself becomes a limiting factor. To address this, we introduced the recovering photostabilization scheme (rCOT), where the photostabilizer is continuously exchanged but still acts directly at the imaging site (Figure 4). rCOT significantly slowed down the loss of DNA-PAINT localizations, even under high excitation intensities and ambient oxygen conditions. Surprisingly, introduction of rCOT to DNA-docking sites also reduced association and dissociation rates of the imager strand.

We further demonstrated the applicability of our approach to complex imaging environments by imaging microtubules in cells (Figure 5). pCOT photostabilization improved the localization rate and precision of super-resolution images, even under oxygen-rich conditions. When combined with the SIMPLER algorithm, we achieved axial resolution and 3D reconstruction capabilities comparable to those obtained with more stable and brighter dyes expanding the palette of fluorescence labels that are suited for super-resolution imaging.

Our minimally invasive photostabilization strategy offers a promising solution for challenging imaging environments where the delivery of high concentrations of additives is prohibited. The modularity of our approach enables its adaptation to various imaging schemes, facilitating the development of multicolor imaging techniques, screening of new photostabilizers, and expansion to different fluorescence labels.

Methods

General materials: For folding, purification and storage of 12HB DNA origami nanostructures, a 1× TAE buffer with 16 mM $MgCl_2$ was used. Bleaching of permanent fluorescent labels and DNA-PAINT with DNA origami were performed in a 2× PBS buffer with 75 mM $MgCl_2$. Bleaching of recovering labels was performed in a 2× PBS buffer with 500 mM NaCl and 0.05% Tween 20. [69, 70]

Oxygen-free single-molecule imaging was performed by addition of 1% (wt/v) *D*-(+)-glucose (Sigma Aldrich, USA), 165 units/mL glucose oxidase (G2133, Sigma Aldrich, USA), and 2170 units/mL catalase (C3155, Sigma Aldrich, USA) to the imaging solution.[23]

The p8064 scaffold strand was extracted from M13mp18 bacteriophages. Unmodified staple strands were purchased from Eurofins Genomics GmbH and Integrated DNA Technology Inc. Dye labeled

oligonucleotides for DNA-PAINT imaging or permanent labeling were purchased from Eurofins Genomics GmbH (Germany).

The activated COT-maleimide linker molecule was synthesized as reported previously.[48] Labeling and purification of the COT-modified oligonucleotides was performed at Ella Biotech GmbH (Germany).

DNA origami folding: All investigated 12HB DNA origami nanostructures (Figure S1) were folded in a 1× TAE buffer containing 16 mM $MgCl_2$ using the corresponding p8064 scaffold strand extracted from M13mp18 bacteriophages with a non-linear thermal annealing ramp over 16 hours (Table S1).[71] Concentrations of scaffold strand, unmodified and modified staple strands in the folding mix are given in Table S2. Modifications of the DNA Origami were designed using caDNAno (version 2.2.0). A full list of the unmodified staple strands and sequences of the 12HB DNA origami[72] is given in Table S8. Folded DNA origami nanostructures were purified with 100 kDa MWCO Amicon Ultra filters (Merck, Germany). Concentrations of purified sample solutions were measured via UV/vis spectroscopy (NanoDrop, Fischer Scientific, USA). Correct folding of the origami structures was confirmed via AFM imaging (Figure S1) on a NanoWizard® 3 ultra AFM (JPK Instruments AG).

Sample preparation: High precision 170 µm thick microscope cover glass slides (22×22 mm, Carl Roth GmbH, Germany) were initially ultrasonicated in a 1% Hellmanex solution. After thoroughly washing with ultra-pure water, the glass slides were irradiated for 30 min in a UV ozone cleaner (PSD-UV4, Novascan Technologies, USA). Cleaned glass slides and microscope slides were assembled into an inverted flow chamber as described previously.[69] The assembled chambers were rinsed with 1× PBS, and passivated with 50 µL of BSA-biotin (0.5 mg/mL in PBS, Sigma Aldrich, USA) for 15 minutes and washed with 50 µL 1× PBS. The passivated surfaces were incubated with 50 µL Neutravidin (0.25 mg/mL in 1× PBS, Sigma Aldrich, USA) or 50 µL Streptavidin (0.5 mg/mL in 1× PBS, Sigma Aldrich, USA) for 15 minutes and washed with 50 µL 1× PBS. The sample solution with DNA origami featuring four staple strands with biotin modifications on the base (Table S8) was diluted to approximately 50 pM in 1× PBS buffer containing 500 mM NaCl and incubated in the chambers for ca. 5 minutes and stored in a 1× TAE containing 10 mM $MgCl_2$. Sufficient surface density was probed with a TIRF microscope.

Imager and photostabilizer strands: To ensure specific hybridization of the imager (labelled with Cy5) and photostabilizer (labelled with COT) oligonucleotides on a single DNA docking site, their corresponding strands were designed to have orthogonal DNA sequences. Fluorescent label strands, so-called imager strands, were designed of varying lengths (8, 11 and 20 nt) to probe permanent and recovering labeling (sequences in Table S3). The photostabilizer strands labeled with a COT moiety on the 5'-end were also of varying lengths (rCOT with 10 nt, pCOT with 17 nt) to compare permanent and recovering photostabilization (sequences in Table S4). For reference measurements without a COT moiety on the DNA docking site, a 17 nt strand with the pCOT sequence without a COT label was used. DNA docking sites, consisting of a combination of complementary sequences of one of the COT strands and one of the imager strands, were modified to the 3'-ends of selected staple strands on the 12HB nanostructure (for sequences, see Table S5-7). For more details, see SI section 1.3.

Labeling of DNA docking sites on 12HB origami: Permanent labels, i.e., label strand with lengths of 17 or more nucleotides, were hybridized to immobilized DNA origami nanostructures by incubation of a 10 nM label solution in a 2× PBS buffer with 75 mM $MgCl_2$ for 60 minutes. After washing away with 2× PBS with 500 mM NaCl and 0.05% Tween 20, the labeled DNA origami was stored in a 1× TAE containing 10 mM $MgCl_2$. Recovering and shorter COT and imager oligonucleotides were added to the imaging solution at different concentrations specified in the manuscript.

Single-molecule fluorescence imaging. Automated bleaching experiments of permanent and recovering fluorescent labels and DNA-PAINT measurements of DNA origami nanostructures were performed on a commercial Nanoimager S (ONI Ltd., UK) with red excitation at 638-nm and green excitation at 532 nm, respectively. The microscope was set to TIRF illumination and widefield movies were acquired with frames of 100 ms (bleaching of permanent labels with 0.3 or 2.0 kW/cm^2) or 200 ms exposure time (bleaching of permanent and recovering labels with 0.1 kW/cm^2). For more details on bleaching experiments of permanent and recovering fluorescent labels, see SI sections 1.6 and 1.7. For more details on DNA-PAINT imaging on DNA origami nanorulers, see SI section 1.8.

Data analysis of single-molecule fluorescence trajectories. Bleaching movies were first background corrected with ImageJ 1.52n (version 1.8.0_172). Individual spots were picked and corresponding single-molecule trajectories were extracted with a custom written ImageJ script. Bleaching trajectories were then analyzed with a custom written Python script using Hidden Markov Modeling (HMM). For every bleaching curve, brightness, i.e., photon count per frame, the total number of photons before bleaching and the time point of bleaching were extracted. Apparent photon numbers were converted in absolute photon numbers using the specifications of the used sCMOS camera.

Fluorescence correlation spectroscopy. Autocorrelation FCS studies were performed on immobilized 12HB origami nanostrucurres labeled with a permanent COT oligonucleotide (pCOT) and a permanent imager strand containing Cy5B in the presence of oxygen scavenging system. Single-molecule fluorescence trajectories of surface immobilized emitters were acquired on a home-built confocal microscope equipped with time-correlated single photon counting (TCSPC) capabilities (as described previously[73]) upon excitation with 639-nm laser (2 µW excitation intensity, measured at the objective). Single photon counting data was read into Python using a home-written script and analysed using the *pcorrelate* function of the module pycorrelate[74]. The corresponding analysis script can be found on GitLab. The function uses an algorithm described in literature[75] to calculate the cross-correlation function between two channels at time lag τ via:

$$\hat{C}_{AB}(\tau) = \frac{n\left(\{(i,j) \ni \tau_i = u_j - \tau\}\right)(T-\tau)}{n(\{i \ni t_i \leq T-\tau\})n\left(\{j \ni u_j \geq \tau\}\right)}$$

where t_i is the arrival time of the i^{th} photon in channel A, u_j is the arrival time of the j^{th} photon in channel B, n is the operator for counting the elements in the list and T is the experimental time. We calculated $\hat{C}_{AB}$ for the timestamps collected in one channel, ("auto-correlation", i.e. channel A = channel B). For each experimental condition, we acquired at least 19 single molecule trajectories for no COT and 43 for pCOT, calculated $\hat{C}_{AB}$ for each trace and averaged the result.

DNA-PAINT measurements of DNA-origami nanostructures. DNA-PAINT measurements on immobilized DNA origamis were also performed on the commercial Nanoimager S (ONI Ltd., UK). The microscope was set to TIRF illumination and an excitation power density of ca. 1.0 kW/cm^2 at 638 nm. Widefield movies totaling 36000 frames were acquired at 100 ms time binning over 60 min.

TIFF files were analyzed using the Picasso software package.[69] For fitting the centroid position information of single point spread functions (PSF) of individual imager strands, the MLE (Maximum Likelihood Estimation) analysis was used with a minimal net gradient of 2500 and a box size of 5. The fitted localizations were further analyzed with the "Render" module from Picasso. X-y-drift correction of the localizations was performed using RCC drift correction algorithm. Individual docking sites on the 12HB nanostructures were picked using Picasso's "Pick tool", setting the pick diameter to 0.6 camera pixels to extract the corresponding binding kinetics and photon statistics per docking site. To obtain accurate

brightness values, the localizations of every picked docking site were filtered in order to remove the contributions from the first and the last frames of a binding event, using a custom written Python code as described previously.[54]

Cell culture. COS-7 cells (ATCC) were cultured in DMEM (Gibco, No. 11965084) medium supplemented with 10% FBS (Gibco, No. 10500064). Cells were passaged twice a week using 0.05% trypsin EDTA (Gibco, No. 25300054).

Preparation for microtubule imaging. COS-7 cells were seeded on Ibidi eight-well glass-bottom chambers (No. 80827) at a density of 25 000 cm^{-2}. In preparation for imaging, cells were fixed using the protocol described by Whelan and Bell[76], using 0.4% Glutaraldehyde (Sigma Aldrich, USA) and 0.25% Triton X-100 (Sigma Aldrich, USA) in CSB (1M NaCl, 100 mM PIPES, 30 mM $MgCl_2$, 10 mM EGTA, 10 mM Sucrose; pH = 6.2) for 90s. After rinsing with 37°C PBS twice, 3 % Glutaraldehyde in CSB were incubated for 15 min, followed by washing with PBS (30s, 1min, 5min, 10min, 15min). The reductant $NaBH_4$ was added at 0.5% (w/v) to quench residual aldehyde, followed by PBS washing steps (30s, 1min, 5min, 10min, 15min). For blocking, the cells were incubated in antibody incubation buffer (Massive Photonics) for 45 minutes. Primary rat anti-tubulin antibody (Massive Photonics) was added 1:100 and incubated overnight, after washing twice with washing buffer (WB, MP) secondary anti-rat Ab (MP) was added at 1:100 and incubated overnight, washed three times, and then stored in washing buffer. Prior to imaging, for pCOT samples, the 17 nt COT strand was incubated at 200 pM for 1.5 h at 37°C to ensure hybridization in WB + 50 mM $MgCl_2$. Directly before imaging, the imager was added to the solution at 200 pM. For rCOT samples, analogously to DNA-origami measurements, the tenfold concentration (2 nM) was added, together with the 200 pM imager before the measurement.

DNA-PAINT in fixed cells. DNA-PAINT measurements in fixed cells were carried out on a custom-built total internal reflection fluorescence (TIRF) microscope, based on an inverted microscope (IX71, Olympus) equipped with a nosepiece (IX2-NPS, Olympus) for drift suppression. For red excitation a 150 mW laser (iBeam smart, Toptica Photonics) spectrally filtered with a clean-up filter (Brightline HC 650/13, Semrock) was used. A diffractive beam shaper (piShaper 6_6_VIS, AdlOptica) generated a flat-top laser beam profile, which guaranteed a homogeneous illumination of the sample across the whole detection plane. For more details, see SI section 1.5. COS-7 samples, without and with pCOT/rCOT were measured using an excitation power density of ca. 0.6 kW/cm^2 for 36000 frames at 100 ms exposure time and EM gain set to 150.

Analysis of DNA-PAINT in fixed cells. From raw data photon counts and x/y coordinates were extracted using the "Localize" feature of the software Picasso. Therein, PSF fitting was performed using MLE with minimal net gradient 12000 and box size 5. To correct for drift, RCC was applied in Picasso "Render". The drift-corrected data was subjected to filtering using a custom written software.[54] With this, first and last frame were excluded to factor out photon count errors due to incompletely acquired binding events. Only localizations that were detected for more than three frames within half a camera pixel size (93 nm size, distance threshold 50 nm) were included in the filtered data. Exemplary rendered images were extracted at the same zoom and contrast settings for all samples and applying the individual localization precision blur. Rendered images with 32 color coding according to photon were extracted setting the maximum photon number to 10000.

To obtain 3D cross sections of microtubules, localizations were picked using the rectangular tool in Render perpendicular to the microtubules' length. Subsequently, the previously reported custom-built SIMPLER software in MATLAB was used to extract the axial positions.[54] We used the following parameters: N_0 (photons expected for z = 0) = 7000, θ_i (incident angle) = 66°, α (evanescent component) = 0.9, NA = 1.45,

λ_0 (excitation wavelength) = 644 nm and λ_d (mean detection wavelength) = 700 nm. From this, the ThunderStorm plugin for Image-J was used to create the z-color coded image rendering, as reported in the SIMPLER publication, using a pixel size of 3.5 nm in the super-resolved image, where every localization is rendered as a Gaussian blurred spot with a width of 7 nm. Localization precision was calculated with a custom software, analysing individual ON-events. Here, also a minimum ON-time of 3 frames is required before calculating standard deviation in x/y and average number of photons from an event.

Acknowledgement

V.G. thankfully acknowledges German Research Foundation (DFG, grant number GL 1079/1-1, project number 503042693); L.Z. and V.G. acknowledge Center for Nanoscience (CeNS) for a collaborative research grant; P.T. gratefully acknowledges financial support from DFG (INST 86/2224) and from the Federal Ministry of Education and Research (BMBF) and the Free State of Bavaria under the Excellence Strategy of the Federal Government and the Länder through the ONE MUNICH Project 'Munich Multiscale Biofabrication' and the BMBF in the framework of the Cluster4Future program (Cluster for Nucleic Acid Therapeutics Munich, CNATM) (Project ID: 03ZU1201AA).

Author contributions

V.G. and M.S. conceived the idea. M.S. and V.G. designed and the experiments on DNA origami nanostructures. C.C., M.S., and V.G. designed DNA-PAINT experiments in fixed COS-7 cells. M.S. synthesized and characterized DNA origami nanostructures. M.S. performed bleaching experiments and DNA-PAINT imaging on DNA nanostructures and subsequent data analysis. C.C. performed DNA-PAINT imaging in fixed COS-7 cells and subsequent data analysis with help of A.S. M.S. and V.G. performed single-molecule fluorescence correlation studies. A.S. provided custom written software and support for filtering and analysis of DNA-PAINT microtubule data. J. B. built the flat-top TIRF setup to enable DNA-PAINT cell measurements. F.C. provided custom-written software for the analysis of single-molecule bleaching data. L.G. provided custom-written software for fluorescence auto correlation analysis. A.S. and J.B. provided custom written software for filtering and analysis of obtained DNA-PAINT data. S.S.M. and M.J.S. synthesized and provided Cy5B-NHS ester. J.K., A.H., L.Z., and TC synthesized and provided the COT-maleimide linker molecule. V.G., A.S., and P.T. supervised the study. M.S and CC. visualized the data. V.G., M.S., C.C., and A.S. wrote the manuscript with additional input from P.T., J.B., and L.G. All authors reviewed and approved the manuscript.

References

(1) Orrit, M.; Bernard, J. Single pentacene molecules detected by fluorescence excitation in a p-terphenyl crystal. *Physical Review Letters* **1990**, *65* (21), 2716-2719. DOI: 10.1103/PhysRevLett.65.2716.
(2) Vale, R. D.; Funatsu, T.; Pierce, D. W.; Romberg, L.; Harada, Y.; Yanagida, T. Direct observation of single kinesin molecules moving along microtubules. *Nature* **1996**, *380* (6573), 451-453. DOI: 10.1038/380451a0.
(3) Deguchi, T.; Iwanski, M. K.; Schentarra, E.-M.; Heidebrecht, C.; Schmidt, L.; Heck, J.; Weihs, T.; Schnorrenberg, S.; Hoess, P.; Liu, S.; et al. Direct observation of motor protein stepping in living cells using MINFLUX. *Science* **2023**, *379* (6636), 1010-1015. DOI: doi:10.1126/science.ade2676.

(4) Wirth, J. O.; Scheiderer, L.; Engelhardt, T.; Engelhardt, J.; Matthias, J.; Hell, S. W. MINFLUX dissects the unimpeded walking of kinesin-1. *Science* **2023**, *379* (6636), 1004-1010. DOI: doi:10.1126/science.ade2650.
(5) Hwang, D.-W.; Maekiniemi, A.; Singer, R. H.; Sato, H. Real-time single-molecule imaging of transcriptional regulatory networks in living cells. *Nature Reviews Genetics* **2024**, *25* (4), 272-285. DOI: 10.1038/s41576-023-00684-9.
(6) Joo, C.; Balci, H.; Ishitsuka, Y.; Buranachai, C.; Ha, T. Advances in Single-Molecule Fluorescence Methods for Molecular Biology. *Annual Review of Biochemistry* **2008**, *77* (Volume 77, 2008), 51-76. DOI: https://doi.org/10.1146/annurev.biochem.77.070606.101543.
(7) Reinhardt, S. C. M.; Masullo, L. A.; Baudrexel, I.; Steen, P. R.; Kowalewski, R.; Eklund, A. S.; Strauss, S.; Unterauer, E. M.; Schlichthaerle, T.; Strauss, M. T.; et al. Ångström-resolution fluorescence microscopy. *Nature* **2023**, *617* (7962), 711-716. DOI: 10.1038/s41586-023-05925-9.
(8) Ha, T.; Tinnefeld, P. Photophysics of fluorescence probes for single molecule biophysics and super-resolution imaging. *Annual review of physical chemistry* **2012**, *63*, 595.
(9) Deschout, H.; Zanacchi, F. C.; Mlodzianoski, M.; Diaspro, A.; Bewersdorf, J.; Hess, S. T.; Braeckmans, K. Precisely and accurately localizing single emitters in fluorescence microscopy. *Nature Methods* **2014**, *11* (3), 253-266. DOI: 10.1038/nmeth.2843.
(10) Benesch, R. E.; Benesch, R. Enzymatic Removal of Oxygen for Polarography and Related Methods. *Science* **1953**, *118* (3068), 447-448. DOI: doi:10.1126/science.118.3068.447.
(11) Aitken, C. E.; Marshall, R. A.; Puglisi, J. D. An Oxygen Scavenging System for Improvement of Dye Stability in Single-Molecule Fluorescence Experiments. *Biophysical Journal* **2008**, *94* (5), 1826-1835. DOI: https://doi.org/10.1529/biophysj.107.117689.
(12) Vogelsang, J.; Kasper, R.; Steinhauer, C.; Person, B.; Heilemann, M.; Sauer, M.; Tinnefeld, P. A Reducing and Oxidizing System Minimizes Photobleaching and Blinking of Fluorescent Dyes. *Angewandte Chemie International Edition* **2008**, *47* (29), 5465-5469. DOI: 10.1002/anie.200801518.
(13) Schols, S.; Kadashchuk, A.; Heremans, P.; Helfer, A.; Scherf, U. *Triplet excitation scavenging as method to control the triplet concentration*; SPIE, 2009.
(14) Targowski, P.; Ziętek, B.; Bączyński, A. Luminescence quenching of rhodamines by cyclooctatetraene. *Zeitschrift Für Naturforschung A* **1987**, *42* (9), 1009-1013.
(15) Heupel, M.; Gregor, I.; Becker, S.; Thiel, E. Photophysical and photochemical properties of electronically excited fluorescent dyes: a new type of time-resolved laser-scanning spectroscopy. *International Journal of Photoenergy* **1999**, *1* (3), 165-172.
(16) Dave, R.; Terry, D. S.; Munro, J. B.; Blanchard, S. C. Mitigating Unwanted Photophysical Processes for Improved Single-Molecule Fluorescence Imaging. *Biophysical Journal* **2009**, *96* (6), 2371-2381. DOI: https://doi.org/10.1016/j.bpj.2008.11.061.
(17) Xu, J.; Fan, S.; Xu, L.; Maruyama, A.; Fujitsuka, M.; Kawai, K. Control of Triplet Blinking Using Cyclooctatetraene to Access the Dynamics of Biomolecules at the Single-Molecule Level. *Angewandte Chemie International Edition* **2021**, *60* (23), 12941-12948. DOI: https://doi.org/10.1002/anie.202101606.
(18) Glembockyte, V.; Lincoln, R.; Cosa, G. Cy3 Photoprotection Mediated by Ni2+ for Extended Single-Molecule Imaging: Old Tricks for New Techniques. *Journal of the American Chemical Society* **2015**, *137* (3), 1116-1122. DOI: 10.1021/ja509923e.
(19) Glembockyte, V.; Lin, J.; Cosa, G. Improving the photostability of red-and green-emissive single-molecule fluorophores via Ni2+ mediated excited triplet-state quenching. *The Journal of Physical Chemistry B* **2016**, *120* (46), 11923-11929.
(20) Glembockyte, V.; Cosa, G. Redox-Based Photostabilizing Agents in Fluorescence Imaging: The Hidden Role of Intersystem Crossing in Geminate Radical Ion Pairs. *Journal of the American Chemical Society* **2017**, *139* (37), 13227-13233. DOI: 10.1021/jacs.7b08134.
(21) Holzmeister, P.; Gietl, A.; Tinnefeld, P. Geminate Recombination as a Photoprotection Mechanism for Fluorescent Dyes. *Angewandte Chemie International Edition* **2014**, *53* (22), 5685-5688. DOI: https://doi.org/10.1002/anie.201310300.

(22) Rasnik, I.; McKinney, S. A.; Ha, T. Nonblinking and long-lasting single-molecule fluorescence imaging. *Nature Methods* **2006**, *3* (11), 891-893. DOI: 10.1038/nmeth934.
(23) Cordes, T.; Vogelsang, J.; Tinnefeld, P. On the mechanism of Trolox as antiblinking and antibleaching reagent. *J Am Chem Soc* **2009**, *131* (14), 5018-5019. DOI: 10.1021/ja809117z From NLM.
(24) Tinnefeld, P.; Cordes, T. 'Self-healing' dyes: intramolecular stabilization of organic fluorophores. *Nature Methods* **2012**, *9* (5), 426-427. DOI: 10.1038/nmeth.1977.
(25) Altman, R. B.; Terry, D. S.; Zhou, Z.; Zheng, Q.; Geggier, P.; Kolster, R. A.; Zhao, Y.; Javitch, J. A.; Warren, J. D.; Blanchard, S. C. Cyanine fluorophore derivatives with enhanced photostability. *Nature Methods* **2012**, *9* (1), 68-71. DOI: 10.1038/nmeth.1774.
(26) Zheng, Q.; Jockusch, S.; Rodríguez-Calero, G. G.; Zhou, Z.; Zhao, H.; Altman, R. B.; Abruña, H. D.; Blanchard, S. C. Intra-molecular triplet energy transfer is a general approach to improve organic fluorophore photostability. *Photochem Photobiol Sci* **2016**, *15* (2), 196-203. DOI: 10.1039/c5pp00400d From NLM.
(27) Zheng, Q.; Jockusch, S.; Zhou, Z.; Altman, R. B.; Zhao, H.; Asher, W.; Holsey, M.; Mathiasen, S.; Geggier, P.; Javitch, J. A.; et al. Electronic tuning of self-healing fluorophores for live-cell and single-molecule imaging. *Chemical Science* **2017**, *8* (1), 755-762, 10.1039/C6SC02976K. DOI: 10.1039/C6SC02976K.
(28) Pati, A. K.; El Bakouri, O.; Jockusch, S.; Zhou, Z.; Altman, R. B.; Fitzgerald, G. A.; Asher, W. B.; Terry, D. S.; Borgia, A.; Holsey, M. D.; et al. Tuning the Baird aromatic triplet-state energy of cyclooctatetraene to maximize the self-healing mechanism in organic fluorophores. *Proceedings of the National Academy of Sciences* **2020**, *117* (39), 24305-24315. DOI: doi:10.1073/pnas.2006517117.
(29) Isselstein, M.; Zhang, L.; Glembockyte, V.; Brix, O.; Cosa, G.; Tinnefeld, P.; Cordes, T. Self-Healing Dyes—Keeping the Promise? *The Journal of Physical Chemistry Letters* **2020**, *11* (11), 4462-4480. DOI: 10.1021/acs.jpclett.9b03833.
(30) Jungmann, R.; Steinhauer, C.; Scheible, M.; Kuzyk, A.; Tinnefeld, P.; Simmel, F. C. Single-Molecule Kinetics and Super-Resolution Microscopy by Fluorescence Imaging of Transient Binding on DNA Origami. **2010**, *10*, 4756-4761. DOI: 10.1021/nl103427w.
(31) Rust, M. J.; Bates, M.; Zhuang, X. Sub-diffraction-limit imaging by stochastic optical reconstruction microscopy (STORM). *Nature Methods* **2006**, *3* (10), 793-796. DOI: 10.1038/nmeth929.
(32) Betzig, E.; Patterson, G. H.; Sougrat, R.; Lindwasser, O. W.; Olenych, S.; Bonifacino, J. S.; Davidson, M. W.; Lippincott-Schwartz, J.; Hess, H. F. Imaging Intracellular Fluorescent Proteins at Nanometer Resolution. *Science* **2006**, *313* (5793), 1642-1645. DOI: doi:10.1126/science.1127344.
(33) Hess, S. T.; Girirajan, T. P.; Mason, M. D. Ultra-high resolution imaging by fluorescence photoactivation localization microscopy. *Biophys J* **2006**, *91* (11), 4258-4272. DOI: 10.1529/biophysj.106.091116 From NLM.
(34) Scheckenbach, M.; Schubert, T.; Forthmann, C.; Glembockyte, V.; Tinnefeld, P. Self-Regeneration and Self-Healing in DNA Origami Nanostructures. *Angewandte Chemie International Edition* **2021**, *60* (9), 4931-4938. DOI: https://doi.org/10.1002/anie.202012986.
(35) Stehr, F.; Stein, J.; Bauer, J.; Niederauer, C.; Jungmann, R.; Ganzinger, K.; Schwille, P. Tracking single particles for hours via continuous DNA-mediated fluorophore exchange. *Nature Communications* **2021**, *12* (1), 4432. DOI: 10.1038/s41467-021-24223-4.
(36) Spahn, C.; Hurter, F.; Glaesmann, M.; Karathanasis, C.; Lampe, M.; Heilemann, M. Protein-Specific, Multicolor and 3D STED Imaging in Cells with DNA-Labeled Antibodies. *Angewandte Chemie International Edition* **2019**, *58* (52), 18835-18838. DOI: https://doi.org/10.1002/anie.201910115.
(37) Kümmerlin, M.; Mazumder, A.; Kapanidis, A. N. Bleaching-resistant, Near-continuous Single-molecule Fluorescence and FRET Based on Fluorogenic and Transient DNA Binding. *ChemPhysChem* **2023**, *24* (12), e202300175. DOI: https://doi.org/10.1002/cphc.202300175.
(38) Vermeer, B.; Schmid, S. Can DyeCycling break the photobleaching limit in single-molecule FRET? *Nano Research* **2022**, *15* (11), 9818-9830. DOI: 10.1007/s12274-022-4420-5.
(39) Kompa, J.; Bruins, J.; Glogger, M.; Wilhelm, J.; Frei, M. S.; Tarnawski, M.; D'Este, E.; Heilemann, M.; Hiblot, J.; Johnsson, K. Exchangeable HaloTag Ligands for Super-Resolution Fluorescence

Microscopy. *Journal of the American Chemical Society* **2023**, *145* (5), 3075-3083. DOI: 10.1021/jacs.2c11969.
(40) Glogger, M.; Wang, D.; Kompa, J.; Balakrishnan, A.; Hiblot, J.; Barth, H.-D.; Johnsson, K.; Heilemann, M. Synergizing Exchangeable Fluorophore Labels for Multitarget STED Microscopy. *ACS Nano* **2022**, *16* (11), 17991-17997. DOI: 10.1021/acsnano.2c07212.
(41) Blumhardt, P.; Stein, J.; Mücksch, J.; Stehr, F.; Bauer, J.; Jungmann, R.; Schwille, P. Photo-Induced Depletion of Binding Sites in DNA-PAINT Microscopy. *Molecules* **2018**, *23* (12), 3165. DOI: 10.3390/molecules23123165 From NLM.
(42) Alejo, J. L.; Blanchard, S. C.; Andersen, O. S. Small-molecule photostabilizing agents are modifiers of lipid bilayer properties. *Biophysical journal* **2013**, *104* (11), 2410-2418.
(43) Shi, X.; Lim, J.; Ha, T. Acidification of the Oxygen Scavenging System in Single-Molecule Fluorescence Studies: In Situ Sensing with a Ratiometric Dual-Emission Probe. *Analytical Chemistry* **2010**, *82* (14), 6132-6138. DOI: 10.1021/ac1008749.
(44) Swoboda, M.; Henig, J.; Cheng, H.-M.; Brugger, D.; Haltrich, D.; Plumeré, N.; Schlierf, M. Enzymatic Oxygen Scavenging for Photostability without pH Drop in Single-Molecule Experiments. *ACS Nano* **2012**, *6* (7), 6364-6369. DOI: 10.1021/nn301895c.
(45) Zimmerman, S. B.; Trach, S. O. Estimation of macromolecule concentrations and excluded volume effects for the cytoplasm of Escherichia coli. *Journal of Molecular Biology* **1991**, *222* (3), 599-620. DOI: https://doi.org/10.1016/0022-2836(91)90499-V.
(46) Ellis, R. J. Macromolecular crowding: obvious but underappreciated. *Trends in Biochemical Sciences* **2001**, *26* (10), 597-604. DOI: https://doi.org/10.1016/S0968-0004(01)01938-7.
(47) Hirvonen, L. M.; Cox, S. STORM without enzymatic oxygen scavenging for correlative atomic force and fluorescence superresolution microscopy. *Methods and Applications in Fluorescence* **2018**, *6* (4), 045002. DOI: 10.1088/2050-6120/aad018.
(48) Zhang, L.; Isselstein, M.; Köhler, J.; Eleftheriadis, N.; Huisjes, N. M.; Guirao-Ortiz, M.; Narducci, A.; Smit, J. H.; Stoffels, J.; Harz, H.; et al. Linker Molecules Convert Commercial Fluorophores into Tailored Functional Probes during Biolabelling. *Angewandte Chemie International Edition* **2022**, *61* (19), e202112959. DOI: https://doi.org/10.1002/anie.202112959.
(49) Widengren, J.; Chmyrov, A.; Eggeling, C.; Löfdahl, P.-Å.; Seidel, C. A. M. Strategies to Improve Photostabilities in Ultrasensitive Fluorescence Spectroscopy. *The Journal of Physical Chemistry A* **2007**, *111* (3), 429-440. DOI: 10.1021/jp0646325.
(50) Abdelsayed, V.; Boukhatem, H.; Olivier, N. An Optimized Buffer for Repeatable Multicolor STORM. *ACS Photonics* **2022**, *9* (12), 3926-3934. DOI: 10.1021/acsphotonics.2c01249.
(51) Michie, M. S.; Götz, R.; Franke, C.; Bowler, M.; Kumari, N.; Magidson, V.; Levitus, M.; Loncarek, J.; Sauer, M.; Schnermann, M. J. Cyanine Conformational Restraint in the Far-Red Range. *Journal of the American Chemical Society* **2017**, *139* (36), 12406-12409. DOI: 10.1021/jacs.7b07272.
(52) Eiring, P.; McLaughlin, R.; Matikonda, S. S.; Han, Z.; Grabenhorst, L.; Helmerich, D. A.; Meub, M.; Beliu, G.; Luciano, M.; Bandi, V.; et al. Targetable Conformationally Restricted Cyanines Enable Photon-Count-Limited Applications. *Angewandte Chemie International Edition* **2021**, *60* (51), 26685-26693. DOI: https://doi.org/10.1002/anie.202109749.
(53) Adam, W.; Klug, G.; Peters, E.-M.; Peters, K.; von Schnering, H. G. Synthesis of endoperoxides derived from cyclooctatetraenes via singlet oxygenation. *Tetrahedron* **1985**, *41* (11), 2045-2056. DOI: https://doi.org/10.1016/S0040-4020(01)96575-5.
(54) Szalai, A. M.; Siarry, B.; Lukin, J.; Williamson, D. J.; Unsain, N.; Cáceres, A.; Pilo-Pais, M.; Acuna, G.; Refojo, D.; Owen, D. M.; et al. Three-dimensional total-internal reflection fluorescence nanoscopy with nanometric axial resolution by photometric localization of single molecules. *Nature Communications* **2021**, *12* (1), 517. DOI: 10.1038/s41467-020-20863-0.
(55) Stehr, F.; Stein, J.; Schueder, F.; Schwille, P.; Jungmann, R. Flat-top TIRF illumination boosts DNA-PAINT imaging and quantification. *Nature Communications* **2019**, *10* (1), 1268. DOI: 10.1038/s41467-019-09064-6.

(56) Früh, S. M.; Matti, U.; Spycher, P. R.; Rubini, M.; Lickert, S.; Schlichthaerle, T.; Jungmann, R.; Vogel, V.; Ries, J.; Schoen, I. Site-Specifically-Labeled Antibodies for Super-Resolution Microscopy Reveal In Situ Linkage Errors. *ACS Nano* **2021**, *15* (7), 12161-12170. DOI: 10.1021/acsnano.1c03677.
(57) Liu, S.; Hoess, P.; Ries, J. Super-Resolution Microscopy for Structural Cell Biology. *Annu Rev Biophys* **2022**, *51*, 301-326. DOI: 10.1146/annurev-biophys-102521-112912.
(58) Ries, J.; Kaplan, C.; Platonova, E.; Eghlidi, H.; Ewers, H. A simple, versatile method for GFP-based super-resolution microscopy via nanobodies. *Nat Methods* **2012**, *9* (6), 582-584. DOI: 10.1038/nmeth.1991.
(59) Schueder, F.; Rivera-Molina, F.; Su, M.; Marin, Z.; Kidd, P.; Rothman, J. E.; Toomre, D.; Bewersdorf, J. Unraveling cellular complexity with transient adapters in highly multiplexed super-resolution imaging. *Cell* **2024**, *187* (7), 1769-1784.e1718. DOI: 10.1016/j.cell.2024.02.033 From NLM.
(60) Unterauer, E. M.; Shetab Boushehri, S.; Jevdokimenko, K.; Masullo, L. A.; Ganji, M.; Sograte-Idrissi, S.; Kowalewski, R.; Strauss, S.; Reinhardt, S. C. M.; Perovic, A.; et al. Spatial proteomics in neurons at single-protein resolution. *Cell* **2024**, *187* (7), 1785-1800.e1716. DOI: 10.1016/j.cell.2024.02.045 (acccessed 2024/11/04).
(61) Eklund, A. S.; Ganji, M.; Gavins, G.; Seitz, O.; Jungmann, R. Peptide-PAINT Super-Resolution Imaging Using Transient Coiled Coil Interactions. *Nano Letters* **2020**, *20* (9), 6732-6737. DOI: 10.1021/acs.nanolett.0c02620.
(62) Lučinskaitė, E.; Bokhobza, A. F. E.; Stannard, A.; Meletiou, A.; Estell, C.; West, S.; Michele, L. D.; Soeller, C.; Clowsley, A. H. Reduced Non-Specific Binding of Super-Resolution DNA-PAINT Markers by Shielded DNA-PAINT Labeling Protocols. *Small n/a* (n/a), 2405032. DOI: https://doi.org/10.1002/smll.202405032.
(63) Verheijen, M.; Lienhard, M.; Schrooders, Y.; Clayton, O.; Nudischer, R.; Boerno, S.; Timmermann, B.; Selevsek, N.; Schlapbach, R.; Gmuender, H.; et al. DMSO induces drastic changes in human cellular processes and epigenetic landscape in vitro. *Scientific Reports* **2019**, *9* (1), 4641. DOI: 10.1038/s41598-019-40660-0.
(64) Bauer, J.; Reichl, A.; Tinnefeld, P. Kinetic Referencing Allows Identification of Epigenetic Cytosine Modifications by Single-Molecule Hybridization Kinetics and Superresolution DNA-PAINT Microscopy. *ACS Nano* **2024**, *18* (2), 1496-1503. DOI: 10.1021/acsnano.3c08451.
(65) Jungmann, R.; Avendaño, M. S.; Dai, M.; Woehrstein, J. B.; Agasti, S. S.; Feiger, Z.; Rodal, A.; Yin, P. Quantitative super-resolution imaging with qPAINT. *Nature Methods* **2016**, *13* (5), 439-442. DOI: 10.1038/nmeth.3804.
(66) van der Velde, J. H. M.; Ploetz, E.; Hiermaier, M.; Oelerich, J.; de Vries, J. W.; Roelfes, G.; Cordes, T. Mechanism of Intramolecular Photostabilization in Self-Healing Cyanine Fluorophores. *ChemPhysChem* **2013**, *14* (18), 4084-4093. DOI: https://doi.org/10.1002/cphc.201300785.
(67) Smit, J. H.; van der Velde, J. H. M.; Huang, J.; Trauschke, V.; Henrikus, S. S.; Chen, S.; Eleftheriadis, N.; Warszawik, E. M.; Herrmann, A.; Cordes, T. On the impact of competing intra- and intermolecular triplet-state quenching on photobleaching and photoswitching kinetics of organic fluorophores. *Physical Chemistry Chemical Physics* **2019**, *21* (7), 3721-3733, 10.1039/C8CP05063E. DOI: 10.1039/C8CP05063E.
(68) Das, T. N.; Priyadarshini, K. I. Triplet of cyclooctatetraene: reactivity and properties. *Journal of the Chemical Society, Faraday Transactions* **1994**, *90* (7), 963-968, 10.1039/FT9949000963. DOI: 10.1039/FT9949000963.
(69) Schnitzbauer, J.; Strauss, M. T.; Schlichthaerle, T.; Schueder, F.; Jungmann, R. Super-resolution microscopy with DNA-PAINT. *Nature Protocols* **2017**, *12* (6), 1198-1228. DOI: 10.1038/nprot.2017.024.
(70) Schueder, F.; Stein, J.; Stehr, F.; Auer, A.; Sperl, B.; Strauss, M. T.; Schwille, P.; Jungmann, R. An order of magnitude faster DNA-PAINT imaging by optimized sequence design and buffer conditions. *Nature Methods* **2019**, *16* (11), 1101-1104. DOI: 10.1038/s41592-019-0584-7.
(71) Nickels, P. C.; Wünsch, B.; Holzmeister, P.; Bae, W.; Kneer, L. M.; Grohmann, D.; Tinnefeld, P.; Liedl, T. Molecular force spectroscopy with a DNA origami–based nanoscopic force clamp. *Science* **2016**, *354* (6310), 305-307. DOI: 10.1126/science.aah5974.

(72) Derr, N. D.; Goodman, B. S.; Jungmann, R.; Leschziner, A. E.; Shih, W. M.; Reck-Peterson, S. L. Tug-of-war in motor protein ensembles revealed with a programmable DNA origami scaffold. *Science* **2012**, *338* (6107), 662-665. DOI: 10.1126/science.1226734 From NLM.
(73) Grabenhorst, L.; Trofymchuk, K.; Steiner, F.; Glembockyte, V.; Tinnefeld, P. Fluorophore photostability and saturation in the hotspot of DNA origami nanoantennas. *Methods Appl Fluoresc* **2020**, *8* (2), 024003. DOI: 10.1088/2050-6120/ab6ac8 From NLM.
(74) Ingargiola, A. 2017-2018. https://github.com/OpenSMFS/pycorrelate (accessed 12.11.2024).
(75) Laurence, T. A.; Fore, S.; Huser, T. Fast, flexible algorithm for calculating photon correlations. *Opt. Lett.* **2006**, *31* (6), 829-831. DOI: 10.1364/OL.31.000829.
(76) Whelan, D. R.; Bell, T. D. M. Image artifacts in Single Molecule Localization Microscopy: why optimization of sample preparation protocols matters. *Scientific Reports* **2015**, *5* (1), 7924. DOI: 10.1038/srep07924.

Supporting Information

Minimally Invasive DNA-Mediated Photostabilization for Extended Single-Molecule and Super-resolution Imaging

Michael Scheckenbach,[1‡] Cindy Close,[1‡] Julian Bauer,[1] Lennart Grabenhorst,[1] Fiona Cole,[1] Jens Köhler,[2,3] Siddharth S. Matikonda,[4] Lei Zhang,[5] Thorben Cordes,[5,6] Martin J. Schnermann,[4] Andreas Herrmann,[3,4] Philip Tinnefeld,[1] Alan Szalai,[1,7] and Viktorija Glembockyte*[1,8]

[1] Department of Chemistry and Center for NanoScience, Ludwig-Maximilians-Universität München, Butenandtstr. 5-13, 81377 München, Germany

[2] DWI – Leibniz Institute for Interactive Materials, Forckenbeckstr. 50, 52056 Aachen, Germany

[3] Institute of Technical and Macromolecular Chemistry, RWTH Aachen University, Worringerweg 2, 52074 Aachen, Germany

[4] Laboratory of Chemical Biology, Center for Cancer Research, National Cancer Institute, Frederick, MD 21702 (USA)

[5] Physical and Synthetic Biology, Faculty of Biology, Ludwig-Maximilians-Universität München, Großhadernerstr. 2-4, 82152 Planegg-Martinsried, Germany

[6] Biophysical Chemistry, Department of Chemistry and Chemical Biology, Technische Universität Dortmund, Otto-Hahn-Str. 4a, 44227 Dortmund, Germany

[7] Centro de Investigaciones en Bionanociencias, Consejo Nacional de Investigaciones Científicas y Técnicas; Ciudad Autónoma de Buenos Aires, C1425FQD, Argentina

[8] Max Planck Institute for Medical Research, Jahnstr. 29, 69120 Heidelberg, Germany

E-mail: viktorija.glembockyte@mr.mpg.de

‡ These authors contributed equally

Table of Content

1. Methods and Materials

1.1. General materials

For folding, purification and storage of 12HB DNA origami nanostructures, a 1×TAE buffer with 16 mM $MgCl_2$ was used. Bleaching of permanent fluorescent labels and DNA-PAINT with DNA origami were performed in a 2× PBS buffer with 75 mM $MgCl_2$. Bleaching of recovering labels was performed in a 2× PBS buffer with 500 mM NaCl and 0.05% Tween 20.[1,2]

Oxygen-free single-molecule was performed by addition of 1% (wt/v) *D*-(+)-glucose (Sigma Aldrich, USA), 165 units/mL glucose oxidase (G2133, Sigma Aldrich, USA), and 2170 units/mL catalase (C3155, Sigma Aldrich, USA) to the imaging solution.[3]

The p8064 scaffold strand for the folding of the DNA Origami nanostructures were extracted from M13mp18 bacteriophages. Unmodified staple strands were purchased from Eurofins Genomics GmbH and Integrated Device Technology Inc. Dye labeled oligonucleotides for DNA-PAINT imaging or permanent labeling were purchased from Eurofins Genomics GmbH (Germany).

The COT-maleimide compound was synthesized by the Cordes Group as previously reported.[4] Labeling of the COT-maleimide to thiol modified DNA was performed at Ella Biotech GmbH (Germany).

Specific materials used for individual experiments are described in the sections below.

1.2. DNA Origami folding

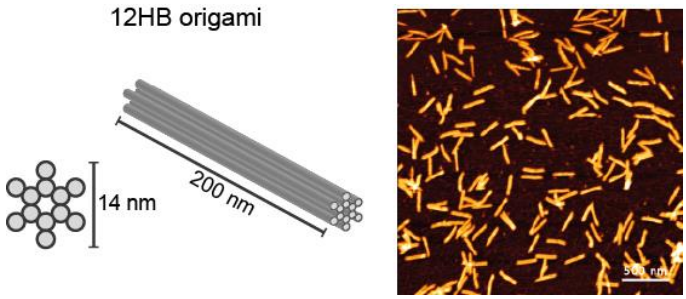

Figure S1. Scheme of the 12HB DNA origami used in this study and exemplary AFM scan of purified 12HB illustrating the successful self-assembly of the designed structures.

Table S1. Thermal ramp used for the folding of the 12HB origami nanostructures.

Temperature (°C)	Time per °C (min)	Temperature (°C)	Time per °C (min)
65	2	44	75
64 – 61	3	43	60
60 – 59	15	42	45
58	30	41-39	30
57	45	38-37	15
56	60	36-30	8
55	75	29-25	2
54-45	90	4	storage

Table S2. Final concentrations and relative equivalents of scaffold strand, unmodified staple strands (core staple strands) and modified staple strands (e.g. biotinylated staple strands for immobilization and DNA-PAINT docking site staple strands for superresolution imaging) used within this study.

Reagent	Final concentration [nM]	Equivalents
Scaffold strand	20	1
Core staple strands	200	10
Docking site staple strands	600	30
Biotinylated staple strands	600	30

1.3. Imager and Photostabilizer strands

All used imager strand sequences are given in Table S3. Three different imager strands all labelled with a fluorophore on the 3'-end, have been employed within this study. To investigate permanent fluorescent labels, a 20 nt long imager strand was used to label to a hybridize to a 20 nt docking site sequence. To investigate the photostability of a recovering label, a 11 nt imager sequence was used as reported previously.[5] For DNA-PAINT imaging, a 8 nt subsequence of the 20 nt permanent sequence was used.

For permanent labeling, the green fluorophores Cy3 and Cy3B and the red fluorophores Cy5 and Atto647N were labelled to the pImg strand. For further investigation of a recovering label, the red fluorophore Cy5 was labelled to the rLabel strand. For DNA-PAINT imaging, the red fluorophores Cy5 and Cy5B were labelled to the 8 nt long fImg strand.

Table S3. Fluorescently labelled imager strands used within this study. A 20 nt long permanent imager (pImg) and 11 nt long recovering label (rLabel) were used for bleaching experiments of permanent and recovering labels. DNA-PAINT imaging was performed with a 8 nt long fast imager strand (fImg). All imager strands were labelled with fluorophores on their 3'-end.

Name	Length (nt)	Sequence (5` to 3`)
pImg	20	TATGAGAAGTTAGGAATGTT-Dye
fImg	8	GGAATGTT-Dye
rLabel	11	TTTCCCTTTTT-Dye

All used COT DNA strands are given in Table S4. To investigate permanent and dynamic COT strands, the COT-maleimide compound was coupled to the 5'-end of a thiolated DNA oligonucleotide (Scheme **S1**) with varying sequence lengths (17 nt for permanent pCOT strand and 10 nt for recovering rCOT strand).

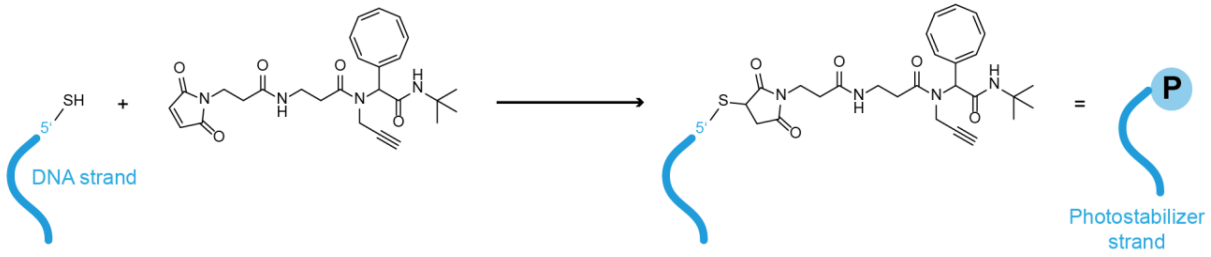

Scheme S1. Coupling of maleimide functionalized COT linker molecule to thiolated DNA oligonucleotide resulting in a photostabilizer strand with the COT entity at the 5' end.

Table S4. COT labelled photostabilizer strands used in this study. For a permanent label, COT was labelled to a 17 nt long permanent strand (pCOT). For a dynamic labeling, COT was modified to a 10 nt fast exchanging photostabilizer strand (rCOT). All photostabilizer strands were labelled with COT on their 5'-end.

Name	Length (nt)	Sequence (5` to 3`)
pCOT	17	COT-ATGATGTAGGTGGTAGA
rCOT	10	COT-ATGATGTAGG

1.4. Widefield TIRF microscopy

Automated bleaching experiments of permanent and recovering fluorescent labels and DNA-PAINT on DNA origami nanostructures were performed on a commercial Nanoimager S (ONI Ltd., UK). Red excitation at 638 nm was realized with a 1100 mW laser, green excitation at 532 nm with a 1000 mW laser, respectively. The microscope was set to TIRF illumination. In order to not corrupt the first frames of the acquired intensity transients by the photobleaching of single DNA origami nanostructures, the objective was first focused into the sample plane on a random section of the glass surface and the auto focus was activated. Subsequently the imaging lasers were shut off. Before starting time lapse measurements, the

sample slide was moved to a new region of interest while still being kept in focus by the auto focus. The data acquisition was initialized by activating the lasers and taking frames of 100 ms to 200 ms over a user defined acquisition protocol.

DNA-PAINT measurements in fixed cells were carried out on a custom-built total internal reflection fluorescence (TIRF) microscope, based on an inverted microscope (IX71, Olympus) equipped with a nosepiece (IX2-NPS, Olympus) for drift suppression. For yellow excitation, a 560 nm/1 W fiber laser (MPB Communications) filtered with a clean-up filter (Brightline HC 561/4, Semrock) was used. Red excitation at 644 nm was realized with a 150 mW laser (iBeam smart, Toptica Photonics) spectrally filtered with a clean-up filter (Brightline HC 650/13, Semrock). The red and the yellow beams were coupled into polarization maintaining single mode fibers (P3-488PM-FC-2 for 560 nm, P3-630PM-FC-2 for 644 nm) to obtain perfect Gaussian beam profiles. Behind the fibers, the excitation beam paths were combined with a dichroic mirror (T612lpxr, Chroma). To obtain a homogenous excitation profile across the whole detection plane, the laser light was guided through a diffractive beam shaper (piShaper 6_6_VIS, AdlOptica) that changes the Gaussian beam profile to a flat-top beam profile. The laser beam was coupled into the microscope body with a triple-color beam splitter (Chroma z476-488/568/647, AHF Analysentechnik) and focused on the back focal plane of an oil-immersion objective (100×, NA = 1.45, UPlanXApo, Olympus) with a telescope, that could be aligned for TIRF illumination. An additional ×1.6 optical magnification lens was applied to the detection path resulting in an effective pixel size of 92.6 nm. The fluorescence light was spectrally cleaned up (ET 700/75, Chroma for red excitation or ET 605/70m, Chroma for yellow excitation) and recorded by an electron multiplying charge-coupled device camera (Ixon X3 DU-897, Andor), which was controlled with the software Micro-Manager 1.4.[6,7]

1.5. Surface-Immobilization of DNA origami nanorulers

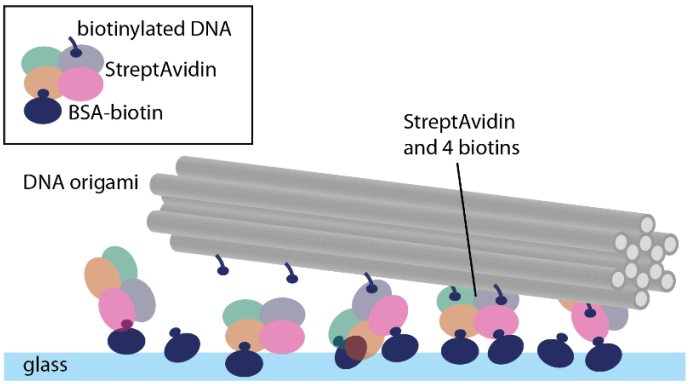

Figure S2. Scheme of components involved in surface immobilization of DNA origami.

1.6. DNA mediated photostabilization of a permanent single-molecule label

To study the photostabilization of a permanent single-molecule label by DNA mediated collision with a COT bound to the same DNA docking site, a staple strand in the central region of the 12HB was modified at the 3'-end (Table S5) with the complementary sequences of the permanent COT strand and permanent imager strand given in Table S3 and Table S4.

After immobilization of DNA origami on neutravidin functionalized glass slides, 10 nM of the COT strand and 10 nM of the permanent imager strand were incubated in a 2×PBS with 500 mM NaCl and 0.05% w/w Tween® 20 for 60 min and excessive label strands were washed away afterwards. For bleaching experiments, the photostabilization buffer was applied to the sample chambers. Bleaching was performed under low (0.3 kW/cm^2) and high (2.0 kW/cm^2) excitation power to investigate photostability in different excitation regimes. For low excitation powers, 3000 frames of 200 ms were acquired over an overall observation period of 10 min. For high excitation powers, 600 frames of 100 ms were acquired over an overall observation period of 1 min.

DNA mediated photostabilization was probed for two permanent green (Cy3, Cy3B) and two permanent red fluorophore labels (Atto647N, Cy5).

Table S5. Modified staple strand in the central region of the 12HB for DNA mediated photostabilization of permanent fluorescent labels Sequences are denoted from 5'- to 3'-end. The docking site staple strand exhibits a 17 nt binding sequence for the pCOT strand, marked in blue, and a 20 nt binding sequence for a permanent imager strand, marked in red, respectively. The numbers for the 5'- end 3'-end of the staples represent the helix number in the corresponding caDNAno file. Number in brackets represent the starting and ending position of the staple in the corresponding helix.

Name	Docking Site Length (nt)	Sequence (5` to 3`)	5'-end ´	3'-end]
pCOT + pImg	17 + 20	TCGTTCACCGCCTGGCCCT-TCTACCACCTACATCAT-AACATTCCTAACTTCTCATA	10[331]	11[344]

1.7. DNA mediated photostabilization of a recovering single-molecule label

To study the photostabilization of a recovering single-molecule label by DNA mediated collision with a COT bound to the same DNA docking site, a staple strand in the central region of the 12HB was modified at the 3'-end (Table S6) with the complementary sequences of the permanent or dynamic COT strand (10 or 17 nt) and recovering imager strand (11 nt) given in Table S3 and Table S4.

Permanent COT strand was labelled to DNA origami immobilized on streptavidin functionalized glass slides by incubation of a 10 nM pCOT strand solution in a 2×PBS with 500 mM NaCl and 0.05% w/w Tween® 20 for 60 min. Dynamic rLabel strands labelled with Cy5 (10 nM) and fast exchanging rCOT strands (100 nM) were added to the photostabilizing imaging buffer with 500 mM NaCl and 0.05% w/w Tween®.

Photostability of the recovering label and the DNA docking site was probed under low excitation power (0.1 kW/cm^2) over 18000 frames of 200 ms over an overall observation period of 60 min.

Table S6. Modified staple strand in the central region of the 12HB for DNA mediated photostabilization of recovering fluorescent labels Sequences are denoted from 5'- to 3'-end. The docking site staple strand exhibits a 10 or 17 nt binding sequence for the rCOT or pCOT strand, marked in blue, and a 11 nt binding sequence for a recovering imager strand, marked in red, respectively. The numbers for the 5'- end 3'-end of the staples represent the helix number in the corresponding caDNAno file. Number in brackets represent the starting and ending position of the staple in the corresponding helix.

Name	Docking Site Length (nt)	Sequence (5` to 3`)	5'-end ´	3'-end]
pCOT + rLabel	17 + 11	TCGTTCACCGCCTGGCCCT-TCTACCACCTACATCAT-AAAAAGGGAAA	10[331]	11[344]
rCOT + rLabel	10 + 11	TCGTTCACCGCCTGGCCCT-CCTACATCAT-AAAAAGGGAAA	10[331]	11[344]

1.8. DNA-PAINT imaging on DNA origami nanorulers

To study the applicability of the DNA mediated photostabilization for super-resolution microscopy, three staple strands with ca. 90 nm distances on the 12HB were modified at the 3'-end (Table S7).with the complementary sequences of the permanent or dynamic COT strand (10 or 17 nt) and fast imager strand (8 nt) given in Table S3 and Table S4.

Permanent COT strand was labelled to DNA origami immobilized on streptavidin functionalized glass slides by incubation of a 10 nM pCOT strand solution in a 2×PBS with 500 mM NaCl and 0.05% w/w Tween® 20 for 60 min. The 8 nt fast imager strand (1 nM) and fast exchanging rCOT strand (100 nM) were added to the photostabilizing imaging buffer with 75 mM $MgCl_2$.

Photostability of the DNA-PAINT docking sites was probed under high excitation power (1.2 kW/cm^2) over 36000 frames of 100 ms over an overall observation period of 60 min.

Table S7. Modified staple strands with 90 nm distances on the 12HB for DNA-PAINT imaging using DNA mediated photostabilization. Sequences are denoted from 5'- to 3'-end. The docking site staple strands exhibit a 10 or 17 nt binding sequence for the rCOT or pCOT strand, marked in blue, and an 8 nt binding sequence for the fast imager strand, marked in red, respectively. The numbers for the 5'- end 3'-end of the staples represent the helix number in the corresponding caDNAno file. Number in brackets represent the starting and ending position of the staple in the corresponding helix.

Name	**Docking Site Length (nt)**	**Sequence (5` to 3`)**	**5'-end ´**	**3'-end]**
pCOT + fImg	17 + 8	GTATGTGAAATTGTTATCC-TCTACCACCTACATCAT-AACATTCC	10[79]	11[92]
		TACCTGGTTTGCCCCAGCA-TCTACCACCTACATCAT-AACATTCC	10[373]	11[386]
		AACACCCTAAAGGGAGCCC-TCTACCACCTACATCAT-AACATTCC	10[625]	11[638]
fCOT + fImg	10 + 8	GTATGTGAAATTGTTATCC-CCTACATCAT-AACATTCC	10[79]	11[92]
		TACCTGGTTTGCCCCAGCA-CCTACATCAT-AACATTCC	10[373]	11[386]
		AACACCCTAAAGGGAGCCC-CCTACATCAT-AACATTCC	10[625]	11[638]

2. Supporting Figures

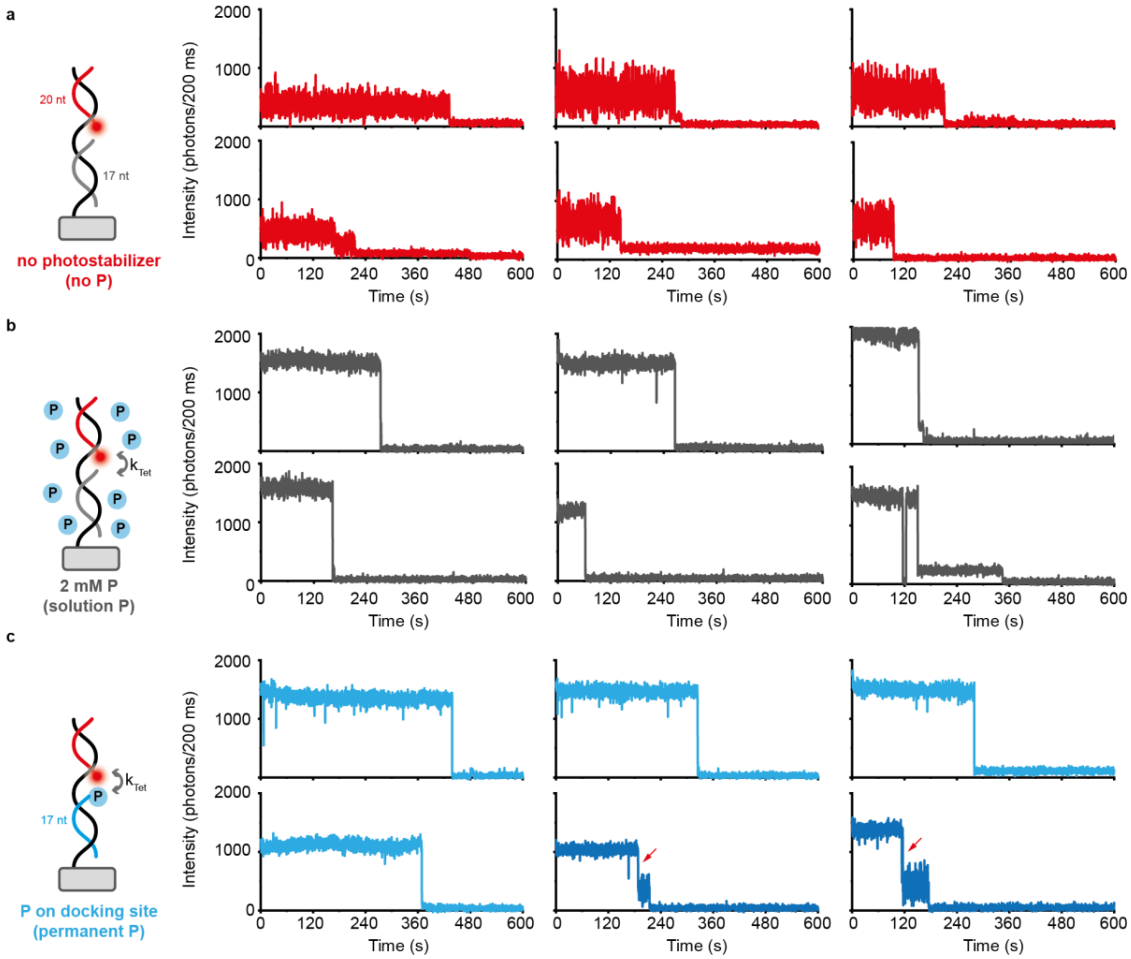

Figure S3. Permanent Cy5 labels with and without COT on docking site under low excitation power (0.3 kW/cm^2). **a)** Scheme and exemplary single-molecule trajectories for individual label spots of Cy5 labels without COT on docking site. **b)** Scheme and exemplary single-molecule trajectories for individual label spots of Cy5 labels with 2 mM COT in solution. **c)** Scheme and exemplary single-molecule trajectories for individual labels spots of Cy5 with a permanent COT label on the docking site.

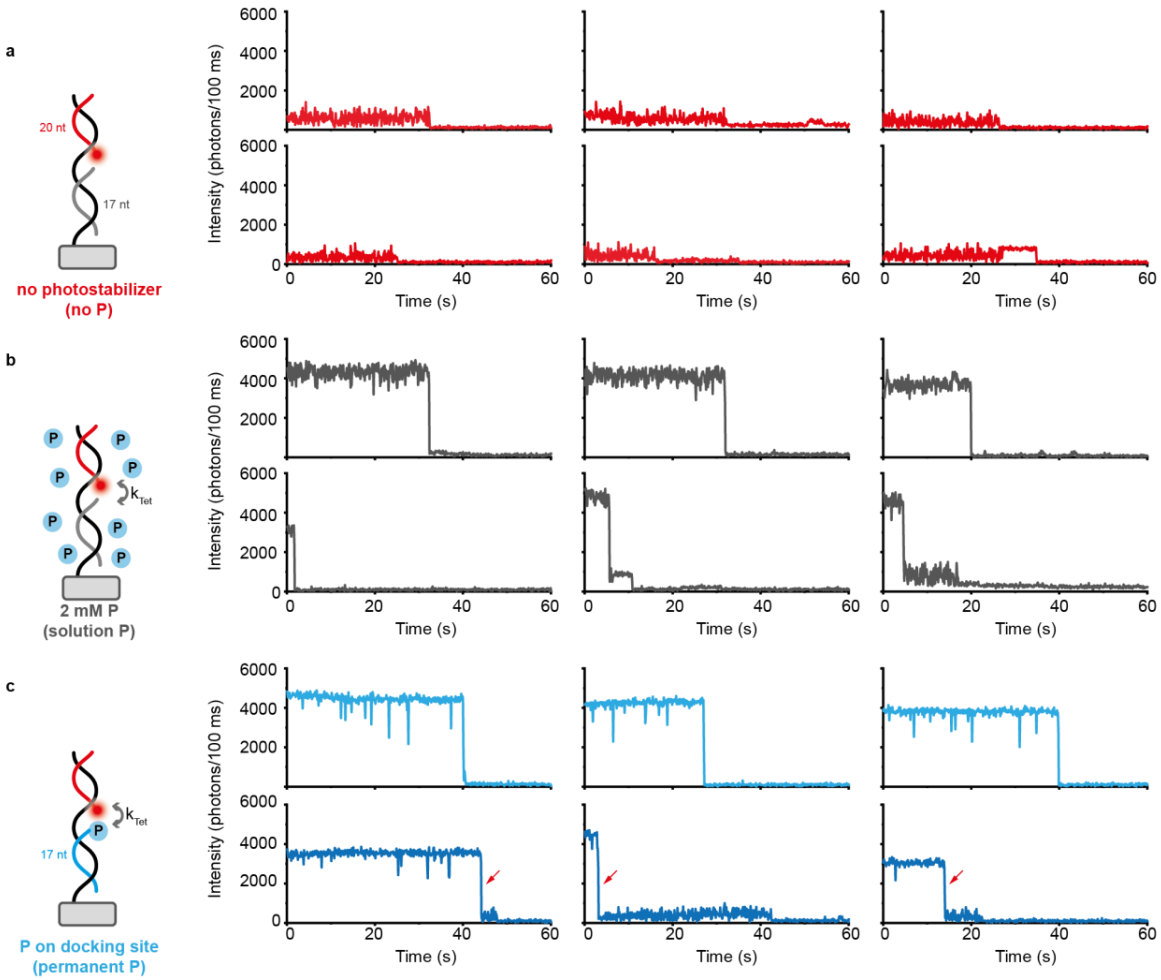

Figure S4. Permanent Cy5 labels with and without COT on docking site under high excitation power (2.0 kW/cm^2). **a)** Scheme and exemplary single-molecule trajectories for individual label spots of Cy5 labels without COT on docking site. **b)** Scheme and exemplary single-molecule trajectories for individual label spots of Cy5 labels with 2 mM COT in solution. **c)** Scheme and exemplary single-molecule trajectories for individual labels spots of Cy5 with a permanent COT label on the docking site.

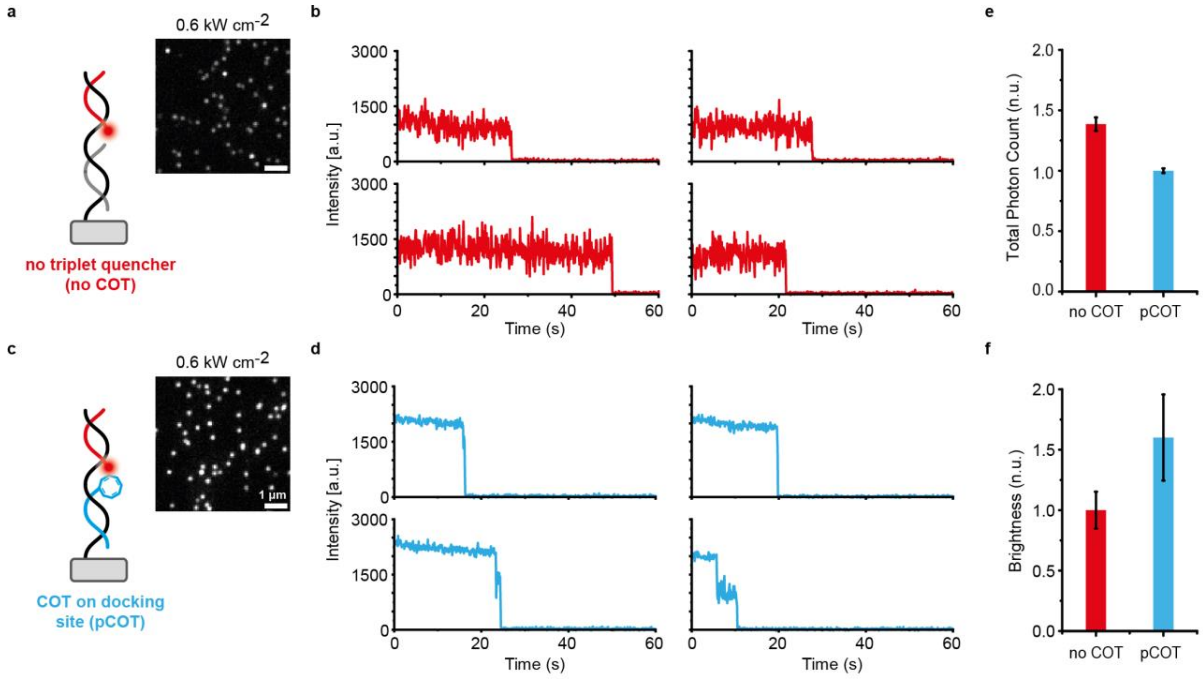

Figure S5. Permanent Cy3 labels with and without COT on docking site under medium excitation power (0.6 kW/cm^2). **a)** Scheme and exemplary TIRF image of Cy3 labels without COT on docking site. **b)** Exemplary single-molecule trajectories for individual label spots of Cy3 labels without COT on docking site. **c)** Scheme and exemplary TIRF image of Cy3 labels with a permanent COT label on the docking site. **d)** Exemplary single-molecule trajectories for individual labels spots of Cy3 with a permanent COT label on the docking site. **e)** Normalized total photon counts for permanent Cy3 labels with and without COT label on the docking site. Error bars represent error of the fit. **f)** Normalized brightness for permanent Cy3B labels with and without COT label on the docking site. Error bars represent standard deviation of gaussian fit.

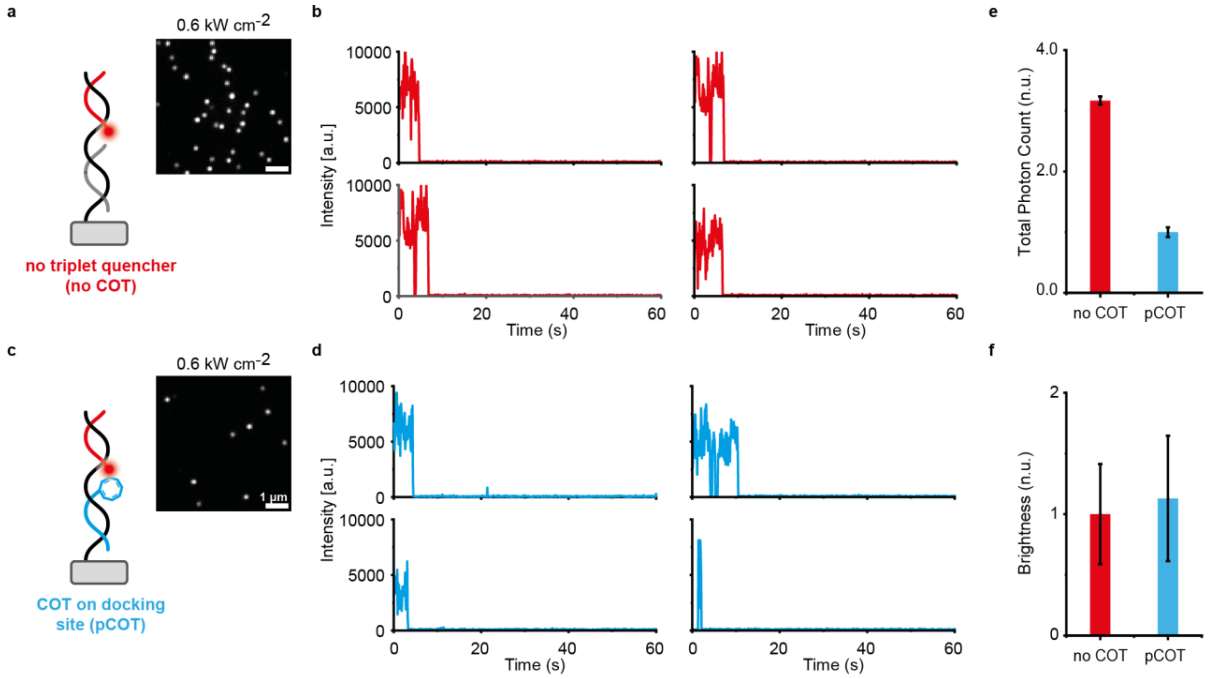

Figure S6. Permanent Cy3B labels with and without COT on docking site under medium excitation power (0.6 kW/cm^2). **a)** Scheme and exemplary TIRF image of Cy3B labels without COT on docking site. **b)** Exemplary single-molecule trajectories for individual label spots of Cy3B labels without COT on docking site. **c)** Scheme and exemplary TIRF image of Cy3B labels with a permanent COT label on the docking site. **d)** Exemplary single-molecule trajectories for individual labels spots of Cy3B with a permanent COT label on the docking site. **e)** Normalized total photon counts for permanent Cy3B labels with and without COT label on the docking site. Error bars represent error of the fit. **f)** Normalized brightness for permanent Cy3B labels with and without COT label on the docking site. Error bars represent standard deviation of gaussian fit.

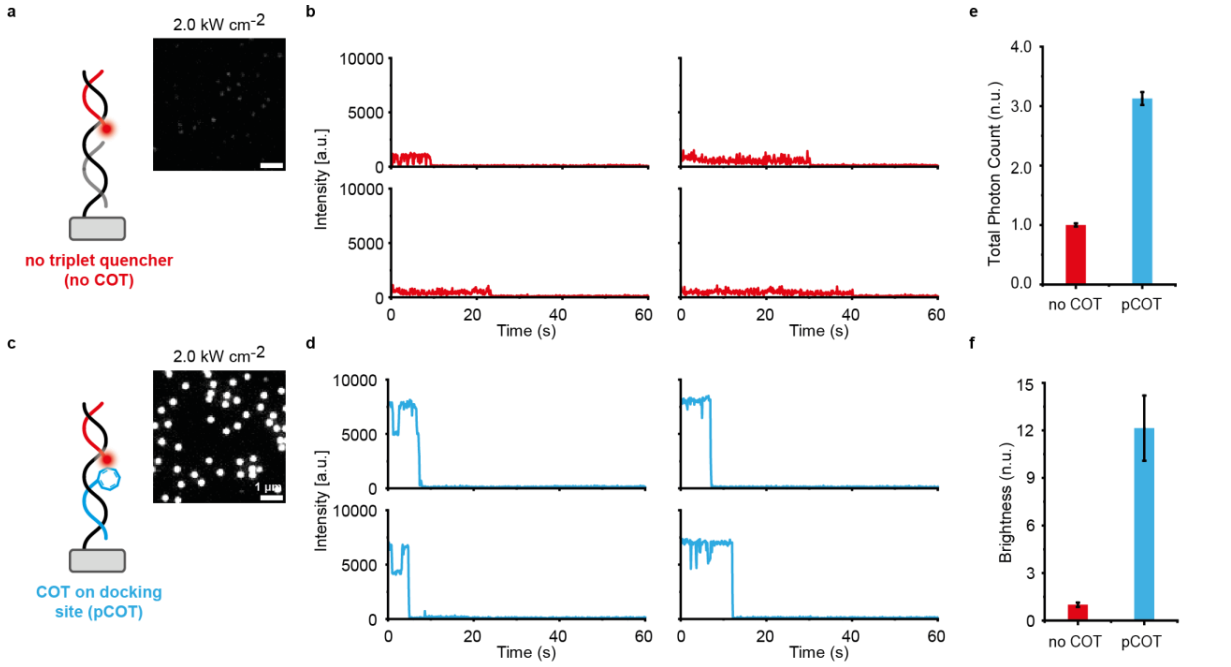

Figure S7. Permanent Atto647N labels with and without COT on docking site under high excitation power (2.0 kW/cm^2). **a)** Scheme and exemplary TIRF image of Atto647N labels without COT on docking site. **b)** Exemplary single-molecule trajectories for individual label spots of Atto647N labels without COT on docking site. **c)** Scheme and exemplary TIRF image of Atto647N labels with a permanent COT label on the docking site. **d)** Exemplary single-molecule trajectories for individual labels spots of Atto647N with a permanent COT label on the docking site. **e)** Normalized total photon counts for permanent Atto647N labels with and without COT label on the docking site. Error bars represent error of the fit. **f)** Normalized brightness for permanent Atto647N labels with and without COT label on the docking site. Error bars represent standard deviation of gaussian fit.

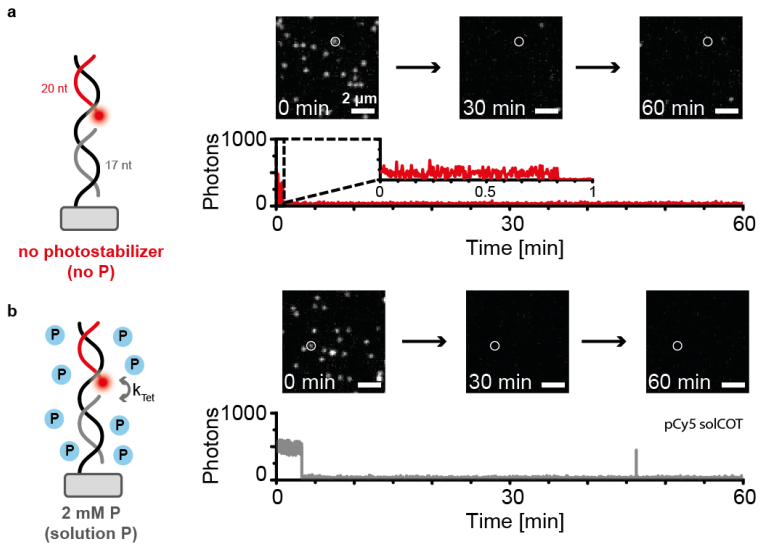

Figure S8. Permanent Cy5 labels without triplet state quencher (no COT) and stabilized by 2 mM COT solution under low excitation power (0.1 kW/cm^2). **a)** Permanent Cy5 label without triplet state quencher imaged over 60 min. **b)** Permanent Cy5 label with 2 mM COT in solution imaged over 60 min.

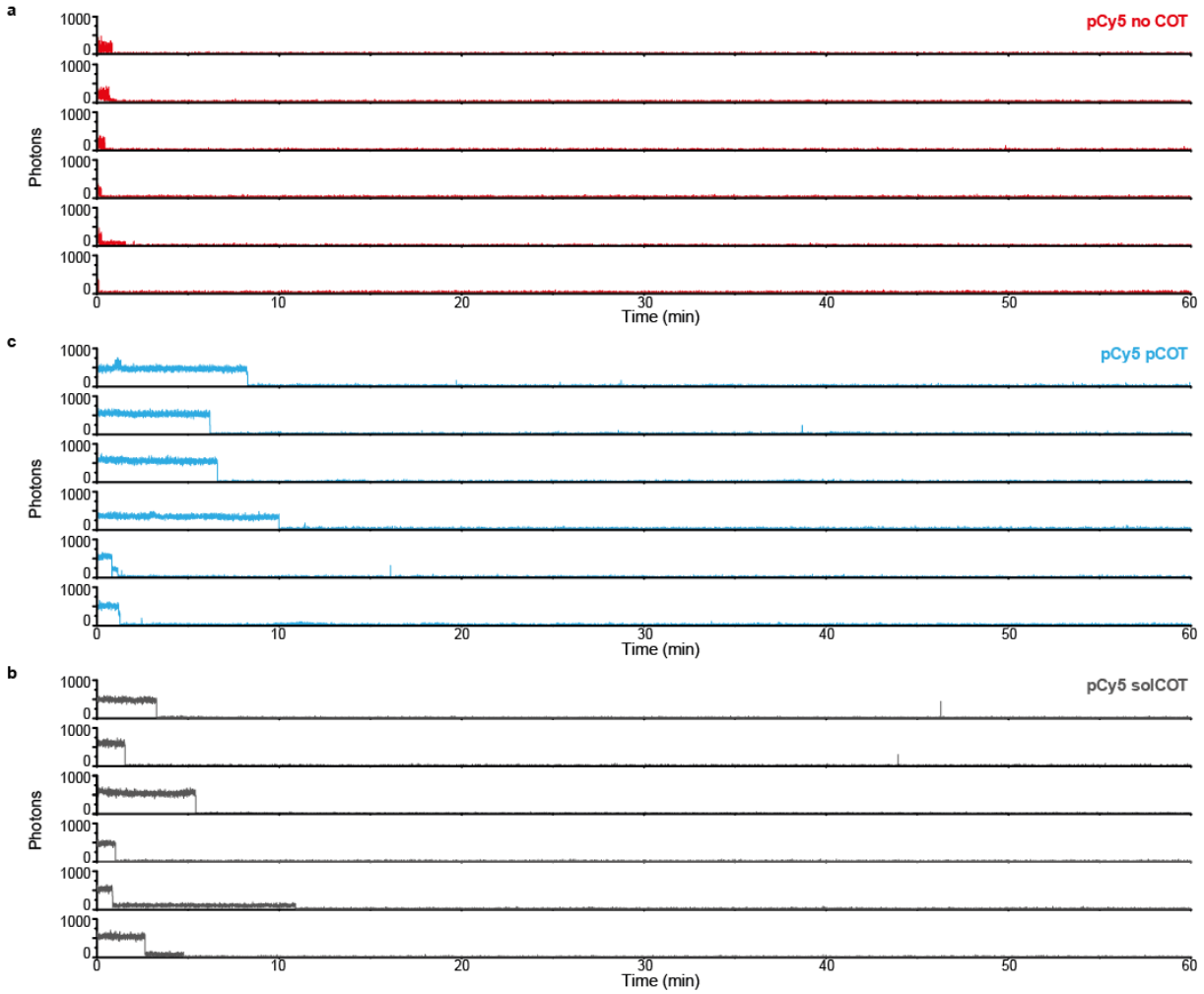

Figure S9. Exemplary single-molecule trajectories of permanent Cy5 labels with and without COT label on the docking site under low excitation power (0.1 kW/cm^2). over 60 min. **a)** Exemplary single-molecule trajectories for individual labels spots of Cy5 without COT label on the docking site (pCy5 no COT). **b)** Exemplary single-molecule trajectories for individual labels spots of Cy5 with a permanent COT label on the docking site (pCy5 pCOT). **c)** Exemplary single-molecule trajectories for individual labels spots of Cy5 with 2 mM COT in solution (pCy5 solCOT).

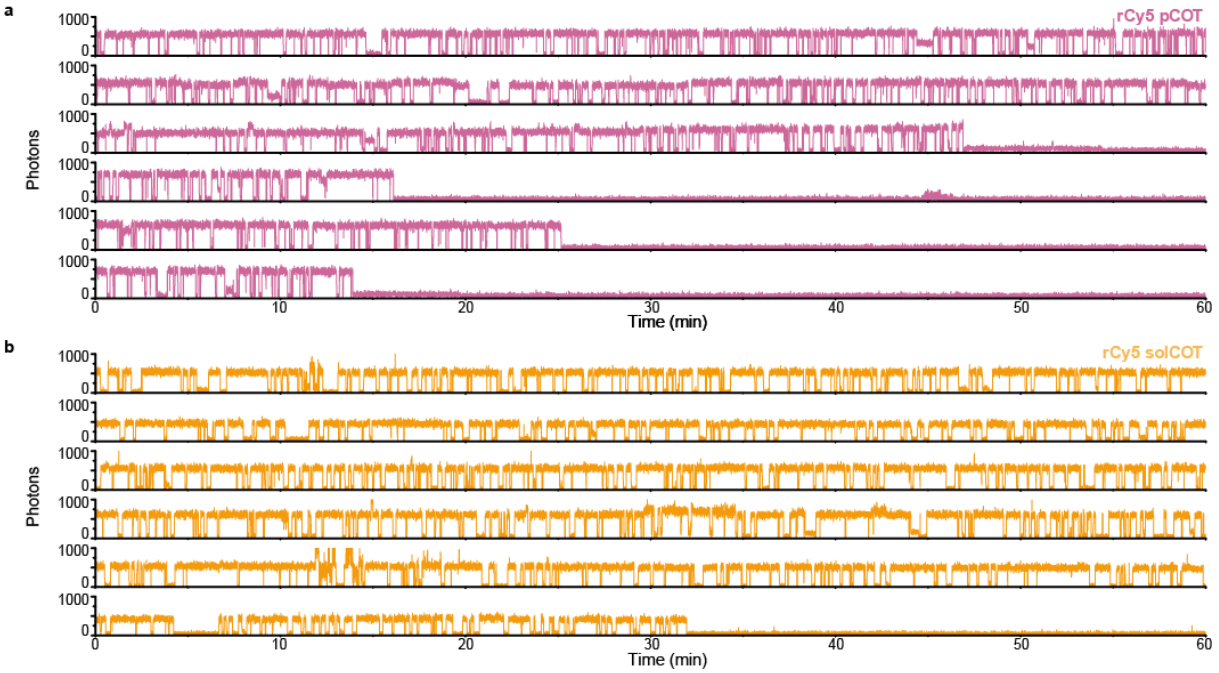

Figure S10. Exemplary single-molecule trajectories of recovering Cy5 labels with COT label on the docking site or in solution under low excitation power (0.1 kW/cm^2). over 60 min. **a)** Exemplary single-molecule trajectories for individual labels spots of recovering Cy5 with a permanent COT label on the docking site (rCy5 pCOT). **b)** Exemplary single-molecule trajectories for individual labels spots of recovering Cy5 with 2 mM COT in solution (rCy5 solCOT).

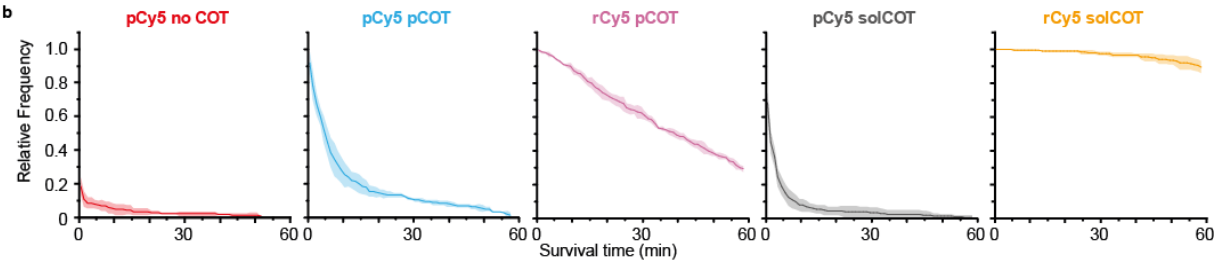

Figure S11. Survival times of permanent and recovering Cy5 labels with and without COT label on the docking site under low excitation power (0.1 kW/cm^2). Lines represent average of XXX measurements, areas represent the standard deviation.

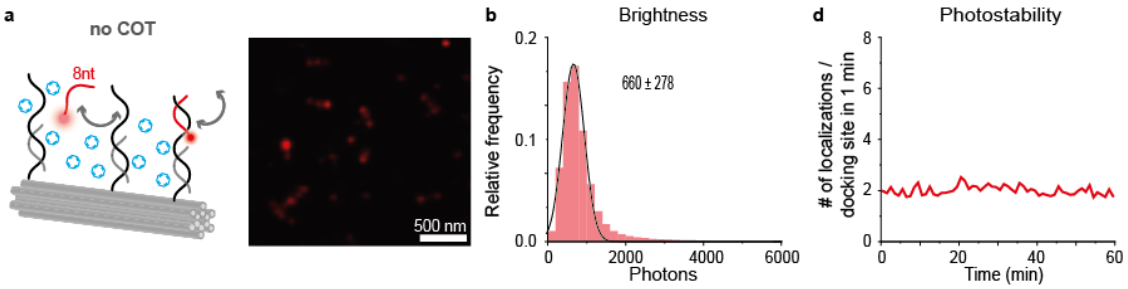

Figure S12. DNA-PAINT pick statistics with Cy5 imager and no COT on the docking site under high illumination power (1.0 kW/cm^2). **a)** Scheme of DNA-PAINT without COT (no COT) and obtained DNA-PAINT image after 60 min. **b)** Obtained photon counts for DNA-PAINT with Cy5 without COT. **c)** DNA-PAINT kinetics, i.e. on- and off-times, for individual DNA-PAINT docking sites without COT. **d)** Observed photostability of DNA-PAINT docking sites over 60 min without COT.

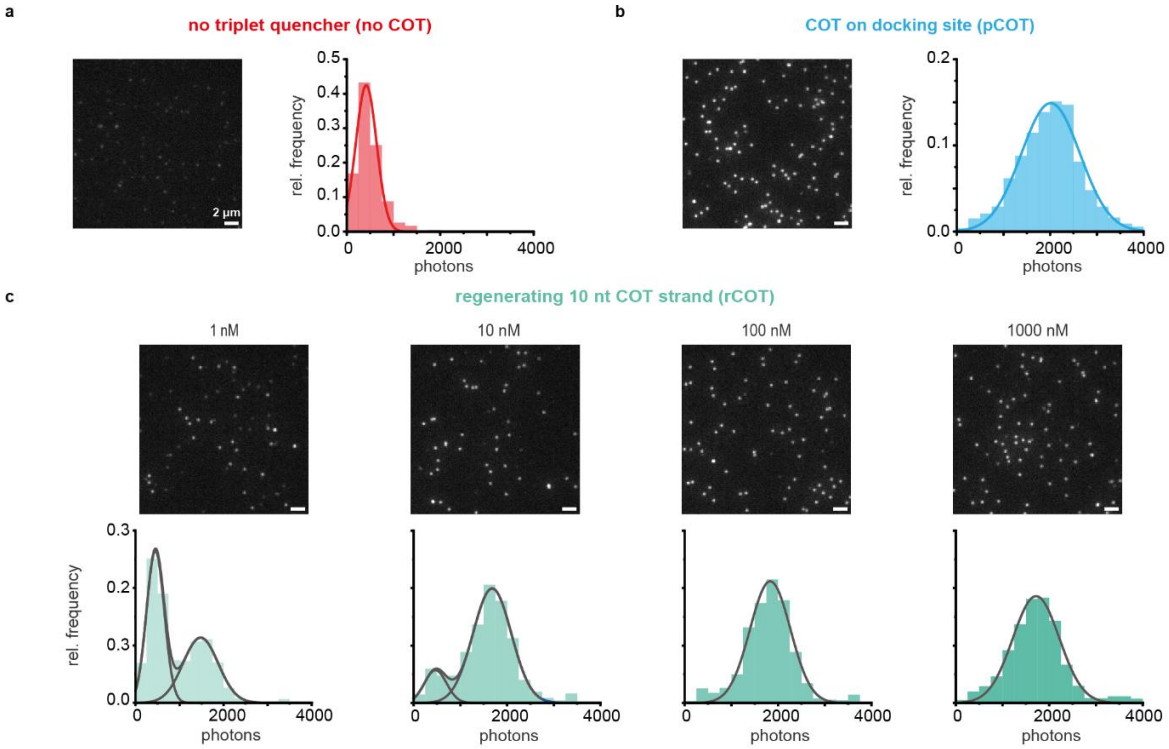

Figure S13. Saturating the DNA docking site with a recovering COT strand. **a)** Exemplary TIRF image of permanent Cy5 label and no COT on the docking site and extracted brightness histogram. **b)** Exemplary TIRF image of permanent Cy5 label and a permanent COT label on the docking site and extracted brightness histogram. **c)** Exemplary TIRF images of permanent Cy5 label and varying concentrations (1 nM – 1000 nM) of a recovering COT label (10 nt) on the docking site and extracted brightness histograms. All data were acquired under medium high excitation power (0.8 kW/cm^2).

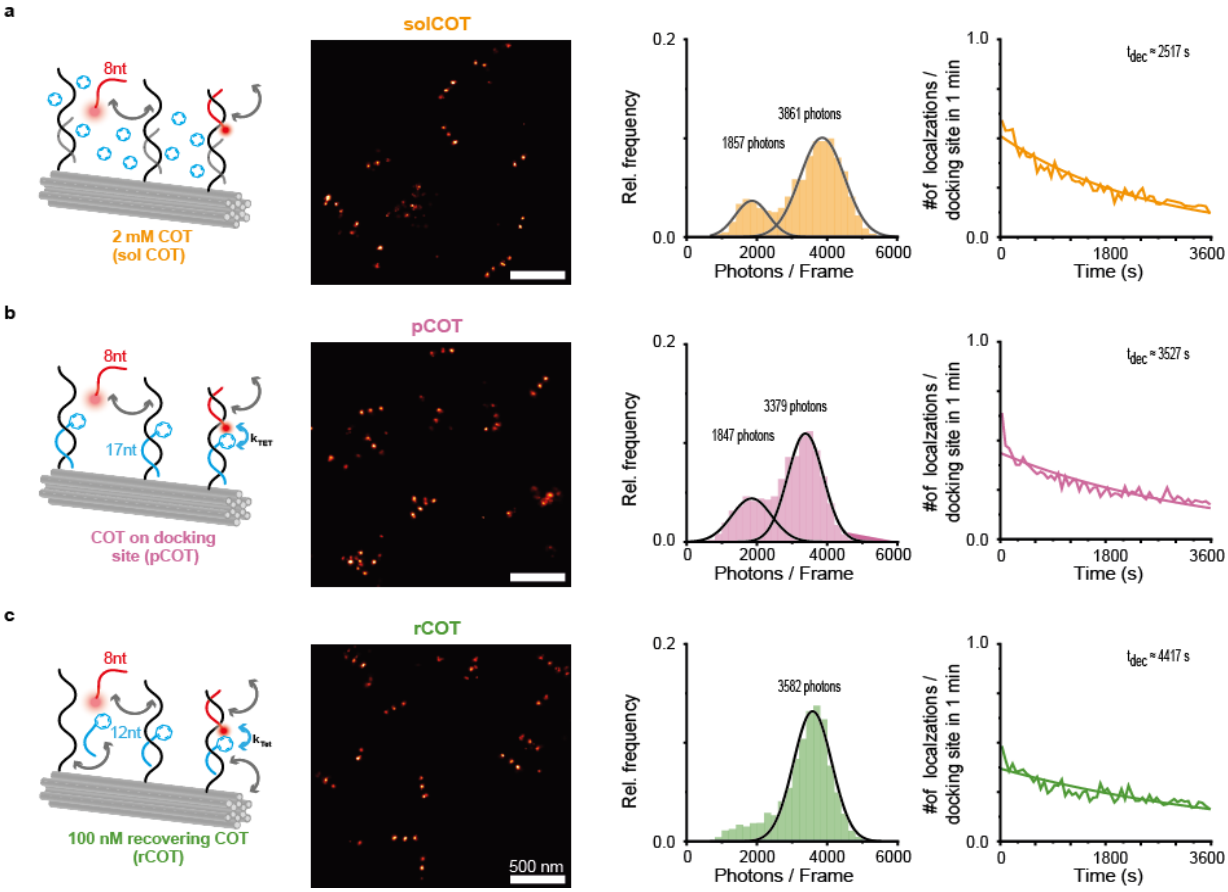

Figure S14. DNA-PAINT with solution-based photostabilization or DNA mediated photostabilization using COT and Cy5 under high illumination power (1.0 kW/cm^2) in the presence of oxygen. Exemplary reconstructed DNA-PAINT images of 3x1 12HB nanorulers, brightness values of picked DNA docking sites and detected localizations per docking site over time obtained with **(a)** 2 mM COT solution-based photostabilization, **(b)** a permanent DNA mediated photostabilization (21 nt binding sequence) and **(c)** a self-regenerating DNA mediated 10 nt self-regenerating COT label, respectively.

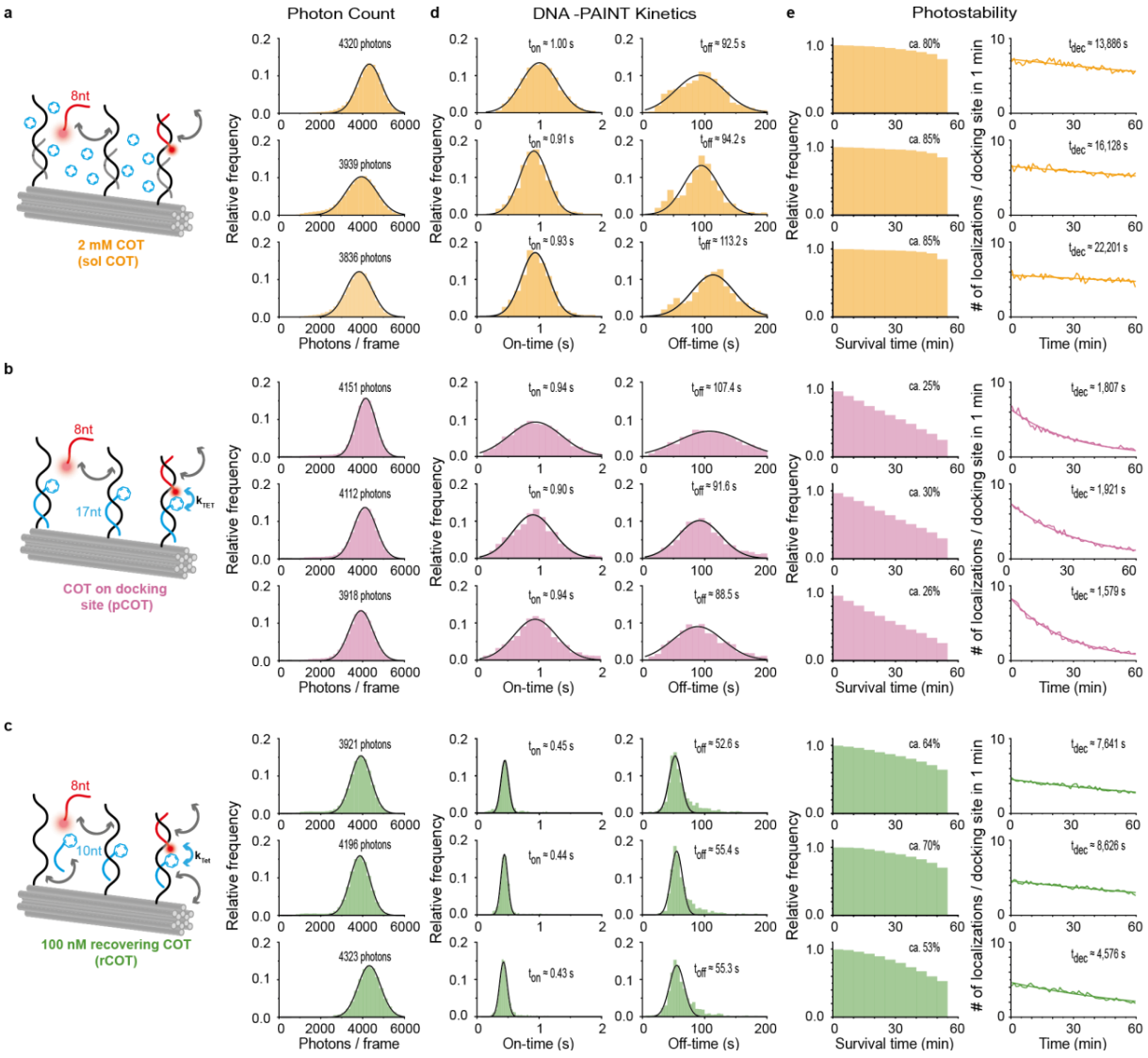

Figure S15. Triplicates and DNA-PAINT pick statistics with Cy5 and solution-based photostabilization vs. DNA mediated photostabilization under high illumination power (1.0 kW/cm^2). **a)** Scheme of DNA-PAINT with 2 mM COT in solution (solCOT) and obtained photon counts for three individual measurements. **b)** Scheme of DNA-PAINT with a permanent COT label (17 nt, pCOT) on the docking site and obtained photon counts for three individual measurements. **c)** Scheme of DNA-PAINT with a fastly recovering COT label (10 nt, rCOT) on the docking site and obtained photon counts for three individual measurements. **d)** DNA-PAINT kinetics, i.e. on- and off-times, for individual DNA-PAINT docking sites. **e)** Observed photostability of DNA-PAINT docking sites over 60 min.

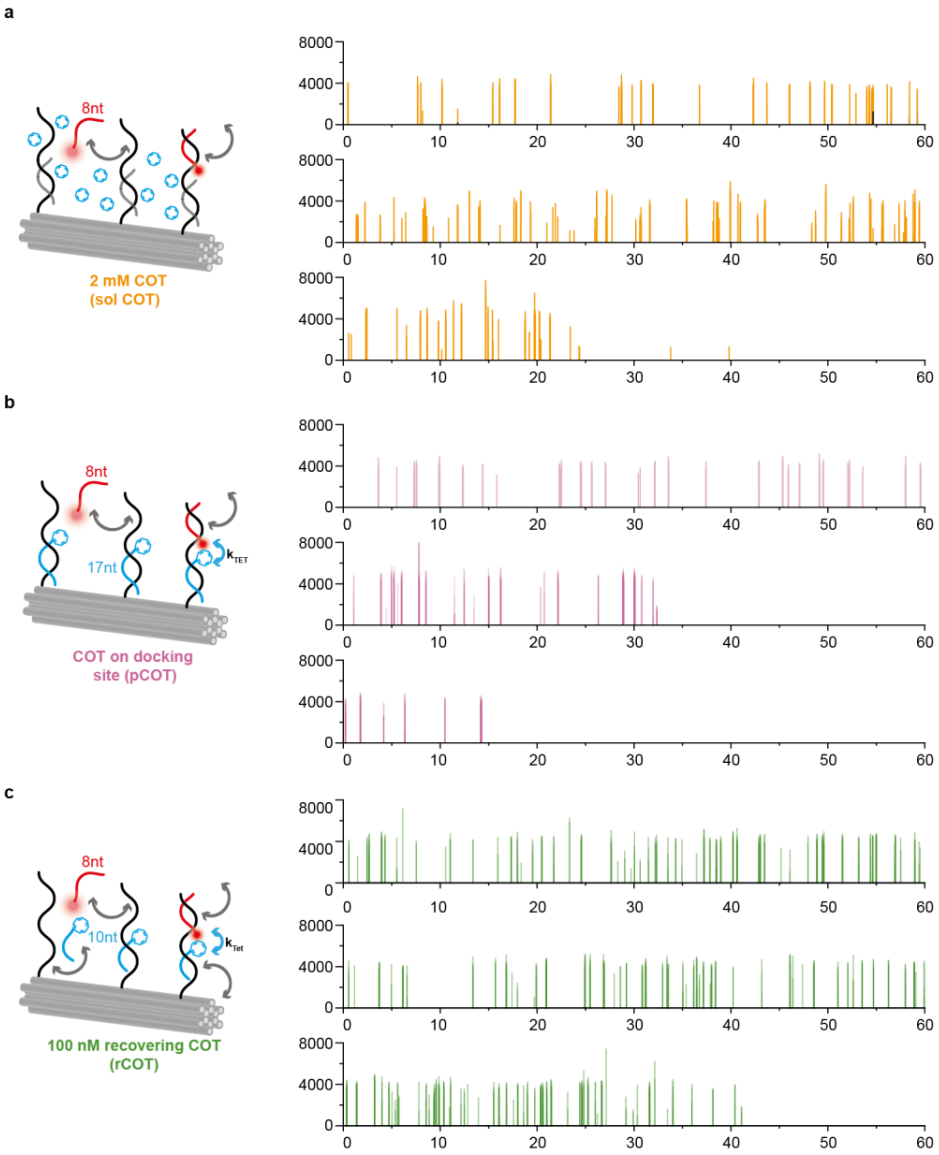

Figure S16. Exemplary single-molecule trajectories of individual DNA-PAINT docking sites with 2 mM COT in solution (**a**), with a permanent COT label on the docking site (**b**) and with a fastly recovering COT label on the docking site (c).

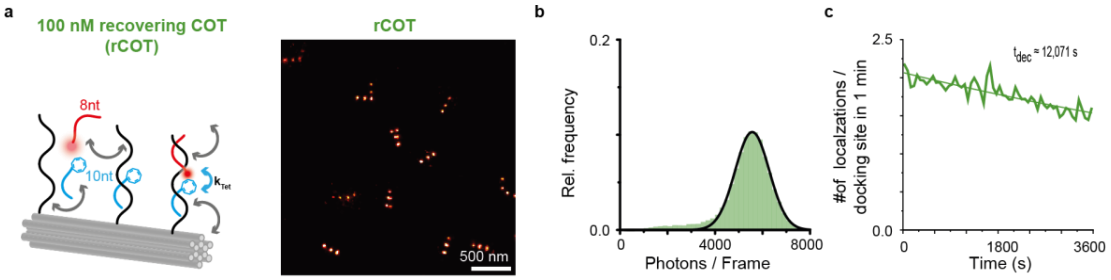

Figure S17. DNA-PAINT with Cy5B imager and fastly recovering COT on the docking site under high illumination power (1.0 kW/cm^2). **a)** Scheme of DNA-PAINT with rCOT and Cy5B and obtained DNA-PAINT image after 60 min. **b)** Obtained photon counts for DNA-PAINT with Cy5B and rCOT. **c)** Observed photostability of DNA-PAINT docking sites over 60 min with Cy5B and rCOT.

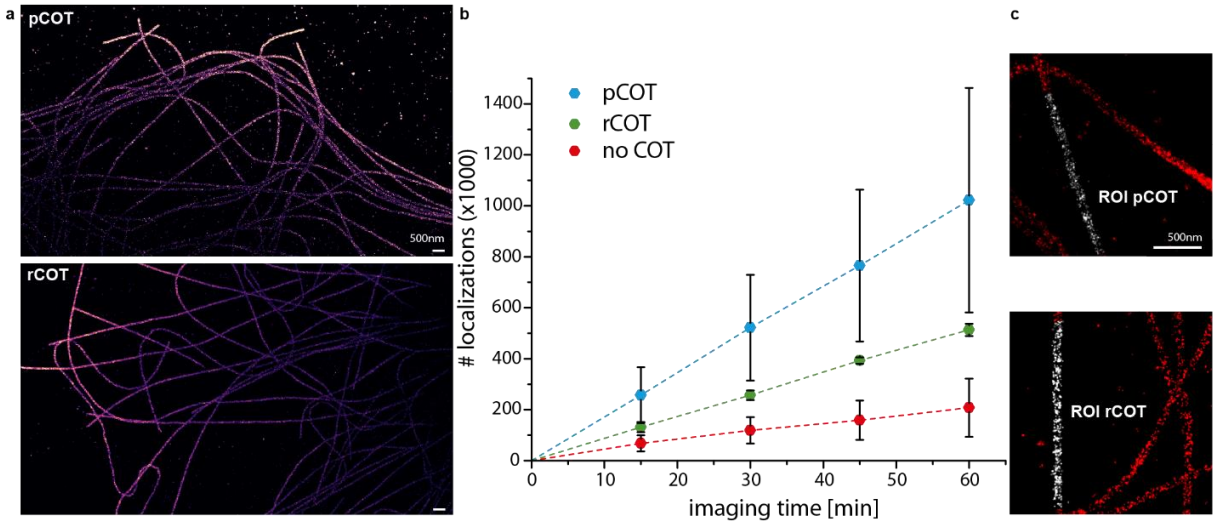

Figure S18. Comparison of permanent COT to recovering COT during 60 min imaging under ambient oxygen conditions. **a)** Overview zoom-in of two representative regions in the sample. **b)** Development of localizations over time for all three conditions. **c)** Exemplary ROIs from which the number of localizations was determined.

Appendix

Table S8. Unmodified staple strands of 12HB DNA origami. Sequences are denoted from 5'- to 3'-end. The numbers for the 5'- end 3'-end of the staples represent the helix number in the corresponding caDNAno file. Number in brackets represent the starting and ending position of the staple in the corresponding helix.

Unmodified staple strands	5'-end	3'-end
AAAGGGCGCTGGCAAGTATTGGC	11[681]	10[668]
GCGCCTGAATGCCAACGGCCCAGCCTCCCGCGTGCCTGTTCTTCTTTTT	7[42]	8[25]
TTGACGGGGAAAGCTTCACCAGAAATGGCATCACT	11[651]	6[658]
CATTCAACCCAAAATGTAGAACCCTCATGAATTAGTACAACC	9[147]	5[160]
TCAGAGGTGTGTCGGCCAGAATGAGTGCACTCTGTGGT	4[60]	7[62]
GGCATAAGCGTCTTCGAGGAAACGCA	8[466]	9[482]
TACATAAATTCTGGGCACTAACAACT	8[634]	9[650]
CAATCCAAAATACTGAACAGTAG	3[457]	10[458]
CATAGTTAATTTGTAAATGTCGC	3[541]	10[542]
GAACAAGAGTCCACCAATTTTTTAGTTGTCGTAGG	11[483]	6[490]
TTGAAGCCCTTTTTAAGAAAAGT	7[441]	7[463]
AAGCACAGAGCCTAATTATTGTTAGCGATTAAGACTCCTT	7[464]	8[448]
GATGTTTTTCTTTTCACCA	10[289]	11[302]
GGTCACGCCAGCACAGGAGTTAG	3[373]	10[374]
TGAACAGCTTGATACCGATAGTT	8[363]	8[341]
AAAATTCCATTCAGGCTTTTGCAAAA	8[256]	9[272]
TCCCATCCTAATGAGAATAACAT	0[496]	0[474]
ATCAGCGGGGTCAGCTTTCAGAG	3[56]	3[78]
TTCGCTATTCGCAAGACAAAGTTAATTTCATCTTC	5[539]	4[546]
TTGAGAATATCTTTCCTTATCACTCATCGAGAACA	5[497]	4[504]
GGGCGTGAAATATTAGCGCCATTCGC	8[130]	9[146]
GGCGCCCCGCCGAATCCTGAGAAGTGAGGCCGATTAAAGG	3[667]	0[665]
TTTTTTGTTTAATAAAGTAATTC	3[476]	3[498]
AAATCAGCCAGTAATAACACTATTTTTGAAGCCTTAAATC	7[506]	8[490]
AGCACTAAATCGGATCGTATTTAGACTTATATCTG	11[609]	6[616]
GGTGCCGTCGAGAGGGTTGATAT	8[405]	8[383]
GTCAGAATCAGGCAGGATTCGCG	3[205]	10[206]
TTTTTTATAACGTGCTTTCCTCTTTATAACAGTACTAT	2[698]	3[678]
AGACGGGAGAATTGACGGAAATT	0[454]	0[432]
TAAGCCAGAGAGCCAGAAGGAAACTCGATAGCCGAACAAA	4[480]	7[482]
CGCCTGACGGTAGAAAGATTCTAATGCAGATACAT	5[245]	4[252]
CAGTCTTGATTTTAAGAACTCAACGTTGCGTAT	0[263]	11[272]
CATAGAATTTGCGGTTTGAAAGAGGA	8[298]	9[314]

GCGCAGCGACCAGCGATTATATATCATCGCCTGAT	5[287]	4[294]
TTTTTAAAAACGCTCATGGAAATA	8[698]	8[679]
AATCAGTTAAAACGTGGGAGAAA	3[121]	10[122]
AGACAACCTGAACAGTATTCGAC	3[625]	10[626]
TTTGCAACCAGCTTACGGCGGTGGTGAGGTTTCAGTTGAGGATCCTTTTT	3[25]	10[29]
TGCAACACTATCATAACCCTCGT	7[231]	7[253]
AACGAACCTCCCGACTTGCGGGA	8[531]	8[509]
CCGAACGGTGTACAGACCAGGCG	8[321]	8[299]
ATTCAAGGGGAAGGTAAATGTGGCAAATAAATC	0[431]	11[440]
GTCACCAGTACAAGGTTGAGGCA	3[350]	3[372]
TAAATCGGTTGGTGCACATCAAAAATAA	6[153]	2[140]
AGACGGCGAACGTGGCGAG	10[667]	11[680]
CCCTTCATATAAAAGAACGTAGAGCCTTAAAGGTGAATTA	11[429]	0[413]
AACTTTAATCATGGGTAGCAACG	3[266]	3[288]
ACCATCACCCAAATAAACAGTTCATTTGATTCGCC	11[567]	6[574]
TGCCTAATGAGTGAGAAAAGCTCATATGTAGCTGA	11[147]	6[154]
TTTTTTGGTAATGGGTAACCATCCCACTTTTT	1[21]	2[25]
GGAGCAGCCACCACCCTTCGCATAACGACAATGACAACAA	7[338]	8[322]
AAAAGTGTCAGCAACAATTGCAGGCGCT	6[69]	2[56]
GGTTTGCGCATTTTAACGCGAGGCGT	8[508]	9[524]
AAAAGAATAGCCCGATACATACGCAGTAAGCTATC	11[441]	6[448]
TTTCACGAGAATGACCATTTTCATTTGGTCAATAACCTGT	7[212]	8[196]
TCGGTCATACCGGGGGTTTCTGC	8[69]	8[47]
CCTCCGAAATCGGCAAAAT	10[415]	11[428]
TTCCATTGACCCAAAGAGGCTTTGAGGA	2[307]	3[307]
ACGCGTCGGCTGTAAGACGACGACAATA	2[517]	3[517]
GTCCGTCCTGCAAGATCGTCGGATTCTCTTCGCATTGGACGA	9[105]	5[118]
GTCAGTCGTTTAACGAGATGGCAATTCA	6[615]	2[602]
GAGCTTAAGAGGTCCCAATTCTGCAATTCCATATAACAGT	4[228]	7[230]
GCAGCACTTTGCTCTGAGCCGGGTCACTGTTGCCCTGCGGCTTTTT	10[48]	0[21]
TACCTGGTTTGCCCCAGCA	10[373]	11[386]
AATGCTGTAGCTGAGAAAGGCCG	4[209]	4[187]
CTATATTAAAGAACGTGGA	10[499]	11[512]
CGGTAGTACTCAATCCGCTGCTGGTCATGGTC	0[53]	11[62]
CTTGAAAACACCCTAACGGCATA	3[247]	10[248]
AAGTAAGAGCCGCCAGTACCAGGCGG	8[382]	9[398]
AAAAGATAGGGTTGAGTGT	10[457]	11[470]
TTCGCCATAAACTCTGGAGGTGTCCAGC	2[55]	3[55]

AGGGCGAAAAACCGATTTAACGTAGGGCAAATACC	11[525]	6[532]
CCCACATGTGAGTGAATAACTGATGCTTTTAACCTCCGGC	11[555]	0[539]
TTTTTAGGAGCGGGCGCTAGGAAGGGAAGAAAGCGAATTTTT	10[702]	11[702]
TGCCATACATAAAGATTAACTGAACACCAACAGCCGGAATAG	9[441]	5[454]
TTTTTCCGGTGCAGCACCGATCCCTTACACTTGCC	5[29]	4[52]
ACAGCTGATTGCCCGTCGCTGCGCCCACACGTTGA	11[315]	6[322]
ATTAAAATAAGTGCGACGATTGGCCTTG	2[391]	3[391]
AAAACGAAAGAGGCTCATTATAC	0[286]	0[264]
TGTCCAAGTACCAGAAACCCCAG	3[499]	10[500]
TTACCAATAAGGCTTGCAGTGCGGAAGTTTAGACTGGATA	7[254]	8[238]
TTAGTGTGAATCCCTCTAATAAAACGAAAGAACGATGAATTA	9[231]	5[244]
ATCAGAGCCTTTAACGGGGTCTTAATGCCCCCTGC	5[371]	4[378]
TTACCTCTTAGCAAATTTCAACCGATTG	6[447]	2[434]
AAAACGGAATACCCAAAAGAACT	8[489]	8[467]
GTCCACGCGCCACCTCACCGTTGAAACA	11[364]	6[364]
TTTTTATCCAGCGCAGTGTCACTGC	7[21]	7[41]
GATGAATAAATCCTGTAGGTGAGGCGGTAGCGTAAGTCCTCA	9[609]	5[622]
GCTAAATCGGTTTGACTATTATA	3[182]	3[204]
CAGCTTTGAATACCAAGTTACAA	7[567]	7[589]
GGTTGCTTTGACGAGCACGTTTTT	3[679]	3[698]
CATGCCAGTGAGCGCTAATATCCAATAATAAGAGC	5[455]	4[462]
TATGCATTACAGAGGATGGTTTAATTTC	2[265]	3[265]
ACTGCCCGCTTTCCTGAAAAGCTATATTTTAAATA	11[189]	6[196]
TGATTTAGAAAACTCAAGAGTCAATAGT	6[573]	2[560]
TGGGCGCCAGGGTGATTCATTAGAGTAACCTGCTC	11[273]	6[280]
TGCAACTCAAAAGGCCGTACCAAAAACA	6[195]	2[182]
AAATAGGTAATTTACAAATAAGAAACGA	2[475]	3[475]
TGTTCCAACGCTAACGAACAAGTCAGCAGGGAAGCGCATT	11[471]	0[455]
GTGCCTGCTTTAAACAGGGAGAGAGTTTCAAAGCGAACCA	11[219]	0[203]
GTTTGATGGTGGTTCAGAACCCCGCCTCACAGAAT	11[399]	6[406]
TCACCGTCACCGGCGCAGTCTCT	0[412]	0[390]
AGACGTCGTCACCCTCAGATCTTGACGCTGGCTGACCTTC	7[296]	8[280]
TTTAGCAAACGCCACAATATAACTATATTCCCTTATAAATGG	9[525]	5[538]
AGCGTATCATTCCACAGACCCGCCACAGTTGCAGCAAGCG	0[347]	11[363]
GTATGTGAAATTGTTATCC	10[79]	11[92]
CCGAACTTTAATAAAAGCAAAGCGGATT	2[223]	3[223]
GTGAGTTAAAGGCCGCTGACACTCATGAAGGCACCAACCT	11[303]	0[287]
GCGCCCGCACCCTCTCGAGGTGAATT	8[340]	9[356]

ACAGTTTTTCAGATTTCAATTACCGTCGCAGAGGCGAATT	4[606]	7[608]
TTTAGAACGCGAATTACTAGAAAACTATAAACACCGGAAT	4[564]	7[566]
TGACCTAAATTTTTAAACCAAGT	4[545]	4[523]
TAAAGAGGCAAAATATTTTATAA	3[163]	10[164]
GTTTACCGCGCCCAATAGCAAGC	7[483]	7[505]
TACCGGGATAGCAATGAATATAT	3[331]	10[332]
AAATTGTGTCGAGAATACCACAT	4[293]	4[271]
AAATGCGTTATACAAATTCTTAC	8[573]	8[551]
CAGATATAGGCTTGAACAGACGTTAGTAAAGCCCAAAAATTT	9[315]	5[328]
TAAGATCTGTAAATCGTTGTTAATTGTAAAGCCAACGCTC	7[548]	8[532]
CATTCTATCAGGGCGATGG	10[541]	11[554]
CTCCAATTTAGGCAGAGACAATCAATCAAGAAAAATAATA	11[513]	0[497]
GAGACAAAGATTATCAGGTCATTGACGAGAGATCTACAAA	4[186]	7[188]
AGGGACAAAATCTTCCAGCGCCAAAGAC	2[433]	3[433]
AAAATTTTTAAAATGAGCAAAAGAA	8[592]	9[608]
CATCGGGAGAAATTCAAATATAT	4[587]	4[565]
ATCATTTACATAAAAGTATCAAAATTATAAGAAACTTCAATA	9[567]	5[580]
GCTACGACAGCAACTAAAAACCG	3[289]	10[290]
TTAGGTTGGGTTATAGATAAGTC	0[538]	0[516]
TATTGCCTTTAGCGTCAGACTGT	7[399]	7[421]
TTTTTCCGGGTACCGAGCTCGAATTCGTAATCTGGTCA	11[29]	10[49]
CTAAAGACTTTTAGGAACCCATG	3[308]	3[330]
GTGGAACGACGGGCTCTCAACTT	3[79]	10[80]
TCAGGTGAAATTTCTACGGAAACAATCG	6[111]	2[98]
AAGACGCTGAGACCAGAAGGAGC	3[560]	3[582]
AGCAGTCGGGAAACCTGTC	10[205]	11[218]
AACAACATGTTCATCCTTGAAAA	3[518]	3[540]
ATAATGAATCCTGAGATTACGAGCATGTGACAAAAACTTATT	9[483]	5[496]
GAGGTAACGTTATTAATTTTAAAACAAATAATGGAAGGGT	11[597]	0[581]
ACCGCATTCCAACGGTATTCTAAGCGAGATATAGAAGGCT	4[522]	7[524]
CAGCATCAACCGCACGGCGGGCCGTT	8[46]	9[62]
GCTCAAGTTGGGTAACGGGCGGAAAAATTTGTGAGAGATA	11[93]	0[77]
GGAATCGGAACATTGCACGTTAA	3[583]	10[584]
ATAAGAAGCCACCCAAACTTGAGCCATTATCAATACATCAGT	9[399]	5[412]
GGCGACACCACCCTCAGGTTGTACTGTACCGTTCCAGTAA	11[387]	0[371]
CATGTCAGAGATTTGATGTGAATTACCT	6[279]	2[266]
AATAGCTGTCACACGCAACGGTACGCCAGCGCTTAATGTAGTA	9[651]	5[664]
GCAGCACCGTAAGTGCCCGTATA	4[419]	4[397]

ATGAATCCCAGTCACGATCGAACGTGCCGGCCAGAGCACA	7[86]	8[70]
TATGTGATAAATAAGGCGTTAAA	7[525]	7[547]
TTAATGAATCGGCCATTCATTCCAATACGCATAGT	11[231]	6[238]
ATTCTTTTCATAATCAAAATCAC	8[447]	8[425]
AATCGTTGAGTAACATTGGAATTACCTAATTACATTTAAC	7[590]	8[574]
ATTTTGCCAGAGGGGGTAATAGT	8[279]	8[257]
AGCGCCACCACGGAATACGCCTCAGACCAGAGCCACCACC	7[422]	8[406]
AAAAAAGGCAGCCTTTACAATCTTACCAGTTTG	0[473]	11[482]
TAATCGTAGCATTACCTGAGAGTCTG	8[172]	9[188]
CAAGTGCTGAGTAAGAAAATAAATCCTC	6[405]	2[392]
GGCTAAAGTACGGTGTCTGGAAG	7[189]	7[211]
CCTACATACGTAGCGGCCAGCCATTGCAACAGGTTTTT	8[678]	9[698]
CTATTTCGGAACGAGTGAGAATA	4[377]	4[355]
TCAACATCAGTTAAATAGCGAGAGTGAGACGACGATAAAA	4[270]	7[272]
AATAACGCGCGGGGAGAGG	10[247]	11[260]
AAGAGATTCATTTTGTTTAAGAGGAAGC	6[237]	2[224]
CAAATGGTTCAGAAGAACGAGTAGAT	8[214]	9[230]
AAAAGGGCGACAATTATTTATCC	3[434]	3[456]
ATAGCTGTTTCCTGGAACGTCCATAACGCCGTAAA	11[63]	6[70]
TGTAGGGGATTTAGTAACACTGAGTTTC	2[349]	3[349]
AAAAATCTACGTGCGTTTTAATT	0[244]	0[222]
AGAGTTTATACCAGTAGCACCTGAAACCATCGATA	5[413]	4[420]
GTGTATTAAGAGGCTGAGACTCC	7[357]	7[379]
GAAGTCAACCCAAATGGCAAAAGAATACTCGGAACAGAATCC	9[273]	5[286]
CGGTTAACAAAGCTGCTGTAACAACAAGGACGTTGGGAAG	11[261]	0[245]
ACTACCTTTAAACGGGTAACAGGGAGACGGGCA	0[305]	11[314]
AATCCAAAAAAAAGGCTCCAAAA	7[315]	7[337]
GAGAGCCTCAGAACCGCATTTTCTGTAACGATCTAAAGTT	11[345]	0[329]
AAATCCCCGAAACAATTCATGAGGAAGT	6[321]	2[308]
TACCTAATATCAAAATCATTCAATATTACGTGA	0[557]	11[566]
GTATACAGGTAATGTGTAGGTAGTCAAATCACCAT	5[161]	4[168]
AACGTTGTAGAAACAGCGGATAGTTGGGCGGTTGT	5[77]	4[84]
GTTTATGTCACATGGGAATCCAC	3[415]	10[416]
ATATTCACAAACAAATTCATATG	3[392]	3[414]
GACCGGAAGCAATTGCGGGAGAA	0[202]	0[180]
TCAAGCAGAACCACCACTCACTCAGGTAGCCCGGAATAGG	7[380]	8[364]
AGCCTCCCCAGGGTCCGGCAAACGCG	8[88]	9[104]
TTCATTTTCTGCTAAACAACTGAACAACTAAAGGA	5[329]	4[336]

TCGTTCACCGCCTGGCCCT	10[331]	11[344]
CGGAAGCACGCAAACTTATTAGCGTT	8[424]	9[440]
GAGCAAGGTGGCATTTACTCCAACAGGTTCTTTACGTCAACA	9[189]	5[202]
ATTGCGAATAATGTACAACGGAG	4[335]	4[313]
CTTTTTTTCGTCTCGTCGCTGGC	8[111]	8[89]
GACCGTCGAACGGGGAAGCTAATGCAGA	6[531]	2[518]
GCGTCATACATGCCCTCATAGTT	0[370]	0[348]
GAAAGTTCAACAATCAGCTTGCTTAGCTTTAATTGTATCG	4[354]	7[356]
TGTAAATCATGCTCCTTTTGATAATTGCTGAATAT	5[203]	4[210]
TTCACCTAGCGTGGCGGGTGAAGGGATACCAGTGCATAAAAA	9[63]	5[76]
ATTTGCCAAGCGGAACTGACCAACGAGTCAATCATAAGGG	4[312]	7[314]
TAGAACCTACCAGTCTGAGAGAC	0[580]	0[558]
GGGTTACCTGCAGCCAGCGGTGTTTTT	4[51]	4[29]
GAATTATCCAATAACGATAGCTTAGATT	2[559]	3[559]
TTGTCGTCTTTCTACGTAATGCC	0[328]	0[306]
ACTACTTAGCCGGAACGAGGCGC	7[273]	7[295]
TTTTTGTCCATCACGCAAATTCCGAGTAAAAGAGTCTTTTTT	4[702]	5[702]
TTTTTCGGGAGCTAAACAGGTTGTTAGAATCAGAGTTTTT	0[694]	1[694]
AATCATAATAACCCGGCGTCAAAAATGA	6[489]	2[476]
AGCAAGCCGTTTAAGAATTGAGT	4[503]	4[481]
AACAGAGTGCCTGGGGTTTTGCTCACAGAAGGATTAGGAT	4[396]	7[398]
CCAGCCAAACTTCTGATTGCCGTTTTGGGTAAAGTTAAAC	4[102]	7[104]
TGAAATTGTTTCAGGGAACTACAACGCC	6[363]	2[350]
GCCCGCACAGGCGGCCTTTAGTG	7[63]	7[85]
CAGTAAGAACCTTGAGCCTGTTTAGT	8[550]	9[566]
ACCAAATTACCAGGTCATAGCCCCGAGTTTTCATCGGCAT	4[438]	7[440]
TCTTATACTCAGAAAGGCTTTTGATGATATTGACACGCTATT	9[357]	5[370]
GCCTTATACCCTGTAATACCAATTCTTGCGCTC	0[179]	11[188]
TTTTTGCGTCCGTGCCTGCATCAGACGTTTTT	9[25]	6[21]
TTATGGCCTGAGCACCTCAGAGCATAAA	2[181]	3[181]
CGAGCACAGACTTCAAATACCTCAAAAGCTGCA	0[221]	11[230]
GCATCAAAAAGAAGTAAATTGGG	3[224]	3[246]
TAAGTAGAAGAACTCAAACTATCG	7[651]	7[673]
ATTTGGCAAATCAACAGTTGAAA	7[609]	7[631]
GTTGAAACAAACATCAAGAAAAC	8[615]	8[593]
GAATTGTAGCCAGAATGGATCAGAGCAAATCCT	0[389]	11[398]
GCTTGACCATTAGATACATTTCG	8[237]	8[215]
CTGAAAACCTGTTTATCAAACATGTAACGTCAA	0[515]	11[524]

GACTTTCTCCGTGGCGCGGTTG	0[76]	0[54]
ACACAACATACGAGGGATGTGGCTATTAATCGGCC	11[105]	6[112]
TTTTTAACAATATTACCGTCGCTGGTAATATCCAGTTTTT	6[694]	7[694]
TGCCTGAACAGCAAATGAATGCGCGAACT	6[657]	2[644]
CAAATATCAAACCAGATGAATAT	4[629]	4[607]
CAATATGATATTGATGGGCGCAT	4[167]	4[145]
TTCTGGAATAATCCTGATTTTGCCCGGCCGTAA	0[599]	11[608]
TTAACAAGAGAATCGATGAACGG	8[195]	8[173]
GGGCCGGAAGCATAAAGTG	10[121]	11[134]
GTTTGAGGGGACCTCATTTGCCG	4[125]	4[103]
GTATTAGAGCCGTCAATAGATAA	8[657]	8[635]
GCTAATGCCGGAGAGGGTAGCTA	7[147]	7[169]
TACTTCTTTGATAAAAATCTAAA	4[671]	4[649]
GAAAGATCGCACTCCAGCCAGCT	7[105]	7[127]
TCAGGCTGCGCAACTGTTGGGAA	8[153]	8[131]
ATACCCTTCGTGCCACGCTGAACCTTGCTGAACCT	5[623]	4[630]
CATAATATTCCGTAATGGGATCCGTGCATCTGCCA	5[119]	4[126]
TTTTTATCCAATAAATCTCTACCCCGGTAAAACTAGCATG	7[170]	8[154]
CCGATAATAAAAGGGACTTAACACCGCGAACCACCAGCAG	11[639]	0[623]
CATCAGCGTCTGGCCTTCCACAGGAACCTGGGG	0[137]	11[146]
GGAATAACAGAGATAGACATACAAACTTGAGGATTTAGAA	7[632]	8[616]
CCGGAAGACGTACAGCGCCGCGATTACAATTCC	0[95]	11[104]
TTCGCGGATTGATTGCTCATTTTTTAAC	2[139]	3[139]
TAAAGGATTGTATAAGCGCACAAACGACATTAAATGTGAG	11[135]	0[119]
GATAAAAATTTTTAGCCAGCTTT	0[160]	0[138]
GATAGTGCAACATGATATTTTTGAATGG	2[643]	3[643]
GGATAACCTCACAATTTTTGTTA	3[98]	3[120]
TCAATAATAAAGTGTATCATCATATTCC	2[601]	3[601]
CAATAGGAACGCAAATTAAGCAA	3[140]	3[162]
GCGAAAGACGCAAAGCCGCCACGGGAAC	2[97]	3[97]
TTCCGAATTGTAAACGTGTCGCCAGCATCGGTGCGGGCCT	7[128]	8[112]
ACATCATTTAAATTGCGTAGAAACAGTACCTTTTA	5[581]	4[588]
AAGATAAAACAGTTGGATTATAC	0[622]	0[600]
AACACCCTAAAGGGAGCCC	10[625]	11[638]
GCATCGAGCCAGATATCTTTAGGACCTGAGGAAGGTTATC	4[648]	7[650]
CGTAAAGGTCACGAAACCAGGCAATAGCACCGCTTCTGGT	4[144]	7[146]
CGAGTAACAACCGTTTACCAGTC	0[118]	0[96]
GCCTTACGCTGCGCGTAAAATTATTTTTTGACGCTCAATC	7[674]	8[658]

CCGAACCCCCTAAAACATCGACCAGTTTAGAGC	0[641]	11[650]
TGCGTACTAATAGTAGTTGAAATGCATATTTCAACGCAAG	11[177]	0[161]
GATTTTAGACAGGCATTAAAAATA	0[664]	0[642]
TGATTATCAGATATACGTGGCAC	3[602]	3[624]
TGGCAAGTTTTTTGGGGTC	10[583]	11[596]
TCAGCTAACTCACATTAAT	10[163]	11[176]
CTATTAGTCTTTCGCCGCTACAG	3[644]	3[666]
AACGCCAAAAGGCGGATGGCTTA	4[251]	4[229]
AAGAAACAATGACCGGAAACGTC	4[461]	4[439]
GTACATCGACATCGTTAACGGCA	4[83]	4[61]
ATACCACCATCAGTGAGGCCAAACCGTTGTAGCAA	5[665]	4[672]

Biotinylated staple strands	**5'-end**	**3'-end**
AACGCCAAAAGGCGGATGGCTTA	4[251]	4[229]
AAGAAACAATGACCGGAAACGTC	4[461]	4[439]
GTACATCGACATCGTTAACGGCA	4[83]	4[61]
ATACCACCATCAGTGAGGCCAAACCGTTGTAGCAA	5[665]	4[672]

References

1 Schueder, F. *et al.* An order of magnitude faster DNA-PAINT imaging by optimized sequence design and buffer conditions. *Nature Methods* **16**, 1101-1104 (2019). https://doi.org:10.1038/s41592-019-0584-7

2 Strauss, S. & Jungmann, R. Up to 100-fold speed-up and multiplexing in optimized DNA-PAINT. *Nature Methods* **17**, 789-791 (2020). https://doi.org:10.1038/s41592-020-0869-x

3 Cordes, T., Vogelsang, J. & Tinnefeld, P. On the mechanism of Trolox as antiblinking and antibleaching reagent. *J Am Chem Soc* **131**, 5018-5019 (2009). https://doi.org:10.1021/ja809117z

4 Zhang, L. *et al.* Linker Molecules Convert Commercial Fluorophores into Tailored Functional Probes during Biolabelling. *Angewandte Chemie International Edition* **61**, e202112959 (2022). https://doi.org:https://doi.org/10.1002/anie.202112959

5 Kümmerlin, M., Mazumder, A. & Kapanidis, A. N. Bleaching-resistant, Near-continuous Single-molecule Fluorescence and FRET Based on Fluorogenic and Transient DNA Binding. *ChemPhysChem* **24**, e202300175 (2023). https://doi.org:https://doi.org/10.1002/cphc.202300175

6 Edelstein, A., Amodaj, N., Hoover, K., Vale, R. & Stuurman, N. Computer Control of Microscopes Using μManager. *Current Protocols in Molecular Biology* **92**, 14.20.11-14.20.17 (2010). https://doi.org:10.1002/0471142727.mb1420s92

7 Edelstein, A. D. *et al.* Advanced methods of microscope control using μManager software. *JBM* **1** (2014). https://doi.org:10.14440/jbm.2014.36

11.2 Associated Publication 2

A silicon rhodamine-fused glibenclamide to label and detect malaria-infected red blood cells

Claudia Bastl*, Cindy Close*, Ingo Holtz*, Blaise Gatin-Fraudet, Mareike Eis, Michelle Werum1, Smilla Konrad, Kilian Roßmann, Christiane Huhn, Souvik Ghosh, Julia Ast, Dorien A. Roosen, Martin Lehmann, Volker Haucke, Luc Reymond, David J. Hodson, Philip Tinnefeld, Kai Johnsson, Viktorija Glembockyte, Nicole Kilian, Johannes Broichhagen

*equal contribution

Preprint on bioRxiv 2025/637098 (2025).
doi: https://doi.org/10.1101/2025.02.07.637098

A silicon rhodamine-fused glibenclamide to label and detect malaria-infected red blood cells

Claudia Bastl[1,†], Cindy M. Close[2,†], Ingo Holtz[1,†], Blaise Gatin-Fraudet[3], Mareike Eis[1], Michelle Werum[1], Smilla Konrad[1], Kilian Roßmann[3], Christiane Huhn[3], Souvik Ghosh[3], Julia Ast[4], Dorien A. Roosen[5], Martin Lehmann[3], Volker Haucke[5], Luc Reymond[6,7], David J. Hodson[4,8], Philip Tinnefeld[2], Kai Johnsson[6,9], Viktorija Glembockyte[2*], Nicole Kilian[10,11,*], Johannes Broichhagen[3,6,9,*]

Affiliations

[1] Centre for Infectious Diseases, Parasitology Heidelberg University Hospital, Im Neuenheimer Feld 324, 69120 Heidelberg, Germany.

[2] Department of Chemistry and Center for NanoScience (CeNS), Ludwig-Maximilians-University, Butenandtstraße 5–13, 81377 Munich, Germany.

[3] Leibniz-Forschungsinstitut für Molekulare Pharmakologie, Robert-Rössle-Straße 10, 13125 Berlin, Germany.

[4] Institute of Metabolism and Systems Research (IMSR), and Centre of Membrane Proteins and Receptors (COMPARE), University of Birmingham, Birmingham, UK.

[5] Department of Molecular Pharmacology and Cell Biology, Leibniz-Forschungsinstitut für Molekulare Pharmakologie, Robert-Rössle-Straße 10, 13125 Berlin, Germany.

[6] Laboratory of Protein Engineering, Institut des Sciences et Ingénierie Chimiques, Sciences de Base, École Polytechnique Fédérale Lausanne, Avenue Forel 2, 1015 Lausanne, Switzerland.

[7] Present address: Biomolecular Screening Facility, École Polytechnique Fédérale Lausanne, Avenue Forel 2, 1015 Lausanne, Switzerland.

[8] Oxford Centre for Diabetes, Endocrinology and Metabolism (OCDEM), NIHR Oxford Biomedical Research Centre, Churchill Hospital, Radcliffe Department of Medicine, University of Oxford, Oxford, UK.

[9] Department of Chemical Biology, Max Planck Institute for Medical Research, Jahnstr. 29, 69120 Heidelberg, Germany.

[10] Department of Biological Sciences, California State University, Chico, USA, 400 W. First St.

Chico, CA 95929–515, USA.

[11] Department of Medical Biochemistry, Faculty of Basic Medical Sciences, Delta State University, P.M.B. 1 Abraka Delta State, Nigeria.

†Equal contribution
*Correspondence should be addressed to:
Viktorija.Glembockyte@cup.lmu.de, nrkilian@csuchico.edu, broichhagen@fmp-berlin.de

Keywords
Silicon Rhodamine; Red Blood Cells; Malaria; *Plasmodium falciparum*; Smartphone-Based Detection

Abstract
The malaria parasite *Plasmodium falciparum* affects the lives of millions of people worldwide every year. The detection of replicating parasites within human red blood cells is of paramount importance, requiring appropriate diagnostic tools. Herein, we design and apply a silicon rhodamine-fused glibenclamide (**SiR-glib**). We first test this far-red fluorescent, fluorogenic and endoplasmic reticulum-targeting sulfonylurea in mammalian cells and pancreatic tissues, before characterizing its labeling performance in red blood cells infected with the asexual developmental stages of *Plasmodium falciparum*. We further combine **SiR-glib** with a portable smartphone-based microscope to easily and rapidly identify parasitized red blood cells, providing proof of principle for diagnostic use in rural endemic areas without major healthcare facilities.

Introduction

The latest World Malaria Report published by the World Health Organization (WHO) in December 2022 recorded 247 million malaria associated clinical cases and 619,000 deaths[1]. Malaria tropica, the major and most dangerous form of human malaria, is caused by the protozoan parasite *Plasmodium falciparum (P. falciparum*) and is responsible for maternal illness, low birth weight and patient deaths in endemic areas[1–3].

Detection of *P. falciparum* is important to initiate the appropriate anti-malarial therapy, especially in the field where access to healthcare facilities, electricity and transportation might be restricted[1,4]. We therefore started with the premise that mature human red blood cells (RBCs), which serve as a host cell during the parasite's asexual reproduction (erythrocytic schizogony), do not contain any organellar structures (i.e. they are anuclear) (**Figure 1A**). *P. falciparum*, on the other hand, contains cell organelles that i) are found in other eukaryotic cells (e.g. endoplasmic reticulum, Golgi apparatus, nucleus); and ii) are specialized, such as the apicoplast and the digestive vacuole. The parasite interacts and reorganizes the cell organelle-deprived host RBCs to acquire nutrients, ultimately maturing from a young ring to a trophozoite and finally to a schizont stage within approximately 48 hours[5–7].

We focused our investigation on the cell organelles of the parasite that may be visualized via fluorescence microscopy with small molecule chemical biology probes[8]. Potential candidates such as ER trackers Green/Red (λ_{ex} = 504 nm or 588 nm), which comprise glibenclamide-BODIPY targeting the sulfonylurea receptor 1, are of limited use as they fall into the same spectral window as (non)-oxygenated hemoglobin (Hb and HbO_2) (**Figure 1B**). Far-red and near-infrared fluorophores are well-suited to use in RBC's, since blood displays an optical window between 600–800 nm where absorbance and hence background fluorescence is low.[9] We therefore decided to design an ER tracker using silicon rhodamine (SiR) as a fluorogenic far-red dye, chemically fused it with glibenclamide and named it **SiR-glib**. The probe was applied across different imaging contexts to stain the ER in live mammalian cells and tissue, and in infected RBCs (iRBCs). To detect infected stages, we used a home-built, cheap smartphone-based microscope[10], which bears the potential for malaria diagnostic applications in endemic areas that have poor access to healthcare facilities and electricity.

Results

We set out to conjugate far-red silicon rhodamine (SiR)[11], a dye previously used in RBCs for actin staining[12], to the sulfonylurea glibenclamide[13], which targets SUR1 expressed on the endoplasmic reticulum (ER). The synthesis starts by activating 5-chloro-2-methoxy-3-

nitrobenzoic acid (**1**) using TSTU and forming a peptide bond with 4-(2-aminoethyl)benzenesulfonamide to obtain sulfonamide **2** in 81% yield (**Scheme 1**). Using cyclohexyl isocyanate in acetone with K_2CO_3 serving as a base, the sulfonylurea motif of **3** was installed in quantitative yield. Reduction of the nitro group using zinc and acetic acid in methanol progressed in 90% yield, and the corresponding aniline **4** was endowed with a 6-carbon atom long linker. To address the rather unreactive aniline, we first formed an acyl chloride *in situ* by stirring Fmoc-Ahx-OH in neat $SOCl_2$. After evaporation of all volatiles and reuptake in DIPEA containing 1,4-dioxanes, the acyl chloride was added to a solution of **4**. The solvents were evaporated, and the crude material containing **5** taken up in DMF with 5% piperidine to deprotect the Fmoc group, allowing the isolation of alkyl amine **6** in 17% yield over this synthetic sequence. Finally, we obtained a fluorogenic (**Figure 2A**) silicon rhodamine-fused glibenclamide, termed **SiR-glib**, in 42% yield after HPLC purification by using NHS-activated ester of silicon rhodamine. We first confirmed the expected spectral properties ($\lambda_{ex}/\lambda_{em}$ = 653/673 nm) (**Figure 2B**) of **SiR-glib**, and tested its fluorogenicity and pH-sensitivity. **SiR-glib** displayed a 10.0-fold fluorescence increase when SDS was added to the buffer medium (**Figure 2B**), and a trend to decreased emission at more acidic pH values (**Figure 2C**). This is warranted because iRBCs maintain a physiological pH while the digestive vacuole, which is responsible for hemoglobin digestion and storage of hemozoin has been shown to exhibit a drop in pH to ~ 5.2 (ref[14,15]).

Next, we set out to determine the performance of **SiR-glib** in live cell imaging by incubating HeLa cells with 5 µM ER tracker green and 50 µM **SiR-glib**, before imaging by confocal fluorescence microscopy (**Figure 2D**). By merging the images, we found good co-localization between ER tracker green and **SiR-glib**, showcasing accurate targeting of the ER by **SiR-glib**. While immortalized cell lines can also be marked with fluorescent proteins containing appropriate targeting sequences (e.g., Sec61[16]), genetic engineering is more difficult in primary cells, let alone in parasites or even patient samples. Accordingly, we compared ER tracker green and **SiR-glib** in primary mouse astrocytes, and were able to acquire similar staining patterns.

Since glibenclamide targets the sulfonylurea receptor 1 (SUR1), which is retained at the ER in the absence of Kir6.2, we decided to test **SiR-glib** in cells that express both SUR1 and Kir6.2. We reasoned that in cells with both subunits- i.e. those that express K_{ATP} channels- staining should be seen within the cell (ER, SUR1) and at the membrane (SUR1 + Kir6.2 octamer i.e. KATP channel).[17] Islets of Langerhans were thus incubated with 100 nM of the fluorescent beta cell marker LUXendin551[18] and 50 µM **SiR-glib**, before confocal live

imaging. **SiR-glib** staining was seen both within the cell (SUR1) as well as at the cell membrane (SUR1 + Kir6.2), further demonstrating specificity of the probe.

Encouraged by this, we applied **SiR-glib** to *in vitro* cultures of *P. falciparum*-iRBCs. We chose two standard laboratory model strains for our investigations, 3D7 (clone of NF54, originating from an airport malaria case) and FCR3 (originating from Gambia)[19–22]. *In vitro* cultures were infected with *P. falciparum* and incubated with either 2 µM **SiR-glib**, 2 µM SiR or remained untreated for 1 h at 37 °C at 5% hematocrit (HCT, volume percentage of RBCs in the human body or in this case, in the in vitro culture). Investigation by confocal laser scanning microscopy revealed distinct labeling of all developmental stages (i.e., ring, trophozoite and schizont) of 3D7 (**Figure 3A**) and FCR3 (**Figure 3B**) *P. falciparum* laboratory strains. More specifically, a punctuate signal was observed in ring stages, whereas in trophozoite and schizont stages a line or circle near or around the digestive vacuole, respectively, was eminent (**Figure 3A, B**). We quantified the fluorescence signal of iRBCs and observed significant differences between **SiR-glib**-, SiR- or non-treated controls of 3D7 (**Figure 3C**) and FCR3 (**Figure 3D**). These results show that the glibenclamide scaffold is needed for successful organellar targeting and yields an 11.5-fold (3D7) and 8.0-fold (FCR3) increase in fluorescence signal in all stages of iRBCs. To test if the parasites may be properly labeled in a higher hematocrit, we prepared a 40% HCT culture and inoculated it with the *P. falciparum* lab strains 3D7 and FCR3. This is particularly important because HCT of human blood for females and males ranges from 36–48% and 40–54%, respectively[23]. After allowing the parasites to adapt and replicate for 48 h, the culture was incubated with **SiR-glib** and SiR as before, or kept untreated for 1 h at 37 °C. Again, successful labeling of the different developmental stages with **SiR-glib** was observed, which differed from the control treatments of the two *P. falciparum* cultures (**Figure 3E, F**). While a loss in fluorescence signal was observed in samples containing ring stages, the overall fluorescence increases for all stages in the infected samples remained significantly high (9.6-fold for 3D7 and 4.2-fold for FCR3). These experiments highlight the sensitivity of **SiR-glib** in dilute samples, as well as in whole blood model systems.

Finally, we were wondering if **SiR-glib** could potentially be used to label *P. falciparum* in point-of-care diagnostic settings in endemic areas[4]. Therefore, the treatment of the *in vitro* cultures was adjusted: the concentration of **SiR-glib** was increased from 2 µM to 50 µM, the incubation time was shortened from 1 h to 10 min and the incubation temperature was lowered to room temperature instead of 37 °C. With this new protocol, we still observed significant differences between the **SiR-glib**-treated samples and untreated controls (**Supporting Figure**

S1) Notably, we verified our measurements at different developmental stages of the parasite in comparison to uninfected RBCs.

These results gave confidence to try **SiR-glib** in a potential diagnostic setup to be used in malaria endemic areas. As such, we turned to a battery-powered, portable smartphone-based microscope which uses a 180 mW 635 nm pen laser for excitation at a ~45° angle, a smartphone as a camera and an 8-USD objective lens[10]. This setup is affordable, easy to assemble and was previously used for detection of single nucleic acid targets with the help of DNA origami nanoantennas[10]. The excitation wavelength of the device is similar to wavelengths of other malaria testing devices that have been used to detect the malaria pigment hemozoin[24,25], and we wondered if **SiR-glib** may enhance the hemozoin-based detection of *P. falciparum*.

To get a first idea of the detection power of the smartphone microscope, we prepared uninfected RBCs and magnetically purified *P. falciparum* (FCR3 and 3D7) iRBCs with mature developmental stages, since these contain a larger amount of hemozoin. Both, RBCs and iRBCS were treated with 2 µM SiR-glib for 1 h. Afterwards, cells were washed and deposited between a glass slide and a glass coverslip to be investigated with the portable smartphone microscope versus untreated controls (**Figure 4A, B**). Videos were exported to single images of unbiased, different regions on which background subtraction was applied. Accordingly, the percentage of pixels above background threshold was counted. In vehicle-treated samples, we obtained images for uninfected, 3D7- and FCR3-iRBCs (**Figure 4C**), and after counting the pixels above threshold, we could not differentiate between non-infected and the 3D7 infected strain. Presumably due to higher auto-fluorescence stemming from the parasite, the FCR3-infected samples showed a significantly higher fluorescence, and could be clearly distinguished (**Figure 4D**). We performed the experiments in **SiR-glib** treated cells (**Figure 4E**) and found that 3D7-infected RBCs could now be significantly distinguished from non-infected cells (**Figure 4F**). FCR3 showed a comparable value to vehicle-treated controls, suggesting that the autofluorescence is either masking the **SiR-glib** signal, or that the staining protocol is less effective. In any case, the iRBCs showed significantly more pixels above the threshold and could thus be confirmed to carry the parasite.

Discussion

In this study, we demonstrate that **SiR-glib** specifically labels malaria-causing *P. falciparum* parasites in iRBCs, especially at the difficult to detect young ring stages. By optimizing the labelling protocol, we show that **SiR-glib** is able to identify parasite-containing RBCs within just 10 minutes. Lastly**, SiR-glib** is compatible with highly-portable smartphone-based

microscopes, which can be deployed in areas without access to healthcare facilities and/or electricity, and with minimal training. As such, **SiR-glib** potentially provides a one-reagent point-of-care diagnostic that might be useful to identify and prioritize individuals with active malarial infection. Our successful approach pairing **SiR-glib** with an affordable and portable smartphone-based microscope creates a simple battery-powered, easy to apply diagnostic procedure that can be used at any location, with a first example of using this device on a cellular setting. The macro we provide for analysis can be run using FIJI (ImageJ), which is open source, without excessive training. While we acknowledge our diagnostic approach is currently not as fast as standard procedures used in malaria endemic areas[1], this study marks a first step towards an alternative with high potential. For this reason, additional *P. falciparum* strains from endemic areas[26] and other human-pathogenic *Plasmodium* species (such as *P. vivax*)[5] need to be investigated and carefully compared.

Several diagnostic approaches utilize the hemozoin pigment to identify the parasite in patient blood[4,15,27]. However, the peripheral blood of malaria tropica patients exclusively contains ring stages and a few mature stage V gametocytes of *P. falciparum*. Only the latter developmental stage contains a high amount of hemozoin and is meant to be picked up by the *Anopheles* mosquito for sexual reproduction in the midgut. Ring stages are the most prominent developmental stage in the blood of a patient infected with *P. falciparum* and their hemozoin concentration is very low. Mature developmental stages of *P. falciparum* that contain a well-detectable amount of hemozoin, trophozoites and schizonts, sequester within the patients' organs only appear within the peripheral blood after a splenectomy or when the patient is close to death. Interestingly, other human-pathogenic *Plasmodium* species do not sequester and all developmental stages of the parasite can be found in the peripheral blood of the patient. This important difference in parasite biology is used as one of the diagnostic criteria to determine which type of malaria the patient is suffering from.

The majority of diagnostic centers and rural diagnostic setups therefore still apply standard methods, which have been used for decades[1]. One of these methods is the Giemsa staining of thick or thin blood smears. Thick blood smears are usually used to determine the presence of a pathogenic organism while thin blood smears identify the (*Plasmodium*) species and the parasitemia (% parasitemia = (parasitized RBCs/total RBCs) × 100). Rapid Giemsa staining in a 10% solution is a procedure which takes up 10-15 min without taking the preparation of the blood film and the subsequent microscopic investigation by trained personnel into account[1]. Slow Giemsa staining using a 3% solution takes 45-60 min for the staining time only. For rapid diagnostic tests (RDTs), several kits are available for the detection of different

antigens of *Plasmodium* species. These tests are mostly based on immunochromatography and are sold in cassette or dipstick format. Depending on the exact method, RDTs provide results in about 20 min[28] and can be performed by trained personnel or the patient themselves. However, the recommended storage temperature for most RDTs is 4 °C, which requires refrigeration facilities that can limit take up in more rural (and tropical locations). The fact that **SiR-glib** can be stored and applied above room temperature for a long time and is easy to use are important requirements for the usage of the dye in a diagnostic field setting.

Experimental Section

Materials

Human blood and serum were obtained from the blood bank in Mannheim (Germany). If not otherwise indicated materials were obtained from: Gibco, c. c. pro GmbH, Thermo Fisher Scientific GmbH, Sigma-Aldrich, AppliChem, Carl-Roth GmbH & Co. KG, VWR Chemicals, Neofroxx GmbH and Serva. Chemicals were purchased from commercial vendors (Aldrich, TCI, Acros, etc.) and have been used without further purification.

Synthesis of SiR-glib

Details on synthesis and chemical characterization are outlined in the Supporting Information.

Mouse islet isolation and labeling

Male 8- to 12-week-old C57BL6 were socially housed in specific-pathogen free conditions under a 12 hour light-dark cycle, relative humidity 55 ± 10% and temperature 21 ± 2 °C. with ad libitum access to food and water. Animals were culled using a schedule-1 method and 1 mg/mL collagenase NB 8 (Serva) injected into the common bile duct, before digestion of the dissected pancreas in a water bath at 37 °C for 12 min with mild shaking. Islets were separated using gradient centrifugation in Histopaque-1119 and 1083 (Sigma-Aldrich). Islets were cultured in RPMI 1640 supplemented with 10% fetal bovine serum (FBS, Gibco), 100 units/mL penicillin, and 100 µg/mL streptomycin (Sigma-Aldrich), at 37 °C and 5% CO_2.

Islets were incubated with 50 uM **SiR-glib** and 100 nM **LUXendin551** in complete medium for 1 hour at 37 °C and 5% CO_2, before washing three times and imaging using a Zeiss LSM780 confocal microscope equipped with C-Apochromat 40x/1.20 W Korr M27 objective. Excitation and emission wavelengths for **SiR-glib** and **LUXendin551** were λex = 633 nm / λem = 639 – 692 nm and λex = 561 nm / λem = 571 – 649 nm, respectively. Animal studies were regulated by the Animals (Scientific Procedures) Act 1986 of the U.K. (Personal Project Licences P2ABC3A83 and PP1778740). Approval was granted by the University of Birmingham and University of Oxford Animal Welfare and Ethical Review Bodies (AWERB).

Parasite strains

For this study the *P. falciparum* clones 3D7 and FCR3 were used. Both strains are laboratory model strains and regularly investigated in malaria research[19,29,30]. 3D7 is the limiting dilution clonal variant of the NF54 isolate[20]. NF54 was originally isolated from a malaria patient living near Amsterdam Airport Schiphol (so-called airport malaria) [21]. The origin of the NF54 clone

remains unknown. FCR3 was first isolated in Gambia and is a particularly dangerous strain for pregnant women[31].

Parasite culture

Parasites were kept in RPMI 1640 cell culture medium with 25 mM and HEPES *L*-glutamine (Gibco). The medium was supplemented with heat-inactivated type A+ human serum (5% (v/v)), AlbuMAX I (5% (v/v), Thermo Fisher Scientific GmbH), 20 µg/ml gentamycin (stock: 50 mg/ml, c. c. pro GmbH), 0.2 mM hypoxanthin (stock: 10 mM; c. c. pro GmbH). For our experiments the parasites were grown in culture with a hematocrit (HCT, volume percentage of RBC) of either 5% or 40%. A HCT of 5% is standard in cell culture, while a HCT of 40% is comparable to the HCT in the human body[23]. The *P. falciparum* 5% HCT cultures are maintained in 10 cm cell culture plates. 40% HCT cultures are kept in 6-well plates to avoid excess usage of RBC. The cultures are incubated in a cell culture incubation cabinet at 37 °C (CO_2: 2.9%; O_2: 5.8%; rH: 93%). The parasitemia of the *P. falciparum* cultures are assessed every day via thin methanol-fixed and Giemsa-stained blood smear[4]. The parasitemia of the culture was kept between 3-5%.

SiR-glib labeling of infected RBCs from a 5% HCT culture

200 µL of a 5% hematocrit culture are required for **SiR-glib** labeling. The 200 µL are placed in a 1.5-ml reaction tube and centrifuged at 1,800 rpm for 30 seconds. The supernatant is discarded. Two washing steps each with 500 µL of cell culture medium and centrifugation for 30 seconds at 1,800 rpm are performed afterwards. The RBC pellet which remained after the second washing step is resuspended in 200 µL of cell culture medium supplemented with 2 µM **SiR-glib** or SiR (concentration of both stock solutions is 3.2 mM in DMSO). RBC which remained untreated were resuspended in 200 µL of cell culture medium. The cells are transferred to a 96-well microtiter plate, with one batch being divided into 2 wells so that each well contains approximately 100 µL. The cells are then incubated for 1 hour at 37 °C. Afterwards, RBC were washed twice with 500 µL of cell culture medium and centrifugation for 30 seconds at 1,800 rpm. The pelleted RBC are resuspended in 500 µL of cell culture medium and are now ready for microscopy. The sample is pipetted into a custom-made imaging chamber and examined[14].

SiR-glib labeling of infected RBCs from a 40% HCT culture

The same principle is used as for labeling a 40% HCT culture but with 400 µL of resuspended parasites from our cultures, placed in a 1.5-ml reaction tube. The washing steps are performed with 200 µL of cell culture medium and at the end of the procedure the pellet is suspended in 200 µL of cell culture medium for imaging.

Short incubation of *P. falciparum*-infected RBCs with SiR-glib

For the short incubation with **SiR-glib**, two samples of 100 µL are taken from a 40% HCT culture. One sample is subsequently treated with **SiR-glib** and the other sample remains untreated as a negative control. The samples are centrifuged once at 1,800 rpm for 30 s. The supernatant is discarded and the pellet is resuspended in 100 µL RPMI cell culture medium supplemented with 50 µM **SiR-glib**. The pellet in the control sample is resuspended in 100 µL RPMI cell culture medium. The samples are incubated for 10 min at r.t. and immediately imaged.

Image acquisition and analyses of *P. falciparum*-infected RBCs

Images (1024 x 1024 px) were acquired with the Axiovert 100 M/Zeiss CLSM 510 with a C-Apochromat 63x/1.2W corr objective. Samples were excited with the HeNe laser at a wavelength of 633 nm. The LP650 filter was used for the detection of the fluorescence. The fluorescence signal of parasitized and non-parasitized RBC is quantified with Fiji.

Sample preparation for measurements on the smartphone microscope

A battery-powered smartphone microscope, previously described by Trofymchuk, Glembockyte et al. was used to demonstrate the detection with low-cost optical equipment[8]. Microscope cover slides (22 mm × 22 mm and 76 x 26 mm, Carl Roth GmbH, Germany) were cleaned using Ethanol 70%, dried with Kimtech Wipes (Merck KgaA, Germany) and 30 min treatment in UV-Ozone cleaner (PSD-UV4, Novascan Technologies, USA) at 100 °C. Dust was removed with compressed air. To create a flow chamber, two stripes of double-sided tape (3M, Germany) were glued onto the long edges of the large slide and the small cover slip was then laid on top. Mature parasites were purified using the MACS system (Miltenyi Biotec) as previously described[29]. 200 µl of iRBC were centrifuged for 30 seconds at 1,800 rpm at RT. The supernatant was discarded and the sediment was washed twice with 500 µl cell culture medium, centrifuging each washing step 30 s at 1,800 rpm RT. For staining, 200 µl of 2 µM **SiR-glib** in medium were added to the sediment and incubated for 1 h at 37 °C. Afterwards the sample was washed twice with 500 µl cell medium, performing centrifugation steps after each

wash (30 s at 1,800 rpm, r.t.). For each sample, the sediment was diluted individually in medium to yield samples with similar blood cell concentration. The diluted blood sample was added to the chamber, which was sealed from one side with one Tough-Tag (Diversified Biotech) and closed with another from the other side.

Measurements and analysis on the smartphone

Inside the home-built box a 638 nm laser diode with output power 180 mW (0638L-11A, Integrated Optics, UAB, Lithuania, driven by a portable power bank) was focused onto the sample at a ~45° angle. After passing spectral filtering (BrightLine HC 731/137, Semrock Inc., USA), fluorescent signal was collected using an objective lens (NA = 0.25, LS-40166, UCTRONICS, USA) that guides the light to the monochrome camera of the smartphone (P20, Huawei, China). Movies were recorded via FreeDCam application (Troopii) and analyzed with ImageJ (Fiji). After file conversion with the FFMPEG plugin to .tif (32-bit), a home-written macro crops a defined region of interest in the video and calculates the area of pixels above a defined threshold. This threshold is individually set to the intensity value that is above the highest pixel intensities detected in the uninfected sample (100 for samples without dye, 120 with dye). The extracted data was analyzed using OriginPro2019, while the significance was determined using an ANOVA test.

Statistical analyses

Statistical analyses of acquired data were conducted with SigmaPlot 13.0 and OriginPro2019.

Image preparation and presentation

Microscopy images were prepared using Fiji.

Conflict of interest

DJH and JB receives licensing revenue from Celtarys Research for provision of chemical probes. DJH has filed patents related to type 1 diabetes and type 2 diabetes therapy, unrelated to the present study.

Acknowledgements

We thank Corentin Charbonnier, Jenny Eichhorst, and Ramona Birke (all FMP) for technical assistance. The authors would also like to thank Guillermo Gomez and Patrick Pitoniak for proofreading the manuscript. N. K. is grateful for Individual Funding from the Equal

Opportunity Office at Heidelberg University. V.G. gratefully acknowledges financial support from the DFG (grant number GL 1079/1-1, project number 503042693). P.T. gratefully acknowledges financial support from the DFG (INST 86/1904-1 FUGG, excellence clusters NIM and e-conversion), BMBF (Grants POCEMON, 13N14336, and SIBOF, 03VP03891), as well as the Bavarian Ministry of Science and the Arts through the ONE MUNICH Project "Munich Multiscale Biofabrication". This project has received funding from the European Union's Horizon Europe Framework Programme (deuterON, grant agreement no. 101042046 to JB). DJH. was supported by MRC (MR/S025618/1), Diabetes UK (17/0005681 and 22/0006389) and UKRI ERC Frontier Research Guarantee (EP/X026833/1) Grants. This work was supported on behalf of the "Steve Morgan Foundation Type 1 Diabetes Grand Challenge" by Diabetes UK and SMF (grant number 23/0006627 to DJH and JB). This project has received funding from the European Research Council (ERC) under the European Union's Horizon 2020 research and innovation programme (Starting Grant 715884 to DJH). This work was supported by grants from the European Research Council (ERC Advanced Grant 884281 "SynapseBuild" to VH) and the Deutsche Forschungsgemeinschaft (DFG, German Research Foundation; NeuroNex2/ HA2686/19-1 to VH). The research was funded by the National Institute for Health Research (NIHR) Oxford Biomedical Research Centre (BRC). The views expressed are those of the author(s) and not necessarily those of the NHS, the NIHR or the Department of Health. The project involves an element of animal work not funded by the NIHR but by another funder, as well as an element focused on patients and people appropriately funded by the NIHR.

AUTHOR CONTRIBUTION

Conceptualization and Methodology: LR, KJ, VG, NK, JB; Formal analysis and investigation: CB, CC, IH, BG-F, ME, MW, SK, KR, CH, SG, JA, DR, ML, DJH, VG, NK and JB; Writing –Original Draft: DJH, NK, and JB; Reviewing and Editing: all authors; Visualization: VG, NK and JB; Supervision: VH, PT, KJ, VG, NK and JB; Funding Acquisition: DJH, PT, VG, and JB.

Figures and Schemes

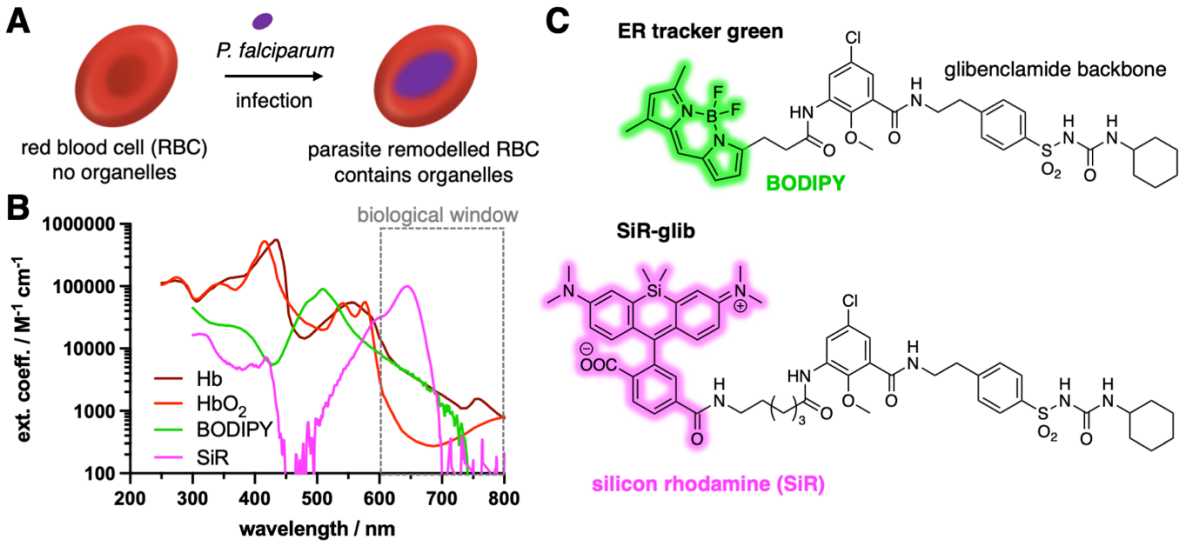

Figure 1. Silicon rhodamine-fused glibenclamide for the detection of *P. falciparum* infected red blood cells (RBCs). A) RBC do not contain any organelles, which changes through the infection by *P. falciparum* parasites due to remodeling and genesis of ER, nucleus, etc. **B**) High absorbance of oxygen free (Hb) and oxygen-bound hemoglobin (HbO_2) in the UV to green range might mask ER tracker green. Far-red silicon rhodamine falls into the biological imaging window above 600 nm. **C**) Chemical structure of glibenclamide and its fluorophore-linked congeners ER tracker green (BODIPY fused) and **SiR-glib** (SiR fused).

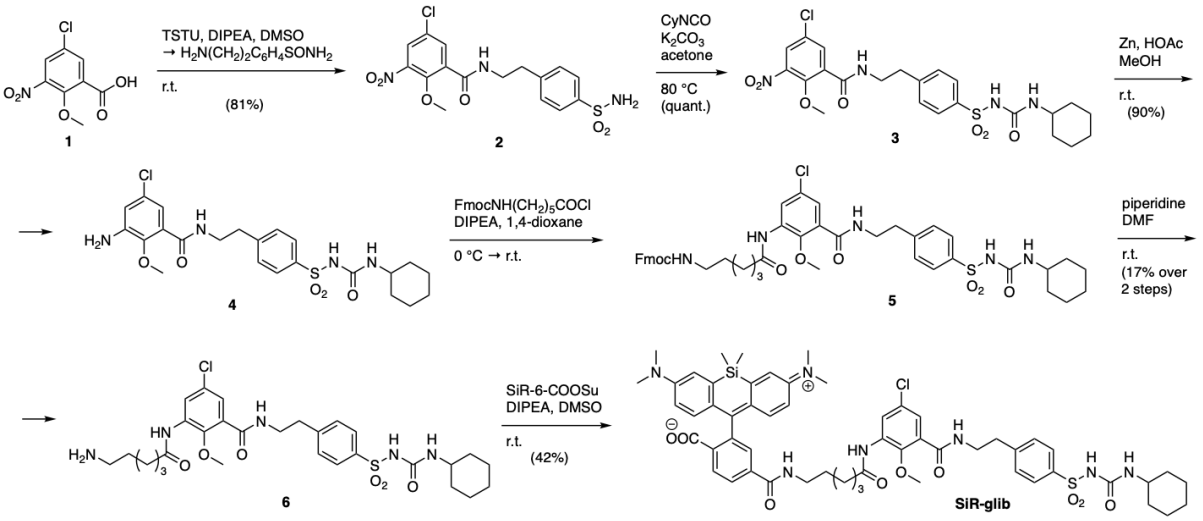

Scheme 1. Synthesis of SiR-glib. Commercially available benzoic acid **1** is peptide coupled after TSTU activation to obtain **2**, on which the sulfonylurea is installed using cyclohexyl isocyanate. Zn-mediated reduction of the nitro group yields aniline **4**, on which an alkyl amine linker is installed using an *in situ* formed acyl chloride before subsequent Fmoc-deprotection. Silicon rhodamine is finally fused onto **6** by using its NHS-activated ester, yielding **SiR-glib**.

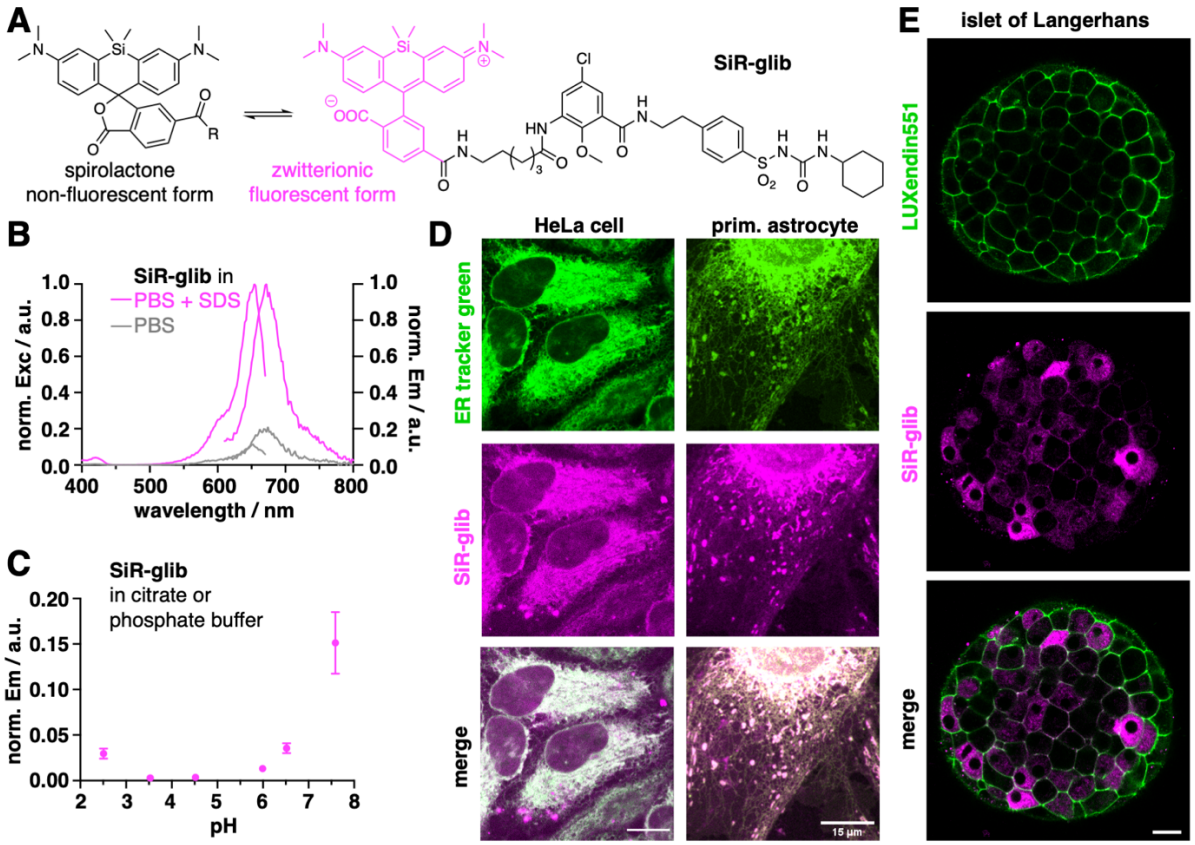

Figure 2. Characterization of SiR-glib. A) SiR-glib may adopt two different isomeric forms, a non-fluorescent spirolactone and an open, fluorescent zwitterionic form. **B)** Excitation and emission spectra of **SiR-glib**, showcasing its fluorogenicity by addition of SDS. **C**) Fluorescence pH dependency of **SiR-glib**. **D**) Live cell imaging by confocal microscopy using ER tracker green and **SiR-glib** in live HeLa cells and live primary astrocytes. **E**) Live cell imaging by confocal microscopy beta-cell marker LUXendin551 and **SiR-glib** in live islets of Langerhans. **SiR-glib** gives rise to stained membrane structures, presumably due to KATP binding. Scale bars = 15 µm.

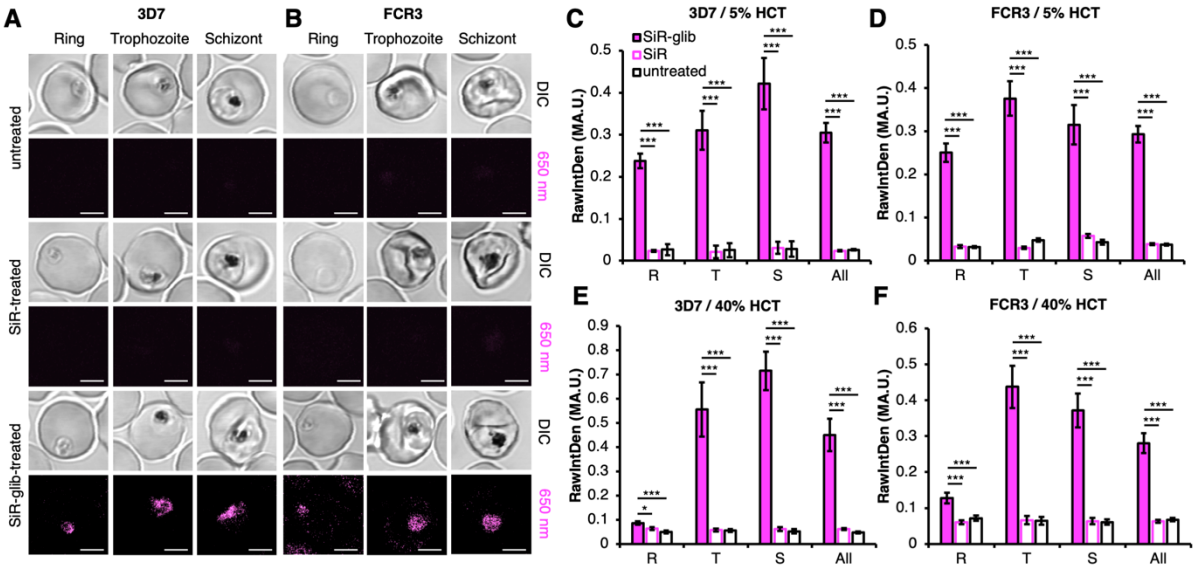

Figure 3. Labeling of two different *P. falciparum* strains with SiR-glib. A) The *P. falciparum* strain 3D7 was grown in a 5% HCT culture. Cells were labeled with 2 µM **SiR-glib**, 2 µM SiR or remained untreated for 1 h. Only **SiR-glib**-treated cells showed a specific labeling of the ring (R), trophozoite (T) and schizont (S) developmental stages of the parasite for both investigated strains. Signals of all stages are included (All). Scale bars = 3 µm. **B)** As for (**A**) but using the *P. falciparum* strain FCR3. **C, D)** Quantification of fluorescence from (A) and (B) reveals a significantly stronger fluorescence of **SiR-glib**-treated RBCs compared to using SiR or untreated RBCs in every developmental stage. N=3; n≥11. *: $p < 0.05$; **: $p < 0.01$; ***: $p < 0.001$. **E, F)** As for (**C**) and (**D**) but in a 40% HCT culture shows lower signal in ring stages when compared to 5% HCT. N=3; n≥12. *: $p < 0.05$; **: $p < 0.01$; ***: $p < 0.001$.

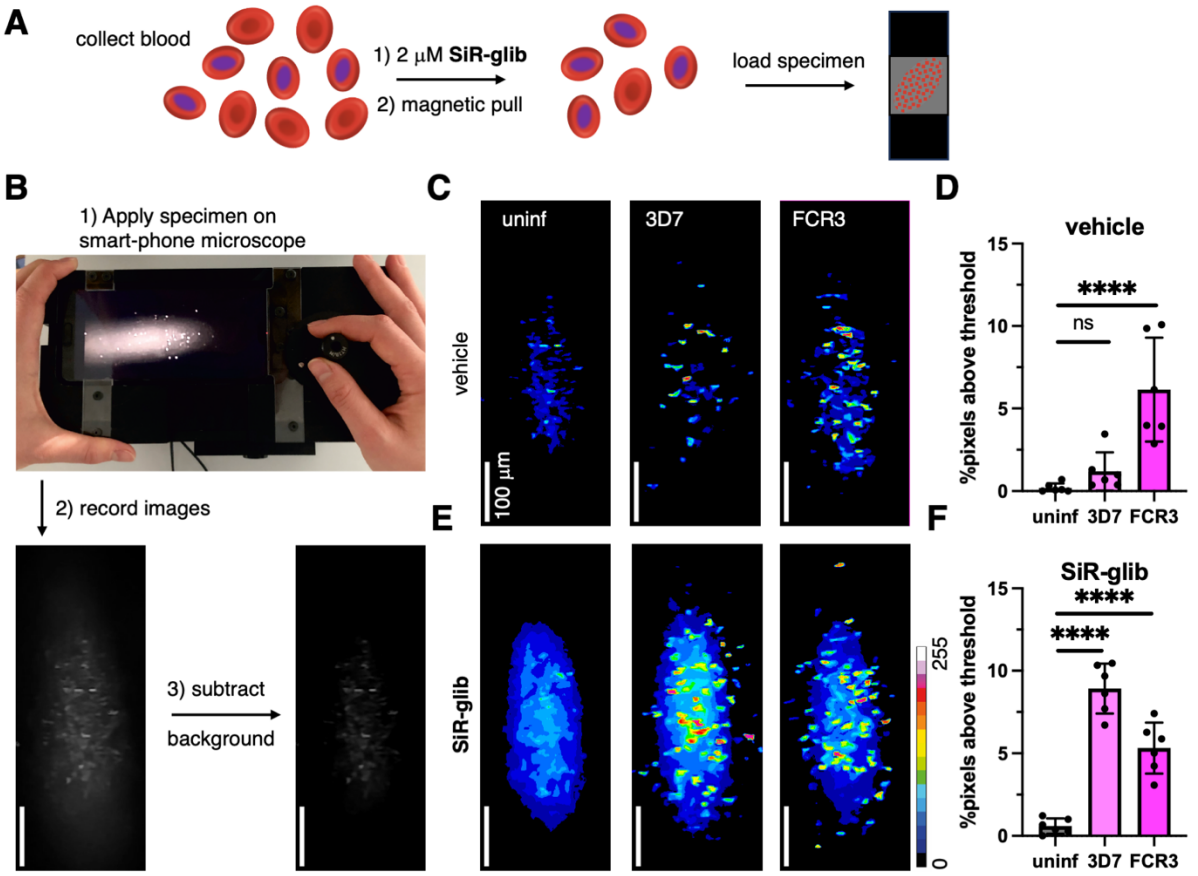

Figure 4. Imaging and analysis of *P. falciparum* infected RBCs using a portable smartphone-based microscope. A) Sample preparation for smart-phone based imaging. **B**) Workflow showing the mounted smartphone, image recording and background subtraction (photo reproduced from ref. [10]). **C**) Vehicle controls of uninfected and 3D7- or FCR3-infected RBCs. **D**) Analysis of vehicle-treated RBCs show a significant increase in pixels above threshold for FCR3-infected RBCs. **E**) As for (**C**) but **SiR-glib**-treated RBCs. **F**) Analysis of **SiR-glib**-treated RBCs show a significant increase in pixels above threshold for RBCs infected with both strains, also enabling the detection of the 3D7 strain.

References

[1] World Health Organization, *World malaria report* **2022**, Geneva. Licence: CC BY-NC-SA 3.0 IGO.
[2] M. E. Feeney, *Immunological Reviews* **2020**, *293*, 216–229.
[3] A. Calderaro, G. Piccolo, C. Gorrini, S. Rossi, S. Montecchini, M. L. Dell'Anna, F. De Conto, M. C. Medici, C. Chezzi, M. C. Arcangeletti, *Malar J* **2013**, *12*, 321.
[4] B. Gitta, N. Kilian, *BioEssays* **2020**, *42*, 1900138.
[5] R. Tuteja, *The FEBS Journal* **2007**, *274*, 4670–4679.
[6] M. Cyrklaff, C. P. Sanchez, N. Kilian, C. Bisseye, J. Simpore, F. Frischknecht, M. Lanzer, *Science* **2011**, *334*, 1283–1286.
[7] V. Bekić, N. Kilian, *BioEssays* **2023**, *45*, 2200241.
[8] J. Broichhagen, N. Kilian, *ChemBioChem* **2021**, *22*, 2219–2236.
[9] Q. Yu, N. Pourmandi, L. Xue, C. Gondrand, S. Fabritz, D. Bardy, L. Patiny, E. Katsyuba, J. Auwerx, K. Johnsson, *Nat Metab* **2019**, *1*, 1219–1225.
[10] K. Trofymchuk, V. Glembockyte, L. Grabenhorst, F. Steiner, C. Vietz, C. Close, M. Pfeiffer, L. Richter, M. L. Schütte, F. Selbach, R. Yaadav, J. Zähringer, Q. Wei, A. Ozcan, B. Lalkens, G. P. Acuna, P. Tinnefeld, *Nat Commun* **2021**, *12*, 950.
[11] G. Lukinavičius, K. Umezawa, N. Olivier, A. Honigmann, G. Yang, T. Plass, V. Mueller, L. Reymond, I. R. Corrêa Jr, Z.-G. Luo, C. Schultz, E. A. Lemke, P. Heppenstall, C. Eggeling, S. Manley, K. Johnsson, *Nat. Chem.* **2013**, *5*, 132–139.
[12] G. Lukinavičius, L. Reymond, E. D'Este, A. Masharina, F. Göttfert, H. Ta, A. Güther, M. Fournier, S. Rizzo, H. Waldmann, C. Blaukopf, C. Sommer, D. W. Gerlich, H.-D. Arndt, S. W. Hell, K. Johnsson, *Nat. Methods* **2014**, *11*, 731–733.
[13] J. Aittoniemi, C. Fotinou, T. J. Craig, H. De Wet, P. Proks, F. M. Ashcroft, *Phil. Trans. R. Soc. B* **2009**, *364*, 257–267.
[14] Y. Kuhn, P. Rohrbach, M. Lanzer, *Cell Microbiol* **2007**, *9*, 1004–1013.
[15] L. M. Coronado, C. T. Nadovich, C. Spadafora, *Biochimica et Biophysica Acta (BBA) - General Subjects* **2014**, *1840*, 2032–2041.
[16] W. Ma, C. Mayr, *Cell* **2018**, *175*, 1492-1506.e19.
[17] N. Inagaki, T. Gonoi, J. P. Clement, N. Namba, J. Inazawa, G. Gonzalez, L. Aguilar-Bryan, S. Seino, J. Bryan, *Science* **1995**, *270*, 1166–1170.
[18] J. Ast, A. N. Novak, T. Podewin, N. H. F. Fine, B. Jones, A. Tomas, R. Birke, K. Roßmann, B. Mathes, J. Eichhorst, M. Lehmann, A. K. Linnemann, D. J. Hodson, J. Broichhagen, *JACS Au* **2022**, *2*, 1007–1017.
[19] K. A. Moser, E. F. Drábek, A. Dwivedi, E. M. Stucke, J. Crabtree, A. Dara, Z. Shah, M. Adams, T. Li, P. T. Rodrigues, S. Koren, A. M. Phillippy, J. B. Munro, A. Ouattara, B. C. Sparklin, J. C. Dunning Hotopp, K. E. Lyke, L. Sadzewicz, L. J. Tallon, M. D. Spring, K. Jongsakul, C. Lon, D. L. Saunders, M. U. Ferreira, M. M. Nyunt, M. K. Laufer, M. A. Travassos, R. W. Sauerwein, S. Takala-Harrison, C. M. Fraser, B. K. L. Sim, S. L. Hoffman, C. V. Plowe, J. C. Silva, *Genome Med* **2020**, *12*, 6.
[20] V. Rosario, *Science* **1981**, *212*, 1037–1038.
[21] T. Ponnudurai, A. D. Leeuwenberg, J. H. Meuwissen, *Trop Geogr Med* **1981**, *33*, 50–54.
[22] N. Kilian, Y. Zhang, L. LaMonica, G. Hooker, D. Toomre, C. B. Mamoun, A. M. Ernst, *BioEssays* **2020**, *42*, 1900145.
[23] H. H. Billett, in *Clinical Methods: The History, Physical, and Laboratory Examinations* (Eds.: H.K. Walker, W.D. Hall, J.W. Hurst), Butterworths, Boston, **1990**.
[24] S. E. McBirney, D. Chen, A. Scholtz, H. Ameri, A. M. Armani, *ACS Sens.* **2018**, *3*, 1264–1270.

[25] O. Rifaie-Graham, J. Pollard, S. Raccio, S. Balog, S. Rusch, M. A. Hernández-Castañeda, P.-Y. Mantel, H.-P. Beck, N. Bruns, *Nat Commun* **2019**, *10*, 1369.
[26] P. Sondo, K. Derra, T. Lefevre, S. Diallo-Nakanabo, Z. Tarnagda, O. Zampa, A. Kazienga, I. Valea, H. Sorgho, J.-B. Ouedraogo, T. R. Guiguemde, H. Tinto, *Sci Rep* **2019**, *9*, 127.
[27] J. C. Niles, J. L. DeRisi, M. A. Marletta, *Proc. Natl. Acad. Sci. U.S.A.* **2009**, *106*, 13266–13271.
[28] J. Maltha, P. Gillet, J. Jacobs, *Clinical Microbiology and Infection* **2013**, *19*, 399–407.
[29] N. Kilian, S. Srismith, M. Dittmer, D. Ouermi, C. Bisseye, J. Simpore, M. Cyrklaff, C. P. Sanchez, M. Lanzer, *Biol. Open* **2015**, *4*, 400–410.
[30] N. K. Viebig, B. Gamain, C. Scheidig, C. Lépolard, J. Przyborski, M. Lanzer, J. Gysin, A. Scherf, *EMBO Reports* **2005**, *6*, 775–781.
[31] J. B. Jensen, W. Trager, *The American Journal of Tropical Medicine and Hygiene* **1978**, *27*, 743–746.

Supplemental Information for:

A silicon rhodamine-fused glibenclamide to label and detect malaria-infected red blood cells

Claudia Bastl[1*], Cindy M. Close[2*], Ingo Holtz[1*], Blaise Gatin-Fraudet[3], Mareike Eis[1], Michelle Werum[1], Smilla Konrad[1], Kilian Roßmann[3], Christiane Huhn[3], Souvik Ghosh[3], Julia Ast[4], Dorien A. Roosen[5], Martin Lehmann[3], Volker Haucke[5], Luc Reymond[6,7], David J. Hodson[4,8], Philip Tinnefeld[2], Kai Johnsson[6,9], Viktorija Glembockyte[2†], Nicole Kilian[10,11†], Johannes Broichhagen[3,6,9†]

Affiliations

[1] Centre for Infectious Diseases, Parasitology Heidelberg University Hospital, Im Neuenheimer Feld 324, 69120 Heidelberg, Germany.

[2] Department of Chemistry and Center for NanoScience (CeNS), Ludwig-Maximilians-University, Butenandtstraße 5–13, 81377 Munich, Germany.

[3] Leibniz-Forschungsinstitut für Molekulare Pharmakologie, Robert-Rössle-Straße 10, 13125 Berlin, Germany.

[4] Institute of Metabolism and Systems Research (IMSR), and Centre of Membrane Proteins and Receptors (COMPARE), University of Birmingham, Birmingham, UK.

[5] Department of Molecular Pharmacology and Cell Biology, Leibniz-Forschungsinstitut für Molekulare Pharmakologie, Robert-Rössle-Straße 10, 13125 Berlin, Germany.

[6] Laboratory of Protein Engineering, Institut des Sciences et Ingénierie Chimiques, Sciences de Base, École Polytechnique Fédérale Lausanne, Avenue Forel 2, 1015 Lausanne, Switzerland.

[7] Present address: Biomolecular Screening Facility, École Polytechnique Fédérale Lausanne, Avenue Forel 2, 1015 Lausanne, Switzerland.

[8] Oxford Centre for Diabetes, Endocrinology and Metabolism (OCDEM), NIHR Oxford Biomedical Research Centre, Churchill Hospital, Radcliffe Department of Medicine, University of Oxford, Oxford, UK.

[9] Department of Chemical Biology, Max Planck Institute for Medical Research, Jahnstr. 29, 69120 Heidelberg, Germany.

[10] Department of Biological Sciences, California State University, Chico, USA, 400 W. First St. Chico, CA 95929–515, USA.

[11] Department of Medical Biochemistry, Faculty of Basic Medical Sciences, Delta State University, P.M.B. 1 Abraka Delta State, Nigeria.

*Equal contribution

† Correspondence should be addressed to:

Viktorija.Glembockyte@cup.lmu.de, nrkilian@csuchico.edu, broichhagen@fmp-berlin.de

Table of Contents

1. General

All chemical reagents and anhydrous solvents for synthesis were purchased from commercial suppliers (Sigma-Aldrich, Fluka, Acros, Fluorochem, TCI) and were used without further purification if not stated otherwise. Commercial coumarin 461 and methylene blue were HPLC purified before concentration assessment and measuring photophysical properties to ensure similar purity and composition as their synthesizes, deuterated counterparts. BG-TMR and BG-SiR were described before.[1]

NMR spectra were recorded at 300 K in deuterated solvents on a Bruker AVANCE III HD 600 equipped with a CryoProbe or on Bruker AV-III spectrometers using either a cryogenically cooled 5 mm TCI-triple resonance probe equipped with one-axis self-shielded gradients or room temperature 5 mm broadband probe and calibrated to residual solvent peaks ($^{1}H/^{13}C$ in ppm): DMSO-d_6 (2.50/39.52), MeOD-d_4 (3.31/49.00). Multiplicities are abbreviated as follows: s = singlet, d = doublet, t = triplet, q = quartet, p = pentet, h = heptet, br = broad, m = multiplet. Coupling constants J are reported in Hz. Spectra are reported based on appearance, not on theoretical multiplicities derived from structural information.

LC-MS was performed on an Agilent 1260 Infinity II LC System equipped with Agilent SB-C18 column (1.8 µm, 2.1 × 50 mm). Buffer A: 0.1% FA in H_2O Buffer B: 0.1% FA acetonitrile. The typical gradient was from 10% B for 0.5 min → gradient to 95% B over 5 min → 95% B for 0.5 min → gradient to 99% B over 1 min with 0.8 mL/min flow. Retention times (t_R) are given in minutes (min). Chromatograms were imported into Graphpad Prism8 and purity was determined by calculating AUC ratios.

Preparative or semi-preparative HPLC was performed on different instruments. An Agilent 1260 Infinity II LC System equipped with columns as followed: preparative column –Reprospher 100 C18 columns (10 µm: 50 x 30 mm at 20 mL/min flow rate; semi-preparative column – 5 µm: 250 x 10 mm at 4 mL/min flow rate. Eluents A (0.1% TFA in H2O) and B (0.1% TFA in MeCN) were applied as a linear gradient. Peak detection was performed at maximal absorbance wavelength. iii) A Waters e2695 system on a Supelco Ascentis® C18 HPLC Column (5 µm, 250 × 21.2 mm at 8 mL/min). Eluents A (0.1% TFA in H_2O) and B (0.1% TFA in MeCN) were applied as a linear gradient.

High resolution mass spectrometry was performed on an Agilent Technologies 6230 series accurate mass TOF LC-MS linked to an Agilent Technologies 1290 Infinity Series machine with a Thermo Accucore™ RP-MS column, 2.6 µm pore size, 30 × 2.1 mm, and a 3 min gradient from 5 to 99% aqueous MeCN with 0.1% TFA and MeCN with 0.1% TFA. flow rate: 0.8 mL/min; UV-detection: 220 nm, 254 nm, 300 nm.

2. Synthesis

2.1. 5-Chloro-2-methoxy-3-nitro-*N*-(4-sulfamoylphenethyl)benzamide (2)

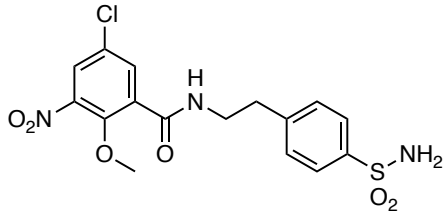

A round bottom flask was charged with 50 mg (0.216 mmol, 1.0 equiv.) 5-chloro-2-methoxy-3-nitrobenzoic acid (**1**) and dissolved in 1.2 mL DMSO and 97 µL (2.4 equiv.) DIPEA before 78.1 mg (0.25 mmol, 1.2 equiv.) of TSTU was added in one portion. The reaction mixture was stirred for 10 minutes before 51.8 mg (0.25 mmol, 1.2 equiv) of 4-(2-aminoethyl)benzenesulfonamide was added in one portion. The reaction mixture was stirred for additional 20 minutes before it was quenched with 10 mL of dH_2O, added dropwise under vigorous stirring. Finally, 1.2 mL of 1 M HCl was added to the reaction and the precipitate was collected by centrifugation at 4,000 rpm for 10 minutes. The supernatant was discarded, and the residue suspended in 10 mL dH_2O / 1.2 mL 1 M HCl, and sedimentation was performed again. After removing the supernatant, the residue was transferred to a round bottom flask with MeOH and all volatiles evaporated to dryness. 72 mg (0.174 mmol) of the desired product was obtained in 81% yield as a yellowish powder.

^{1}H NMR (300 MHz, DMSO-d_6): δ [ppm] = 8.71 (t, J = 5.5 Hz, 1H, NH), 8.16 (d, J = 2.8 Hz, 1H), 7.75 (d, J = 8.3 Hz, 2H), 7.73 (d, J = 2.7 Hz, 2H), 7.46 (d, J = 8.3 Hz, 2H), 7.32 (s, 2H, NH_2), 3.68 (s, 3H, CH_3), 3.51-3.59 (m, 2H), 2.92 (t, J = 7.1 Hz, 2H).

^{13}C NMR (75 MHz, DMSO-d_6): δ [ppm] = 163.5, 148.4, 144.5, 143.4, 142.2, 134.0, 132.9, 129.2, 127.5, 125.7, 125.4, 63.2, 34.4. (one carbon signal is missing as it's overlapping with DMSO signal)

HRMS (ESI): calc. for $C_{16}H_{17}ClN_3O_6S$ $[M+H]^+$: 414.0521, found: 414.0511.

2.2. 5-Chloro-*N*-(4-(*N*-(cyclohexylcarbamoyl)sulfamoyl)phenethyl)-2-methoxy-3-nitrobenzamide (3)

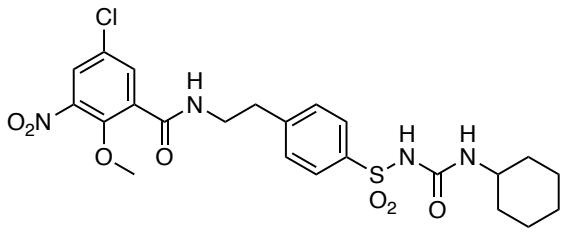

A round bottom flask was charged with 50 mg (121 µmol, 1.0 equiv.) of **2** and dissolved in 3 mL acetone before 33.2 mg (240 µmol, 2.0 equiv) of K_2CO_3 was added. The reaction mixture was heated to 70 °C and 23 µL (180 µmol, 22.6 mg, 1.5 equiv.) of cyclohexyl isocyanate diluted in 1 mL acetone was added dropwise. The reaction mixture was heated for an additional hour before 1 mL of 1 M HCl was added, and all volatiles were removed on a rotary evaporator. The residue was suspended in 10 mL dH_2O / 1 mL 1 M HCl and the precipitate was collected after centrifugation at 4,000 rpm for 10 minutes. After removing the supernatant, the residue was transferred to a round bottom flask with MeOH and all volatiles evaporated to dryness. 64 mg (121 µmol) of the desired product was obtained in quantitative yield as a white powder.

^{1}H NMR (600 MHz, DMSO-d_6): δ [ppm] = 10.29 (s, 1H, NH), 8.67 (t, J = 5.5 Hz, 1H, NH), 8.14 (d, J = 2.7 Hz, 1H), 7.82 (d, J = 8.3 Hz, 2H), 7.71 (d, J = 2.7 Hz, 1H), 7.50 (d, J = 8.3 Hz, 2H), 6.32 (d, J = 7.9 Hz, 1H, NH), 3.61 (s, 3H, CH_3), 3.57 (q, J = 6.5 Hz, 2H), 3.23-3.29 (m, 1H), 2.95 (t, J = 7.0 Hz, 2H), 1.61-1.67 (m, 2H), 1.55-1.61 (m, 2H), 1.46-1.51 (m, 1H), 1.17-1.25 (m, 2H), 1.05-1.15 (m, 3H).

^{13}C NMR (150 MHz, DMSO-d_6): δ [ppm] = 163.4, 150.35, 148.3, 145.0, 144.45, 138.2, 133.9, 132.85, 129.25, 127.4, 127.25, 125.3, 63.0, 48.0, 34.3, 32.2 (2C), 24.9, 24.1 (2C).

HRMS (ESI): calc. for $C_{23}H_{28}ClN_4O_7S$ $[M+H]^+$: 539.1362, found: 539.1392.

2.3. 3-Amino-5-chloro-*N*-(4-(*N*-(cyclohexylcarbamoyl)sulfamoyl)phenethyl)-2-methoxybenzamide (4)

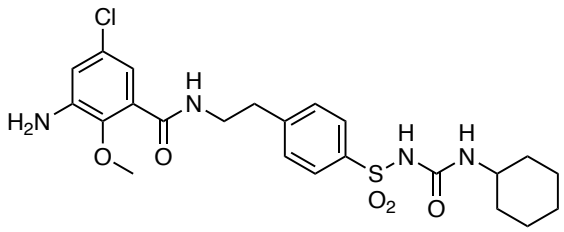

A round bottom flask was charged with 40 mg (74.3 µmol, 1.0 equiv.) of **3** under a nitrogen atmosphere and dissolved in 5 mL MeOH and 270 µL HOAc before 189 mg (12 mmol, 160 equiv.) of Zn dust was added in one portion. The reaction mixture was stirred for 1.5 hours at room temperature (solution turns red, and color fades over time) before it was centrifuged at 4,000 rpm for ten minutes to settle the remaining solids. The supernatant was collected and all volatiles were removed on a rotary evaporator. The crude was washed with 10 mL dH_2O, the solid filtered off and finally dried to obtain 34 mg (66.9 µmol) of the desired product in 90% yield as a white powder.

^{1}H NMR (600 MHz, MeOD-d_4): δ [ppm] = 7.91 (d, J = 8.2 Hz, 2H), 7.51 (d, J = 8.2 Hz, 2H), 6.86 (d, J = 2.6 Hz, 1H), 6.84 (d, J = 2.6 Hz, 1H), 3.69 (t, J = 7.0 Hz, 2H), 3.49 (s, 3H, CH_3), 3.05 (t, J = 7.0 Hz, 2H), 1.82-1.87 (m, 1H), 1.63-1.78 (m, 3H), 1.54-1.61 (m, 1H), 1.26-1.40 (m, 3H), 1.10-1.23 (m, 3H).

^{13}C NMR (150 MHz, MeOD-d_4): δ [ppm] = 168.0, 146.65, 144.7, 144.5, 140.1, 130.8, 130.6, 129.9, 128.8, 118.3, 117.8, 60.9, 50.1, 41.5, 35.9, 34.75, 33.8, 26.7, 26.5, 26.05, 25.8.

HRMS (ESI): calc. for $C_{23}H_{30}ClN_4O_5S$ $[M+H]^+$: 509.1620, found: 509.1625.

2.4. 3-(6-Aminohexanamido)-5-chloro-*N*-(4-(*N*-(cyclohexylcarbamoyl)sulfamoyl)phenethyl)-2-methoxybenzamide (6)

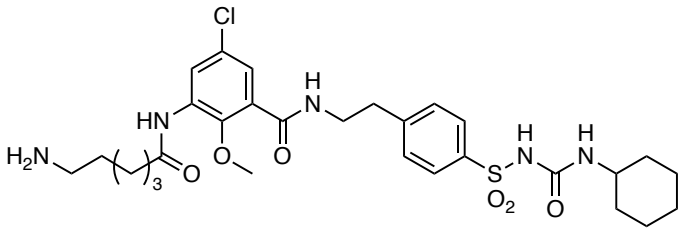

Under a nitrogen atmosphere, a round bottom flask was charged with 41 mg (117 µmol) of Fmoc-Ahx-OH and suspended in 1 mL $SOCl_2$. The reaction mixture was stirred for 1.5 hours at room temperature, and all volatiles were carefully removed under a stream of nitrogen in a well-ventilated fume hood. The residue was taken up in 1 mL of dry dioxanes, which was again carefully removed under a stream of nitrogen in a well-ventilated fume hood. Addition of 1 mL of dry dioxanes yielded a 117 mM stock solution, which was used immediately. A round bottom flask was charged with 10 mg (19.7 µmol, 1.0 equiv) of **4** dissolved in 2 mL of dry dioxanes and 13.3 µL of NEt_3, to which 505 µL of the acyl chloride (~3.0 equiv) was added dropwise under vigorous stirring. The reaction was stirred over night at room temperature before it was quenched with 1 mL of dH_2O and all volatiles were removed in vacuo. The crude material was taken up in 800 µL DMF and 40 µL piperidine and allowed to incubate for 1 hour at room temperature, before it was quenched with 50 µL HOAc and 200 µL dH_2O and subjected to RP-HPLC purification. The product containing fractions were pooled and 2.5 mg (3.40 µmol) of the desired product was obtained as a TFA salt after lyophilization in 17% yield over two steps as a white powder.

^{1}H NMR (600 MHz, DMSO-d_6): δ [ppm] = 10.34 (s, 1H, NH), 9.47 (s, 1H, NH), 8.43 (bs, 1H, NH), 8.16 (s, 1H), 7.83 (dd, J = 8.2 Hz, J = 1.8 Hz, 2H), 7.63 (bs, 2H, NH_2), 7.50 (dd, J = 8.2 Hz, J = 1.8 Hz, 2H), 7.12 (bs, 1H), 6.38 (d, J = 6.8 Hz, 1H, NH), 3.55 (bs, 5H, CH_2 and CH_3), 3.23-3.31 (m, 1H), 2.95 (bt, J = 6.8 Hz, 2H), 2.75-2.81 (m, 2H), 2.45 (bt, J = 6.8 Hz, 2H), 1.51-1.67 (m, 8H), 1.44-1.51 (m, 1H), 1.30-1.37 (m, 2H), 1.16-1.26 (m, 2H), 1.07-1.15 (m, 3H).

^{19}F NMR (564 MHz, DMSO-d_6): δ [ppm] = -73.8.

^{13}C NMR (150 MHz, DMSO-d_6): δ [ppm] = 172.0, 164.6, 150.4, 146.4, 145.1, 138.2, 133.2, 131.2, 129.2, 127.2, 127.0, 123.0, 122.9, 61.4, 48.0, 40.0, 38.7, 35.7, 34.4, 32.2 (2C), 26.8, 25.4, 24.9, 24.5, 24.1 (2C).

HRMS (ESI): calc. for $C_{23}H_{27}ClN_4O_7S$ $[M+H]^+$: 622.2461, found: 622.2438.

2.5. 4-((6-((5-Chloro-3-((4-(*N*-(cyclohexylcarbamoyl)sulfamoyl)phenethyl)carbamoyl)-2-methoxyphenyl)amino)-6-oxohexyl)carbamoyl)-2-(7-(dimethylamino)-3-(dimethyliminio)-5,5-dimethyl-3,5-dihydrodibenzo[*b*,*e*]silin-10-yl)benzoate (SiR-glib)

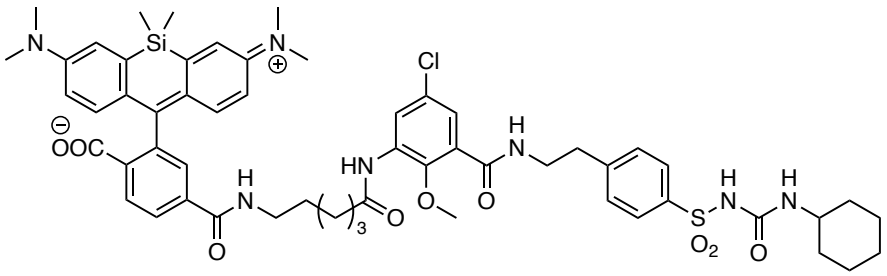

An Eppendorf tube was charged with 2.0 mg (4.24 µmol, 1.2 equiv.) of SiR-6-COOH and dissolved in 0.5 mL DMSO and 2.0 µL DIPEA before 1.6 mg (5.31 µmol, 1.5 equiv.) of TSTU was added in one portion. The reaction mixture was allowed to incubate for 10 minutes before it was added to an Eppendorf tube containing 2.6 mg (3.54 µmol, 1.0 equiv.) of **6** dissolved in 0.5 mL DMSO. The reaction mixture was vortexed and allowed to incubate for 2 hours, before it was quenched with 20 µL HOAc and 100 µL dH_2O and subjected to RP-HPLC purification. The product containing fractions were pooled and 1.8 mg (1.50 µmol) of the desired product was obtained after lyophilization in 42% yield over two steps as a blue powder.

^{1}H NMR (600 MHz, DMSO-d_6): δ [ppm] = 10.29 (s, 1H, NH), 9.44 (s, 1H, NH), 8.43 (t, J = 5.5 Hz, NH), 8.30 (d, J = 8.5 Hz, 1H), 8.21 (d, J = 8.5 Hz, 1H), 8.16 (bd, J = 2.4 Hz, 1H), 7.88 (t, J = 5.5 Hz, NH), 7.82 (d, J = 8.3 Hz, 2H), 7.77 (bs, 1H), 7.50 (d, J = 8.3 Hz, 2H), 7.12 (d, J = 2.7 Hz, 1H), 7.04 (bs, 2H), 6.69 (bs, 4H), 6.32 (d, J = 7.9 Hz, 1H, NH), 3.55 (m, 4H), 3.23-3.27 (m, 1H), 3.02-3.05 (m, 1H), 2.94 (bs, 12H), 2.87 (bs, 3H), 2.75 (bs, 1H), 2.43 (t, J = 7.7 Hz, 1H), 2.29 (t, J = 7.4 Hz, 1H), 1.95-2.02 (m, 1H), 1.62-1.67 (m, 1H), 1.56-1.59 (m, 2H), 1.40-1.49 (m, 2H), 1.19-1.32 (m, 4H), 1.08-1.14 (m, 1H), 0.94 (d, J = 6.6 Hz, 1H), 0.85 (t, J = 7.0 Hz, 1H), 0.62 (s, 3H), 0.53 (s, 3H).

^{19}F NMR (564 MHz, DMSO-d_6): δ [ppm] = -73.8.

HRMS (ESI): calc. for $C_{56}H_{66}ClN_7O_9SSi$ $[M+H]^+$: 1076.4173, found: 1076.4180.

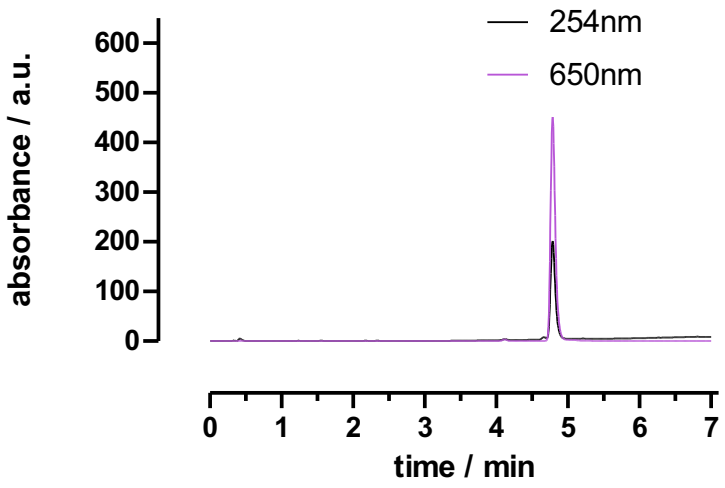

3. NMR spectra

3.1. 5-Chloro-2-methoxy-3-nitro-*N*-(4-sulfamoylphenethyl)benzamide (2)

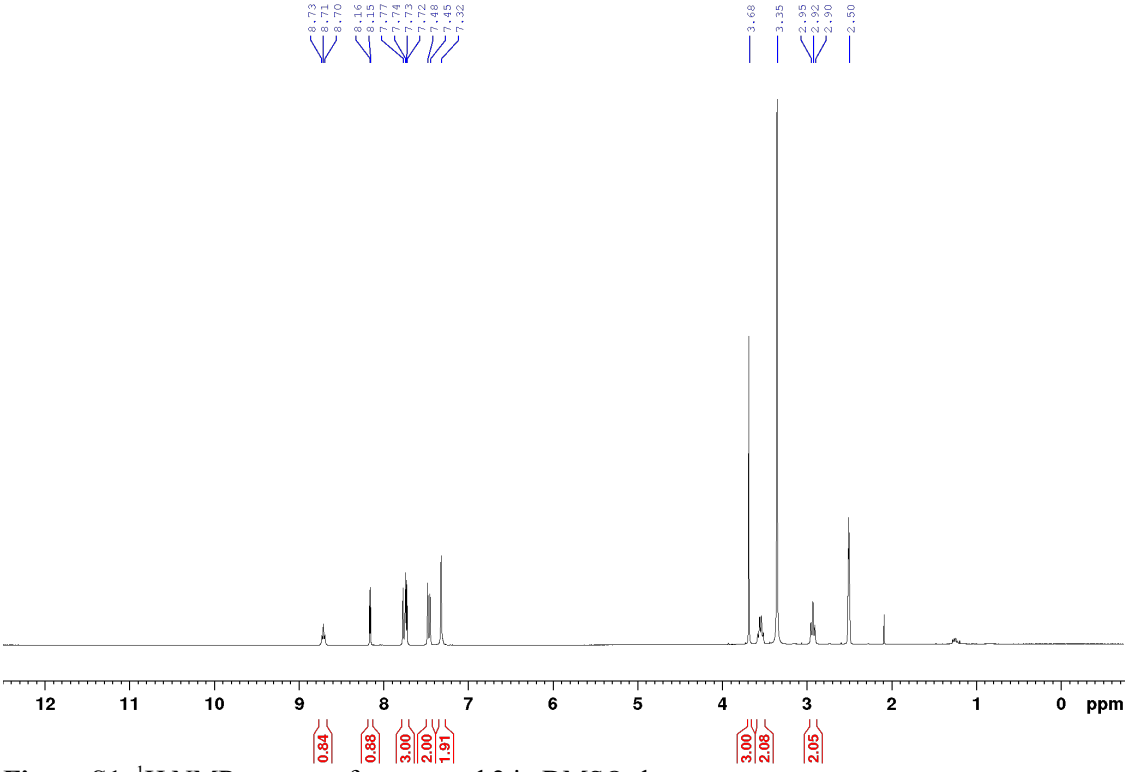

Figure S1. ^{1}H NMR spectra of compound **2** in DMSO-d$_6$.

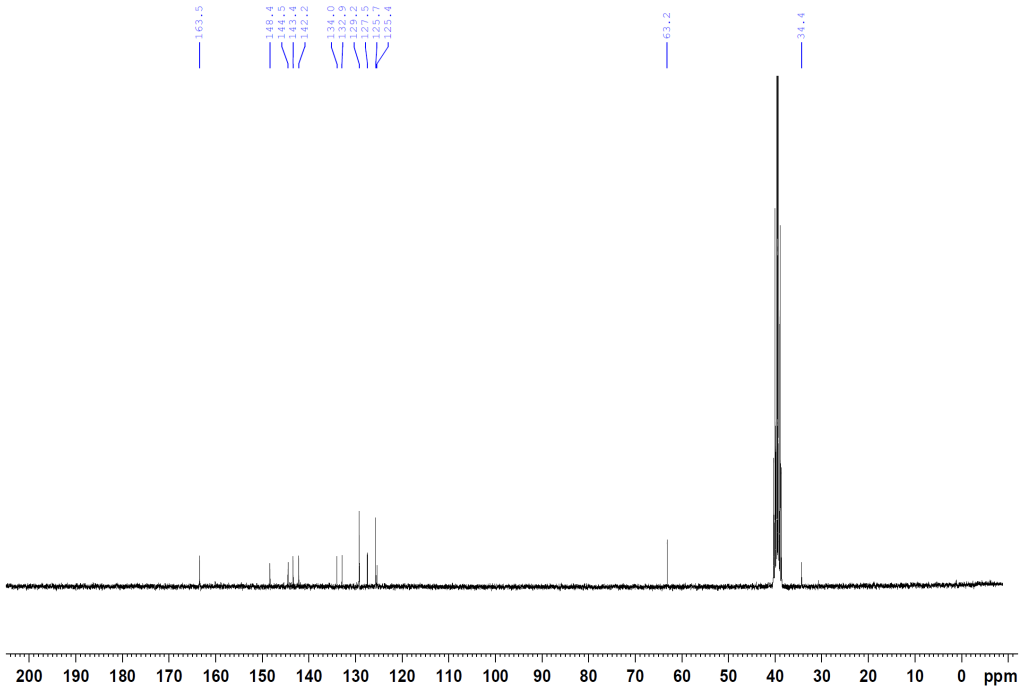

Figure S2. ^{13}C NMR spectra of compound **2** in DMSO-d$_6$.

3.2. 5-Chloro-*N*-(4-(*N*-(cyclohexylcarbamoyl)sulfamoyl)phenethyl)-2-methoxy-3-nitrobenzamide (3)

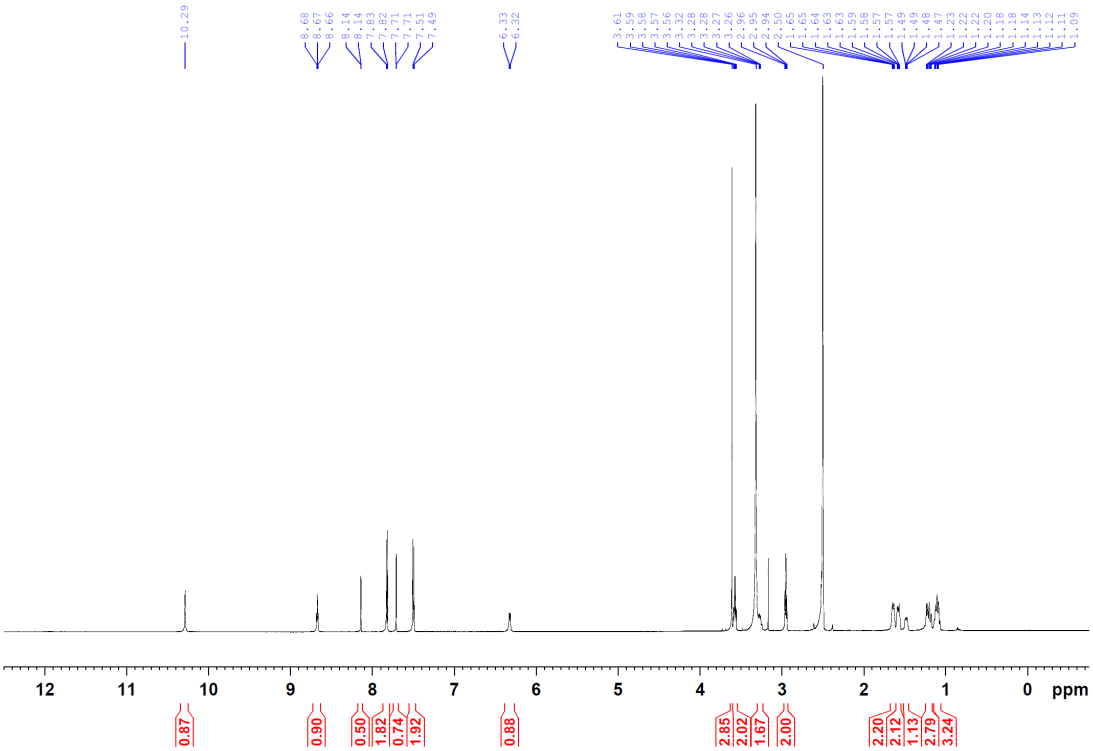

Figure S3. ^{1}H NMR spectra of compound **3** in DMSO-d$_6$.

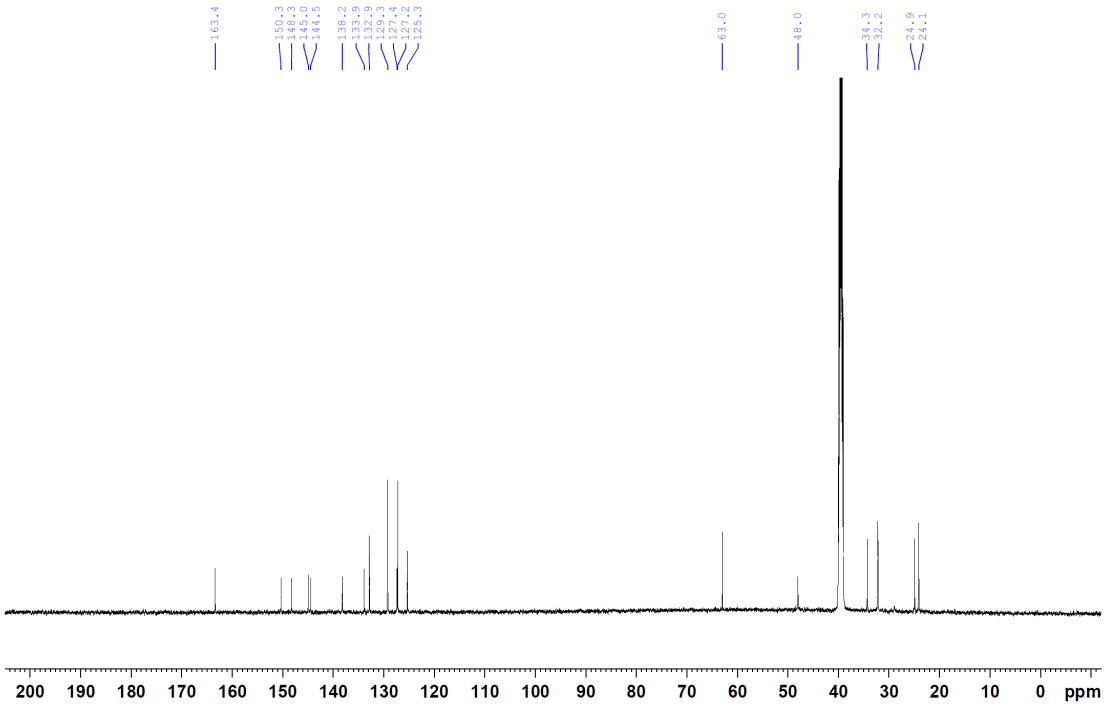

Figure S4. ^{13}C NMR spectra of compound **3** in DMSO-d$_6$.

3.3. 3-Amino-5-chloro-*N*-(4-(*N*-(cyclohexylcarbamoyl)sulfamoyl)phenethyl)-2-methoxybenzamide (4)

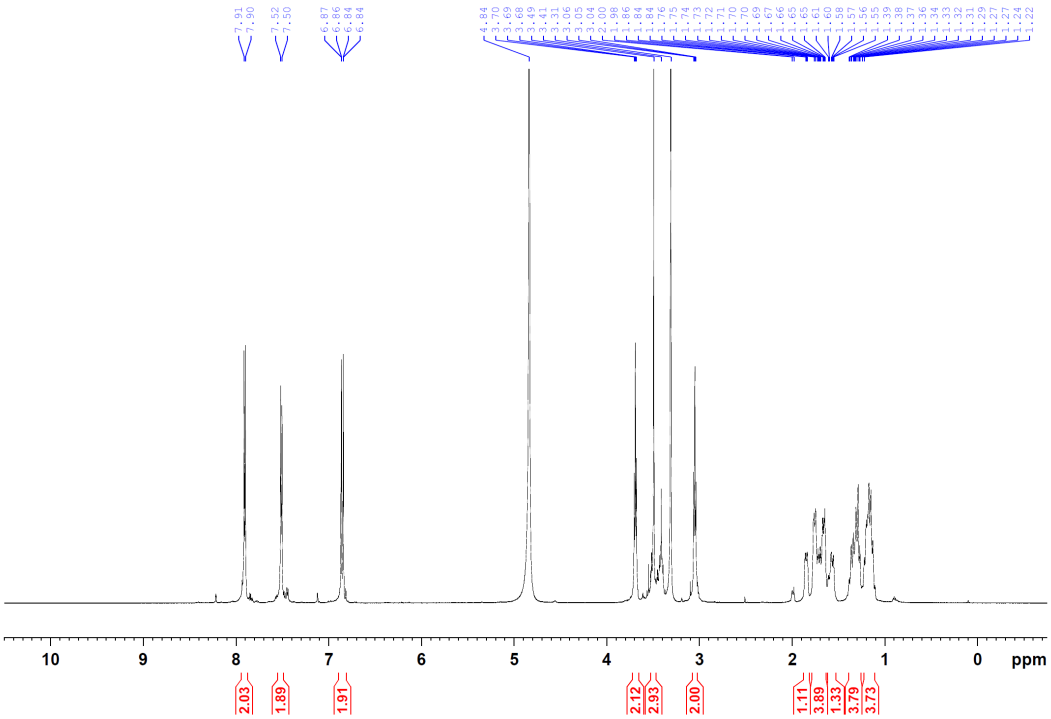

Figure S5. ^{1}H NMR spectra of compound **4** in MeOD-d$_4$.

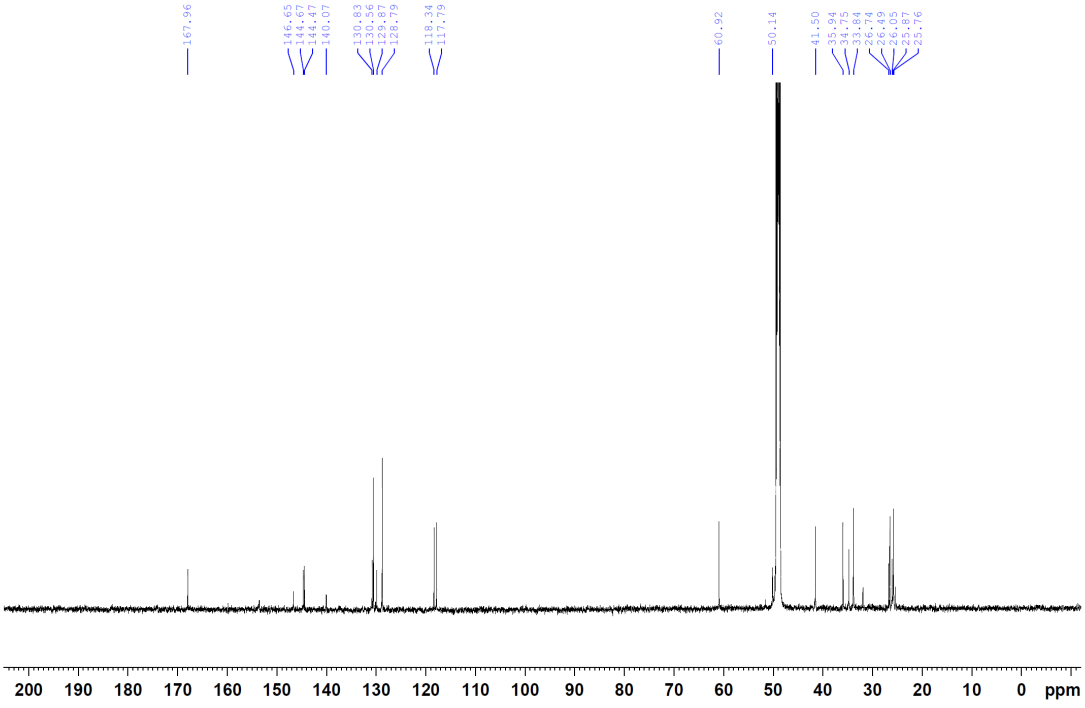

Figure S6. ^{13}C NMR spectra of compound **4** in MeOD-d$_4$.

3.4. 3-(6-Aminohexanamido)-5-chloro-*N*-(4-(*N*-(cyclohexylcarbamoyl)sulfamoyl)phenethyl)-2-methoxybenzamide (6)

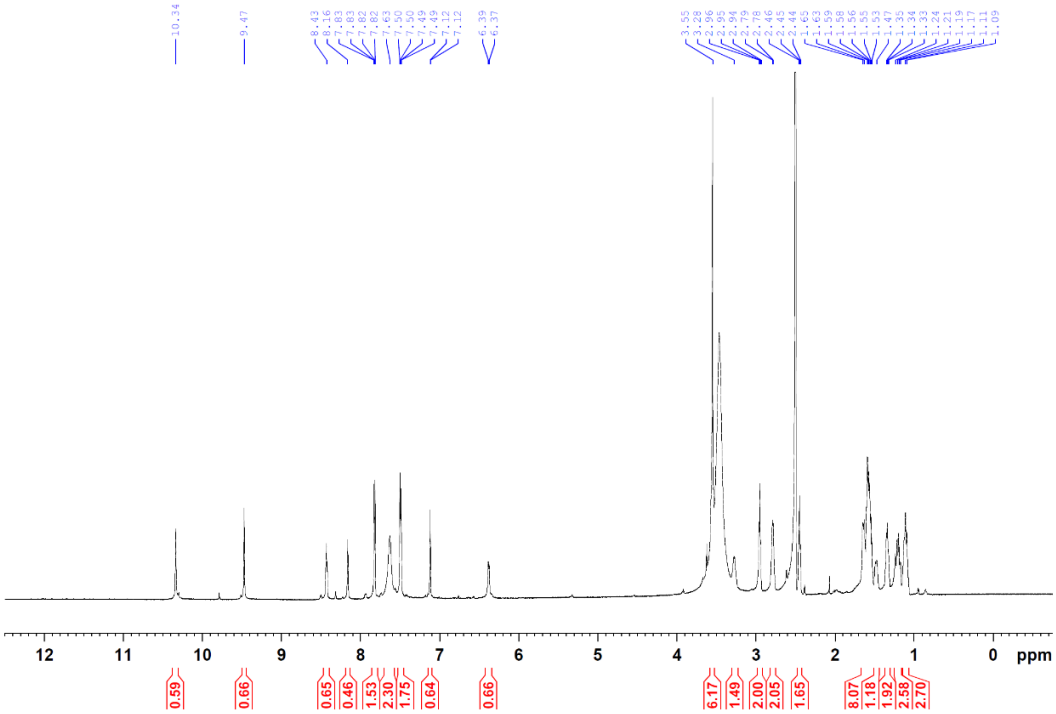

Figure S7. ^{1}H NMR spectra of compound **6** in DMSO-d$_6$.

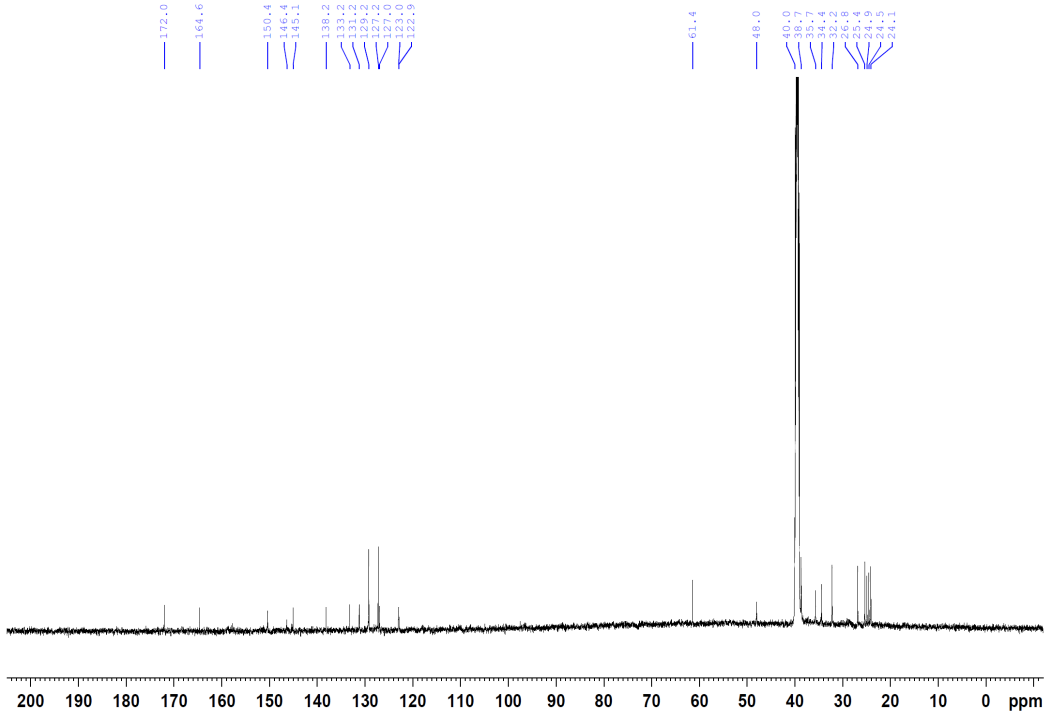

Figure S8. ^{13}C NMR spectra of compound **6** in DMSO-d$_6$.

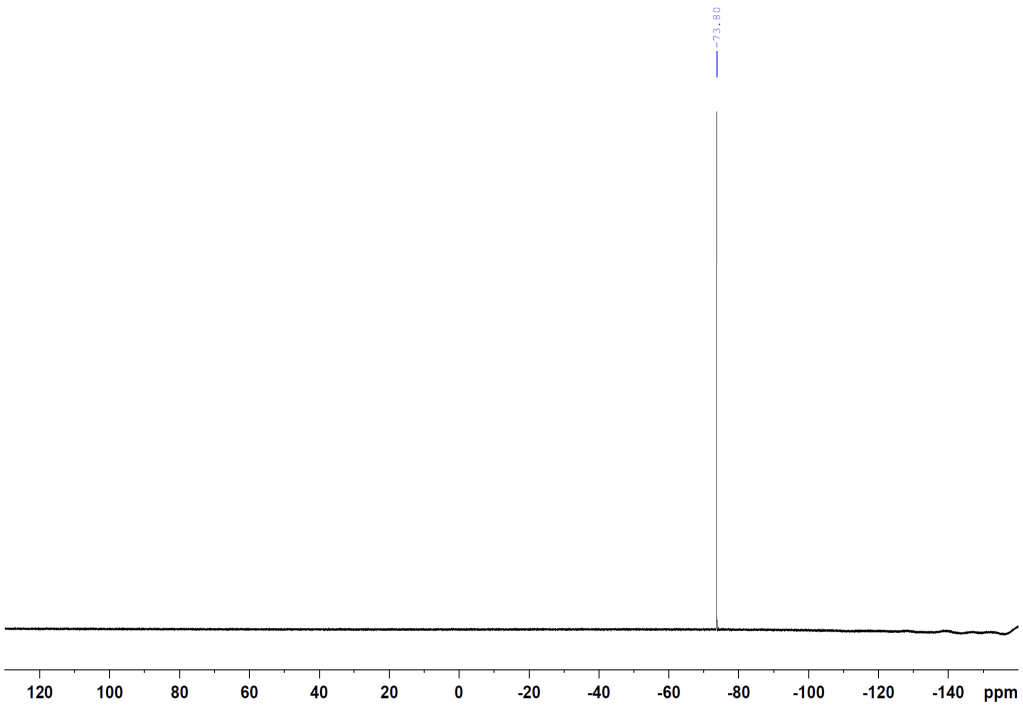

Figure S9. ^{19}F NMR spectra of compound **6** in DMSO-d_6.

3.5. 4-((6-((5-Chloro-3-((4-(*N*-(cyclohexylcarbamoyl)sulfamoyl)phenethyl)carbamoyl)-2-methoxyphenyl)amino)-6-oxohexyl)carbamoyl)-2-(7-(dimethylamino)-3-(dimethyliminio)-5,5-dimethyl-3,5-dihydrodibenzo[*b*,*e*]silin-10-yl)benzoate (SiR-glib)

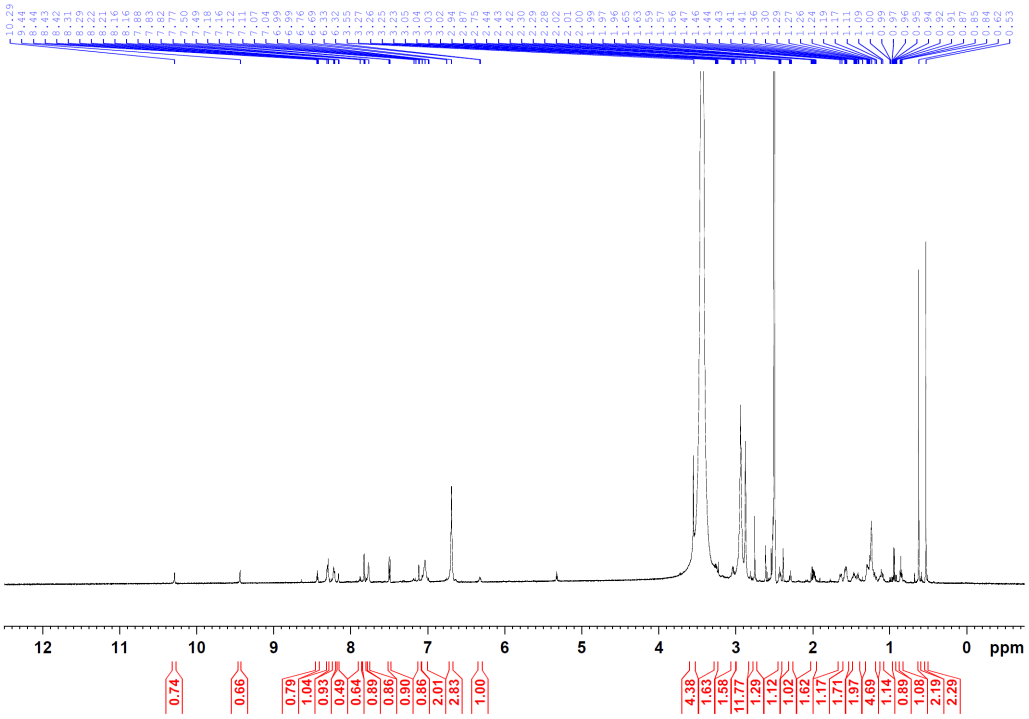

Figure S10. ^{1}H NMR spectra of compound **SiR-glib** in DMSO-d_6.

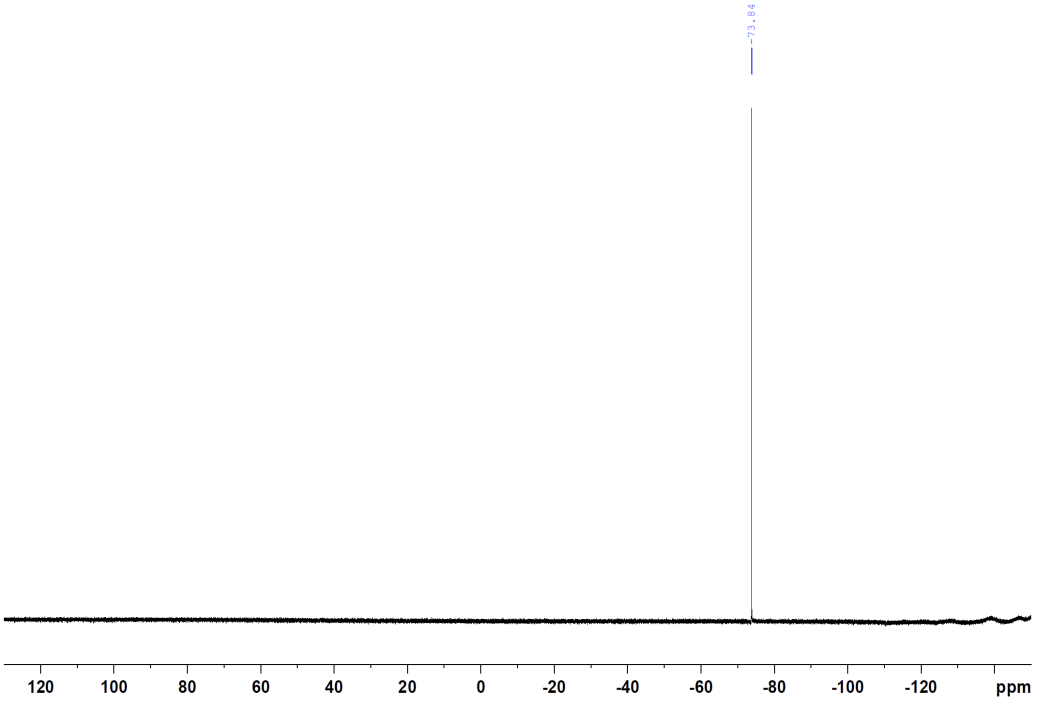

Figure S11. ^{19}F NMR spectra of compound **SiR-glib** in DMSO-d_6.

11.3 Associated Publication 3

Addressable nanoantennas with cleared hotspots for single-molecule detection on a portable smartphone microscope

Kateryna Trofymchuk*, Viktorija Glembockyte*, Lennart Grabenhorst, Florian Steiner, Carolin Vietz, Cindy Close, Martina Pfeiffer, Lars Richter, Max L. Schütte, Florian Selbach, Renukka Yaadav, Jonas Zähringer, Qingshan Wei, Aydogan Ozcan, Birka Lalkens, Guillermo P. Acuna, Philip Tinnefeld

*equal contribution

Nature Communications 12, 950 (2021). doi: 10.1038/s41467-021-21238-9

nature COMMUNICATIONS

ARTICLE

https://doi.org/10.1038/s41467-021-21238-9 OPEN

Addressable nanoantennas with cleared hotspots for single-molecule detection on a portable smartphone microscope

Kateryna Trofymchuk[1,2,7✉], Viktorija Glembockyte[1,7✉], Lennart Grabenhorst[1], Florian Steiner[1], Carolin Vietz[2], Cindy Close[1], Martina Pfeiffer[1], Lars Richter[2], Max L. Schütte[2], Florian Selbach[1], Renukka Yaadav[1], Jonas Zähringer[1], Qingshan Wei[3], Aydogan Ozcan[4], Birka Lalkens[5], Guillermo P. Acuna[6✉] & Philip Tinnefeld[1✉]

The advent of highly sensitive photodetectors and the development of photostabilization strategies made detecting the fluorescence of single molecules a routine task in many labs around the world. However, to this day, this process requires cost-intensive optical instruments due to the truly nanoscopic signal of a single emitter. Simplifying single-molecule detection would enable many exciting applications, e.g., in point-of-care diagnostic settings, where costly equipment would be prohibitive. Here, we introduce addressable NanoAntennas with Cleared HOtSpots (NACHOS) that are scaffolded by DNA origami nanostructures and can be specifically tailored for the incorporation of bioassays. Single emitters placed in NACHOS emit up to 461-fold (average of 89 ± 7-fold) brighter enabling their detection with a customary smartphone camera and an 8-US-dollar objective lens. To prove the applicability of our system, we built a portable, battery-powered smartphone microscope and successfully carried out an exemplary single-molecule detection assay for DNA specific to antibiotic-resistant *Klebsiella pneumonia* on the road.

[1] Department of Chemistry and Center for NanoScience, Ludwig-Maximilians-Universität München, München, Germany. [2] Institute for Physical and Theoretical Chemistry - NanoBioScience and Braunschweig Integrated Centre of Systems Biology (BRICS), Technische Universität Braunschweig, Braunschweig, Germany. [3] Department of Chemical and Biomolecular Engineering, North Carolina State University, Raleigh, NC, USA. [4] Electrical & Computer Engineering Department, Bioengineering Department, California NanoSystems Institute (CNSI), and Department of Surgery, University of California, Los Angeles, CA, USA. [5] Institut für Halbleitertechnik, Laboratory for Emerging Nanometrology LENA, TU Braunschweig, Langer Kamp 6a/b, Braunschweig, Germany. [6] Département de Physique - Photonic Nanosystems, Université de Fribourg - Faculté des Sciences et Médicine, Fribourg, Switzerland. [7] These authors contributed equally: Kateryna Trofymchuk and Viktorija Glembockyte. ✉email: kateryna.trofymchuk@cup.lmu.de; viktorija.glembockyte@cup.lmu.de; guillermo.acuna@unifr.ch; philip.tinnefeld@cup.lmu.de

Early detection of disease biomarkers generally requires high sensitivity enabled by molecular amplification mechanisms[1–5] or physical signal enhancement of commonly used fluorescence signals[6–9]. Physical fluorescence signal enhancement could enable sensitivity improvement, detection of single molecules on cost-effective and mobile devices and therefore help to distinguish specific signals against an unavoidable background of impurities even in low-resource settings. Fluorescence from emitters such as fluorescent dyes can be enhanced using plasmonic nanoantennas[10–12], and the challenge of placing quantum emitters in their hotspots was overcome using DNA origami as constructing material[13,14]. The immense requirements for small, defined and rigid gaps between the gold or silver nanoparticles forming the gap in the nanoantenna aggravated the usability of the space between the nanoparticles for a biosensing assay. While it was demonstrated that incorporation of a fluorescence quenched hairpin in a nanoantenna hotspot allowed for the specific detection of DNA specific to Zika virus, the limited accessibility of the hotspot and the steric constraints imposed by the DNA origami nanopillar, the capturing strands and the nanoparticles only allowed for the binding of a single nanoparticle (monomer antenna) strongly reducing the achievable enhancement values (average of 7.3)[15]. These moderate fluorescence enhancement values were not sufficient for detecting single fluorescence molecules with low numerical aperture(NA) optics. For example, our previous work on benchmarking the sensitivity of smartphone-based detection systems suggested that a signal equivalent to at least 16 single emitters is required for detection on a smartphone-based low-NA microscope[16]. Therefore, a diagnostic single-molecule assay fully exploiting the signal amplification potential of DNA origami nanoantennas has not been presented to date and remained highly desirable to enable detection of single molecules with affordable low-NA optics.

In this work, we introduce NanoAntennas with Cleared HOtSpots (NACHOS) that enable high fluorescence signal amplification and are fully addressable, i.e., new analytes can be introduced into the confined regions of dimer nanoantennas. We use these NACHOS for a single-molecule diagnostic assay on a portable and inexpensive smartphone microscope.

Results

Design and fluorescence enhancement of NACHOS. A novel three-dimensional DNA origami structure was designed (Fig. 1a) and folded from an M13mp18-derived scaffold strand and complementary staple strands (Supplementary Tables 1–3). The NACHOS origami design uses two pillars to attach silver nanoparticles and creates the plasmonic hotspot at the bifurcation in the gap between the two pillars and the nanoparticles (see DNA origami sketches in Fig. 1a and full NACHOS structure in Fig. 1b and Fig. 1c). Thus, the space of the hotspot, i.e., between the nanoparticles is left free for placing baits and for binding targets as needed for nucleic acid bioassays. For immobilization, the DNA origami structure is equipped with a rigid cross-like shaped base (approximately 35 nm by 33 nm, Supplementary Figs. 1 and 2) that contains six biotin-modified staple strands (Supplementary Table 3) used for immobilization on BSA-biotin coated coverslips via biotin-NeutrAvidin interactions (Fig. 1b). The two pillars of the DNA origami structure (total height ~83 nm) each contain six protruding staple strands (A_{20}, Supplementary Table 3) which provide anchor points for binding DNA (T_{20})-functionalized 100 nm silver nanoparticles (Fig. 1b). The estimated distance between the nanoparticles is ~12 nm. A transmission electron microscopy (TEM) image of an exemplary nanoantenna produced via solution synthesis is shown in Fig. 1c (see Materials and Methods section for details on magnetic bead-based solution synthesis). We evaluated the signal amplification that can be achieved in this DNA origami nanoantenna design by incorporating an Alexa Fluor 647-labeled DNA staple strand (Supplementary Table 3) directly into the plasmonic hotspot of the nanoantenna. Single-molecule fluorescence transients of the dye (Fig. 1d, Supplementary Fig. 3) were recorded on a confocal microscope for the DNA origami sample without nanoparticles (orange) as well as for NACHOS containing two 100 nm silver nanoparticles attached to the DNA origami after immobilization on the coverslip (blue, see Materials and Methods section for NACHOS synthesis on the coverslip). Single-step photobleaching in the intensity versus time transients (Fig. 1c) confirms that the detected signal originates from a single fluorescent molecule. Further analysis of single-molecule transients demonstrates that the signal-to-background ratio (SBR) could be significantly improved by the nanoantenna (361 ± 35) when compared to the reference structure (7.4 ± 0.9). The fluorescence enhancement obtained for each nanoantenna was calculated by comparing the intensity of Alexa Fluor 647 in the NACHOS to the mean intensity of Alexa Fluor 647 in the reference structure without nanoparticles. Fluorescence enhancement values of up to 417-fold (average of 74 ± 3-fold) could be achieved in the new nanoantenna design (Fig. 1e). The broad fluorescence enhancement distribution reflects some heterogeneity with regard to nanoparticle size, shape and orientation, and also includes a subpopulation of monomer nanoantennas. Care was taken that all fluorescent molecules incorporated in the DNA origami nanoantennas were included in the analysis to obtain a representative distribution of fluorescence enhancement values in Fig. 1e. Most importantly, we note that increasing the accessibility of the hotspot region did not compromise the fluorescence enhancement values which are slightly higher than previously reported values for more compact nanoantenna designs[14,17,18].

Amplified single-molecule detection of DNA with NACHOS. To utilize the plasmonic hotspot for single-molecule diagnostics we designed a sandwich binding assay capable of detecting a DNA fragment specific to *OXA-48*, which is the gene that codes for carbapenemase and is used for the diagnosis of an antibiotic resistant *Klebsiella pneumoniae* infection[19,20]. Three capture strands specific to the target DNA (Supplementary Table 4) were incorporated, protruding directly into the plasmonic hotspot of the NACHOS. The rationale of using three capturing strands was to optimize the probability of each DNA origami having binding strands accessible to capture the target[21]. The principle of this assay is illustrated in Fig. 2a: a 17-nt long capture strand is complementary to one half of the 34-nt long target DNA strand. Binding of the target DNA sequence then provides an overhang for the 17-nt long dye-labeled imager strand to be incorporated directly in the plasmonic hotspot where the signal of the reporter dye is amplified by the nanoantenna. In addition, the DNA origami structure is labeled with a single ATTO 542 dye close to the base.

Surface scans before incubation with the target and imager strands show green fluorescent spots that represent single NACHOS (Fig. 2b, Supplementary Fig. 4). After incubating (2 h at 37 °C) the NACHOS with the target DNA sequence (2 nM, Supplementary Table 4) as well as with the Alexa Fluor 647-labeled imager strand (6 nM, Supplementary Table 4), the presence of the target DNA could be detected and quantified by counting the number of colocalized green (ATTO 542) and red (Alexa Fluor 647) spots in confocal fluorescence scans (Fig. 2c, Supplementary Fig. 4). Although 2 h were used for the assay, we note that significant binding of target sequence in the hotspot of NACHOS was already achieved after 15 min of incubation at

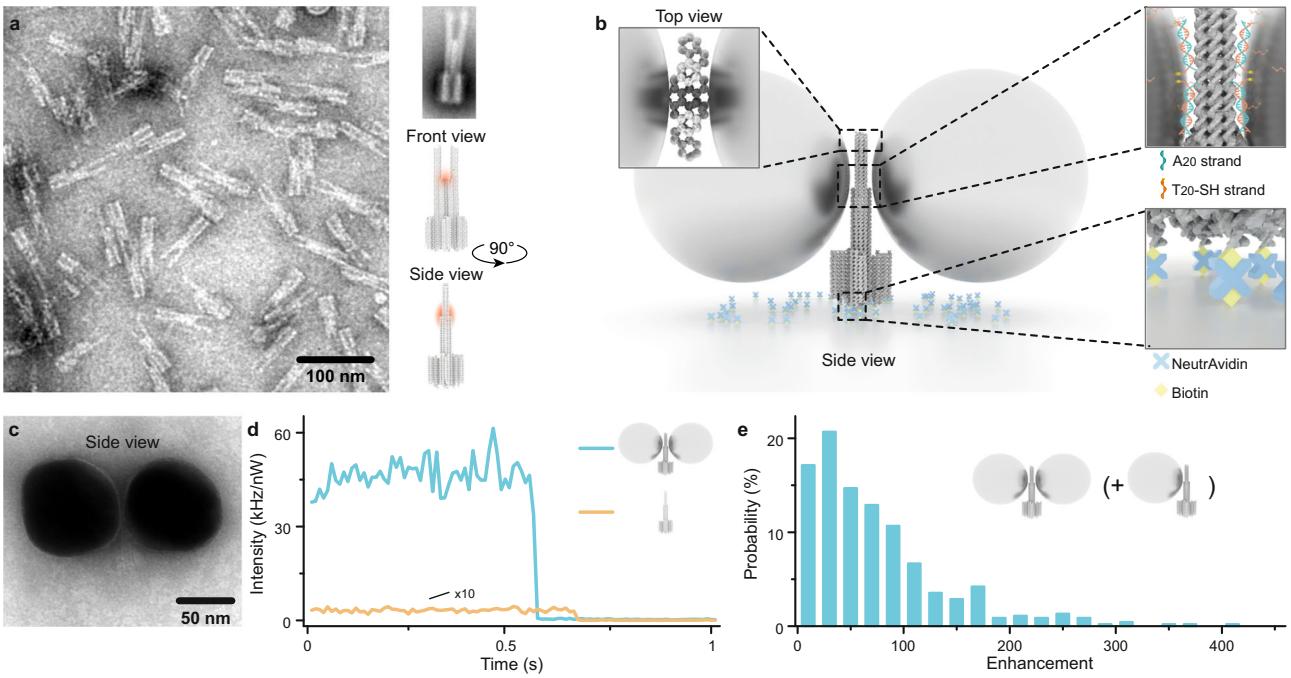

Fig. 1 Concept of the DNA origami nanoantenna with a cleared hotspot. a TEM image (left, reproduced at least 3 times) and sketches (right) of the DNA origami structure used for the nanoantenna assembly with the position of the plasmonic hotspot indicated in red. A representative class averaged TEM image of the DNA origami used is shown on the upper right. **b** Schematics of NACHOS assembly: the DNA origami construct is bound to the BSA-biotin coated surface via biotin-NeutrAvidin interactions, thiolated DNA-functionalized 100 nm silver particles are attached to the DNA origami nanoantenna via polyadenine (A_{20}) binding strands in the zipper-like geometry to minimize the distance between the origami and the nanoparticles[30]. **c** TEM image of a NACHOS with 100 nm silver nanoparticles (reproduced at least 3 times). **d** Single-molecule fluorescence intensity transients, measured by confocal microscopy, normalized to the same excitation power of a single Alexa Fluor 647 dye incorporated in a DNA origami (orange) and in a DNA origami nanoantenna with two 100 nm silver nanoparticles (blue) excited at 639 nm **e**. Fluorescence enhancement distribution of Alexa Fluor 647 measured in NACHOS with 100 nm silver nanoparticles. A total number of 164 and 449 single molecules in the reference (more examples are provided in Supplementary Fig. 3) and NACHOS structures were analyzed, respectively.

37 °C (Supplementary Fig. 5). When the nanoantennas were incubated with the imager strand only (Fig. 2d, f, and Supplementary Fig. 4), very few co-localized spots were observed. This control demonstrated a low fraction (~2.5%) of false positive signals. Incubation of NACHOS with 34-nt long target sequence containing 1-nt, 2-nt and 3-nt mismatches in the target region led to a drop in the number of co-localized spots (Supplementary Fig. 6), indicating a certain degree of selectivity in this assay, which potentially can be further improved by optimizing the sequence and length of the DNA capture strand.

Next, we studied the fluorescence enhancement that could be achieved in this single-molecule DNA diagnostics assay (Fig. 2e). Fluorescence enhancement values were calculated by comparing the intensity of Alexa Fluor 647 in NACHOS that contained only one dye incorporated in the hotspot (i.e., displayed single-step bleaching events in fluorescence transients) to the intensity of single Alexa Fluor 647 dyes incorporated in the reference structure without nanoparticles. As shown in Fig. 2e, fluorescence enhancement values of up to 461-fold (average 89 ± 7-fold) could be achieved representing more than an order of magnitude improvement compared to previous DNA nanoantennas specific to Zika virus[15]. One major advantage of using NACHOS for the sandwich binding assay is that only the signal originating from the specific binding to the target sequence in the zeptoliter volume of the nanoantenna hotspot is amplified. In contrast, any signal originating from non-specific binding of the imager strand to the DNA origami scaffold or the surface of the glass coverslip is not amplified. The clear differentiation between single-molecule emission amplified by the nanoantenna and the one observed from single fluorescent molecules is illustrated in the inset of Fig. 2e.

We quantified the efficiency of the sandwich binding assay in the reference DNA origami structure without nanoparticles as well as in NACHOS containing 100 nm silver nanoparticles by calculating the fraction of DNA origami structures containing the target and imager (% colocalization of green and red spots, Fig. 2f). Binding efficiencies of 66% and 84% were measured in NACHOS (light blue) and in the reference structures (orange), respectively, confirming that the hotspot accessibility for the target DNA sequence is not significantly compromised by attaching two 100 nm silver nanoparticles. We note that ~10 % higher imager binding yield was observed for the reference structure in the presence as well as in the absence of the target strand, which we attribute to higher non-specific sticking of the imager to the reference structure. We hypothesize this non-specific sticking is related to the single-stranded DNA for nanoparticle binding as unspecific binding is reduced after incorporation of two silver nanoparticles in the full nanoantenna construct (Fig. 2f).

To quantify the number of target molecules incorporated in each nanoantenna hotspot, we performed a single-molecule fluorescence photobleaching analysis (Fig. 2g) which allowed us to determine the number of Alexa Fluor 647 imager strands per DNA origami structure by counting the photobleaching steps in single-molecule fluorescence transients (Supplementary Fig. 7). The majority (~60%) of NACHOS contained one imager strand incorporated in the hotspot, one third of nanoantennas contained two imager strands, while three imager strands were observed in ~8–11% of single-molecule transients. The distribution of bleaching steps obtained for NACHOS as well as for the reference structures (Fig. 2g) further supports the observation that the

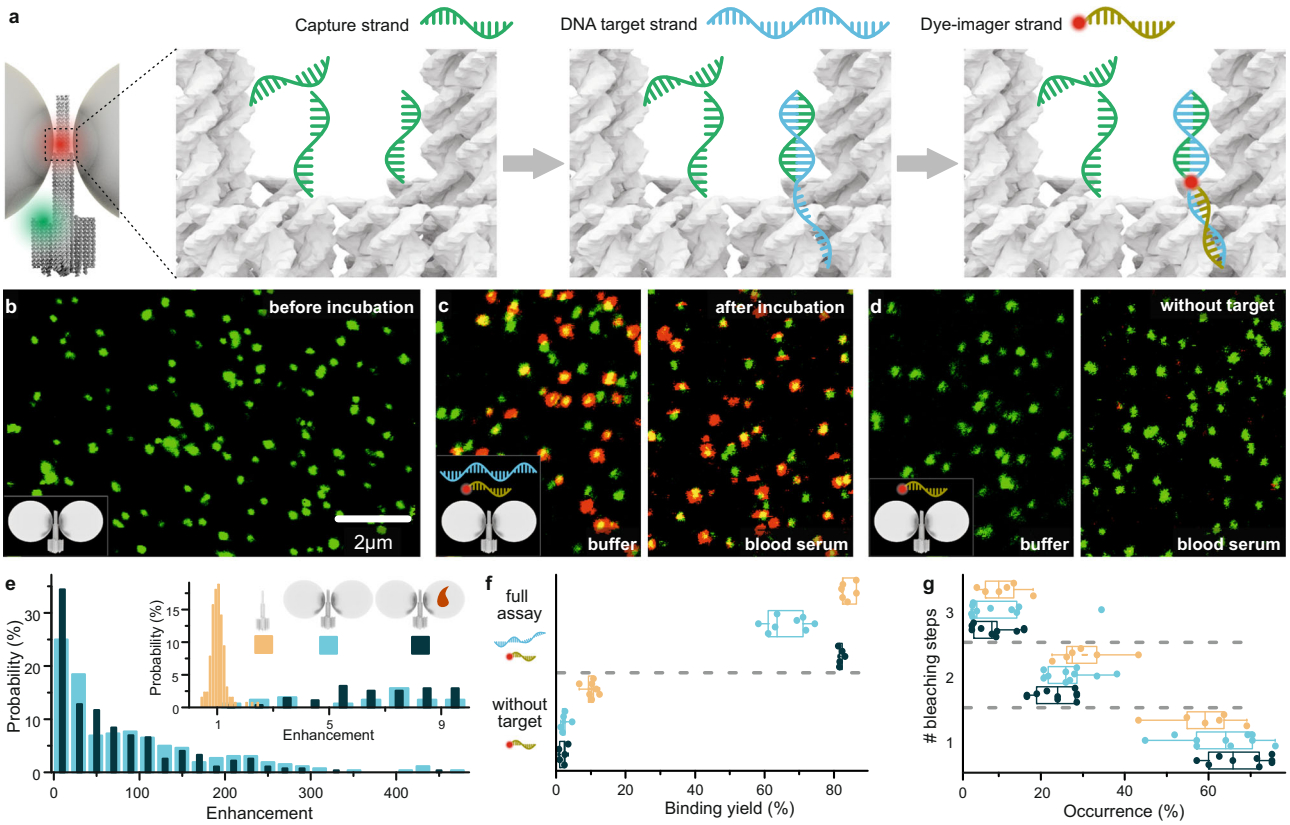

Fig. 2 Single-molecule diagnostic assay with NACHOS. a Sketch of NACHOS with three capture strands in the hotspot and a green reference dye (ATTO 542) for labeling of the DNA origami. Capture strands are placed in the NACHOS hotspot region. Upon incubation, they hybridize with DNA target strands specific to *Klebsiella pneumonia*, exposing a specific, 17-nt long region for the hybridization with the imager strand labeled with Alexa Fluor 647. **b** Confocal fluorescence image of the NACHOS before incubation with DNA target and imager strands. **c** Confocal fluorescence images after incubation with DNA target (2 nM) and imager strands (6 nM) in buffer solution (left) and blood serum (right), scale same as in panel **b**; **d** Confocal fluorescence image of the NACHOS after incubation with only the DNA imager strand (6 nM) in buffer solution (left) and blood serum (right), scale same as in panel b. The scans in panels b-d are representative for at least 20 images. **e** Fluorescence enhancement histogram of the sandwich assay in NACHOS measured in buffer solution (light blue) as well as in blood serum (dark blue). The inset includes a zoom in into the enhancement histogram overlaid with an enhancement histogram obtained for non-enhanced single Alexa Fluor 647 dyes (orange). Between 127 and 273 NACHOS and reference structures were analyzed in buffer solution and blood serum, respectively. **f** Binding yield obtained for the full sandwich assay (2 nM target and 6 nM imager strands) and for the control experiment (imager strand only) without nanoparticles (orange) as well as with nanoparticles in buffer solution (light blue) and in blood serum (dark blue). At least 546 spots were analyzed out of at least 5 different areas for each sample. Alexa Fluor 647 was excited at 639 nm and ATTO 542 at 532 nm. **g** Distribution of fluorescence bleaching steps observed in fluorescence transients for NACHOS in buffer solution and in blood serum and reference structures. Over 240 structures from at least 6 different areas per sample were analyzed. The box plots in panels **f** and **g** show the 25/75 percentiles and the whisker represents the 1.5*IQR (inter quartile range) length, the center lines represent the average values.

presence of silver nanoparticles does not obstruct the hotspot accessibility for the DNA target.

Single-molecule detection in human blood serum. To demonstrate that NACHOS can still function in complex biological fluids that compromise many diagnostic assays, we have also performed the sandwich detection assay described above in human blood serum spiked with the target DNA sequence specific to the *OXA-48* gene. The serum was first heat-inactivated and then enriched with 2 nM target DNA sequence as well as 6 nM Alexa Fluor 647 imager strand. The fully assembled NACHOS were then incubated in the serum mixture for 2 h at 37 °C. Fluorescence scans of the NACHOS after incubation with serum and target DNA sequence are included in Fig. 2c, d (as well as Supplementary Fig. 8). Almost identical fluorescence enhancement values (Fig. 2e), target binding efficiencies (Fig. 2f) and number of single-molecule photobleaching steps (Fig. 2g) were obtained for reference and NACHOS samples in highly purified buffer (light blue) and serum (dark blue) conditions confirming that neither the stability of NACHOS nor the performance of the sandwich assay in NACHOS are compromised. On the contrary, fluorescence enhancement values reaching 457-fold (average of 70 ± 4) could be achieved for the DNA detection assay in target spiked human serum. These findings proof the robustness of NACHOS under realistic assay conditions and provide an important stepping stone towards diagnostic applications.

Single-molecule detection on a portable microscope using NACHOS. Recently, the detection of only 10–16 ATTO 542 molecules was demonstrated using a simple table top setup with a monochrome smartphone camera as detector and a consumer product lens for light collection[16]. This inspired us that single-molecule detection might be possible on a portable smartphone microscope with non-specialized low-NA optics[2,22–24] (see Fig. 3a, b). The microscope uses the monochrome camera of a Huawei P20 smartphone for detection, data processing and interfacing and a battery-driven 638 nm excitation laser with

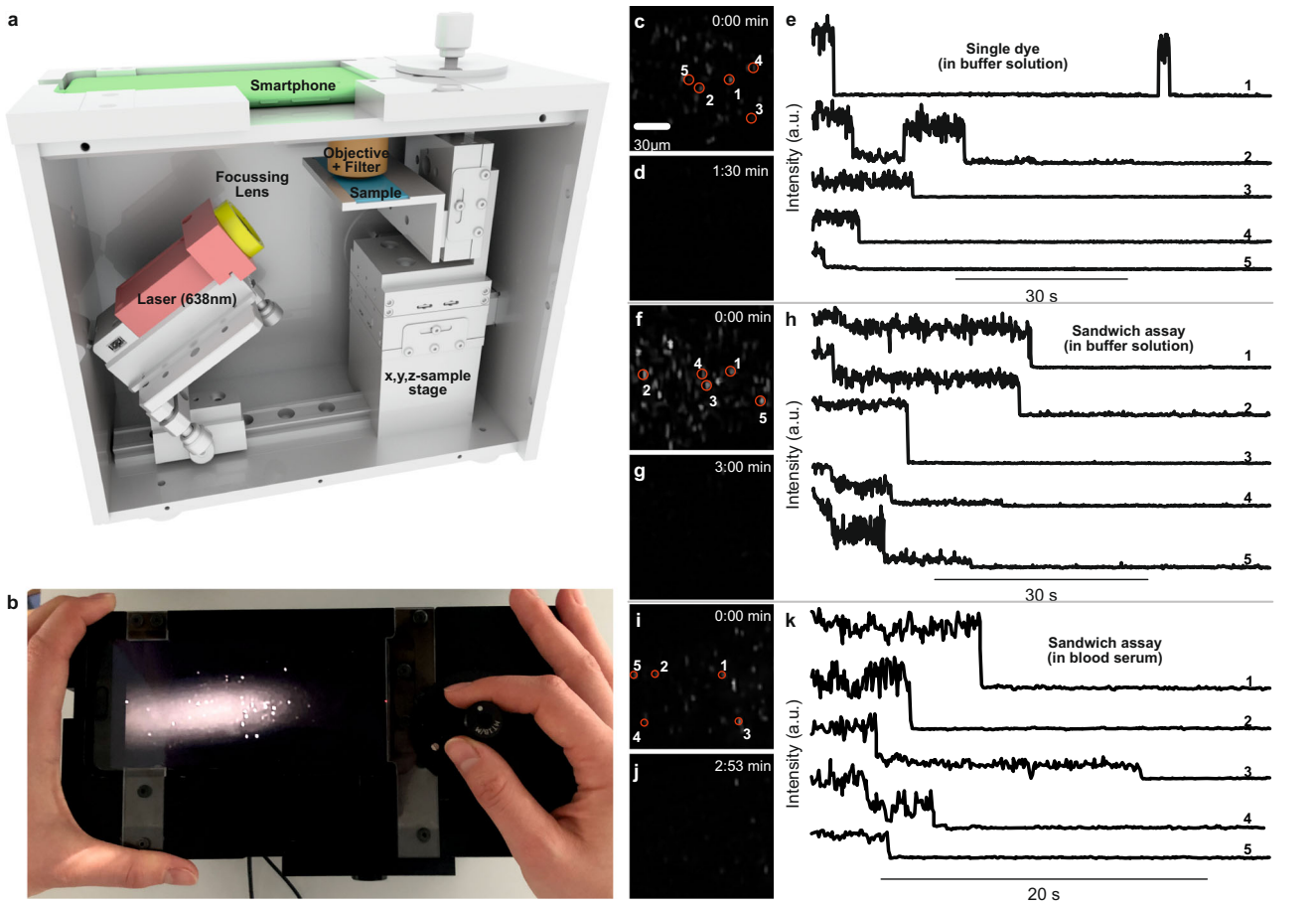

Fig. 3 Single-molecule detection on a portable smartphone microscope. a Sketch of the portable smartphone microscope with the battery driven 638 nm laser (red), the focusing lens ($f = 5$ cm) (yellow), the microscope coverslip with the sample (blue), the objective lens and the emission filter (brown), and the smartphone monochrome camera as detector (green). **b** Top view photograph of the portable smartphone microscope. **c** Background corrected fluorescence image of NACHOS with 100 nm silver nanoparticles and a single Alexa Fluor 647 dye. **d** Fluorescence image as in **c** after illumination for 1:30 min. **e** Exemplary fluorescence transients of a single Alexa Fluor 647 in NACHOS measured on the portable microscope setup. Single bleaching steps of dyes and long-time blinking events are visible. **f** Background corrected fluorescence image of NACHOS equipped with a sandwich assay with 100 nm silver nanoparticles and Alexa Fluor 647 imager strands. **g** Fluorescence image as in **f** after illumination of the area for 3:00 min. **h** Exemplary fluorescence transients of Alexa Fluor 647 in a three-capture-strand DNA origami nanoantenna measured on the portable smartphone microscope. **i** Background corrected fluorescence image of NACHOS equipped with the sandwich assay with 100 nm silver nanoparticles and Alexa Fluor 647 imager strands after incubation in blood serum. **j** Fluorescence image as in **i** after illumination of the area for 2:53 min. **k** Exemplary fluorescence transients of Alexa Fluor 647 in a three-capture-strand NACHOS measured on the portable smartphone microscope. Fluorescence transients with one, two, and three bleaching steps (analogous to single-molecule confocal measurements) were observed. The movies represented in the panels **c**, **d**, **f**, **g**, **i** and **j** were reproduced at least 5 times. Three movies for each measurement are provided in the Supplementary Movies. The fluorescence transients shown in panels **e**, **h** and **k** were extracted from a single movie.

180 mW output power. The excitation laser (red in Fig. 3a) is focused on the sample plane at approximately 45° using a lens with a focal length of 5 cm to illuminate an elliptical area of ~150 × 200 µm^2. Fluorescence emission is collected and collimated with a consumer product lens (NA = 0.25, 8 US$, yielding a resolution of ~1.2 µm in the red wavelength range), bandpass filtered and focused onto the smartphone detector using the internal lens in the infinite focal distance mode. A discussion of the total price of the components used in the prototype smartphone microscope (sum of ~ 4200 €) can be found in Supplementary Note 1. We envision that the price can be reduced in the case of upscaling production (<1000 €). Importantly, the affordable microscope does not imply expensive sample preparation. The single-molecule nature of measurements requires substantial dilution of the DNA origami samples and DNA functionalized nanoparticles yielding an estimated price per NACHOS coverslip preparation of below 5 € (Supplementary Note 2).

First, we prepared NACHOS with 100 nm silver nanoparticles and a single Alexa Fluor 647 dye in the hotspot. Considering the low resolution of the smartphone microscope, the concentration of NACHOS on the surface was adjusted to a reasonably low density to ensure that only one nanoantenna is present per diffraction limited spot (see Materials and Methods section). To improve the photostability of Alexa Fluor 647 and demonstrate single-molecule bleaching steps, the measurements were carried out in a reducing and oxidizing system (ROXS)[25,26] with enzymatic oxygen removal. Upon illumination, multiple bright spots were observed on the smartphone screen (Fig. 3c). In the movies recorded with 80 ms per frame, slow single-molecule blinking and bleaching (Supplementary Fig. 9) was observed (see Supplementary Movies 1–3) as indicated by the disappearance of spots over time (compare Fig. 3c, d). Extracted fluorescence transients (spots from one movie) are shown in Fig. 3e, demonstrating typical single-molecule behavior with

blinking and single-step bleaching events. These transients represent the first examples of single-molecule fluorescence detection with a portable smartphone microscope and non-dedicated optics bringing single-molecule detection a step closer to point-of-care settings. The signal-to-background ratio (SBR) and the signal-to-noise ratio (SNR) of the transients on the smartphone microscope are determined to be 25 ± 2 and 3.8 ± 0.2, respectively. Examples of fast blinking of single ATTO 647N dyes in the hotspot of NACHOS with 100 nm silver nanoparticles can be found in Supplementary Movie 4 and Supplementary Fig. 10.

Next, we tested whether the portable smartphone microscope could also be used for the detection of single DNA molecules in analogy to the sandwich assay discussed in Fig. 2. The sandwich assay with three capture strands for the detection of the resistance gene *OXA-48* imaged with the portable smartphone microscope is shown in Fig. 3f. All fluorescence spots acquired on the smartphone camera were photobleached after 3 min of movie recording (see Supplementary Movies 5–7). The extracted transients (Fig. 3h) exhibit bleaching of the imager strands with 1–3 bleaching steps in accordance with the single-molecule fluorescence transients acquired on the confocal microscope shown in Supplementary Fig. 7. More examples of extracted transients for the sandwich assay with three binding strands in the NACHOS hotspot are included in Supplementary Fig. 12. In control measurements under identical conditions leaving out the nanoparticles, no signal could be detected. As a further control, we incubated the coverslips with silver nanoparticles only. A few dim spots that did not disappear after long illumination are ascribed to scattering from silver nanoparticle aggregates (Supplementary Fig. 11). These results confirm that single-molecule detection of disease-specific DNA can also be performed on our portable smartphone microscope omitting the need for advanced and expensive microscopes. Finally, the DNA detection assay after incubation with human blood serum was also measured on the portable smartphone microscope. Images at the beginning as well as at the end of the movie and exemplary fluorescence transients are shown in Fig. 3i, j, k. The results are almost identical to the measurements in purified buffer solution (Fig. 3f–h) with a decreasing number of isolated fluorescent spots detected on the camera (Fig. 3i, j) due to photobleaching. In a similar way the fluorescent transients (Fig. 3k) show clear single, double and triple bleaching steps with no difference visible between the purified buffer and the blood serum assays. More example movies and transients for the measurements of the sandwich assay inside the NACHOS are shown in Supplementary Movies 8–10 and Supplementary Fig. 13. The photobleaching analysis for the transients from the movie taken on the smartphone microscope is shown in Supplementary Fig. 14 and yields similar distributions for single, double and triple photobleaching steps as compared to the data shown in Fig. 2g, highlighting the ability of the smartphone microscope in combination with NACHOS to provide analytical power comparable to conventional single-molecule microscopy tools.

Self-assembled nanoantennas with a cleared and addressable hotspot represent an inexpensive and versatile platform for fluorescence signal enhancement assays. Single fluorescent molecules immobilized in the hotspot of these newly designed nanoantennas yield higher fluorescence enhancement values than previous approaches with hotspots blocked by the DNA origami nanostructure. NACHOS are robust (see Supplementary Fig. 15 for single-molecule data of a similar sample measured over 13 weeks), stable in complex biological fluids such as human serum, and importantly, the accessibility of the hotspot for target DNA molecules and imagers is not impaired despite the constricted dimensions. A single-molecule sandwich assay with three capturing strands shows equally high fluorescence enhancement as direct incorporation of a single fluorescent dye in the hotspot and enables single-molecule detection with amplified signal that facilitates discrimination of single-molecule binding events against an unavoidable background of single-molecule impurities (Fig. 2e inset). The demonstration of single-molecule assays on a simple battery-operated smartphone microscope makes DNA origami nanoantennas a stepping-stone for democratizing single-molecule detection with cost-effective and mobile devices relevant for point-of-care applications.

Methods

DNA origami. DNA origami structures were designed in caDNAno2[27] and assembled and purified using protocols inspired by Wagenbauer et al.[28]. Briefly, 25 µL of p8064 scaffold (produced in-house) at 100 nM were mixed with 18 µL of unmodified staples pooled from 100 µM original concentration and 2 µL of modified staples, pooled from 100 µM original concentration. All staples were purchased from Eurofins Genomics GmbH (Germany) - for the exact sequences see Supplementary Table 2. 5 µL of folding buffer (200 mM $MgCl_2$, 50 mM Tris, 50 mM NaCl, 10 mM EDTA) were added and the mixture was subjected to a thermal annealing ramp (see Supplementary Table 1). Samples were purified using 100 kDa MWCO Amicon Ultra filters (Merck KGaA, Germany) with 4 washing steps with a lower ionic strength buffer (5 mM $MgCl_2$, 5 mM Tris, 5 mM NaCl, 1 mM EDTA) for 8 mins at 8 krcf, 20 °C.

Functionalization of silver nanoparticles. 100 nm silver nanoparticles (100 nm BioPure Silver Nanospheres (Citrate), nanoComposix, USA) were functionalized with T_{20} single-stranded DNA oligonucleotides with a thiol modification at the 3'-end (Ella Biotech GmbH, Germany)[15]. Briefly, 2 mL of 0.025 mg/mL nanoparticle solution in ultra pure water was heated to 40 °C under permanent stirring. 20 µL of 10 % Tween 20 and 20 µL of a potassium phosphate buffer (4:5 mixture of 1 M monobasic and dibasic potassium phosphate, Sigma Aldrich, USA) were added as well as 10 µL of a 2 nmol thiol-modified single-stranded DNA solution (5'-T_{20}-SH-3') and incubated for 1 h at 40 °C. A salting procedure was then carried out by adding 1× PBS buffer containing 3.3 M NaCl stepwise over 45 min to the heated and stirred solution, until a final concentration of 750 mM NaCl was reached. Afterwards, the particles were mixed 1:1 with 1× PBS 10 mM NaCl, 2.11 mM P8709 buffer (Sigma Aldrich, USA), 2.89 mM P8584 buffer (Sigma Aldrich, USA), 0.01 % Tween® 20 and 1 mM EDTA. To remove the excess thiolated single-stranded DNA, the solution was centrifuged for 15 min at 2.8 krcf and 20 °C. A pellet was formed in which the particles were concentrated. The supernatant was discarded, and the washing step was repeated six more times. After functionalization of the silver nanoparticles were diluted in 1× TE buffer (10 mM Tris, 1 mM EDTA) containing 750 mM NaCl to reach the final extinction of 0.05 (0.1 mm path length) at the extinction maxima on a UV-Vis spectrometer (Nanodrop 2000, Thermo Fisher Scientific, USA).

Solution synthesis of DNA origami nanoantennas for TEM imaging. To obtain DNA origami nanoantennas in solution, the structures were initially assembled on streptavidin-coated magnetic beads (Dynabeads™ MyOne™ Streptavidin C1, 1 µm diameter, 10 mg/mL, Thermo Fischer Scientific, USA). Preparation of magnetic beads: 3.0 µL of bead stock solution (~20–30 ×10^6 beads) were washed three times with 50 µL 1× B&W buffer (0.5 mM EDTA, 5 mM Tris-HCl (pH = 8), 1 M NaCl, 0.001 % v/v Tween® 20). After removing the supernatant, the beads were diluted in 6.0 µL 1× B&W and incubated with 6.0 µL of 4 µM biotinylated ssDNA (mag1, Supplementary Table 5) for 20 min at room temperature. The functionalized beads were purified from excess of ssDNA by placing the tube on a magnet and discarding the supernatant. The beads were redispersed in 50 µL 1× B&W and washed with 1× B&W buffer (3× 50 µL). Immobilization of DNA Origami on Magnetic Beads: DNA origami (100 µL, 200 pM in 1× B&W buffer) with three ssDNA overhang strands on a bottom partially complementary to the sequence on the magnetic beads (mag2, Supplementary Table 5) were incubated together for 2 h at 37 °C under gentle shaking (450 rpm, Eppendorf ThermoMixer® C, Eppendorf AG, Germany). Unbound DNA origami was removed by placing the tube on a magnet and discarding the supernatant. The beads were redispersed in 50 µL 1× B&W and washed with 1× B&W buffer (5× 50 µL). Binding of 100 nm silver nanoparticles: Nanoantennas were fabricated on magnetic beads by hybridizing with DNA functionalized (5'-T_{20}-SH-3') 100 nm silver nanoparticles to the DNA origamis. For this the supernatant of the with DNA origami coated beads was removed and incubated with 100 µL of 100 nm silver nanoparticles solution using an excess of five nanoparticles per binding site. During the first three hours of incubation, the solution was mixed every 30 min by gentle pipetting. After overnight incubation at room temperature, the excess of nanoparticles was removed by placing the tube on a magnet and discarding the supernatant. The beads were re-dissolved in 50 µL 1× B&W and washed with 1× B&W buffer (5× 50 µL). Cleavage of the assembled structures: Nanoantennas were cleaved from the beads surface by performing a toehold-mediated strand displacement reaction. For cleavage, the supernatant of

the bead solution was removed and nanoantennas coated beads were incubated with 20 µL 10 µM of the displacement strand (mag3, Supplementary Table 5) for 4 h at room temperature. Unbound DNA origami nanoantennas were recovered for further use by placing the tube on a magnet.

Transmision electron microscopy (TEM) measurements. TEM grids (Formvar/carbon, 400 mesh, Cu, TedPella, Inc., USA) were Ar-plasma cleaned and incubated for 60 s with DNA origami sample (5 µL, ~ 2–10 nM). Grids were washed with 2 % uranyl formate solution (5 µL) and incubated again afterwards again 4 s with 2% uranyl formate solution (5 µL) for staining. TEM imaging were performed on a JEM-1100 microscope (JEOL GmbH, Japan) with an acceleration voltage of 80 kV.

Sample preparation on the coverslip for single-molecule confocal measurements. Microscope coverslips of 24 mm × 60 mm size and 170 µm thickness (Carl Roth GmbH, Germany) were cleaned with UV-Ozone cleaner (PSD-UV4, Novascan Technologies, USA) for 30 min at 100 °C. Adhesive SecureSeal™ Hybridization Chambers (2.6 mm depth, Grace Bio-Labs, USA) were glued on the clean coverslips. The created wells were washed three times with PBS buffer and then incubated with BSA-biotin (0.5 mg/mL, Sigma-Aldrich, USA) and NeutrAvidin (0.2 mg/mL, Thermo Fisher Scientific, USA). The DNA origami (50–100 pM in 1× TE buffer containing 750 mM NaCl) was immobilized on the biotin-NeutrAvidn surfaces using covalently attached biotin modifications on the six staple strands on the base. Density of DNA origami nanoantennas on the surface suitable for single-molecule measurements was checked on a microscope. The binding of silver nanoparticles was then performed by incubating the surfaces with 100 µL of T_{20}-functionalized silver nanoparticles in 1× TE buffer containing 2 M NaCl overnight at room temperature. To prevent the evaporation of samples, samples were kept in a sealed humidity chambers during the incubation. The nanoantennas were then imaged in 1× TE buffer containing 14 mM $MgCl_2$.

Diagnostic sandwich assay. To specifically detect the DNA sequence specific to the *OXA-48* gene carrying the antibiotic resistance[19,20], DNA origami nanoantennas were folded containing three specific capture strands (Supplementary Table 4) extruding from the hotspot region of the nanoantenna. After the assembly of the full nanoantenna in the analogous way to the previous section, the samples were incubated with 2 nM target DNA sequence (34 nt) specific to the *OXA-48* gene (Supplementary Table 4) as well as 6 nM Alexa Fluor 647 imager strand (17 nt) labeled with Alexa Fluor 647 (Supplementary Table 4) in 1× TE buffer containing 2 M NaCl. The sample was incubated for at 37 °C for 2 h and the excess of the target and imager strands was removed by washing six times with 1× TE buffer containing 2 M NaCl. The nanoantennas were then imaged in 1× TE buffer containing 14 mM $MgCl_2$.

For the sandwich assay in serum clotted, whole blood, sterile and filtered human blood serum (Human Serum, (from male AB clotted whole blood), USA origin, sterile-filtered, Sigma-Aldrich, USA) was used. Before adding the serum to the NACHOS and reference samples, the serum was heat inactivated by exposing it for 30 min to 56 °C and spiked with 2 nM target DNA, 6 nM imager strand and 2 M NaCl. The fully assembled NACHOS or reference DNA origami structures were incubated with target-spiked blood serum for 2 h at 37 °C and the excess of target and imager strands was removed by washing six times with 1× TE buffer containing 2 M NaCl. NACHOS were then imaged in 1× TE buffer containing 14 mM $MgCl_2$.

Confocal measurements and data analysis. Confocal fluorescence measurements were performed using a home-built confocal setup based on an inverted microscope (IX-83, Olympus Corporation, Japan) and a 78 MHz-pulsed supercontinuum white light laser (SuperK Extreme EXW-12, NKT Photonics A/S, Denmark) with selected wavelengths of 532 nm and 639 nm. The wavelengths are selected via an acousto-optically tunable filter (AOTF, SuperK Dual AOTF, NKT Photonics A/S, Denmark). This is controlled by a digital controller (AODS 20160 8 R, Crystal Technology, USA) via a computer software (AODS 20160 Control Panel, Crystal Technology, Inc., USA). A second AOTF (AA.AOTF.ns: TN, AA Opto-Electronic, France) was used to alternate 532 nm and 639 nm wavelengths if required, as well as to further spectrally clean the laser beam. It is controlled via home-made LabVIEW software (National Instruments, USA). A neutral density filter was used to regulate the laser intensity, followed by a linear polarizer and a λ/4 plate to achieve circularly polarized excitation. A dichroic beam splitter (ZT532/640rpc, Chroma Technology, USA) and an immersion oil objective (UPlanSApo 100×, NA = 1.4, WD = 0.12 mm, Olympus Corporation, Japan) were used to focus the excitation laser onto the sample. Micropositioning was performed using a Piezo-Stage (P-517.3CL, E-501.00, Physik Instrumente GmbH&Co. KG, Germany). The excitation powers at 639 nm were set to 200 nW or for 500 nW for the reference samples and to 50 nW for the NACHOS for the recording of the fluorescence transients. These powers were chosen to ensure that the samples are excited in the linear regime and to avoid saturation in the nanoantenna hotspot[29]. For the confocal scans, 2 µW at 532 nm and 2 µW and 500 nW at 639 nm were used for the reference and NACHOS samples, respectively. Emitted light was then collected using the same objective and filtered from the excitation light by the dichroic beam splitter. The light was later focused on a 50 µm pinhole (Linos AG, Germany) and detected using avalanche photodiodes (SPCM, AQR 14, PerkinElmer, Inc., USA) registered by an TCSPC system (HydraHarp 400, PicoQuant GmbH, Germany) after additional spectral filtering (RazorEdge 647, Semrock Inc., USA for the red channel and BrightLine HC 582/75, Semrock Inc., USA for the green channel). A custom-made LabVIEW software (National Instruments, USA) was used to process the acquired raw data. Background correction was made individually for each transient. The extracted data were analyzed in OriginPro2016.

Sample preparation for single-molecule measurements on the smartphone microscope. The geometry of the smartphone-based microscope required samples to be sealed. To this end, microscope cover slides of 22 mm × 22 mm size and 170 µm thickness (Carl Roth GmbH, Germany) were cleaned with UV-Ozone cleaner (PSD-UV4, Novascan Technologies, USA) for 30 min at 100 °C. After this a home-made silicon mask with an opening around 15 mm × 15 mm was glued on a coverslip to create an incubation chamber. Surface functionalization, DNA origami immobilization (5 - 10 pM), nanoantenna formation, and the sandwich sensing assay were performed the same was as described above for the NACHOS assembly on coverslips. To seal the samples, the silicon mask was removed, and a double-sided tape was glued on both sides of the cover slide. Then the cover slides were covered with 76 mm × 26 mm microscope slides (1 mm thickness, Carl Roth GmbH, Germany) which were priory cleaned with UV-Ozone cleaner for 30 min at 100 °C. Due to limited photostability of Alexa Fluor 647, samples containing the sandwich assay were imaged in the presence of ROXS photostabilization system. A reducing and oxidizing buffer system with enzymatic oxygen removal consisting of 90 % buffer A (14 mM $MgCl_2$, 50 mM Tris, 2 mM Trolox/Troloxquinone and 1 % w/v Glucose) and 10 % buffer B (glucose oxidase (1 mg/mL), 0.4 % (v/v) catalase (50 µg/mL), 30 % glycerol, 12.5 mM KCl) was used. After this the chambers were sealed with nail polish and imaged after the drying of the glue.

Single-molecule measurements and analysis on the smartphone. Single-molecule measurements on the smartphone were performed using a home-built portable box. The 638 nm laser diode (0638L-11A, Integrated Optics, UAB, Lithuania) with an output power 180 mW that can be driven by various (portable) voltage sources (Power plug, mobile power bank, (rechargeable) batteries) was focused (f = 50 mm) in 45° angle onto the sample. The fluorescence of the molecules was collected using an objective lens (NA = 0.25, LS-40166, UCTRONICS, USA) guiding the light to the monochrome camera of the smartphone (P20, Huawei, China) after spectral filtering (BrightLine HC 731/137, Semrock Inc., USA). Movies were recorded via FreeDCam application and analyzed with ImageJ (FIJI) equipped with FFMPEG plugin using a home written macro to convert MP4 format of the acquired movies to a TIFF format and find the single-molecule signals and extract the fluorescence intensity as a function of illumination time. The extracted data were analyzed in OriginPro2016.

Reporting summary. Further information on research design is available in the Nature Research Reporting Summary linked to this article.

Data availability

The raw data acquired in this study are available in a public Zenodo repository (DOI: 10.5281/zenodo.4384169). This includes TEM images, raw and analyzed confocal data, raw movies acquired on the smartphone device, as well as the caDNAno file for the DNA origami nanostructure reported in this work. Further information is available from the authors upon request.

Code availability

A custom script used to analyze the movies obtained on the smartphone device is available in the Zenodo repository under DOI: 10.5281/zenodo.4384169.

Received: 12 October 2020; Accepted: 13 January 2021;
Published online: 11 February 2021

References

1. Gill, P. & Ghaemi, A. Nucleic acid isothermal amplification technologies: a review. *Nucleosides Nucleotides Nucleic Acids* **27**, 224–243 (2008).
2. Diederich, B., Then, P., Jügler, A., Förster, R. & Heintzmann, R. cellSTORM-Cost-effective super-resolution on a cellphone using dSTORM. *PLoS ONE* **14**, e0209827–e0209827 (2019).
3. Gu, L. et al. Research progress on rolling circle amplification (RCA)-based biomedical sensing. *Pharmaceuticals* **11**, 35 (2018).
4. Fakruddin, M. et al. Nucleic acid amplification: alternative methods of polymerase chain reaction. *J. Pharm. Bioallied. Sci.* **5**, 245–252 (2013).
5. Kühnemund, M. et al. Targeted DNA sequencing and in situ mutation analysis using mobile phone microscopy. *Nat. Commun.* **8**, 13913 (2017).

6. Taylor, A. B. & Zijlstra, P. Single-molecule plasmon sensing: current status and future prospects. *ACS Sens.* **2**, 1103–1122 (2017).
7. Walt, D. R. Optical methods for single molecule detection and analysis. *Anal. Chem.* **85**, 1258–1263 (2013).
8. Li, J.-F., Li, C.-Y. & Aroca, R. F. Plasmon-enhanced fluorescence spectroscopy. *Chem. Soc. Rev.* **46**, 3962–3979 (2017).
9. Bauch, M., Toma, K., Toma, M., Zhang, Q. & Dostalek, J. Plasmon-enhanced fluorescence biosensors: a review. *Plasmonics* **9**, 781–799 (2014).
10. Punj, D. et al. A plasmonic 'antenna-in-box' platform for enhanced single-molecule analysis at micromolar concentrations. *Nat. Nanotechnol.* **8**, 512–516 (2013).
11. Anger, P., Bharadwaj, P. & Novotny, L. Enhancement and quenching of single-molecule fluorescence. *Phys. Rev. Lett.* **96**, 113002 (2006).
12. Curto, A. G. et al. Unidirectional emission of a quantum dot coupled to a nanoantenna. *Science* **329**, 930–933 (2010).
13. Rothemund, P. W. K. Folding DNA to create nanoscale shapes and patterns. *Nature* **440**, 297–302 (2006).
14. Acuna, G. P. et al. Fluorescence enhancement at docking sites of DNA-directed self-assembled nanoantennas. *Science* **338**, 506–510 (2012).
15. Ochmann, S. E. et al. Optical nanoantenna for single molecule-based detection of zika virus nucleic acids without molecular multiplication. *Anal. Chem.* **89**, 13000–13007 (2017).
16. Vietz, C. et al. Benchmarking smartphone fluorescence-based microscopy with DNA origami nanobeads: reducing the gap toward single-molecule sensitivity. *ACS Omega* **4**, 637–642 (2019).
17. Puchkova, A. et al. DNA origami nanoantennas with over 5000-fold fluorescence enhancement and single-molecule detection at 25 mm. *Nano Lett.* **15**, 8354 (2015).
18. Vietz, C., Lalkens, B., Acuna, G. P. & Tinnefeld, P. Synergistic combination of unquenching and plasmonic fluorescence enhancement in fluorogenic nucleic acid hybridization probes. *Nano Lett.* **17**, 6496 (2017).
19. Hrabak, J., Chudackova, E. & Papagiannitsis, C. C. Detection of carbapenemases in Enterobacteriaceae: a challenge for diagnostic microbiological laboratories. *Clin. Microbiol. Infect.* **20**, 839–853 (2014).
20. Poirel, L., Héritier, C., Tolün, V. & Nordmann, P. Emergence of oxacillinase-mediated resistance to imipenem in Klebsiella pneumoniae. *Antimicrob. Agents Chemother.* **48**, 15–22 (2004).
21. Strauss, M. T., Schueder, F., Haas, D., Nickels, P. C. & Jungmann, R. Quantifying absolute addressability in DNA origami with molecular resolution. *Nat. Commun.* **9**, 1600 (2018).
22. Wei, Q. et al. Fluorescent imaging of single nanoparticles and viruses on a smart phone. *ACS Nano* **7**, 9147–9155 (2013).
23. Wei, Q. et al. Imaging and sizing of single DNA molecules on a mobile phone. *ACS Nano* **8**, 12725–12733 (2014).
24. Ozcan, A. Mobile phones democratize and cultivate next-generation imaging, diagnostics and measurement tools. *Lab Chip* **14**, 3187–3194 (2014).
25. Vogelsang, J. et al. A reducing and oxidizing system minimizes photobleaching and blinking of fluorescent dyes. *Angew. Chem. Int. Ed.* **47**, 5465–5469 (2008).
26. Ha, T. & Tinnefeld, P. Photophysics of fluorescent probes for single-molecule biophysics and super-resolution imaging. *Annu. Rev. Phys. Chem.* **63**, 595–617 (2012).
27. Douglas, S. M. et al. Rapid prototyping of 3D DNA-origami shapes with caDNAno. *Nucleic Acids Res.* **37**, 5001–5006 (2009).
28. Wagenbauer, K. F. et al. How we make DNA origami. *ChemBioChem* **18**, 1873–1885 (2017).
29. Grabenhorst, L., Trofymchuk, K., Steiner, F., Glembockyte, V. & Tinnefeld, P. Fluorophore photostability and saturation in the hotspot of DNA origami nanoantennas. *Methods Appl. Fluoresc.* **8**, 024003 (2020).
30. Vietz, C., Lalkens, B., Acuna, G. P. & Tinnefeld, P. Functionalizing large nanoparticles for small gaps in dimer nanoantennas. *N. J. Phys.* **18**, 045012 (2016).

Acknowledgements

The authors thank Vivien Behrendt and Benedikt Hauer (Fraunhofer-Institut für Physikalische Messtechnik IPM, Freiburg, Germany) for cooperation on the assay development and Prof. Tim Liedl/Prof. Joachim Rädler (Ludwig-Maximilians-Universität, Department für Physik, Munich, Germany) for providing access to their facilities especially to the transmission electron microscope. The authors thank Tomas Gisicius for manufacturing the portable smartphone microscope. P.T. gratefully acknowledges financial support from the DFG (INST 86/1904-1 FUGG, excellence clusters NIM and e-conversion), BMBF (Grants POCEMON, 13N14336, and SIBOF, 03VP03891), and the European Union's Horizon 2020 research and innovation program under grant agreement No. 737089 (Chipscope). G.P.A. gratefully acknowledges support by the Swiss National Science Foundation through the National Center of Competence in Research Bio-Inspired Materials and through grant number 200021_184687. V.G. and K.T. acknowledge the support by Humboldt Research Fellowships from the Alexander von Humboldt Foundation. A.O. acknowledges the support of NSF PATHS-UP and HHMI. BL acknowledges funding by the Deutsche Forschungsgemeinschaft (DFG, German Research Foundation) under Germany's Excellence Strategy – EXC-2123 QuantumFrontiers – 390837967 and "Niedersächsisches Vorab" through "Quantum- and Nano-Metrology (QUANOMET)" initiative within the project NL-1.

Author contributions

P.T., A.O. and G.P.A. conceived the project, L.G. and B.L. developed the DNA origami structure, K.T., V.G. and M.P. optimized the solution synthesis procedure, F.Se. performed the TEM measurements, K.T., V.G., C.C., M.P. and R.Y. developed the sandwich assay and prepared samples, performed and analyzed the measurements on the confocal microscope, C.V., L.R., M.L.S., Q.W., A.O. and G.P.A. worked on an earlier version of the smartphone microscope, K.T., V.G., F.St. and J.Z. constructed the portable smartphone microscope, K.T., V.G. and F.St. performed and analyzed the measurements on the smartphone microscope, K.T., V.G., L.G., F.St. and P.T. wrote the manuscript. All authors have read and aproved the final manuscript.

Funding

Open Access funding enabled and organized by Projekt DEAL.

Competing interests

P.T. and G.P.A. are inventors on an awarded patent of the described bottom-up method for fluorescence enhancement in molecular assays, EP1260316.1, 2012, US20130252825 A1. The remaining authors declare no competing interests.

Additional information

Supplementary information The online version contains supplementary material available at https://doi.org/10.1038/s41467-021-21238-9.

Correspondence and requests for materials should be addressed to K.T., V.G., G.P.A. or P.T.

Peer review information *Nature Communications* thanks the anonymous reviewer(s) for their contribution to the peer review of this work. Peer reviewer reports are available.

Reprints and permission information is available at http://www.nature.com/reprints

Publisher's note Springer Nature remains neutral with regard to jurisdictional claims in published maps and institutional affiliations.

Supporting Information for

Addressable Nanoantennas with Cleared Hotspots for Single-Molecule Detection on a Portable Smartphone Microscope

Kateryna Trofymchuk[1,2]†*, Viktorija Glembockyte[1]†*, Lennart Grabenhorst[1], Florian Steiner[1], Carolin Vietz[2], Cindy Close[1], Martina Pfeiffer[1], Lars Richter[2], Max L. Schütte[2], Florian Selbach[1], Renukka Yaadav[1], Jonas Zähringer[1], Qingshan Wei[3], Aydogan Ozcan[4], Birka Lalkens[5], Guillermo P. Acuna[6] *, and Philip Tinnefeld[1]*

[1] Department of Chemistry and Center for NanoScience, Ludwig-Maximilians-Universität München, Butenandtstr. 5-13, 81377 München, Germany
[2] Institute for Physical and Theoretical Chemistry - NanoBioScience and Braunschweig Integrated Centre of Systems Biology (BRICS), Technische Universität Braunschweig, Braunschweig, Germany
[3] Department of Chemical and Biomolecular Engineering, North Carolina State University, Raleigh, NC, 27695, Unites States
[4] Electrical & Computer Engineering Department, Bioengineering Department, California NanoSystems Institute (CNSI), and Department of Surgery, University of California, Los Angeles, California 90095, United States
[5] Institut für Halbleitertechnik, Laboratory for Emerging Nanometrology LENA, TU Braunschweig, Langer Kamp 6a/b, 38106 Braunschweig, Germany
[6] Département de Physique - Photonic Nanosystems, Université de Fribourg - Faculté des Sciences et Médicine Chemin de Musée 3, CH-1700 Fribourg, Switzerland

† These authors contributed equally: Kateryna Trofymchuk, Viktorija Glembockyte

* email: kateryna.trofymchuk@cup.lmu.de; viktorija.glembockyte@cup.lmu.de; guillermo.acuna@unifr.ch; philip.tinnefeld@cup.uni-muenchen.de

Table of contents

Supplementary Table 1. Temperature ramp used for folding DNA origami nanostructures

Temperature [°C]	Time [s]
65	300
65	50
64	95
63	95
62	95
61	95
60	540
59	540
58	1140
57	1740
56	2340
55	2940
54	3540
53	3540
52	3540
51	3540
50	3540
49	3540
48	3540
47	3540
46	3540
45	3540
44	2940
43	2340
42	1740
41	1140
40	1140
39	1140
38	540
37	540
36	290
35	290
34	290
33	290
32	290
31	290
30	290
29	50
28	50
27	50
26	50
25	50

Supplementary Table 2. Unmodified staple strands used to fold the DNA origami nanostructures

Name	Sequence (5'→3')
1	TTTAAATGTTTGCTGAGATTTAGGACCCACGCGAA
2	TTAGAACGCAATTAAGACAAATACATACATAAA
3	TTTAAGCAAATTCACAAAGTATTAAGAGGCTCGGA
4	TAAATACCCGGATATCATCAACGGTCAATCATAAGACCATCGATAC
5	GAAGGGATAGCGAGATAGTTCCGGCCAGGAAGAAGAATGAGGT
6	GCAACTGGCGAAAGGGGAGTAAAGTTGCCGGAGTGAGACCGGTCCAAAC
7	ACGAGGAGAGGCGGTTTGATGGTGGGGCCCACCCT
8	CGGTGTACAGACCAACAAAGCTAACGGAAAAAATCTACG
9	AATATCGGCACGCGCGGGCCGGAAGCATAAAAGCT
10	CAGAACAATATATCGGCCATCAAACACAGTTGAAAGGAA
11	TGAGGAAAACAGCCTGATTGCTTTGTTGC
12	GAACGCCTCCATATTATTTTA
13	AGTTCTGTCCCCCCCGAGGCGCTGGCAAGTGTTTG
14	CTTAAATCCCGGCGGTTGTG
15	AGCAATACTTCATCACGCAAATATCGCCAGTA
16	TTCATTTACCATATTGCGGAACAAAGAA
17	CTACAATTTTTTTGAAGAAAAAGCTTTAAAACAGAAATAAAGAAAAAT
18	CCTACATATCTAAAGCATCACCTCAAATTTGC
19	GGTGGCTCCAACGGCATTTCGCACTCAATCCACGCCATCCA
20	CGGAATTACCGTGTCGCAAGACAAAGAAAACAGTAAACAAAC
21	TTTCAATGATAAATTAATGC
22	GTCGAGGACCCGCCGCACCTTTTACATCCGCTGAGCAT
23	GTAATCAGAAACGAGCCTTTAGTGCCTTCTCAGAACGA
24	GCGACCCACCAAGTAGAATCATTAAAGGTGAAAATA
25	GTCTGAGCAAAAGAAGATAATGGGAAGGAG
26	TCACGCGTGGGAACAAATGTCACTGCGCGCCGCGG
27	ATTAGAGCATTTTTGCGAGCTGAAAAGGTCTA
28	TGTGATAAATTTAGCCGGAACGAGATATATTCTCA
29	TCCCGGGCGAAAGCCACCGTCTTTCCAGAGCCGAA
30	AATAAACCAGAATCTTTTCATAATCAGGA
31	CAGACCAGTTACAAAATAAAGGCTTCAGTAGGAGTATTATTAATGC
32	CGTAGGCGCATAACTGACCAACTTTGTTGCGCGATACATTGCAAAAG
33	AATAATAACCGGCGCAGAGAGTAATCTCGCCT
34	CATTATATTTTATCTTCTGACCTAAAGATGATCAATATA
35	AGGACGTTAAGAACGGTTTAATTTCAACGAGAAACCAA
36	AGGAGGCTTTAACGCCAAACGAACTGCTCAT
37	ACCACCCTTAGATGAGTGACCTGTCGTGCCAGAAT
38	GGTGATAAGAACTGGCATGATAATAACAGCCCTTTAATATC
39	CCCCTTTTCTTGTGTGAAATTGTTAAAGCACTTGT
40	CATTTAAACTCCATATAGATTCATCAGTGAACAAGAAACTCATC
41	AACAGACAATAGTTTATCCGCTGGTAAATGTGCAG
42	CGGATCGGATGTGCTGCAAGGCGATCAGTGCCAGGTGGAGCC
43	CCGAGCTCGAACTTGACGAAAGGTAAGAGGCATTTATTT
44	TGGGCACTAAAAAAGAGTCTGTCCTTTGATTTCAAACTTAC

45	GAGTCAACTAATTTAGGCAAGTAATCCTGAACAGA
46	AGAGTTCGTAAAGCTGATCTCATAAGGATTGACTGCCAGTTTGAGGCAG
47	TACGCGGGATACGAGGGCAACGGAATTATACCAAG
48	ATCCTTTGCAACAGGAAAAACGCT
49	GAAGGTATTATCACCCAGCAAAATCACCTTACCATTAGC
50	TTGCAAAGACAAAAGGGAATGAAATAGCAAGCAGCACC
51	GCAAGACTGGATAGCGTGAATCCCCTGTATGCGC
52	AGCACCCTCAAATCCTCCAGGAAGGGTCATTCCTTTAATTGTACAGGTG
53	TTTGCGTATTGACAATTCCACACAAAATTGGG
54	AAACGGACGACGTCGGTGACGCAACAGCGAGTATAGTTATTTTGATGGGG
55	ATATAATACACGTACTACACCAGCTAACACCATTCACCAGTCACA
56	TATTTTAACCTCAAAAGCTGCATTGCCTGGGGTGCCTAAATCCTTAGAC
57	AAAGGAAGCTTGATGTTGAAACCTG
58	GTCAGACCTCAAGAGAAGGAT
59	TTATCAGCTTGCTTACACTAT
60	AAAAATTAAAGCCTATTATTCTGAAGTTGATAGATTGCAAACCCTC
61	TTTGCGGGCCTCTGTGGTGCT
62	CACCGGAATCATTTCAAAATTATTT
63	TAAAGGAAGCTCTGGAACTGCGAACGAGTAGGCATAAACTGTAATGTCA
64	GAGCGTCCACTACCTCCGTAATTTTAGTTACAAAATCGCCGT
65	TACCAGAATCAAGTTTGCCTTATTTAAAAACTAATAAGACCGCCATGC
66	GCAGCAGAGGTCGTCGCAATTGCG
67	TGAGATCGGCTATAATATACCGACAGGGAAAGAGCGAAAGGAGCGGCAGT
68	CTTGGTAACGCCAGGGTACGACGTGGAT
69	CGCGCAGTATATTCGACAATGAATATACAGTA
70	AAGAGGTAGTACCTTGAGAAAGGCCGGACAATGCCATAGTAG
71	TGCACGACAATTGCGAATGCCCCCTCGGCTGGCCA
72	GCTTTGAGGACTAATACGAAGAAAACGAAAGAGGCCCCAGCGGATT
73	ATATAAAATTCATATGGTTTATTACCGAGGAA
74	GCAGTTGGTAAAAAGGCGGCCGCGTGGTGGGTGGTAGCAGGCTGCA
75	GTCCTTTCATGCATGTCCCAGTAAAGTGCCCGTATAAAAGGAGGTAATC
76	ACATTACAAAGGATTAAGGTGCCGTCGAGAGGACATGAAACAA
77	TAGTACTAAAGTACGGTGCCGAAAGATTTTTGATTGTAATTTTGTTGGGT
78	AGTGAATTTTCCTCAAACCCTCAGAGCCACCGAACCCACAC
79	TTATTCGGTCGGGTATTAGCCGTTTTTTCGATTTA
80	TCATCGTAACATTCCAAGAACATAGCCCCCT
81	GCCGCTACCACCACTGCCGTATCCGCTCGGCGCCAGCTGGTC
82	ACAGTGCTTTACCGAACGAACTGGTTGCTAGCGGTAAC
83	TGCCCGCTTTCCAGGTGTTGTTC
84	ATAGAGCCGCACTCCAAGTC
85	GCGGTCAGTATAGAAGATTAGCCCTTAAAGGGATTTTAG
86	GGGGTTTATATCGCATATGCATTGACCATTAGATA
87	ATTCTAGCGATGTGTAAAAATGAATCGGCCAAAAA
88	AAGTTTTGACGCTCAAATCCGGTATTCTAATAA
89	TACTGTGTCGAAATCCGCAAAGTATAGCAAC
90	TATTAAATCATACAAAATCATAGCGTCAAATTAT
91	CACGGGGGTAATAGTAAAACAGTTAGACGTTAGCCCTCAACAACCCAG

92	GACACGTAGATCCTTATTACG
93	ACCAACATGGCGCGTAACGATCTTACAACATTTTG
94	TTAAAGAGATCTATGACCGCTAAATCGGTTGTCCC
95	AAAAGAATTTCTTAAACATTACGAGACCAAAA
96	CCTAGTTTCCTTTCACCACTTGTAGCAGCACCGACAGTATCGGCCTACCG
97	CTGTCATACCGGCCCTGGCCCTGAGAAGA
98	AACTGTAAAACGACGGCTAAGTTGCGC
99	AAAGTCTTTCCTTATAAGAGTGTACACAGACAGTAAATGAG
100	GCAAACCACGGTTTTGTCACAATCAAAAGTAACCG
101	CATTGAAGACAGTTCATGAGGAAGTTGGGTAAATAC
102	AATTGTTTCATTCCATATTCAAAAAGCTATCAATTG
103	AGAGAGAAATAACAAGCGTTTGCCATAAGTA
104	TCAATGCTCAGTACCAGGGAGACTCGATTGGCCCA
105	ACCTTATGCGATTTTGGGAAGACAACATTAA
106	TAGTATCAAATTCTTACAGGCGTTTTAGCGAAACG
107	AGCGGGAGCTAAACAGGAGTTTTTACAATAGATTT
108	ACGGAGCCGTTAATCAGTGAGGCCTTG
109	TTTGACCGCCAGGAAAGCTAATCAGAGCAAACAAA
110	AGGAAGCGCAGCGATCCCGTGCCGCCGGAACGTAAACGATGCTGATACG
111	AGGACGTCAGACTGTAGC
112	ACTGTATCACCGTACTCCAGTTAACTGAATTCCGCCACTACGTGAAAATC
113	GAAAATTCGCAGGCGCTCAGATGCCGGGTTAATCTCCAAAGAGAACCTG
114	TCGCCGGCTGGAGGTTTCTTTGCTCACTTTTGGGTAGCTACT
115	CGACACGCCAAATTACCGCGCCCAAAATCCAAGCC
116	CAGAGCGGGGTCATTGCGTCTGGCCGGTTGAGCAGTCTTGCCCCC
117	TCCCATGCGTTCTTTGCCGATTTTCAGGTTTACGG
118	TAAAAGGAATGGCTATTAGTCGAACTGAAAAA
119	TCAGTGAGAATCAAATCAGATATAGAACAGCCCTCAGAGTACCGTTAATC
120	CTATGAGTAATGTGTAGAAAAGGGTTAA
121	AGACCGGCAAACGCGGTCCGTTTT
122	GGACAAATCACCTCAATATGAAAATTTGACGCTCA
123	TTTGACCAAAAGAAATACGTAATGCCACAGACTTTCATC
124	AAAAATAGGAGCCGGGCTCAGCAAATCGTTAAAAGGAGGCC
125	AATCAAGAATTGAGTTAAATAGCATTTTTTGTTATCCCTAGCAAGCGCC
126	GAATTGCCAGAATTCAACTATTACACCCAAATACCAGAACGAGTAG
127	GTTGCGTCGGATTCTCGTAGCATTCCTCGTAA
128	AGCCAACGTGGCACCAGAATCTTACCAACGCTACC
129	GCCACGAAACGTTCGCCACGTGCATCCGTAATGGGATAGGGCC
130	ATCCTGAAAACAAACCTTTTTTAATGGACGCGAGAGGTTTGA
131	TGCCTATAATAGGTATTATAGGATAAAAGCATAGTAAGAGCATCGA
132	ATCAAGATTGTTTGTATTCCTGATTATCATTTAATAAACTTT
133	CAAGGGGCAACTCATGGTCATAGCTAAGGGAGAGA
134	ACCGAGGCTGGCTGACCTTTCATTAGGTAGAAACCAGTC
135	GAGAACAAGCAAAACCAAATCAATATTTCGTCACTACAAGGATTTT
136	TTTGGACATTCTGGCCAATTGGCAGGCCTGCA
137	TGTACGGAGGGAAGTGAGCGCTTTAAGAATAGAAAAGAAACGCAAA
138	TACGTATCATGACTTGCGGGAGGTATCCTGAACCACCACTTGATATAT

139	ACGGAACGTCATTTAGTGATGAAGGCATAAAACTGGTGCCCCGGAA
140	GCAGCAACAATATCGAAGAACAGTAATAACATCACACC
141	GAGGGAATCCTGAGAAGTGGCCGATAAAACATATT
142	AAAACCGCCACCCTCAGATTTTAACGATACAGTCACCGGGATA
143	GTTTACCAGACGACTCAGAAGAGTCTGGAAAAGCCCAAA
144	AGACAATCGCCATTAAAAAAGAATCAGCAGA
145	TAGCGAGTCTTTACTCGATGATGTACCCCTTCCTGCTG
146	ATAACGGTAATTTTCACACCGATAGAAAGAG
147	TTCAAATTGAATTAATTAATT
148	GTACGAACGTTATTAATCTGTTTACTTTTTAATTAAAGCGA
149	TGTGCGGTTGCGGTATGCTCA
150	AGGCTTGCCCTGACTTTAATC
151	TGCTTCTGTAAACGAATTA
152	ATCTAGCCAGCAGCATCCCAGCGGTGCCGGTAATAATTTCGTAAA
153	AAGTTTGACCATAACAAAGTTTTGTCGAAGGAATGACAACAGGA
154	GGACGTCACCCGGTCGCAGTTTCATGTGCACGTTT
155	AATCAAATTAGTACCGCCACCGAGTAACGCGTCATCCGGAACCGCGCCTAAC
156	CGGAGAGCGGGAGAAATAAAGCCTCAGAATT
157	ACAGTGCGACTTTACAAACAAAAGCCAAGTCAATACTATCATTTCC
158	TACATCAAACTGAAAAAGAGACGCATACCAGTCGG
159	CGTGTGAATTATTAAGAGGGAGAAACAATAAACGTCAGACTCG
160	ACTAAATGGGCTTGAGATTGGCT
161	TGAGCAAAGCGTAAGTATAGCCCGGTTCGGAACCAGAATCCCTCAGAAAC
162	TCACAGAGAGTAACCCAAGCTATCCCAGCGCACGGAAATTGCAAC
163	ATACAGAACCCTTCTGACGTCTGAAAGAGCCA
164	GATAAAATCAGAGCCGGGACATCCCTTACACTAAA
165	CGCCAGCCAGAAAGCGTACTGAGTATGGTGCT
166	ATCCATGTAATAGATTAAGCACGTATAACGTGCGCTAGTTT
167	CATAACAGTTGATTACTCGGT
168	AACAAAATCGGCACGCTGCGCGTAACAGGGCGTTT
169	TGAAAGCCCAAAAGAAACCGACATTAGGGAGG
170	CCAGAGCGCCATACAGCGCCATGTTGATTCAGAAGCTAACAG
171	TTCCTCGCACGCTGATGGATTATTTACACAGAGATGTGGCAC
172	CTTAGCATCAGACGATCCACAACTATCTTTCCCAG
173	TACGCCAATTTAGAGCTTAATCTCACCCACCATAAGAAA
174	TATTTGCCGTTGCACATCTGCCCTTCACCGGTGTA
175	ACCATCGATAGGCCGGAAATTAGAGCGTCACCGACT
176	TTTAGAACCCTCATATATTTTAAATGGACAGTCGGTCAGG
177	TAGCATTTTGGGGCGCGGATGGCTTAGATCCAACA
178	AGCAAACGCTTAATAGCTATATTTTCATAACATCCAATA
179	TAATTACTAGCCTTAAATCAAGATTTTGCACAGCATTGGAGGCAG
180	TGATCGGGAAAGCTAACTCACATTTATTAATGCTTAGGTTG
181	GAAAGGAAGGGAAGAACCGGCGATCCCCGGCCGTGAGAGCCTCCGTCACGT
182	GAAGGTTATCTAAAAT
183	AAGGCCGCTTTTTGCG
184	CACCCTGAACAAGCCG
185	CTCGTCGCTGGCCCTCCTCCGTGCCTTAATTTAGAAACCAGTAC

186	TTTGGAACAAGACGCCGCCCCAG

Supplementary Table 3. Modified staple strands used for the immobilization of the DNA origami structure (biotinX), nanoparticle binding (npbindX) and fluorescence labelling.

Name	Sequence (5'→3')
biotin1	biotin - AGAATATAAAGTCCCATCCGTTCTTCGGGG
biotin2	biotin - AGTTACCAGAAGGAAAGCAGATAAGTCAGAGGGTAATCGCA
biotin3	biotin - ACAACTTTCAACTGAGGCTATGT
biotin4	biotin - AGGGCGATCGGTGCGGTGCGCAACCGGAAACAATCGGCGGG
biotin5	biotin - TTCATCGGCATTGACGGGACCAATAGACCCTCAATTCATTCCAA
biotin6	biotin - TAGATGGGCGCATCGTAACTTCAGGCGCCT
npbind1	CATTTCGTCAACATGTTTTAAGTTTTAATTCGAGAAAAAAAAAAAA AAAAAAAA
npbind2	GGTTATATAACTATATGTGAATAAAAAAAAAAAAAAAAAAAAAA
npbind3	ACCATCAACCGTTCTAGCCGCAAAAAAAAAAAAAAAAAAAAAA
npbind4	ATAAAAATGCTGATGCAATGTGAAAAAAAAAAAAAAAAAAAAA
npbind5	AAAGAATTAGCAAAATTAAGCAGCCTTTAAAAAAAAAAAAAAAAAAAA
npbind6	ACCACCAAAGGGTTAGAACCTCAATTACGAATAACCTAAAAAAAAAAAAAAAAAA AAA
npbind7	AATCATACAGCCTGTTTTGCTGAATATAATGCGAAAAAAAAAAAAAAAAAAAAA
npbind8	AATATAATCCAATGATAAATAAGGCGTTAAAAAAAAAAAAAAAAAAAAAA
npbind9	AAATCACCATCAATATGATATGACCGGAAAAAAAAAAAAAAAAAAAA
npbind10	CTTCAAAGCTGTAGCCAAATGGTCAATAAGCAAGGCATAAAAATTAAAAAAAAAA AAAAAAAAAAA
npbind11	AAAAGTTTGAGTAACATTATCAAAAAAAAAAAAAAAAAAAA
npbind12	AATACCGATCATCAGATTATACTTCTGAATGATGACATAAATCAAAAAAAAAAAA AAAAAAAA
base_dye ATTO542	TTTGTGATCTCACGTAAATTTCTGCTCA-ATTO542
hotspot_dye ATTO647N	TAATCACTGTTGCCCTGATTAAATACGTTAATA-ATTO647N
hotspot_dye AlexaFluor 647	TAATCACTGTTGCCCTGATTAAATACGTTAATA-AlexaFluor647

Supplementary Table 4. Modified staple strands used for the sandwich detection assay: 3 capture staples (captureX), synthetic 34 nt target strand (target34) and Alexa Fluor 647 imager strand (Alexa647 imager). Complementary regions are depicted in the same colour. The unmodified staple strands from Supplementary Table 2 and modified staple strands from Supplementary Table 3 which are replaced by the capture strands and therefore should be left in order to fabricate the NACHOS out are indicated in the second column.

Name	**Strands to leave out**	**Sequence (5'→3')**
capture1	hotspot_dye strand from Table3	TAATCACTGTTGCCCTGATTAAATACGTTAATATTTTTCGGGCAATGTAGACA
capture2	186 from Table 2	TTCGGGCAATGTAGACATTTGGAACAAGACGCCGCCCCAG
capture3	156 from Table 2	TTCGGGCAATGTAGACACGGAGAGCGGGAGAAATAAAGCCTCAGAATT
target34		TGTCTACATTGCCCGAAATGTCCTCATTACCATA
Alexa647 imager		TATGGTAATGAGGACAT-AlexaFluor647

Supplementary Table 5. Modified staple strands used for solution synthesis of NACHOS. Overhang modifications (modificationX) exchange biotinX staples from the Supplementary Table 3 of the DNA origami structure. Complementary regions are depicted in the same colour. Corresponding unmodified strands from Supplementary Table 2 and modified strands from Supplementary Table 3 should be left out.

Name	Replacing strand	Sequence (5'→3')
modification1	biotin1 Table 3	GTGATGTAGGTGGTAGAGGAAAGAATATAAAGTCCCATCCGTTCTTCGGGG
modification2	biotin2 Table 3	AGTTACCAGAAGGAAAGCAGATAAGTCAGAGGGTAATCGCA
modification3	biotin3 Table 3	GTGATGTAGGTGGTAGAGGAAACAACTTTCAACTGAGGCTATGT
modification4	biotin4 Table 3	AGGGCGATCGGTGCGGTGCGCAACCGGAAACAATCGGCGGG
modification5	biotin5 Table 3	TTCATCGGCATTGACGGGACCAATAGACCCTCAATTCATTCCAA
modification6	biotin6 Table 3	GTGATGTAGGTGGTAGAGGAATAGATGGGCGCATCGTAACTTCAGGCGCCT
mag1		TCTCCATGTCACTTCTTCCTCTACCACCTACATCACCTTCTTCTTCTTCTT - biotin
mag2		GTGATGTAGGTGGTAGAGGAA
mag3		AAGAAGAAGAAGGTGATGTAGGTGGTAGAGGAAGAAGTGACATGGAGA

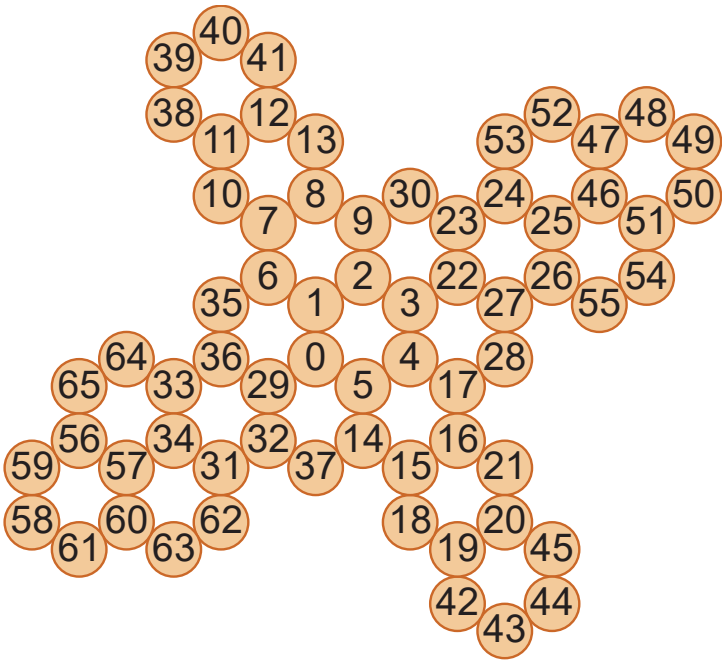

Supplementary Figure 1. Base layout of the DNA origami nanostructure used to build NACHOS

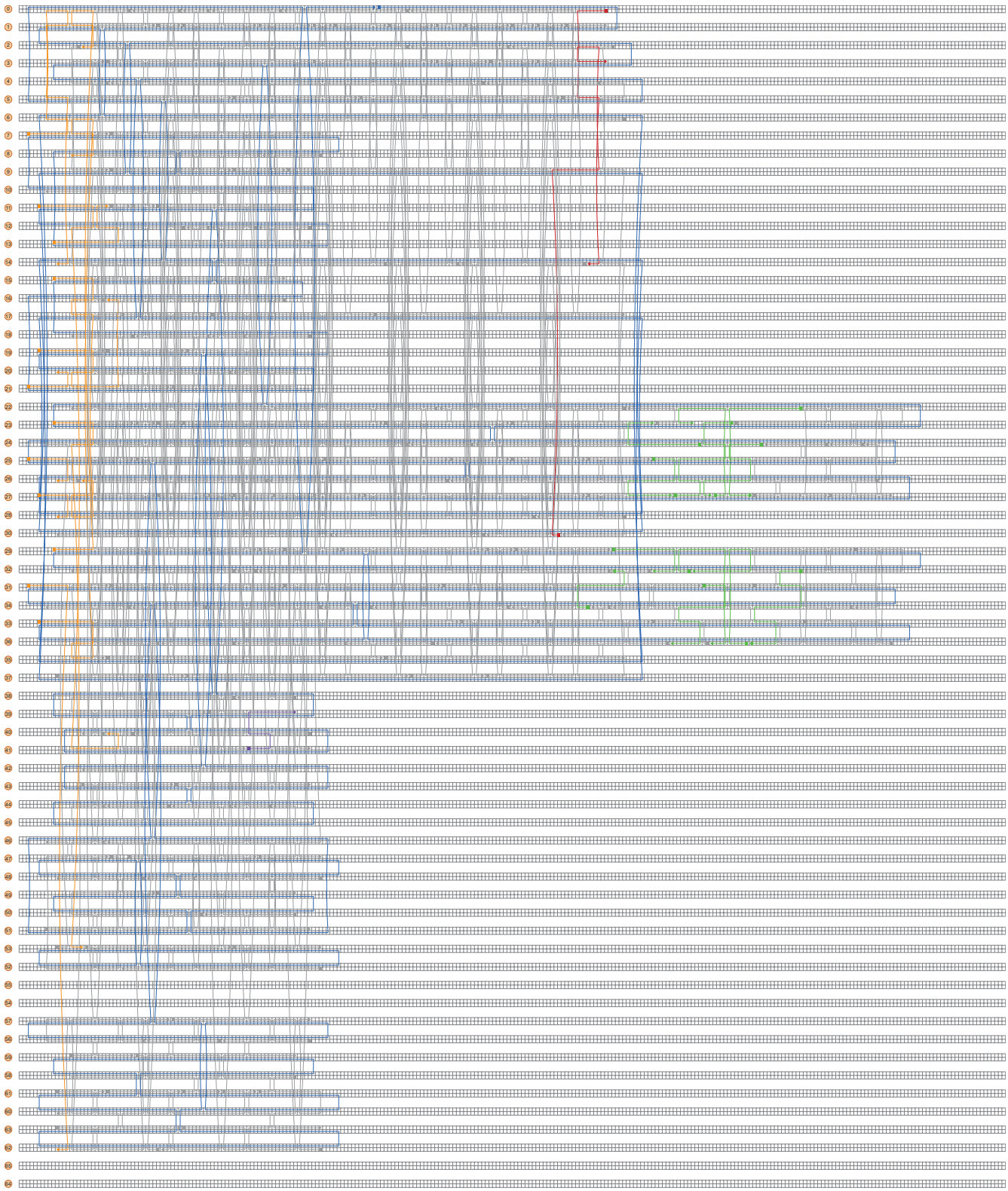

Supplementary Figure 2. Staple layout of the DNA origami nanostructure used to build NACHOS (yellow = biotin staples, red = hotspot staple, green= nanoparticle binding staples, purple = base dye staple)

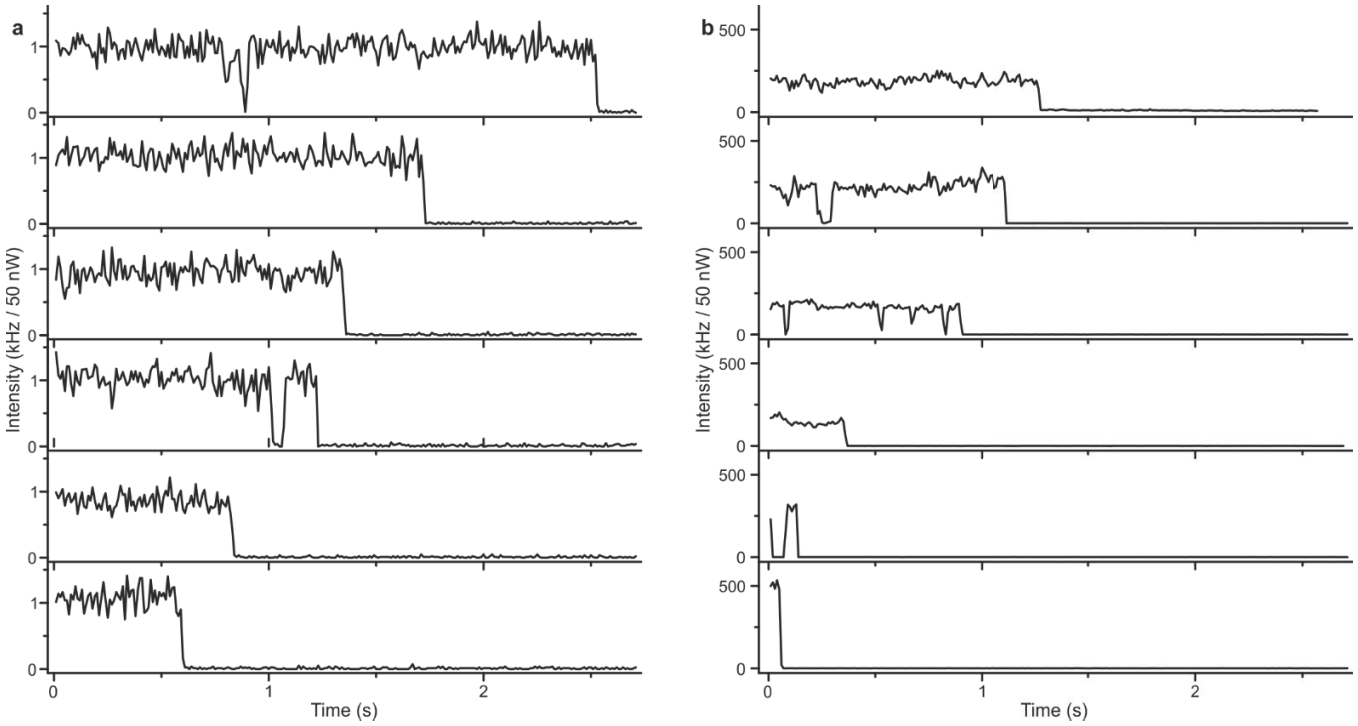

Supplementary Figure 3. Exemplary single-molecule fluorescence transients of Alexa Fluor 647 dye in DNA origami reference structures without nanoparticles (a) and in NACHOS (b). The samples are measured at 639 nm with 200 nW and 50 nW excitation power for panel (a) and (b), respectively, and the transients are normalized to the same excitation power.

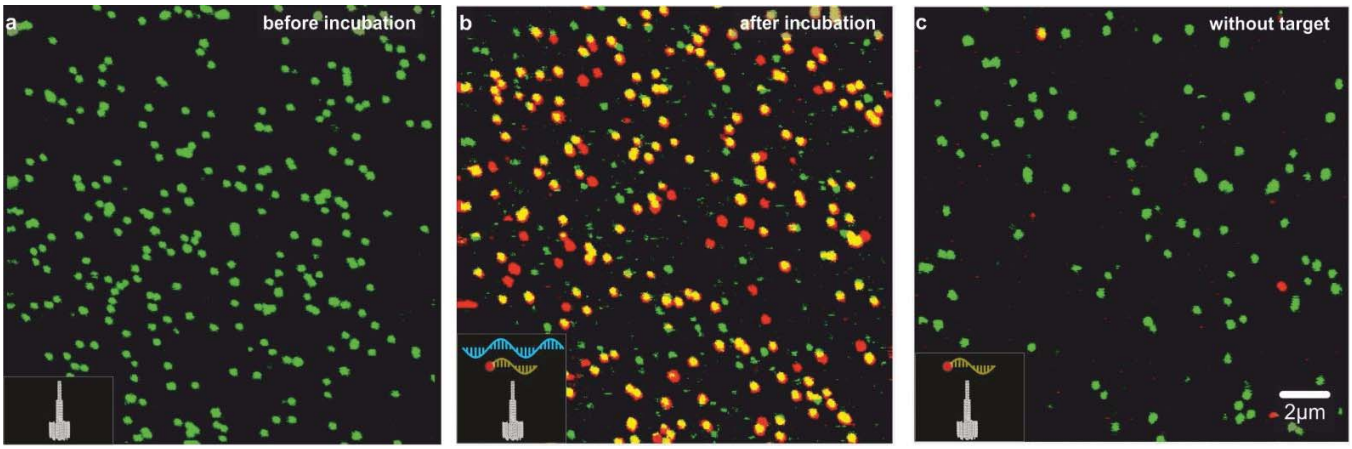

Supplementary Figure 4. Fluorescence scans of the DNA origami reference structure (without nanoparticles) measured in buffer solution acquired before incubation (a), after incubation with the full sandwich assay (b), and after incubation with the imager strand only (c). Excitation was carried out at 532 nm and 639 nm with 2 µW excitation power. At least 20 different areas were measured for each sample.

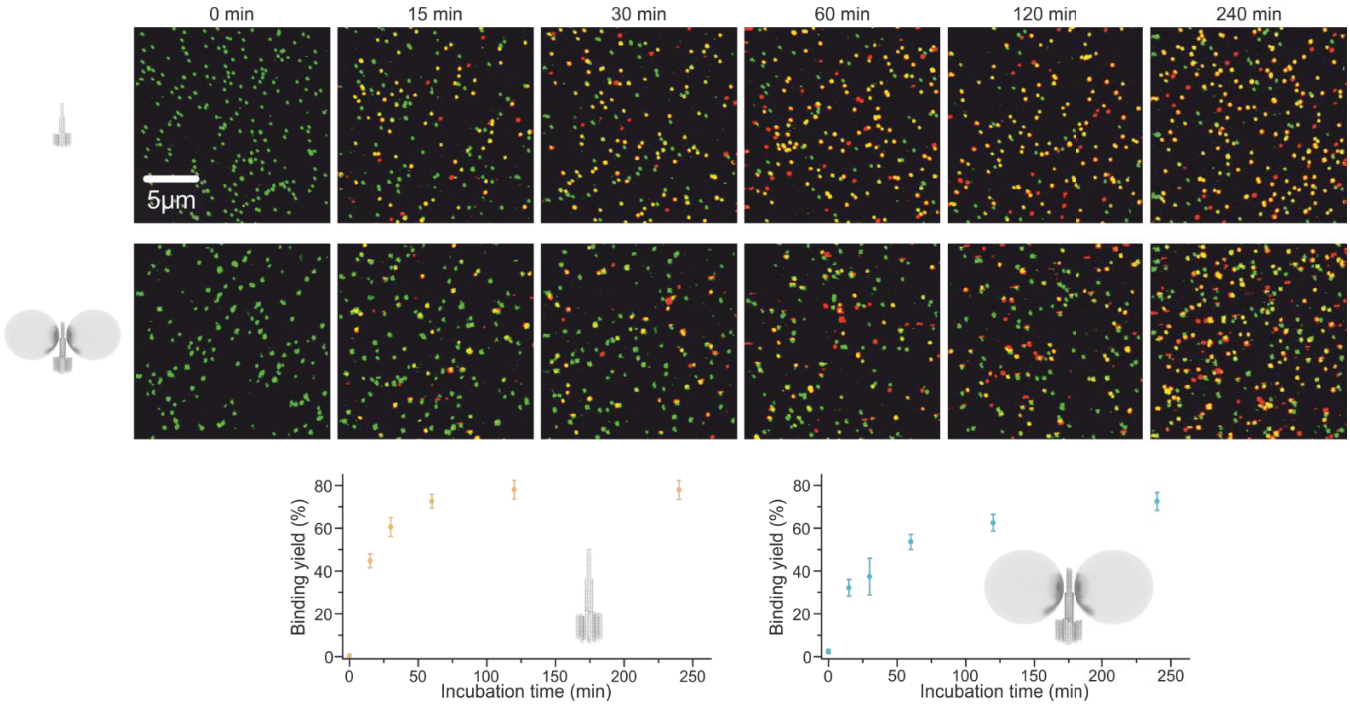

Supplementary Figure 5. Incubation time series for the reference DNA origami structure (first row) and the NACHOS (second row). The binding yield efficiency for every incubation time is calculated from at least 4 different areas of the sample and represented at the bottom. The error bars represent the standard deviation from the mean. Measured at 532 nm and 639 nm with 2 µW excitation power for the reference structure and at 532 nm with 2 µW and 639 nm with 500 nW for the NACHOS structure.

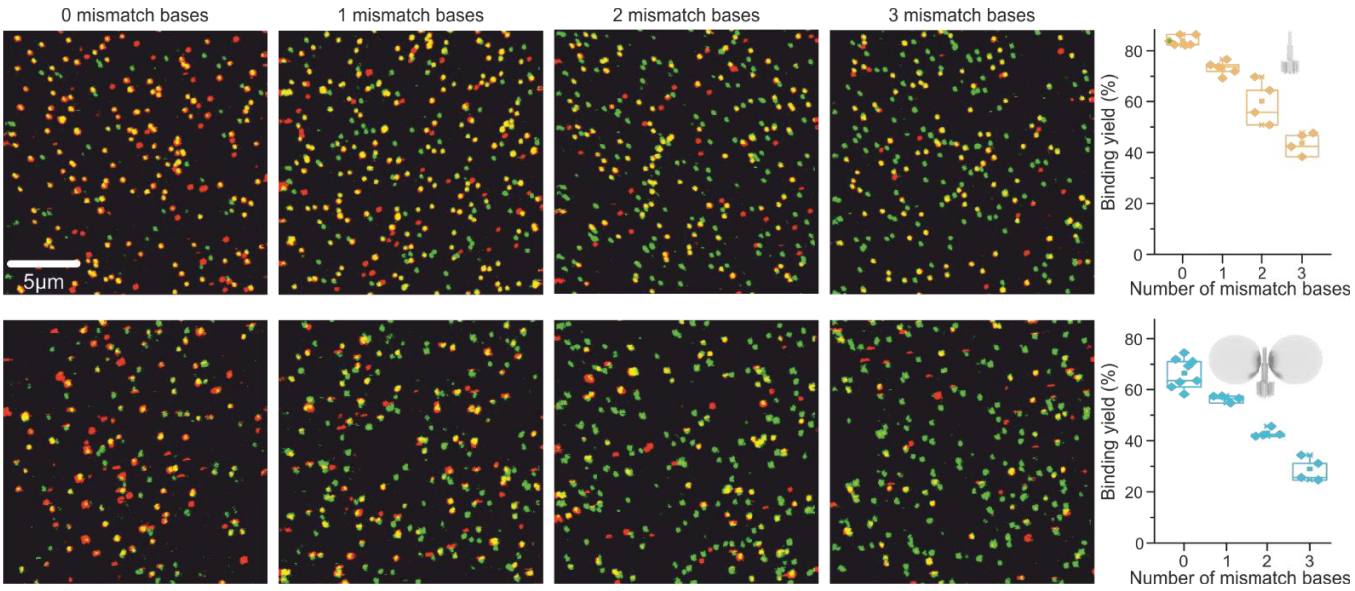

Supplementary Figure 6. Testing specificity of binding for variations of the Oxa-48 DNA sequence: scans and binding yield for perfectly matching DNA target and targets with 1, 2, and 3 mismatches in the reference DNA nanostructure (top row) and in NACHOS (bottom row). The calculated binding yield efficiency is represented in the right panels from at least 4 different areas of each sample. The box plots show the 25/75 percentiles and the whiskers represent the 1.5*IQR (inter quartile range) values, the canter lines represent the average values. Measured at 532 nm and 639 nm with 2 µW excitation power for the reference structure and at 532 nm with 2 µW and 639 nm with 500 nW for the NACHOS structure.

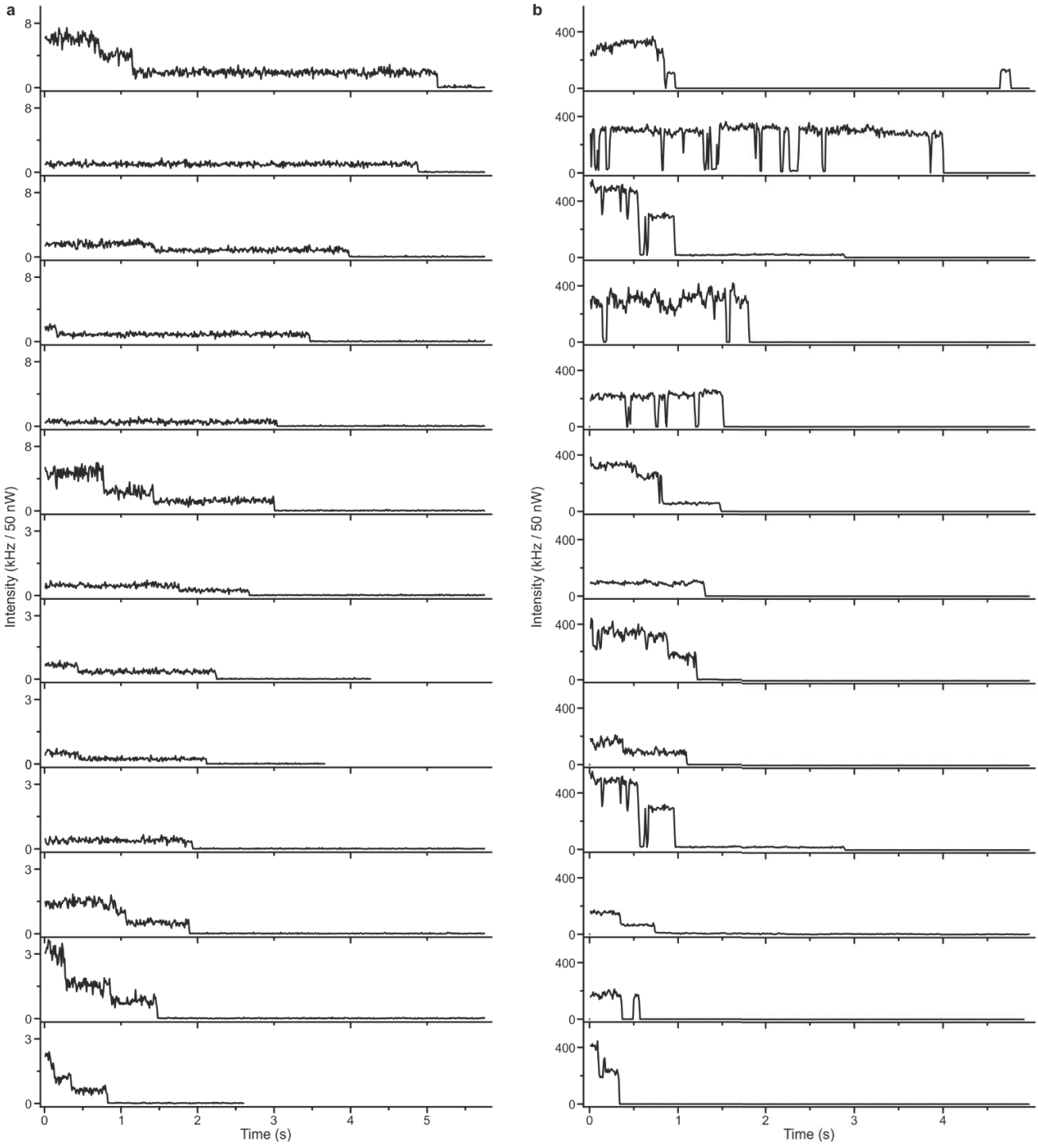

Supplementary Figure 7. Exemplary fluorescence transients of the sandwich assay in DNA origami reference structures without nanoparticles (a) and in NACHOS (b) The samples are measured at 639 nm with 500 nW and 50 nW excitation power for panel (a) and (b), respectively, and the transients are normalized to the same excitation power.

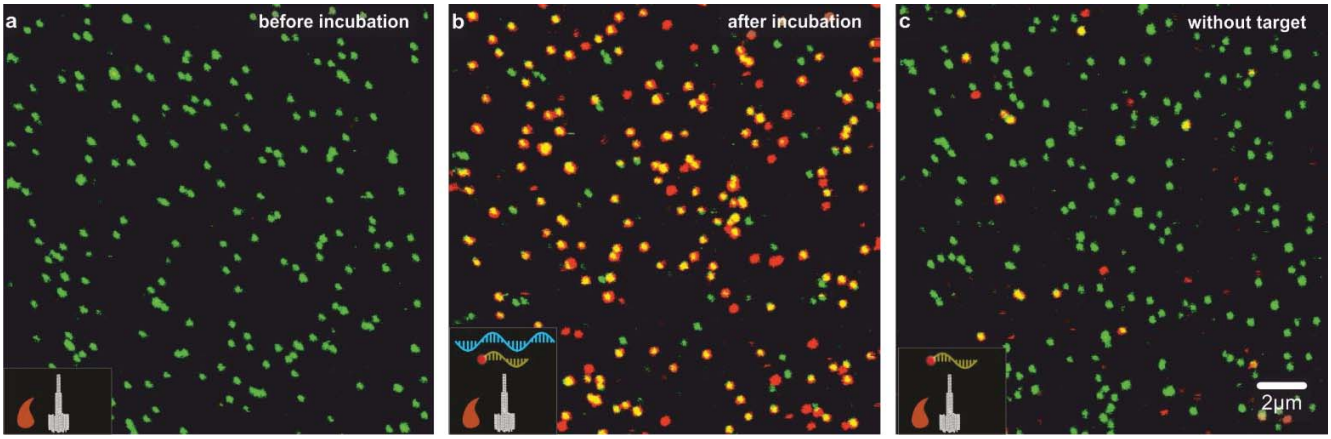

Supplementary Figure 8. Fluorescence scans of the DNA origami reference structure (without nanoparticles) acquired in blood serum before incubation (a), after incubation with the full sandwich assay (b), and after incubation with the imager strand only (c). Measured at 532 nm and 639 nm with 2 µW excitation power. At least 20 different areas were measured for each sample.

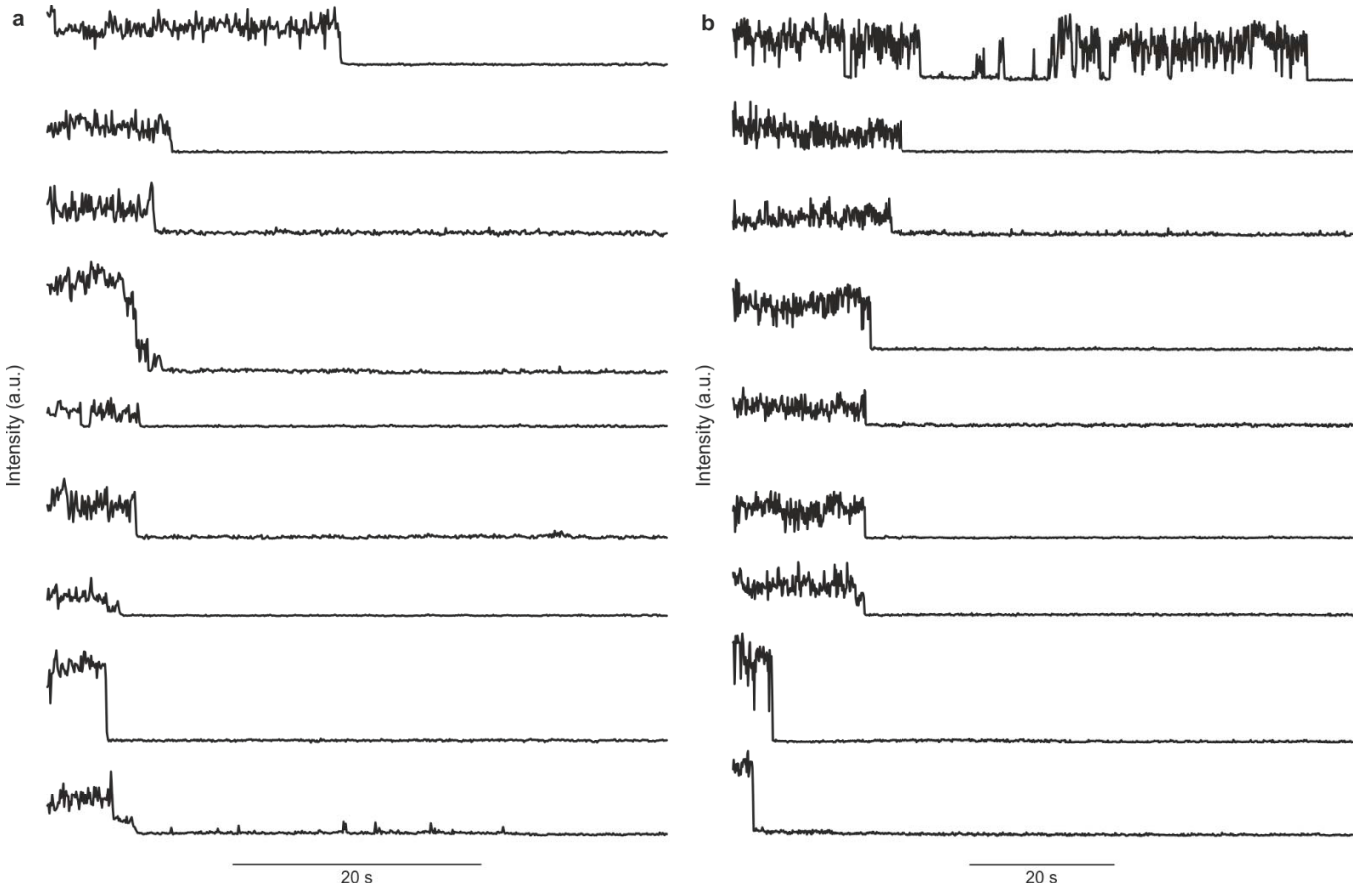

Supplementary Figure 9. Additional fluorescence transients of single Alexa Fluor 647 dyes in NACHOS obtained from two more movies (a, b) recorded on the smartphone microscope.

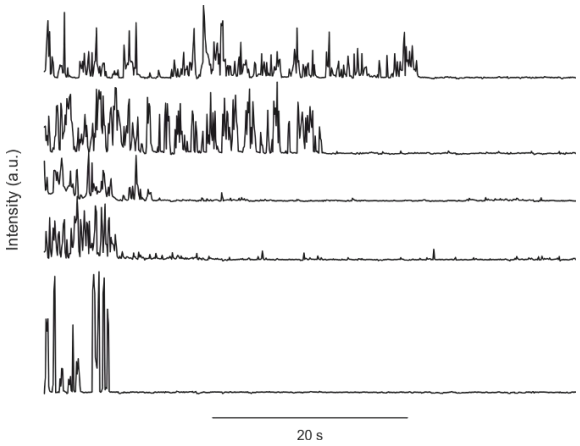

Supplementary Figure 10. Fluorescence transients of single ATTO647N dyes in NACHOS recorded on the smartphone microscope (80 ms integration time).

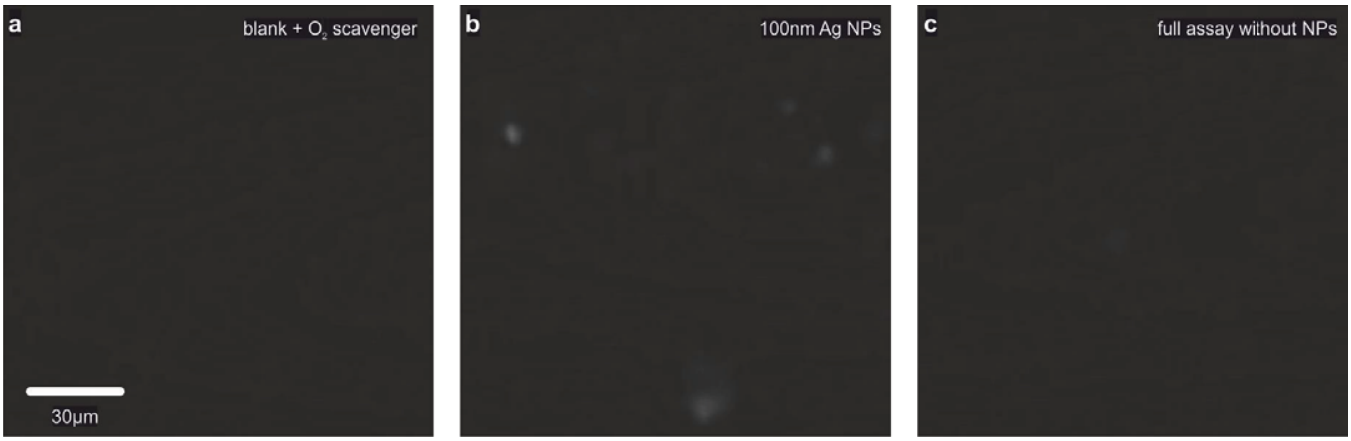

Supplementary Figure 11. Negative controls on the smartphone (a) cleaned surface with buffer solution, (b) incubated only with 100 nm silver nanoparticles, and (c) full sandwich assay on NACHOS without silver nanoparticles in ROXS[1]. For each control measurement at least 4 movies were recorded.

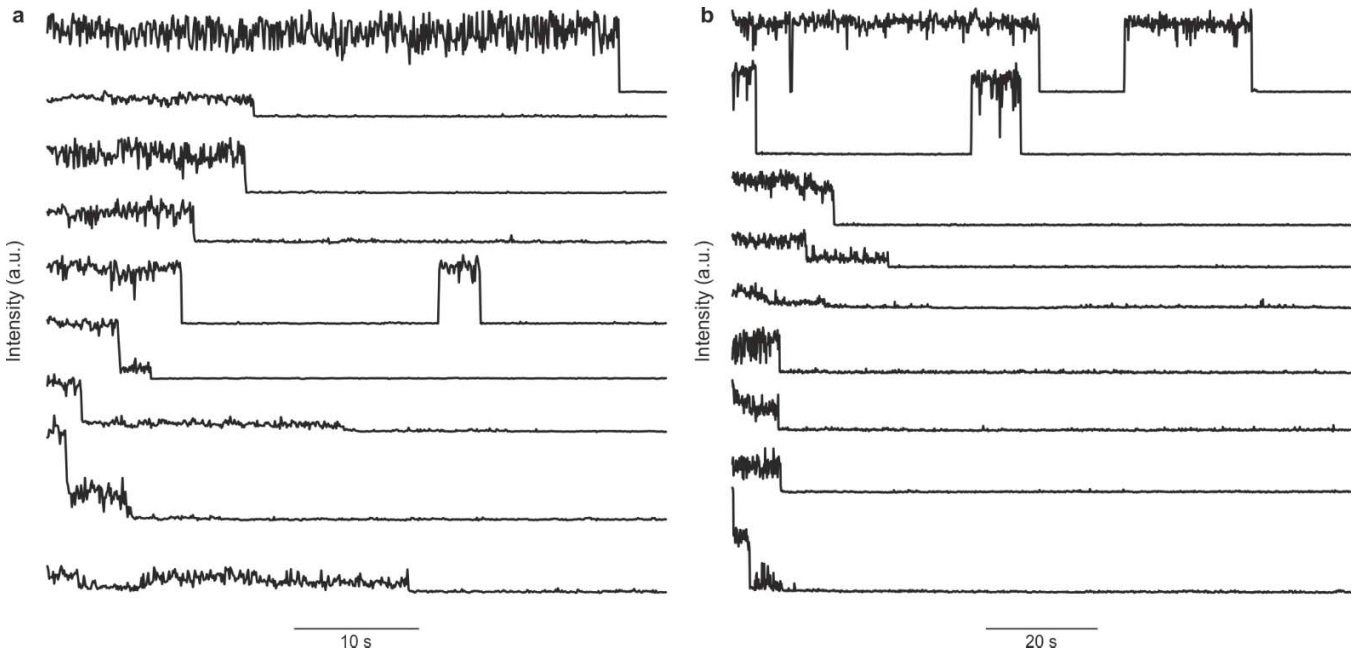

Supplementary Figure 12. Additional fluorescence transients of the sandwich assay in NACHOS measured in buffer solution from two more movies (a, b) recorded on the smartphone microscope.

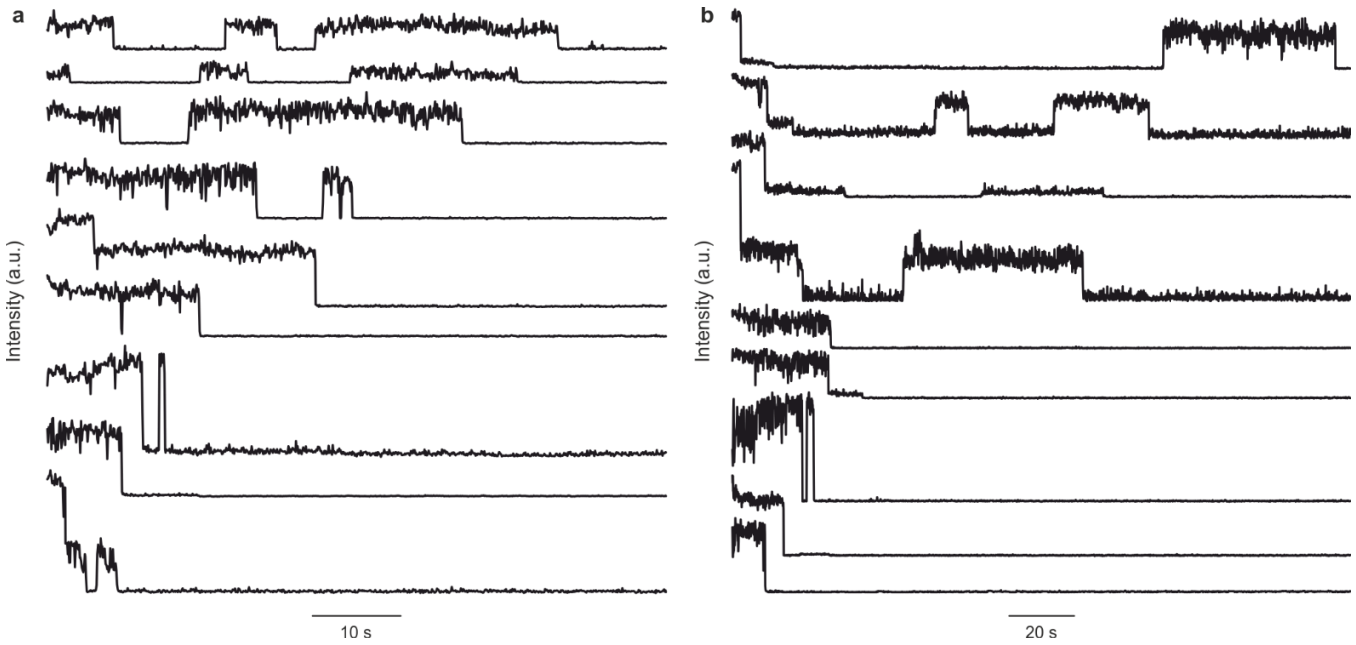

Supplementary Figure 13. Additional fluorescence transients of the sandwich assay inside NACHOS measured in blood serum from two more movies (a, b) recorded on the smartphone microscope.

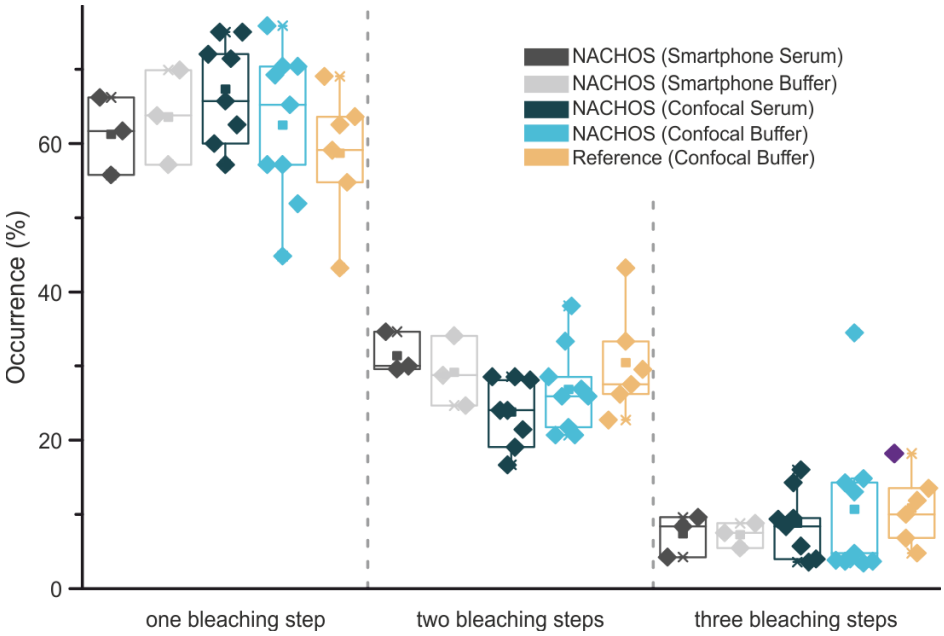

Supplementary Figure 14. Bleaching step analysis obtained for the reference structure (orange) and for NACHOS measured on the confocal setup in buffer solution (light blue) as well as in blood serum (dark blue) (same data as shown in Fig. 2g) and for 244 traces extracted from the smartphone microscope in buffer solution (light grey) as well as in blood serum (dark grey). The box plots represent the statistics of at least 4 different areas for each sample with the 25/75 percentiles and the whiskers represent the 1.5*IQR values, the canter lines represent the average values.

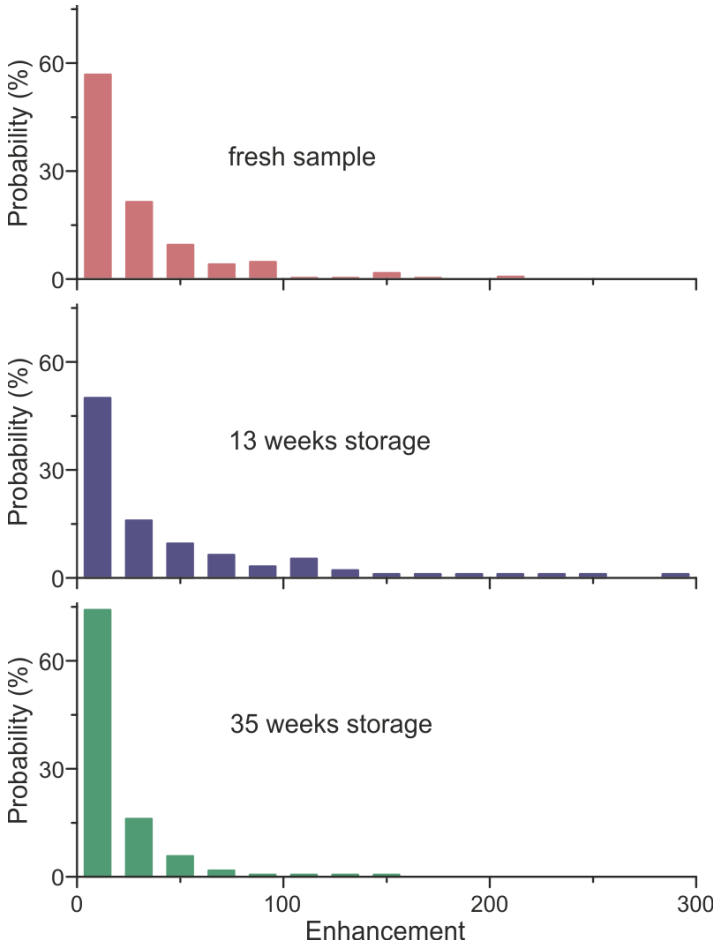

Supplementary Figure 15. Fluorescence enhancement histograms of a single ATTO 647N dye in NACHOS of a previous design (only eight binding strands of A_{25} for nanoparticles, T_{25}-SH used for nanoparticles functionalization). No difference between the fresh sample (red, 294 molecules measured) and the sample measured after 13 weeks (blue, 94 molecules) were observed. Slight changes are visible for the sample measured after ~35 weeks (green, 174 molecules). The sample (Lab-Tek™ II-chambers with TE buffer containing 14 mM $MgCl_2$ was stored at 4 °C and care was taken to avoid drying of the sample. At least 5 areas were measured for each time point.

Supplementary Note 1. Discussion pertaining the costs of the smartphone microscope

Price list of the current smartphone microscope

Name of the component	Price
Excitation source: Integrated Optics 0638L-11A (Lithuania) Laser incl. power bank and cooling system	1892 €
Smartphone: Huawei P20 (China)	439 €
Objective Lens: UCTRONICS LS-40166 (USA)	~8 €
Filter: Semrock Inc. BrightLine HC 731/137 (USA)	472 €
Focussing lens: Thorlabs Inc. AC254-050-A-ML (USA)	114 €
Sample positioner: 3× Thorlabs Inc. MT1/M (USA)	3× 341 € = 1023 €
Laser positioning: Thorlabs Inc. Optomechanical Components	218 €
Total sum:	~4200 €

Estimated pricelist of future smartphone microscopes

X and Y positioners can be omitted or substituted by cheaper ones since the accuracy is not needed inside the microscope.
Large scale production of the filters with a customize size can reduce the price by at least one order of magnitude, as a currently used standard commercially available filter is big enough to provide material for over 10 filters for smartphone microscopes.
Focussing lens does not have to be an achromatic one, i.e. price reduction to ~30 % of original price possible.
Smartphone can be cheaper especially if the smartphone is specialized for camera performance -> price reduction ~50 % possible. We also note that the current smartphone was purchased in early 2019 and the current value of the same smartphone is substantially lower right now. The power density in the current configuration is set to ~ 600 μWcm^{-1}. Due to the high signal-to-background ratio we estimate that a lower power density would also be enough to make NACHOS visible on the smartphone microscope. This can be easily achieved by a high-power LED and an excitation filter to narrow down the excitation spectrum. This kind of LED in combination with a high-end excitation filter in suitable size can reduce the price to ~ 200 €.

Name of the component	Estimated price
Excitation source: e.g. Mouser, 897-LZ110R1020000 incl. power bank and bandpass filter Chroma 620/60 ET (USA)	200 €
Smartphone	220 €
Objective Lens: UCTRONICS LS-40166 (USA)	~8 €
Filter: Semrock Inc. BrightLine HC 731/137 (USA)	45 €
Focussing lens	37 €
Sample positioner (Z axis): Thorlabs Inc. MT1/M (USA)	341 €
Laser positioning: Thorlabs Inc. Optomechanical Components	218 €
Total sum:	**~1000 €**

Additional discounts of at least 30 % can be expected for large scale purchase of the single components -> final price < 700 € possible.

Supplementary Note 2. Discussion pertaining the costs per sample for the diagnostic assay on a smartphone microscope.

To estimate the price of materials and consumables used for the preparation of one sample, the prices stated in recent bills were used and then divided by the amount of samples that can be prepared from the ordered product.

Name of the product	Price, €	Total volume/ mass/ number of pieces of the product	Volume/ mass/ number of pieces used for one sample	Estimated price for one sample, €
Coverslip 22 mm × 22 mm	21.5	200 pieces	1	0.11
Microscope slide	2.95	50 pieces	1	0.06
BSA-biotin[a]	158	10 mg	0.075 mg	1.19
NeutrAvidin[a]	204	10 mg	0.03 mg	0.67
Unmodified DNA staple strands[b]	1200	200 staples, 100 µl each	1 set per 30,000 samples	0.04
Modified staples[b]	300	6 biotin strands, 100 uL each	1 set per 180,000 samples	0.02
Scaffold*[b]	125	0.5 ml of 100 nM	1 bottle for 12,000 samples	0.01
Amicon filter[b]	407	96	1 filter per 600 samples	0.07
100 nm BioPure Silver Nanospheres (nanoComposix, USA)[a]	215	1 ml	1 bottle for 250 samples	0.86
Thiolated oligos[a]	170	50 bottles of 1 nmol	1 bottle for 5 samples	0.68
Imager strand[a]	150	100 uL of 100 µM	1 bottle for 17000 samples	0.09
Other (buffers, silicon form, electricity, water...)[c]				< 1
			Total:	**~ 4.8 €**

[a] Calculation is done based on concentrations given in materials and methods section

[b] One preparation of the DNA origami stock (~20 µl of ~ 50 nM) requires 18 uL of pool from unmodified staples, 2 uL of pool from modified staples, 25 uL of the scaffold, and 1 Amicon filter. To prepare one sample for the smartphone measurements 150 µl of 10 pM is required, that is, one DNA origami stock is enough to prepare > 600 samples for the smartphone measurements.

* For the estimation, the price of commercially available scaffold was used. Produced in-house scaffold will yield a lower price.

[c] Estimation takes into account costs that are hard to estimate and handling mistakes

The prices can be further reduced by larger scale purchases.

Supplementary References

1. Vogelsang, J. et al. A Reducing and Oxidizing System Minimizes Photobleaching and Blinking of Fluorescent Dyes. *Angewandte Chemie International Edition* **47**, 5465-5469 (2008).

11.4 Associated Publication 4

Maximizing the Accessibility in DNA Origami Nanoantenna Plasmonic Hotspots

Cindy Close, Kateryna Trofymchuk, Lennart Grabenhorst, Birka Lalkens, Viktorija Glembockyte, Philip Tinnefeld

Advanced Materials Interfaces 9, 24 (2022). doi: 10.1002/admi.202200255

RESEARCH ARTICLE

ADVANCED MATERIALS INTERFACES
www.advmatinterfaces.de

Maximizing the Accessibility in DNA Origami Nanoantenna Plasmonic Hotspots

*Cindy Close, Kateryna Trofymchuk, Lennart Grabenhorst, Birka Lalkens, Viktorija Glembockyte, and Philip Tinnefeld**

DNA nanotechnology has conquered the challenge of positioning quantum emitters in the hotspot of optical antenna structures for fluorescence enhancement. Therefore, DNA origami serves as the scaffold to arrange nanoparticles and emitters, such as fluorescent dyes. For the next challenge of optimizing the applicability of plasmonic hotspots for molecular assays, a Trident DNA origami structure that increases the accessibility of the hotspot is introduced, thereby improving the kinetics of target molecule binding. This Trident NanoAntenna with Cleared HOtSpot (NACHOS) is compared with previous DNA origami nanoantennas and improved hotspot accessibility is demonstrated without compromising fluorescence enhancement. The approach taps into the potential of Trident NACHOS for single-molecule-based plasmonic biosensing.

1. Introduction

The DNA origami technique enables targeted placement of nanoobjects in defined patterns.[1–13] This unique way of engineering with the help of nucleic acids at dimensions below the wavelength of electromagnetic radiation proved to be especially advantageous for the field of nanophotonics.[14–17] Firm positioning of a plasmonic nanoparticle (NP), thereby controlling the distance of its surface to a molecule, is, for example, one of the main parameters to control the interaction of a target molecule with the excited localized surface plasmon resonance (LSPR), as used in surface-enhanced spectroscopies such as Raman or fluorescence.[15,18–28] The LSPR effect is based on the interaction of electromagnetic radiation with conduction electrons of noble metal NPs and the resonance strongly depends on the correspondence of the excitation wavelength to size, shape, and material of the NP.[29,30] When placing a single fluorescent molecule in proximity, multiple effects simultaneously influence transitions between electronic states. The increased intensity of the local electric field, created by LSPR, and distance to NPs affect excitation rates, as well as radiative and non-radiative decay rates.[18,31,32] In consequence, the distance dependence results in a continuous transition from fluorescence quenching (FQ) in close proximity and fluorescence enhancement (FE) at an increased distance, reaching maximum FE values at a defined position (hotspot).[21,33,34] Besides their distance, the size of NPs influences the relation of quenching and enhancement. In first approximation, larger particles lead to higher FE.[35,36] Finally, electric field enhancement only occurs at the poles of particles or in between particles depending on the relative alignment of particles, emitters, and the excitation polarization.

The first examples of so-called dimer nanoantennas (NAs) were achieved using electron-beam lithography, relying on dyes stochastically placed in the hotspot.[33] Controlled positioning of a fluorophore in the hotspot of two NPs was presented by Acuna et al., utilizing a pillar-shaped DNA origami that bears anchoring poly-adenine strands for the attachment of two gold (Au) NPs (functionalized via thiol chemistry with poly-thymine) at a fixed position, while placing a fluorophore in between (**Figure 1**a).[37,38] FE values up to 117-fold were achieved by positioning an ATTO647N molecule in the created 23 nm gap between two 100 nm Au NPs.[35,36] Although FE values of over 400-fold were reached in refined DNA origami structures, the mentioned NA designs suffered from the limitation that the hotspot region was blocked by the DNA origami itself, thereby prohibiting the placement of a detection assay in this region.[29,39–41] To this end, the DNA origami NA proved to be applicable for the detection of Zika virus-specific oligonucleotides, both in buffer and heat-deactivated serum.[39] However, due to the steric hindrance in the hotspot, only the binding of one plasmonic NP was feasible, resulting in moderate FE values (approximately sevenfold) in the monomer NA arrangement.

Only recently, a DNA origami dimer NanoAntenna with Cleared HOtSpot (NACHOS, Figure 1b) was realized that

C. Close, K. Trofymchuk, L. Grabenhorst, V. Glembockyte, P. Tinnefeld
Department of Chemistry and Center for NanoScience
Ludwig-Maximilians-Universität München
Butenandtstr. 5-13, 81377 Munich, Germany
E-mail: philip.tinnefeld@cup.uni-muenchen.de
B. Lalkens
Institut für Halbleitertechnik
Laboratory for Emerging Nanometrology LENA
TU Braunschweig
Langer Kamp 6a/b, 38106 Braunschweig, Germany

The ORCID identification number(s) for the author(s) of this article can be found under https://doi.org/10.1002/admi.202200255.

DOI: 10.1002/admi.202200255

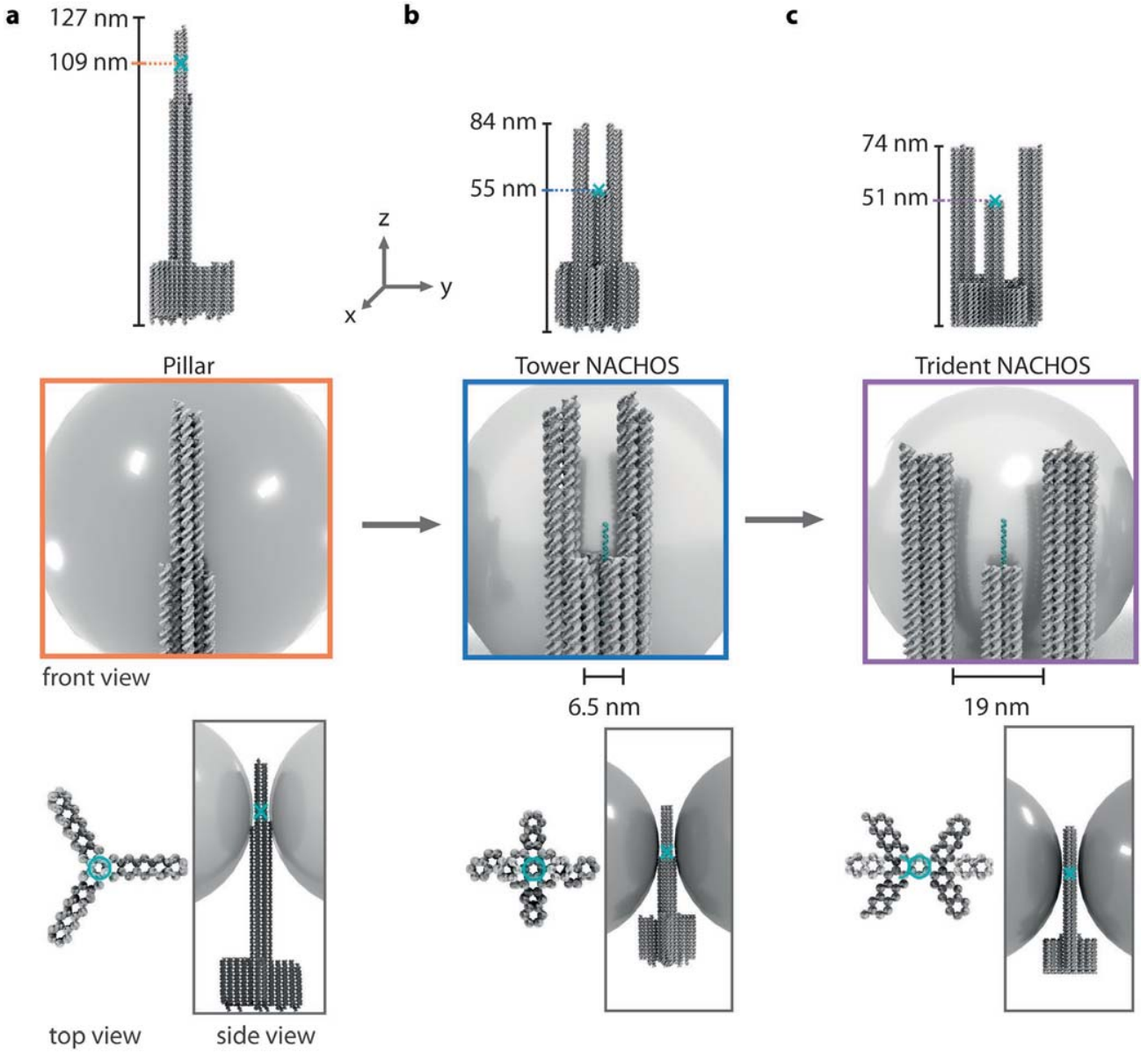

Figure 1. Schematic representation of three different DNA origami designs used for DNA origami NAs: a) Pillar,[29,39] b) Tower NACHOS,[42,43] c) Trident NACHOS. Hotspot position (marked with a cross) and overall height (top); Zoom-in on the hotspot regions showing the attached NP (100 nm diameter) and comparing the regions that are cleared from DNA origami and can be utilized for placing diagnostic assays (middle); Top view of DNA origami and side view with 100 nm NPs. Hotspot region is marked in cyan (bottom).

provides space of ≈12 nm × 6.5 nm in the plasmonic hotspot region between the particles, freed from DNA, for placing a biomolecular assay, while maintaining maximum FE values of over 400-fold.[42] The achieved high signal amplification enabled the first detection of 34 nt ssDNA and even single antibodies using a portable smartphone microscope.[35,42–44]

The experience with developing DNA origami NAs has yielded a few design rules for further evolution. One lesson learned is that FE distributions are commonly quite broad, reflecting that a small deviation from the exact placement of the structural components can have detrimental impact on the properties of the individual constructs. Heterogeneity is likely related to non-spherical NPs that bind in varying orientations, the distribution of positions of the bound strands on NPs, as well as a flexible dye position and orientation in the DNA origami. While the dye itself should be rotating freely, it was shown that fluorophores often stick to regions inside the DNA origami.[45] Nevertheless, FE distributions are well reproducible within each DNA origami design, and the respective average FE correlates well with the maximally achieved FE values. The sensitivity of FE on subtle factors, however, indicates that the structural control of the immediate hotspot surrounding is critical. We concluded that rigid and distance-controlled arrangement of NPs is obligatory, implying that NP binding should occur as close to the hotspot as possible, while not compromising the space required for assays in the hotspot. Binding NPs on a

flat DNA origami without a steric blockade resulted in heterogeneity (due to, e.g., NP size distribution), which limited the achievable FE, but could still be useful, for example, for Raman studies.[46–49]

In NACHOS, this paradigm was followed by placing two rigid pillars next to the hotspot, thereby creating a space that was similar to the size of the central pillar in the first generation of DNA origami NAs. In order to tap the full potential of DNA origami NAs for fluorescence-enhanced single-molecule biosensing, here, we followed the line of argumentation in a more drastic manner and created Trident NACHOS (Figure 1c). Therein, we increased the cleared hotspot region by creating a larger transversal distance between the pillars that served as spacers and attachment sites for NPs. For placement of the biomolecular assay, a third pillar between the NP attachment pillars was required. This central pillar is designed shorter so that biomolecular assays are placed directly in the equatorial plane between the NPs for optimal FE (Figure 1c).[35]

In this work, we present the Trident DNA origami for biosensing of larger targets with improved kinetics. We optimized the NA design with respect to NP binding and enhancement and drew a comparison of all three NA generations to investigate the impact of less steric constraints in the DNA origami NA hotspot on FE and accessibility. The new Trident NACHOS design thereby aims to improve both FE and accessibility in the plasmonic hotspot, which, ultimately, could be a step forward in democratization of evidence-based health care.[50]

2. Results and Discussion

2.1. DNA Origami Design

In this work, we introduce our next step in the evolution of DNA origami NAs. We specifically sought out the application of this technology for sensing of larger biomolecules on the single-molecule level, making use of the signal enhancement through LSPR. To this end, using a M13mp18-derived scaffold strand we adjusted the design of the previous NACHOS DNA origami to remodel the dimensions of the cleared hotspot region.[42] We expanded the distance between the two outer pillars to 19 nm (dimension in y in Figure 1c and **Figure 2**), leading to a decrease in overall height of the structure to 74 nm and an overall increased width of ≈40.5 nm (Figures S1,S2 and Tables S3,S4, Supporting information).[41] Additionally, the cross-shaped base was rotated by 45° relative to the y–axis compared to the previous Tower NACHOS design (see Figure 1b,c) to facilitate closer binding of both NPs to the central 51 nm high pillar, consisting of eight DNA helices (see colored area in bottom Figure 1c). This creates a designed interparticle distance of 12 nm, which is required for high FE (dimension in x in Figure 2b).[42] To achieve the simultaneous positioning of larger molecules and sufficiently high FE values, a compromise was necessary between structural stability to control NP arrangement and providing a spatially accessible attachment site for molecules in the hotspot region. Simulations using the online tool CanDo were used to estimate the structural rigidity and flexibility of the design (see Experimental Section and Figure S3, Supporting Information).[51] As the new design includes larger regions cleared from DNA origami, the simulation confirms that features in the Trident, such as the top region of the central pillar are less rigid compared to the more compact Tower NACHOS. Correct folding of the DNA origami structure was confirmed by negative stain transmission electron microscopy (TEM) after purification via ultrafiltration and gel electrophoresis (Figure S4, Supporting Information). Figure 2a and Figure S5, Supporting Information show the formation of the cross-shaped base, designed at 21 nm height, and all three pillars, of which the central one is shorter than the outer two.

To perform bottom-up self-assembly and single-molecule detection on the surface, twelve staple strands on the bottom of the Trident base were replaced with biotinylated oligonucleotides protruding from the structure (Tables S1 and S4, Supporting Information). This allows stable and upright positioning via biotin-NeutrAvidin interaction on a BSA-biotin coated coverslip and is crucial for co-alignment of the NA dipole with incident light.[35] For the purpose of assembling Trident NACHOS on the surface, we extended staple strands in both outlying pillars by a polyadenine sequence (see Figure 2c and Figure S1 and Table S4, Supporting Information). NPs, functionalized with thiolated polythymine ssDNA, are hybridized in zipper geometry to the NP binding strands protruding from the DNA origami at four different heights (46, 51, 53, and 57 nm in z).[36,52] This way, NPs attach in a middle position among the available complementary 20 base pair (bp) binding strands, corresponding to the position with least strain on the formed dsDNA NP binding interactions. By design, this average position of NPs is at the same height as the central pillar, corresponding to the plasmonic hotspot region.[53] A fluorophore, biomolecule, or detection assay of choice is placed in the plasmonic hotspot region between the two NPs via incorporation of the accordingly modified staple in the central pillar. To identify the position of the DNA origami on the surface, the base of the structure was equipped with a localization dye at ≈21 nm height (Figure 2b). The choice of separate excitation wavelengths for the localization and hotspot dye (532 and 639 nm, respectively) enabled colocalization measurements, quantifying the incorporation of molecules in the NA hotspot.[54]

To ensure correct formation of our NAs, we first measured confocal fluorescence scans of immobilized Trident DNA origami before addition of NPs (Figure 2d Reference) and after overnight incubation with 100 nm silver (Ag) NPs (Figure 2d 100 nm Ag NP). We determined the colocalization of red and green spots to 81% ± 5% (Figure S6, Supporting Information), indicating successful labeling of the DNA origami structure with both the localization and hotspot dyes (ATTO542 and ATTO647N, respectively). When observing the sample after incubation with 100 nm AgNPs, confocal scans acquired under the same excitation conditions showed colocalized spots with far higher intensities than in the reference sample, indicating the positioning of the dye (ATTO647N) in the hotspot formed by the NPs. For direct comparison, we recorded fluorescence transients of the NA (violet in Figure 2e) and the reference sample NA (grey in Figure 2e). To ensure the excitation of samples in the linear regime and avoid saturation in the hotspot, transients of NA samples were acquired at 50 nW (200 nW for reference) and normalized to the respective laser power for

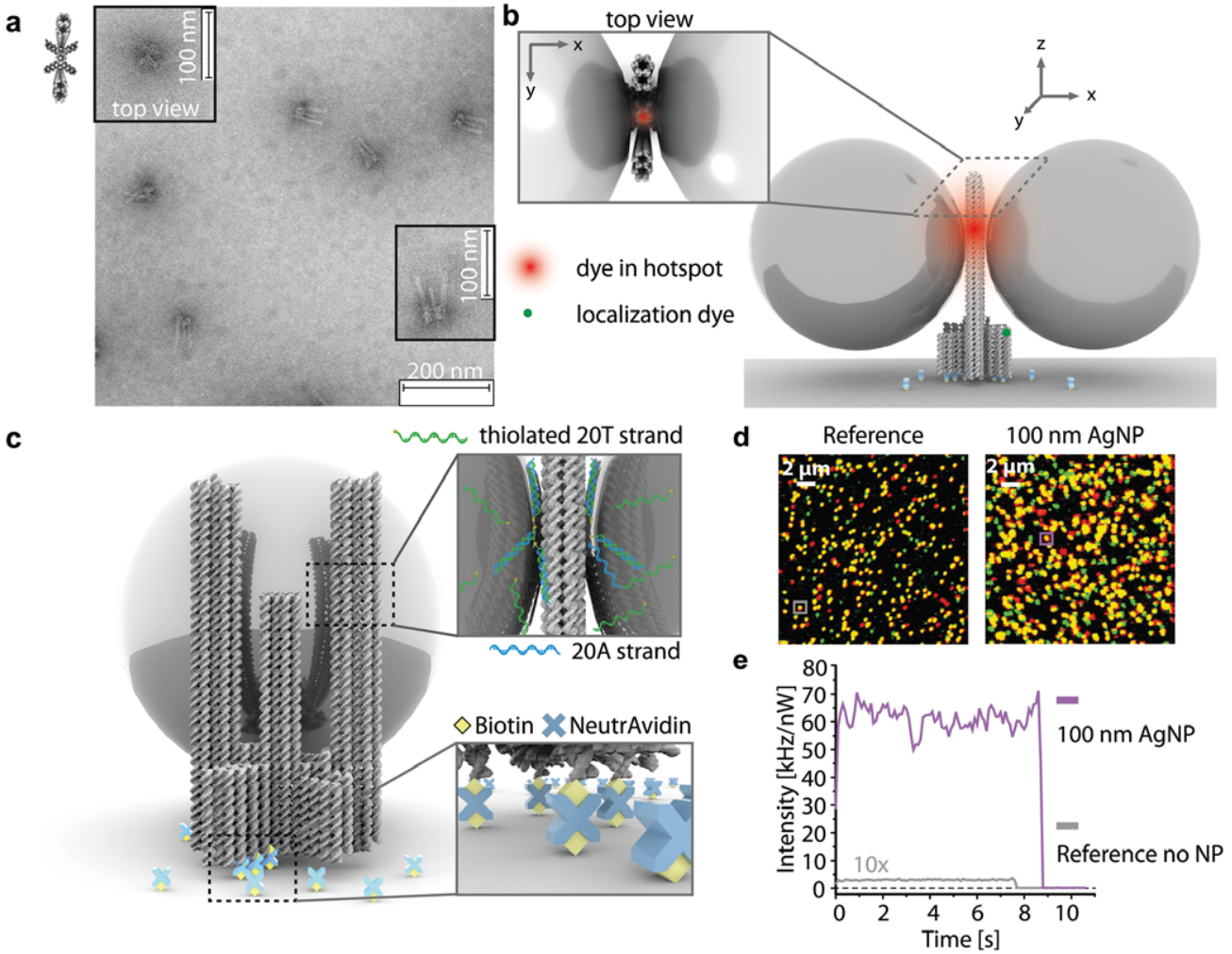

Figure 2. Trident NACHOS design. a) TEM image of the folded and purified structures. b) Schematic representation of the assembled Trident NA including the dye placed in the hotspot (red) and the dye for localization of DNA origami on the surface (green); Inset: top view. c) Strategies for immobilization of the Trident structure on a BSA-biotin-NeutrAvidin coated glass surface and binding NPs. d) Exemplary single-molecule fluorescence scans acquired on a confocal microscope. False-color coded red fluorescence spots obtained from the sample containing 100 nm AgNPs (right) exhibit fluorescence enhancement (FE) for the red fluorophore placed in the hotspot in comparison to the reference (left). Green spots correspond to an ATTO542 molecule for localization of DNA origami. Colocalization of red and green dyes within one construct is indicated by yellow spots. Both images were acquired at laser powers of 2 µW. e) Exemplary fluorescence transients for Trident NA and reference sample. To avoid saturation effects in the hotspot lower excitation powers were chosen for the NP sample (50 nW, reference 200 nW). Intensities were normalized to the laser power, justified as we worked in the linear regime.[43] The intensity of the reference sample without NP was multiplied 10× for visual purposes.

comparison.[43] As seen in both Figure 2d and Figure 2e, the intensity of a single ATTO647N molecule in the hotspot of a 100 nm Ag Trident NA is greatly increased over the dye in the reference sample without NPs.

2.2. Optimizing Conditions for NP Attachment to Trident DNA Origami

After first experiments confirmed the successful incorporation of dye molecules in the hotspot and attachment of NPs, the conditions for formation of the Trident NA were adjusted to reach highest FE values. Stable attachment and positioning of NPs at the designed distance are required, as the NP-fluorophore distance is one of the parameters determining if the emitter is in the FQ or FE regime. As the proximity to the NP alters the transition rates between electronic states of the fluorophore, the fluorescence lifetime (τ_{fl}) of a dye serves as an indicator for NP attachment. To reach our goal of high FE values, we measured changes in the distribution of τ_{fl} and intensity values of single molecules in samples prepared under different NA formation conditions. FE values were determined after normalization to the respective laser power and by dividing each value for molecules in the NA sample by the mean intensity of all molecules in the reference sample. All spots corresponding to single NAs displayed

in the fluorescence scan images were analyzed and only transients showing single-step bleaching behavior were included. We chose ATTO647N (τ_{fl} of ≈4 ns in reference samples) for the dye in the hotspot, as the long intrinsic lifetime allows to visualize small changes and relatively strong lifetime reductions.

2.2.1. Number of NP Binding Strands on the DNA Origami

As a first step, we determined the influence of different numbers of NP binding strands protruding from the DNA origami structure (**Figure 3**a). We expected an increasing number of accessible binding strands to improve the attachment of NPs and ensure correct positioning of both NPs in the designed distance to each other. The observed trend toward decreased fluorescence lifetimes (Figure 3a, left and Figure S7, Supporting Information)

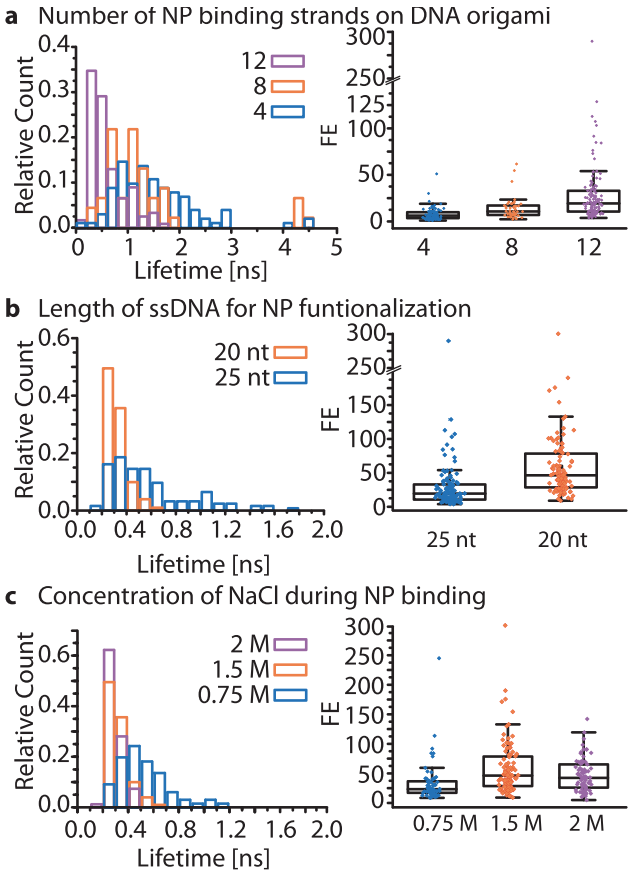

Figure 3. Optimization of τ_{fl} and FE values in the Trident NACHOS structure using an ATTO647N dye molecule in the hotspot. a) Comparison of FE values obtained for different numbers of NP binding strands on the DNA origami. Incubation of 25 nt functionalized NPs in buffer containing 750 mM NaCl. b) Comparing τ_{fl} and FE values obtained for different lengths of strands used for NP functionalization. Comparison was made on Trident with twelve binding strands and buffer containing 750 mM NaCl. c) Effect of NaCl concentration in the NP incubation buffer on τ_{fl} FE values for Trident origami with twelve NP binding strands (20 nt). More than 100 molecules per sample were analyzed. See Figure S7, Supporting Information for scatter plots of fluorescence lifetime versus respective FE values.

and higher FE values of ATTO647N (Figure 3a, middle panel and Figure S7a, Supporting Information) is consistent with this hypothesis. At the same time, the distribution of τ_{fl} (Figure 3a left panel) and τ_{fl}/enhancement plots for the samples containing four and eight NP binding strands (Figure S7a, Supporting Information) shows a substantial fraction of molecules having a lifetime between 1.0 and 3.0 ns. As the accessibility of NP binding strands in the DNA origami could be limited by effects such as molecular threading, we assume that these moderately reduced τ_{fl} values with low FE correspond to a monomer subpopulation of NAs in the sample.[54,55] The distribution of datapoints for a specifically designed monomer NAs significantly differs from the values we obtained in dimer NACHOS designs. Therefore, we conclude less monomers, but rather a sufficiently high fraction of dimer constructs in NA samples with 8 and 12 NP binding strands (see Figures S2, S7, and S8, Supporting Information and Supplementary Notes). For the Trident DNA origami NA design in particular, these samples demonstrated a clear advantage in forming Trident NAs with high FE values (Figure 3a, right panel and Supplementary Notes). Based on the obtained data, the Trident design containing twelve binding strands was used in the following.

2.2.2. Length of Strands Used for NP Functionalization

Pursuing the goal of optimizing the formation of the Trident NA, we adjusted the length of ssDNA used for functionalization of the 100 nm AgNPs (Figure 3b).[36] Reducing it from 25 to 20 nt on the NP showed an effect on the formation of NAs, as shorter NP binding strands (20 nt, T_{20}) led to a more narrowed distribution of τ_{fl} values (concentrated below 1.0 ns, see Figure 3b, left panel) and gave higher FE values than samples with 25 nt NP binding strands (Figure 3b, right panel and Figure S7b, Supporting Information).[36] We hypothesize that shortening the number of interacting nucleotides on NPs that are available for hybridization to DNA origami influences the thermodynamic equilibrium of NP attachment. For shorter interaction lengths the formation of less optimal binding configurations by partial hybridization of strands plays a smaller role.[56] In turn, interparticle distances that significantly vary from the optimal case, resulting in lower FE values could be reduced when using the interaction of 20 nt for NA formation.[57,58]

2.2.3. Concentration of NaCl during NP Binding

The rate of DNA hybridization is also sensitive to salt (NaCl) concentration. Furthermore, during overnight incubation of the DNA origami with the ssDNA coated NPs the composition of the buffer can influence the stability of the NP functionalization, which also affects potential NP aggregation.[59,60] To this end, we studied the influence of varying NaCl concentrations in the NP incubation buffer (Figure 3c, Figures S7c and S9, Supporting Information, see Experimental Section and Supporting Information for details). While a few molecules at the lowest salt concentration in buffer show τ_{fl} with a maximum of molecules around 0.5 ns (Figure 3c, left panel), highest FE values and reduced τ_{fl} were observed at intermediate (1.5 M) NaCl concentration.

Further increasing the concentration to 2 M NaCl did not improve the values for FE or τ_{fl} (Figure 3c, right panel and Figure S7c, Supporting Information). To sum up, we determined the optimal conditions for Trident NACHOS formation, which include:

I. Using DNA origami structures with 12 NP binding strands.
II. Using NP covered with 20 nt ssDNA.
III. Performing NP incubation at 1.5 M NaCl concentration.

2.3. Comparison of Three DNA Origami Nanoantennas for FE

To compare the efficiency of signal enhancement of the newly designed and optimized Trident structure to that obtained in previous DNA origami NA constructs we evaluated the behavior of a single Alexa Fluor 647 molecule (AF647, $\tau_{fl} \approx 1$ ns) in the hotspot of a dimer 100 nm Ag NP NA. To reliably detect each fluorophore before photobleaching, a reducing/oxidizing system was used for photostabilization.[61–63] To this end, we prepared separate samples of all three DNA origami structures on the surface and incubated with 100 nm AgNPs (functionalized with T_{20} ssDNA) under the discussed optimal NA formation conditions (Pillar: 6 NP binding strands, 750 mM NaCl; Tower: 12 NP strands, 750 mM NaCl; Trident: 12 NP strands, 1.5 M NaCl). In all three presented structures the central pillar separating both particles of a dimer NA served as the attachment site for molecules in the hotspot and therefore defines the interparticle distance. In this position, the distance of the NPs to each other was estimated to be similar for all three NA structures, as the central pillar consists of a six-helix bundle motif (see Figure 1). Confocal fluorescence scans were first acquired at an excitation power of 2 µW to confirm colocalization of both dyes with the DNA origami. Subsequently, fluorescence transients were recorded (excitation power of 50 nW for NA and 200 nW for reference samples). From the recorded transients, FE values of all DNA origami NA structures were determined by dividing the intensity of each acquired molecule (≥175) by the mean intensity of all molecules (≥190) in the respective reference sample without NPs (grey in left panels of **Figure 4**, Figure S10, Supporting Information). Corresponding fluorescence lifetime values of all molecules were extracted from the acquired fluorescence transients (see Experimental Section). In both NACHOS structures, we measured shorter τ_{fl} and higher mean FE values for a single AF647 molecule placed in the hotspot compared to the Pillar design with a blocked hotspot region (see Figure 4 and **Table 1**). The inherent heterogeneity in all three DNA origami NA samples potentially originates from the multiple factors involved in optimal NA formation, such as functionalization and orientation of NPs, as well as the arrangement of strands in the DNA origami structure itself.[60] Although this is reflected in the broadness of the FE distributions for all three DNA origami designs, the overall trend for the two NACHOS are distributions narrowed to lower τ_{fl} and higher FE values. Comparing the mean FE values for all three designs (grey in right panels of Figure 4) shows similar values for the two NACHOS generations (Tower: 61 ± 46, Trident: 67 ± 58), both higher than for the Pillar design (17 ± 17). The moderate increase in FE might be related to the fact that hybridization of ssDNA-coated NPs to the DNA origami Pillar occurs to the central pillar, creating a slightly larger gap compared to the NACHOS design, where

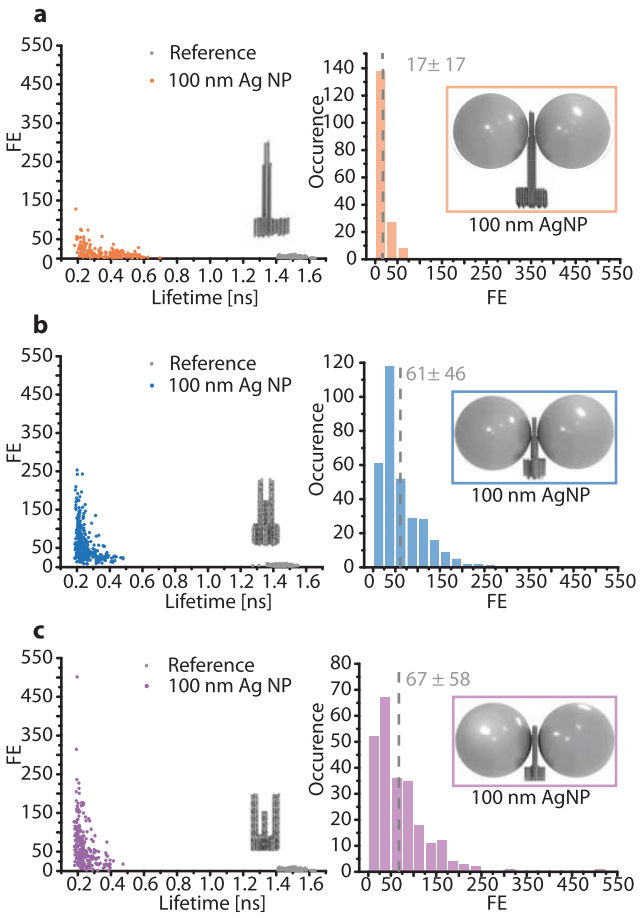

Figure 4. Comparison of FE and τ_{fl} values obtained for AF647 in the hotspot region of three DNA origami NA structures. Mean FE values were calculated from the arithmetic average and reported with the according standard deviation (SD). a) Pillar NA structure (mean FE: 17 ± 17), b) Tower NACHOS structure (mean FE: 61 ± 46), c) Trident NACHOS structure (mean FE: 67 ± 58). The dashed vertical line corresponds to the obtained mean value of FE. Reference structure corresponds to DNA origami without NPs. Samples were prepared using T_{20} strands for NP functionalization, 6 NP binding strands on the Pillar DNA origami (12 on Tower and Trident), and 750 mM NaCl during NP incubation for Pillar and Tower (1.5 M NaCl for Trident). More than 175 molecules were analyzed for each NA sample, more than 190 for each reference sample.

Table 1. Comparison of designed dimensions and experimentally acquired FE of a single AF647 molecule and sandwich hybridization assay (up to three AF647) in the hotspot of three reported DNA origami structures. Mean FE values were calculated from the arithmetic average and the according SD.[35]

DNA origami design	Pillar	Tower	Trident
Interparticle distance *X* [nm]	12	12	12
Cleared hotspot width *Y* [nm]	Blocked by DNA	6.5	19
Overall height *Z* [nm]	127	84	74
Hotspot position *Z* [nm]	109	55	51
Cleared hotspot volume [zL]	Blocked by DNA	4.7	7.0
Mean FE for a fixed AF647 dye	17 ± 17	61 ± 46	67 ± 58
Mean FE in diagnostic assay	17 ± 17	69 ± 67	76 ± 57

binding strands protrude from the two outer pillars. We conclude that increasing the size of the plasmonic hotspot region in NACHOS from 6.5 to 19 nm in the transversal direction did not compromise FE (see Table 1) but rather optimized FE by enabling smaller gaps along the longitudinal mode of the NA.

2.4. Comparing the Accessibility of Nanoantenna Hotspots for Binding of 151 nt ssDNA

In our NA approach, capturing large biomolecules in the plasmonic hotspot region is ultimately limited by the diffusion of the molecule into the hotspot of zL volume, which is sterically hindered by DNA origami and NPs. Considering this, it is conceivable that capturing larger molecules might take place on an overall faster timescale for the more open Trident origami design. Additional to limited space in the DNA origami structure, the accessibility of the plasmonic hotspot may also be restricted by the surface of attached NPs (coated with negatively charged DNA). This is particularly relevant for dimer NA constructs containing two large NPs. Geometric approximations for NP attachment result in a theoretical accessible hotspot volume of 4.7 zeptoliters for the dimer Tower NA (Figure S12, Supporting Information). Due to the larger region cleared from

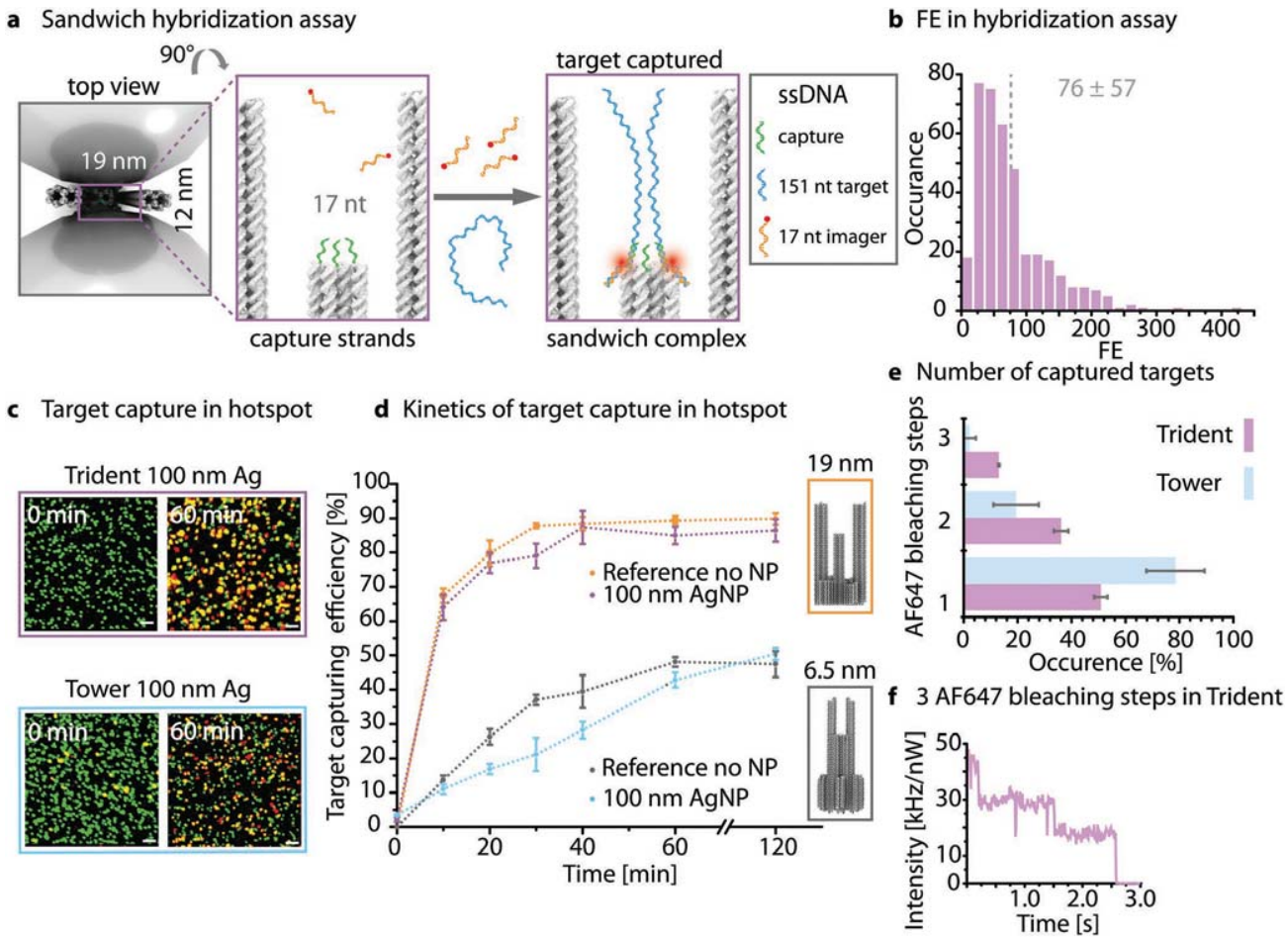

Figure 5. Comparing the accessibility of DNA Origami NA hotspots for the two NACHOS designs. a) Illustration of sandwich hybridization assay for detection of 151 nt target DNA. Addition of both target and 17 nt AF647 labeled imager strands to DNA origami NAs containing three 17 nt capture strands in the hotspots of NACHOS leads to hybridization of the target strand, followed by the binding of the AF647 labeled imager strand in the hotspot and subsequent FE. b) FE values, acquired for AF647 labeled imager strand in Trident NACHOS. 382 single-molecule transients were analyzed. After normalizing to the excitation laser power, each value for molecules in the NA sample was divided by the mean intensity of AF647 molecules in the reference sample without NPs. For multiple bleaching steps, each was considered separately and normalized to the average intensity of a single molecule in the reference sample. c) Confocal fluorescence scans acquired for both NACHOS before and after 60 min incubation with the target/imager solution (4 and 12 nM, respectively). Scale bar corresponds to 2 µm. Exemplary scans for all timepoints in Figure S11, Supporting Information. d) Comparison of kinetics of target capturing obtained for the two structures with different cleared hotspot volumes. Reference Trident without NP (grey); Trident 100 nm AgNP NA (violet); Reference Tower without NP (orange), Tower 100 nm AgNP NA (blue). Dashed lines are included for guiding the eye. (Trident: $n \geq 504$ molecules per time point, Tower: $n \geq 791$ per time point). e) Quantification of target ssDNA molecules binding in the NA hotspot for the two NACHOS via bleaching step analysis of AF647 after 120 min incubation. Error bars correspond to the standard deviation acquired for three separate measurements. f) Exemplary fluorescence transient for Trident NA with 3 capturing sites exhibiting 3 bleaching steps of AF647. To avoid saturation effects in the hotspot lower excitation powers were chosen for the NP sample (50 nW). Intensities were normalized to the laser power.

DNA, the accessible volume of the Trident in and above the designed hotspot at 51 nm height amounts to 7.0 zL and might be accessed more easily due to the larger gaps inside the structure. To prove the increased accessibility of the cleared hotspot region in the new Trident DNA origami NA design and its advantage for diagnostic assays involving larger molecules we carried out a sandwich hybridization assay (**Figure 5**). Therefore, staple strands in the hotspot region were extended by a TTT linker and a 17 nt sequence, creating so-called capture strands which are complementary to part of a 151 nt long, synthetic ssDNA target molecule. We chose a target sequence specific to the OXA-48 gene, that plays an important role in diagnosis of an antibiotic-resistant *Klebsiella pneumonia* infection.[64,65] Binding of the long ssDNA target was visualized by adding a 17 nt AF647 labeled imager strand in solution (Figure 5a and Experimental Section). This strand can hybridize to a 17 nt region within the target ssDNA. Upon capturing both DNA strands inside the NA, the dye is placed in the theoretically optimal position for FE in the plasmonic hotspot. Due to the resulting influence on the fluorophore properties in this position, τ_{fl} and FE of AF647 were used as parameters to confirm positioning of the entire sandwich complex inside the NA hotspot (see Figures S9 and S13, Supporting Information). The overall detection efficiency was quantified via colocalization of the red imager dye with the green ATTO542 labeled DNA origami using confocal microscopy. The amount of red/green colocalized spots (yellow in false-color confocal scans in Figure 5b) was divided by the number of all DNA origamis (green + yellow spots). The resulting values for colocalization of imager dye with the DNA origami NAs are plotted in Figure 5c (all scans in Figure S10, Supporting Information). We performed a comparative study of the Trident NACHOS with the Tower construct to determine the effect of increased dimensions of the region cleared from DNA origami on the accessibility of the hotspot (Trident NA: violet, Tower NA: blue in Figure 5c). To also check for NPs potentially blocking the hotspot region when bound, the two DNA origami structures were prepared both with and without 100 nm AgNPs (Figure 5c Trident: orange, Tower: grey for samples without NP) before incubating with the target/imager solution. Confocal fluorescence scans before incubation (0 min) show only green spots due to the presence of only DNA origami on the surface. In NA samples, apparently colocalized spots appear, for example, due to the effect of NP aggregates scattering (3.5% ± 0.1% in Tower, 2.0% ± 0.7% in Trident), however, the analysis of single-step photobleaching events in fluorescent transients can eliminate this background signal. Already after 10 min of incubation with both target and imager strands (4 and 12 nM, respectively) we measured a notable difference between the amount of the target molecules bound to the capture strand in the hotspot of Tower or Trident DNA origami NAs. 11% ± 1% of ATTO542 labeled Tower DNA origami NAs (blue in Figure 5d) were colocalized with a red AF647 imager in the hotspot. In contrast, after incubating the Trident NA for 10 min with the target/imager mixture, 64% ± 4% of the observed Trident NAs had already bound at least one sandwich complex (violet in Figure 5d, Tower: blue/grey, Trident: violet/orange). Interestingly, our results showed only a small influence of attached NPs on the kinetics of hybridization in the hotspot (Figure 5d), the DNA origami design being a more crucial factor influencing the accessibility of the diagnostic assay. Observing colocalization as a function of target/imager incubation time indicates overall faster kinetics for binding the sandwich complex in the Trident DNA origami. When comparing the time needed for target capturing to be clearly distinguishable over background (e.g., 30%) this point is reached in less than 10 min for Trident, whereas the Tower NACHOS design requires at least 30 min of incubation. The increased accessibility to the hotspot of the Trident design is further reflected in the overall maximum of visited capture sites in the sample. Trident NACHOS are 87% ± 5% colocalized after 40 min of incubation in comparison to 60 min needed for 43% ± 2% colocalization in Tower NACHOS. Considering that three capturing sites are available to bind the target/imager duplex, single-molecule analysis of colocalized spots gives further insight into how many target molecules were captured in a given design. We acquired fluorescence transients from hundreds of single NAs and used bleaching step analysis to resolve the actual number of AF647 molecules captured by each DNA origami nanostructure both with NPs. As each red spot corresponds to at least one hybridized imager/target complex, the observed number of photobleaching steps of AF647 reports on the number of imager and thus target strands bound in the hotspot (Figure 5d). As for the DNA origami comparison in Figure 4, we used a photostabilizing agent and low excitation powers (50 nW) to ensure the detection of each AF647 molecule before photobleaching. Due to less than 100% labeling efficiency of imager strands, we expected the actual number of bound target molecules to be slightly higher than what was detected in previous NACHOS.[54] The improved accessibility of the larger hotspot is reflected in the increased fraction of NAs capable of capturing multiple target molecules in the Trident DNA origami NA. Three bleaching steps, and thereby occupation of all available capturing sites by a sandwich complex were observed in 13% of the Trident NA origami in the sample (4% in Tower). The fraction of NAs binding two target molecules also increased to 36% in the Trident DNA origami NA over 19% in the Tower design. Accordingly, the ratio of spots in the sample that exhibit only one photobleaching step of the dye in the hotspot decreased from 79% for Tower to 51% in Trident NA samples. While the increased dimensions of the Trident NACHOS hotspot clearly improved its accessibility, the attained FE within this NA structure was not compromised (Figures S12, S14, and S15, Supporting Information). As shown in Table 1 the obtained FE values for the diagnostic assay placed in the Trident structure are distributed around a maximum of 76 ± 57 and therefore are even slightly higher than the FE values we acquired for a fixed AF647 dye in the Trident DNA origami NA hotspot.

3. Conclusion

We presented a novel Trident DNA origami design for NACHOS to detect larger targets, such as a 151 nt long ssDNA. The Trident DNA origami architecture was optimized for NA formation, by reducing the length and increasing the number of NP binding strands, as well as optimizing the NP binding conditions.

We then compared the Trident NACHOS to previous designs and found that FE in the Trident NACHOS was similar to or better than in previous NA realizations (see summary in

Table 1, Figure S15, Supporting Information). The advantage of the newly presented DNA origami Trident design lies in the increased accessibility of the plasmonic hotspot region. We expanded the cleared space between the two pillars for NP attachment to 19 nm, while keeping the interparticle distance equal to the previous designs. This enabled not only the detection of a 151 nt ssDNA target molecule with improved binding yield, but also accelerated binding kinetics. This was demonstrated by, for example, 30% of the DNA origami binding at least one target/imager construct in under 10 min, corresponding an approximately threefold increase in speed compared to the Tower NACHOS. Further, the plateau of target molecule binding, representing the maximum hotspot accessibility was higher in Trident NACHOS and reached faster than in the Tower design. Incorporating microfluidic methods to increase mass transport should further improve the assay speed and bring it into a relevant range of sensitivity for many applications.[66–68] While the DNA origami design played a key role, attachment of NPs interestingly only had a minimal influence on hotspot accessibility and binding kinetics.

The achieved duality of high FE values and improved accessibility of the hotspot region expands the applicability of our technology for single-molecule-based plasmonic biosensing, thereby making it possible to carry out an assay with cost-effective and mobile optical equipment.[42] The presented binding of multiple target DNA molecules in our Trident NA hotspot suggests the feasibility of multiplexed detection within one NA. In this manner, the capturing of several target DNA molecules with varying sequences inside one Trident NACHOS construct is conceivable. In turn, each sequence then could be visualized using spectrally separate imager strands. Furthermore, the large clearing in the hotspot could also facilitate placement of active proteins in the plasmonic hotspots (e.g., polymerases), thereby expanding the application of DNA origami NAs to different avenues, such as nanopore plasmonics, DNA sequencing, or detailed studies of transition paths in conformational dynamics of protein folding inside the plasmonic hotspot.[68–77]

4. Experimental Section

DNA Origami Design, Folding, and Purification: DNA origami structures were designed and adapted in CaDNAno version 2.3.0 (staple layout in Figure S1 and Table S4, Supporting Information).[4] Simulations to estimate structural rigidity and flexibility were performed using the online tool CanDo (Figure S3 and Table S1, Supporting Information).[6,51] The DNA origami structures were prepared by performing previously published protocols in adaption of Wagenbauer et al.[39] For preparation of the Trident DNA origami, 25 µL of 100 nM in-house produced p8064 scaffold strand solution was combined with tenfold excess of staple strands (Integrated DNA Technologies Europe GmbH, Germany; Eurofins Genomics GmbH, Germany and biomers.net GmbH, Germany). To simplify the process, mastermix solutions of modified and unmodified staple strands were pooled from their 100 µM concentration. 18 µL of unmodified staples, together with 2 µL modified strands were added to the scaffold and filled up with 2.5 µL 10 × FoB20 (containing Tris, EDTA, MgCl2, and NaCl, see Table S2, Supporting Information for recipe). Table S3, Supporting Information shows adapted recipes for Tower and Pillar DNA origami. Heating to 95 °C and cooling down to 25 °C were performed according to the annealing ramp shown in Table S5, Supporting Information. Excess staple strands were removed by purifying with Amicon filtering through a 100 kDa MWCO membrane (Merck KGaA, Germany). The mixture was purified by centrifugation at 20 °C and 10 000 × *g* for 5 min after washing with 1 × FoB5; the procedure was performed five times. The Amicon filter was then flipped and placed in a new Amicon tube, centrifuging at 1000 rpm at 20 °C for 1 min to extract the purified DNA origami. The presence of DNA origami in the solution was confirmed and quantified via UV-vis spectroscopy (NanoDrop, Fischer Scientific, USA). Determined yields from synthesis using 100 nM scaffold strand were commonly in the range of 72 ± 18 nM.

TEM: TEM grids (Formvar/carbon, 400 mesh, Cu, TedPella, Inc. USA) were cleaned in Ar-plasma and incubated for 60 s with the DNA origami sample (5 µL, ≈2 to 10 nM). 2% uranyl formeate solution (5 µL) was used to wash the grids and incubate 4 s for staining. Imaging was performed on a JEM-1100 microscope (JEOL GmbH, Japan) with acceleration voltage of 80 kV.

Silver NP Functionalization: Functionalization of plasmonic NPs with ssDNA was performed using a modification of a published protocol.[39] During the entire preparation procedure 2 mL of the NP solution (1 mg mL^{-1} 100 nm Ag, BioPure Silver Nanospheres (in 2 mM Citrate), nanoComposix, USA) were continuously stirred at 550 rpm at 40 °C. In the following, 20 µL of polysorbate 20 (10%, Sigma Aldrich, USA), as well as 20 µL potassium phosphate buffer (1 M solutions of mono- and dibasic potassium phosphate in a 4:5 mixture, Sigma Aldrich, USA) and 10 µL of a 2 nM thiol-modified single stranded DNA solution (5″-thiol-25T-3″ or 5″-thiol-20T-3,″ Ella Biotech GmbH) were added successively. The mixture was then stirred at 40 °C for 1 h. To reach a final concentration 750 mM of NaCl in PBS3300 buffer (see Table S2, Supporting Information) a salting procedure was performed by gradually adding portions of the buffer over a period of 45 min (see Table S6, Supporting Information). The solution was then diluted 1:1 with PBS 10 buffer (1 × PBS, 10 mM NaCl, 2.11 mM P8709, 89 mM P8584 (Sigma Aldrich, USA), 0.01% polysorbate 20, and 1 mM EDTA (Thermo Fisher Scientific, USA)). Excess of thiolated ssDNA was removed by centrifuging the solution for 10 min at 2800 × *g* and 20 °C. After centrifugation, the supernatant was discarded and the pellet containing the concentrated particles was again dissolved in PBS 10 buffer. This washing step was repeated four times. The silver NPs were then diluted in 1 × TE containing 750 mM, 1.5 M, or 2 M of NaCl to reach an approximate value of 0.1 for the extinction maximum on the UV-Vis spectrometer (Nanodrop 2000, Thermo Fisher, USA).

Nanoantenna Preparation: To prepare the surface for immobilization of DNA origami microscope coverslips (24 mm × 60 mm and 170 µm thickness) were UV-Ozone cleaned (PSD-UV4, Novascan Technologies, USA). SecureSeal Hybridization Chambers (2.6 mm depth, Grace Bio-Labs, USA) were glued on the clean coverslips and laid on a heating plate (1 min at 80 °C) to ensure sufficient sealing. The obtained chambers were washed three times with 1 × PBS buffer. Bovine serum albumin (BSA)-biotin (1 mg mL^{-1}, Sigma Aldrich, USA) was used to passivate the surface and incubated for 30 min. After washing the chambers 3 × with 1 × PBS, NeutrAvidin 0.25 mg mL^{-1} (Sigma Aldrich, USA) was added and incubated for 30 min. Afterward, three washing steps with 1 × PBS were performed. The purified DNA origami solution was diluted in TE buffer containing 750 mM NaCl (TE750) to prepare a solution with concentration in a range between 250 and 400 pM. After 5 min of incubating with the diluted DNA origami solution, three washing steps were performed with TE750 buffer. Afterward, appropriate surface density for single-molecule measurements was confirmed on the microscope (see "Confocal Microscopy, Data, and Statistical Analysis" in Experimental Section). AgNPs solution was added and incubated in the TE buffer (see Table S2, Supporting Information) containing 750 mM, 1.5 M, or 2 M of NaCl. After overnight incubation, samples were washed three times with the same buffer. Afterward, the surface was stored in TE750 to avoid drying and degradation of the samples.

Sandwich Hybridization Assay: DNA origami structures were folded containing three capture strands (see sequences in Table S4, Supporting Information) for the 151 nt DNA target, specific to the OXA-48 gene carrying the antibiotic resistance.[64,65] Prepared NA samples were incubated with 4 nM target DNA (Table S4, Supporting Information) and 12 nM AF647 labeled imager strand (17 nt, see Table S4, Supporting

Information) in 1 × TE containing 2 M NaCl and 0.01% polysorbate 20 (Sigma Aldrich, USA) for the denoted amount of time. After incubation, samples were washed three times with the incubation buffer and stored in TE750 for imaging.

Confocal Microscopy, Data, and Statistical Analysis: To detect the fluorescence of single molecules a custom-build setup based on an Olympus IX-83 inverted microscope (Olympus Corporation, Japan) with a 78 MHz pulsed supercontinuum white-light laser (SuperK Extreme, NKT Photonics A/S, Denmark) was used. Wavelength selection between 532 and 639 nm was achieved with an acousto-optically tunable filter (AOTF, SuperK Dual AOTF, NKT Photonics, Denmark) and a digital controller (AODS 20160 8R, Crystal Technology, Inc., USA) via computer software (AODS 20160 Control Panel, Crystal Technology, Inc. USA). A second AOTF (AA.AOTF. ns: TN, AA-Opto-Electronic, France) was used to alternate between the two wavelengths if required. The second AOTF, controlled via LabVIEW software, was further used to set laser intensity and spectrally clean the laser beam. A neutral density filter (ndF, OD 0-2, Thorlabs, Germany) was used to manually regulate the laser intensity followed by a linear polarizer (LPVISE100-A, Thorlabs, Germany) and lambda quarter plate (AQWP05M-600, Thorlabs, Germany) for circular polarized excitation. The height difference between excitation path and microscope body was overcome in the setup by coupling the laser into a polarization maintaining fiber (PM-Faser, P1-488PM-FC-2, Thorlabs, Germany). The laser was focused onto the sample with an oil-immersion objective (UPlanSApo100×, NA = 1.4, WD = 0.12 mm, Olympus Corporation, Japan). Positioning of the sample was performed with a piezo stage (P-517.3CL, E-501.00, Physik Instrumente GmbH & Co. KG, Germany). Excitation light was separated from the emitted light through the dichroic beam splitter and then focused on a 50 µm pinhole (Linos AG, Germany). The emission channels for red and green were spectrally filtered (red: RazorEdge 647, Semrock Inc., USA and green: Brightline HC582/75, Semrock Inc, USA). The light was detected by a Single-Photon Avalanche Diode (SPCM, AQR 14, PerkinElmer Inc., USA) and registered by a TCSPC system (HydraHarp 400, PicoQuant GmbH, Germany). Settings for scans were 2 µW, powers of 50 nW were used to record transients of samples with NPs, 200 nW for samples without NPs. A custom-made LabVIEW software (National Instruments, USA) was used to process the acquired data. Background correction was performed for each transient. Fluorescence lifetime decays were extracted and monoexponentially fitted for the shortest lifetime component. Datapoints presented in Figure 4 were further deconvolved from the instrument response function using FluoFit (PicoQuant GmbH, Germany). FE values were determined by dividing intensity values of every NA sample by the mean intensity measured in the reference sample, normalized by the set laser power. The extracted data were analyzed in OriginPro2019. Samples were prepared according to the protocol described above. Samples containing AF647 were imaged in a reducing and oxidizing buffer system for enzymatic oxygen removal (ROXS, see Table S2, Supporting Information).

Supporting Information

Supporting Information is available from the Wiley Online Library or from the author.

Acknowledgements

The authors thank Vivien Behrendt, Dr. Benedikt Hauer, and Dr.-Ing. Albrecht Brandenburg (Fraunhofer-Institut für Physikalische Messtechnik IPM, Freiburg, Germany) for cooperation on the DNA origami and assay development and Prof. Tim Liedl/Prof. Joachim Rädler (Ludwig-Maximilians-Universität, Department für Physik, Munich, Germany) for providing access to their facilities, especially to the transmission electron microscope, and to Dr. Florian Selbach for preforming TEM measurements. C.C. thanks Maximilian Sacherer and Jakob Hartmann for help with experiments in the early project stages and Renukka Yaadav, as well as Martina Pfeiffer for fruitful cooperation on related projects. P.T. gratefully acknowledges financial support from the DFG (grant number TI 329/9-2, project number 267681426, INST 86/1904-1 FUGG, excellence cluster e-conversion EXC 2089/1-390776260), Sino-German Center for Research Promotion (grant agreement C-0008), BMBF (Grants POCEMON, 13N14336, and SIBOF, 03VP03891). B.L. acknowledges funding by the Deutsche Forschungsgemeinschaft (DFG, German Research Foundation) under Germany's Excellence Strategy—EXC-2123 QuantumFrontiers—390837967 and "Niedersächsisches Vorab" through "Quantum- and Nano-Metrology (QUANOMET)" initiative within the project NL-1. V.G. acknowledges the support from European Union's Horizon 2020 research and innovation program under the Marie Skłodowska-Curie actions (grant agreement No. 840741). K.T. and V.G. acknowledge the support by Humboldt Research Fellowships from the Alexander von Humboldt Foundation.

Open access funding enabled and organized by Projekt DEAL.

Conflict of Interest

The authors declare no conflict of interest.

Data Availability Statement

The data that support the findings of this study are available from the corresponding author upon reasonable request.

Keywords

biosensing, DNA nanotechnology, nanoantenna hotspot, plasmonics, plasmonic hotspot accessibility, single-molecule detection, single-molecule fluorescence

Received: February 9, 2022
Revised: April 18, 2022
Published online:

[1] N. C. Seeman, *J. Theor. Biol.* **1982**, *99*, 237.
[2] N. C. Seeman, A. M. Belcher, *Proc. Natl. Acad. Sci. USA* **2002**, *99*, 6451.
[3] P. W. K. Rothemund, *Nature* **2006**, *440*, 297.
[4] S. M. Douglas, A. H. Marblestone, S. Teerapittayanon, A. Vazquez, G. M. Church, W. M. Shih, *Nucleic Acids Res.* **2009**, *37*, 5001.
[5] S. M. Douglas, H. Dietz, T. Liedl, B. Hogberg, F. Graf, W. M. Shih, *Nature* **2009**, *459*, 414.
[6] C. E. Castro, F. Kilchherr, D. N. Kim, E. L. Shiao, T. Wauer, P. Wortmann, M. Bathe, H. Dietz, *Nat. Methods* **2011**, *8*, 221.
[7] D. R. Walt, *Anal. Chem.* **2013**, *85*, 1258.
[8] M. Bauch, K. Toma, M. Toma, Q. Zhang, J. Dostalek, *Plasmonics* **2014**, *9*, 781.
[9] E. D. Fabrizio, S. Schlücker, J. Wenger, R. Regmi, H. Rigneault, G. Calafiore, M. West, S. Cabrini, M. Fleischer, N. F. van Hulst, M. F. Garcia-Parajo, A. Pucci, D. Cojoc, C. A. E. Hauser, M. Ni, *J. Opt.* **2016**, *18*, 063003.
[10] A. B. Taylor, P. Zijlstra, *ACS Sens.* **2017**, *2*, 1103.
[11] M. Madsen, K. V. Gothelf, *Chem. Rev.* **2019**, *119*, 6384.
[12] S. Wang, Z. Zhou, N. Ma, S. Yang, K. Li, C. Teng, Y. Ke, Y. Tian, *Sensors* **2020**, *20*, 6899.

[13] S. Dey, C. Fan, K. V. Gothelf, J. Li, C. Lin, L. Liu, N. Liu, M. A. D. Nijenhuis, B. Saccà, F. C. Simmel, H. Yan, P. Zhan, *Nat. Rev. Methods Primers* **2021**, *1*, 13.
[14] F. Hong, F. Zhang, Y. Liu, H. Yan, *Chem. Rev.* **2017**, *117*, 12584.
[15] P. Kuhler, E. M. Roller, R. Schreiber, T. Liedl, T. Lohmuller, J. Feldmann, *Nano Lett.* **2014**, *14*, 2914.
[16] V. Giannini, A. I. Fernandez-Dominguez, S. C. Heck, S. A. Maier, *Chem. Rev.* **2011**, *111*, 3888.
[17] J. M. Kim, C. Lee, Y. Lee, J. Lee, S. J. Park, S. Park, J. M. Nam, *Adv. Mater.* **2021**, *33*, 2006966.
[18] Y. Fu, J. R. Lakowicz, *Laser Photonics Rev.* **2009**, *3*, 221.
[19] P. Anger, P. Bharadwaj, L. Novotny, *Phys. Rev. Lett.* **2006**, *96*, 113002.
[20] R. Carminati, J. J. Greffet, C. Henkel, J. M. Vigoureux, *Opt. Commun.* **2006**, *261*, 368.
[21] G. P. Acuna, M. Bucher, I. H. Stein, C. Steinhauer, A. Kuzyk, P. Holzmeister, R. Schreiber, A. Moroz, F. D. Stefani, T. Liedl, F. C. Simmel, P. Tinnefeld, *ACS Nano* **2012**, *6*, 3189.
[22] R. Chikkaraddy, V. A. Turek, N. Kongsuwan, F. Benz, C. Carnegie, T. van de Goor, B. de Nijs, A. Demetriadou, O. Hess, U. F. Keyser, J. J. Baumberg, *Nano Lett.* **2018**, *18*, 405.
[23] V. V. Thacker, L. O. Herrmann, D. O. Sigle, T. Zhang, T. Liedl, J. J. Baumberg, U. F. Keyser, *Nat. Commun.* **2014**, *5*, 3448.
[24] J. Prinz, B. Schreiber, L. Olejko, J. Oertel, J. Rackwitz, A. Keller, I. Bald, *J. Phys. Chem. Lett.* **2013**, *4*, 4140.
[25] M. Moskovits, *J. Raman Spectrosc.* **2005**, *36*, 485.
[26] K. A. Willets, R. P. Van Duyne, *Annu. Rev. Phys. Chem.* **2007**, *58*, 267.
[27] K. Tapio, A. Mostafa, Y. Kanehira, A. Suma, A. Dutta, I. Bald, *ACS Nano* **2021**, *15*, 7065.
[28] M. Dass, F. N. Gur, K. Kolataj, M. J. Urban, T. Liedl, *J. Phys. Chem. C* **2021**, *125*, 5969.
[29] C. Vietz, I. Kaminska, M. Sanz Paz, P. Tinnefeld, G. P. Acuna, *ACS Nano* **2017**, *11*, 4969.
[30] P. Bharadwaj, L. Novotny, *Opt. Express* **2007**, *15*, 14266.
[31] P. Holzmeister, E. Pibiri, J. J. Schmied, T. Sen, G. P. Acuna, P. Tinnefeld, *Nat. Commun.* **2014**, *5*, 5356.
[32] H. Chew, *Phys. Rev. A* **1988**, *38*, 3410.
[33] A. Kinkhabwala, Z. Yu, S. Fan, Y. Avlasevich, K. Müllen, W. E. Moerner, *Nat. Photonics* **2009**, *3*, 654.
[34] J. Seelig, K. Leslie, A. Renn, S. Kühn, V. Jacobsen, M. Van De Corput, C. Wyman, V. Sandoghdar, *Nano Lett.* **2007**, *7*, 685.
[35] V. Glembockyte, L. Grabenhorst, K. Trofymchuk, P. Tinnefeld, *Acc. Chem. Res.* **2021**, *54*, 3338.
[36] C. Vietz, B. Lalkens, G. P. Acuna, P. Tinnefeld, *New J. Phys.* **2016**, *18*, 045012.
[37] G. P. Acuna, F. M. Möller, P. Holzmeister, S. Beater, B. Lalkens, P. Tinnefeld, *Science* **2012**, *338*, 506.
[38] C. A. Mirkin, R. L. Letsinger, R. C. Mucic, J. J. Storhoff, *Nature* **1996**, *382*, 607.
[39] S. E. Ochmann, C. Vietz, K. Trofymchuk, G. P. Acuna, B. Lalkens, P. Tinnefeld, *Anal. Chem.* **2017**, *89*, 13000.
[40] C. Vietz, B. Lalkens, G. P. Acuna, P. Tinnefeld, *Nano Lett.* **2017**, *17*, 6496.
[41] J. J. Schmied, C. Forthmann, E. Pibiri, B. Lalkens, P. Nickels, T. Liedl, P. Tinnefeld, *Nano Lett.* **2013**, *13*, 781.
[42] K. Trofymchuk, V. Glembockyte, L. Grabenhorst, F. Steiner, C. Vietz, C. Close, M. Pfeiffer, L. Richter, M. L. Schutte, F. Selbach, R. Yaadav, J. Zahringer, Q. Wei, A. Ozcan, B. Lalkens, G. P. Acuna, P. Tinnefeld, *Nat. Commun.* **2021**, *12*, 950.
[43] L. Grabenhorst, K. Trofymchuk, F. Steiner, V. Glembockyte, P. Tinnefeld, *Methods Appl. Fluoresc.* **2020**, *8*, 024003.
[44] M. Pfeiffer, K. Trofymchuk, S. Ranallo, F. Ricci, F. Steiner, F. Cole, V. Glembockyte, P. Tinnefeld, *iScience* **2021**, *24*, 103072.
[45] K. Huebner, H. Joshi, A. Aksimentiev, F. D. Stefani, P. Tinnefeld, G. P. Acuna, *ACS Nano* **2021**, *15*, 5109.
[46] V. Kaur, S. Tanwar, G. Kaur, T. Sen, *ChemPhysChem* **2021**, *22*, 160.
[47] P. Zhan, T. Wen, Z. G. Wang, Y. He, J. Shi, T. Wang, X. Liu, G. Lu, B. Ding, *Angew. Chem., Int. Ed.* **2018**, *57*, 2846.
[48] T. Zhang, N. Gao, S. Li, M. J. Lang, Q. H. Xu, *J. Phys. Chem. Lett.* **2015**, *6*, 2043.
[49] D. Wang, S. L. Capehart, S. Pal, M. Liu, L. Zhang, P. J. Schuck, Y. Liu, H. Yan, M. B. Francis, J. J. De Yoreo, *ACS Nano* **2014**, *8*, 7896.
[50] I. Hernandez-Neuta, F. Neumann, J. Brightmeyer, T. Ba Tis, N. Madaboosi, Q. Wei, A. Ozcan, M. Nilsson, *J. Intern. Med.* **2019**, *285*, 19.
[51] D. - N. Kim, F. Kilchherr, H. Dietz, M. Bathe, *Nucleic Acids Res.* **2012**, *40*, 2862.
[52] S. J. Hurst, A. K. R. Lytton-Jean, C. A. Mirkin, *Anal. Chem.* **2006**, *78*, 8313.
[53] X. Wei, J. Nangreave, Y. Liu, *Acc. Chem. Res.* **2014**, *47*, 1861.
[54] M. T. Strauss, F. Schueder, D. Haas, P. C. Nickels, R. Jungmann, *Nat. Commun.* **2018**, *9*, 1600.
[55] N. Wu, D. M. Czajkowsky, J. Zhang, J. Qu, M. Ye, D. Zeng, X. Zhou, J. Hu, Z. Shao, B. Li, C. Fan, *J. Am. Chem. Soc.* **2013**, *135*, 12172.
[56] E. Sambriski, D. Schwartz, J. De Pablo, *Proc. Natl. Acad. Sci. USA* **2009**, *106*, 18125.
[57] H. Ramezani, H. Dietz, *Nat. Rev. Genet.* **2020**, *21*, 5.
[58] P. C. Whitford, J. N. Onuchic, *Curr. Opin. Struct. Biol.* **2015**, *30*, 57.
[59] M. Horacek, R. E. Armstrong, P. Zijlstra, *Langmuir* **2018**, *34*, 131.
[60] M. Horacek, D. J. Engels, P. Zijlstra, *Nanoscale* **2020**, *12*, 4128.
[61] T. Cordes, J. Vogelsang, P. Tinnefeld, *J. Am. Chem. Soc.* **2009**, *131*, 5018.
[62] T. Ha, P. Tinnefeld, *Annu. Rev. Phys. Chem.* **2012**, *63*, 595.
[63] J. Vogelsang, R. Kasper, C. Steinhauer, B. Person, M. Heilemann, M. Sauer, P. Tinnefeld, *Angew. Chem., Int. Ed.* **2008**, *47*, 5465.
[64] L. Poirel, C. Héritier, V. Tolün, P. Nordmann, *Antimicrob. Agents Chemother.* **2004**, *48*, 15.
[65] J. Hrabák, E. Chudáčkova, C. C. Papagiannitsis, *Clin. Microbiol. Infect.* **2014**, *20*, 839.
[66] P. Pattanayak, S. K. Singh, M. Gulati, S. Vishwas, B. Kapoor, D. K. Chellappan, K. Anand, G. Gupta, N. K. Jha, P. K. Gupta, P. Prasher, K. Dua, H. Dureja, D. Kumar, V. Kumar, *Microfluid. Nanofluid.* **2021**, *25*, 99.
[67] X. Weng, H. Jiang, D. Li, *Microfluid. Nanofluid.* **2011**, *11*, 367.
[68] H. S. Chung, K. McHale, J. M. Louis, W. A. Eaton, *Science* **2012**, *335*, 981.
[69] J. Hahn, L. Y. T. Chou, R. S. Sorensen, R. M. Guerra, W. M. Shih, *ACS Nano* **2020**, *14*, 1550.
[70] J. Eid, A. Fehr, J. Gray, K. Luong, J. Lyle, G. Otto, P. Peluso, D. Rank, P. Baybayan, B. Bettman, A. Bibillo, K. Bjornson, B. Chaudhuri, F. Christians, R. Cicero, S. Clark, R. Dalal, A. deWinter, J. Dixon, M. Foquet, A. Gaertner, P. Hardenbol, C. Heiner, K. Hester, D. Holden, G. Kearns, X. Kong, R. Kuse, Y. Lacroix, S. Lin, et al., *Science* **2009**, *323*, 133.
[71] V. Jadhav, D. P. Hoogerheide, J. Korlach, M. Wanunu, *Nano Lett.* **2019**, *19*, 921.
[72] T. Gilboa, C. Torfstein, M. Juhasz, A. Grunwald, Y. Ebenstein, E. Weinhold, A. Meller, *ACS Nano* **2016**, *10*, 8861.
[73] J. D. Spitzberg, A. Zrehen, X. F. van Kooten, A. Meller, *Adv. Mater.* **2019**, *31*, e1900422.
[74] R. Wang, T. Gilboa, J. Song, D. Huttner, M. W. Grinstaff, A. Meller, *ACS Nano* **2018**, *12*, 11648.
[75] M. Belkin, S. - H. Chao, M. P. Jonsson, C. Dekker, A. Aksimentiev, *ACS Nano* **2015**, *9*, 10598.
[76] F. Nicoli, D. Verschueren, M. Klein, C. Dekker, M. P. Jonsson, *Nano Lett.* **2014**, *14*, 6917.
[77] D. Garoli, H. Yamazaki, N. Maccaferri, M. Wanunu, *Nano Lett.* **2019**, *19*, 7553.

ADVANCED MATERIALS INTERFACES

Supporting Information

for *Adv. Mater. Interfaces,* DOI: 10.1002/admi.202200255

Maximizing the Accessibility in DNA Origami Nanoantenna Plasmonic Hotspots

*Cindy Close, Kateryna Trofymchuk, Lennart Grabenhorst, Birka Lalkens, Viktorija Glembockyte, and Philip Tinnefeld**

WILEY-VCH

Supporting Information

Maximizing the Accessibility in DNA Origami Nanoantenna Plasmonic Hotspots

*Cindy Close, Lennart Grabenhorst, Birka Lalkens, Kateryna Trofymchuk, Viktorija Glembockyte, Philip Tinnefeld**

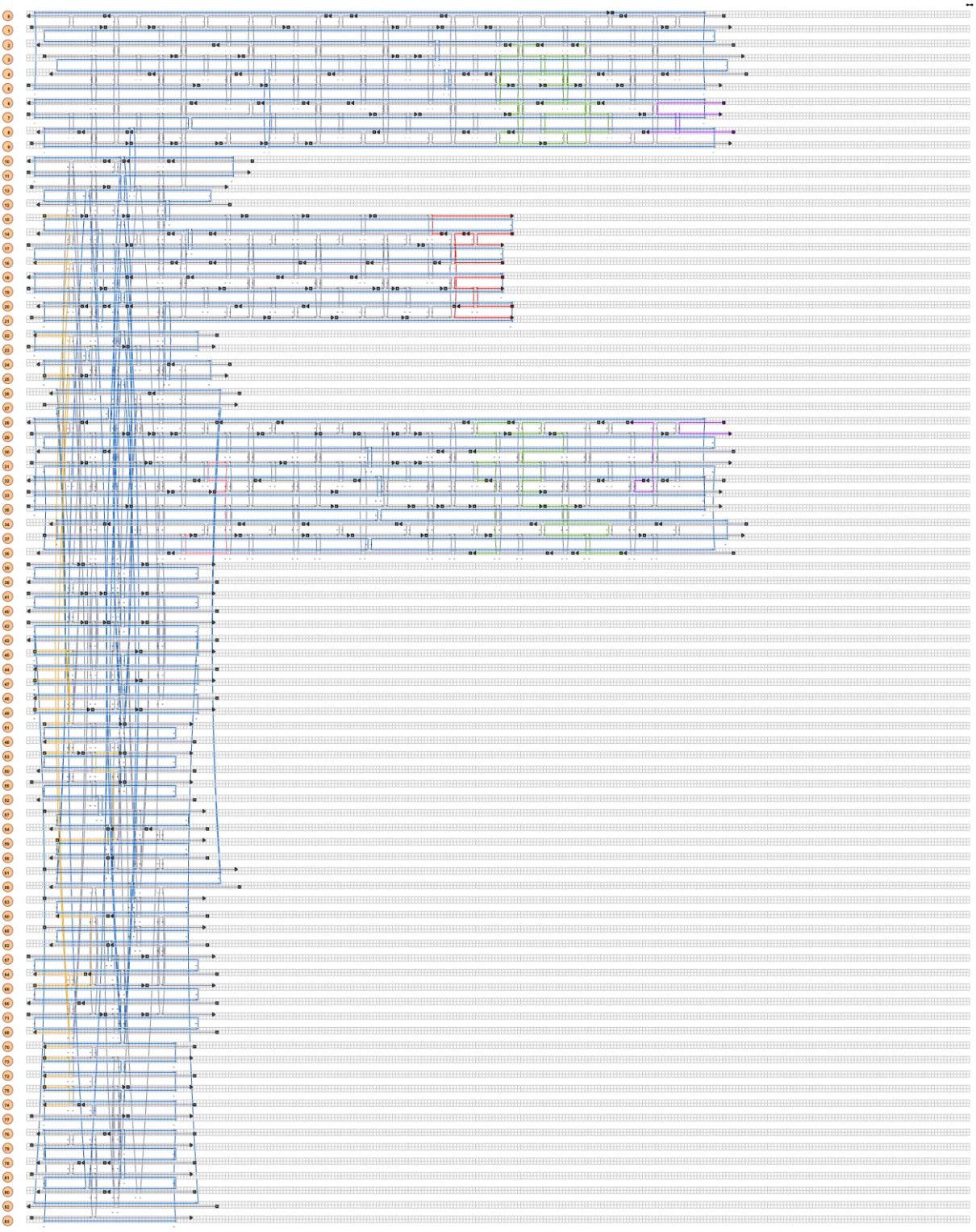

Figure S1. Staple strand layout of DNA origami Trident in CaDNAno.[1] (Yellow: strands for modification with biotin, magenta: strand for labeling with localization dye ATTO 542, red: available strands in the hotspot region, green: strands for NP binding, purple: strands for further modifications).

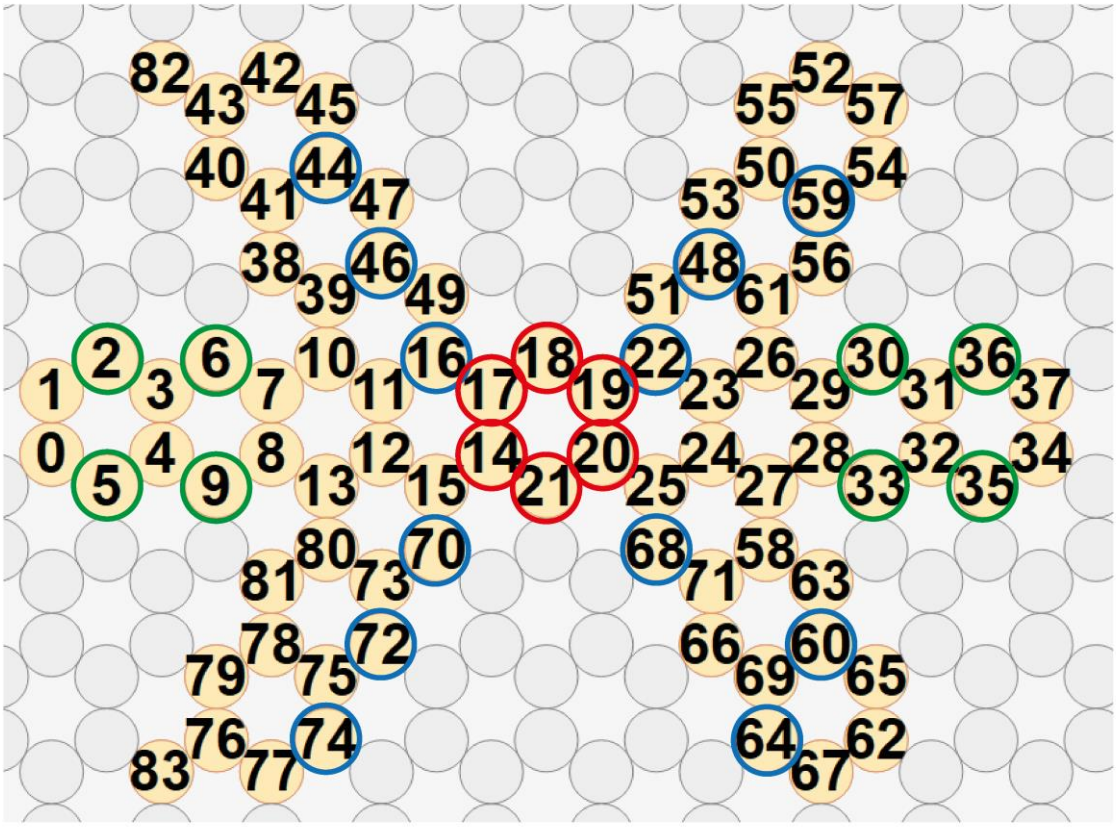

Figure S2. Helix layout in CaDNAno. (Blue: modification with biotin, red: available strands in hotspot, green: helices for NP binding).

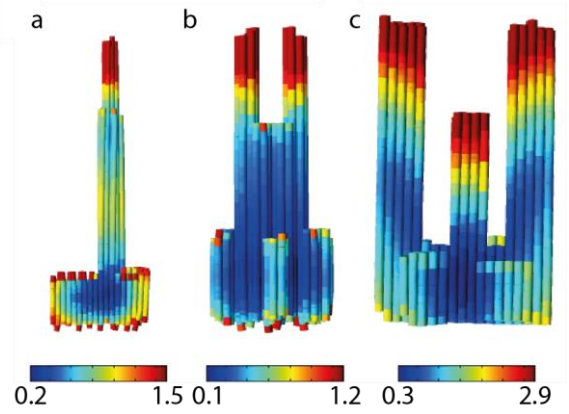

Figure S3. CanDo simulation of structural rigidity for all three discussed DNA origami structures. (a) Pillar, (b) Tower, (c) Trident. Color scale indicates root mean square displacement (rmsd) due to thermal fluctuations at 298K.[2, 3]

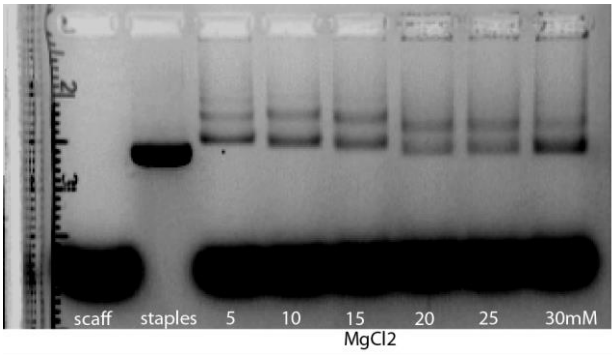

Figure S4. Gel electrophoresis to scan for optimal $MgCl_2$ concentration to fold DNA origami Trident.

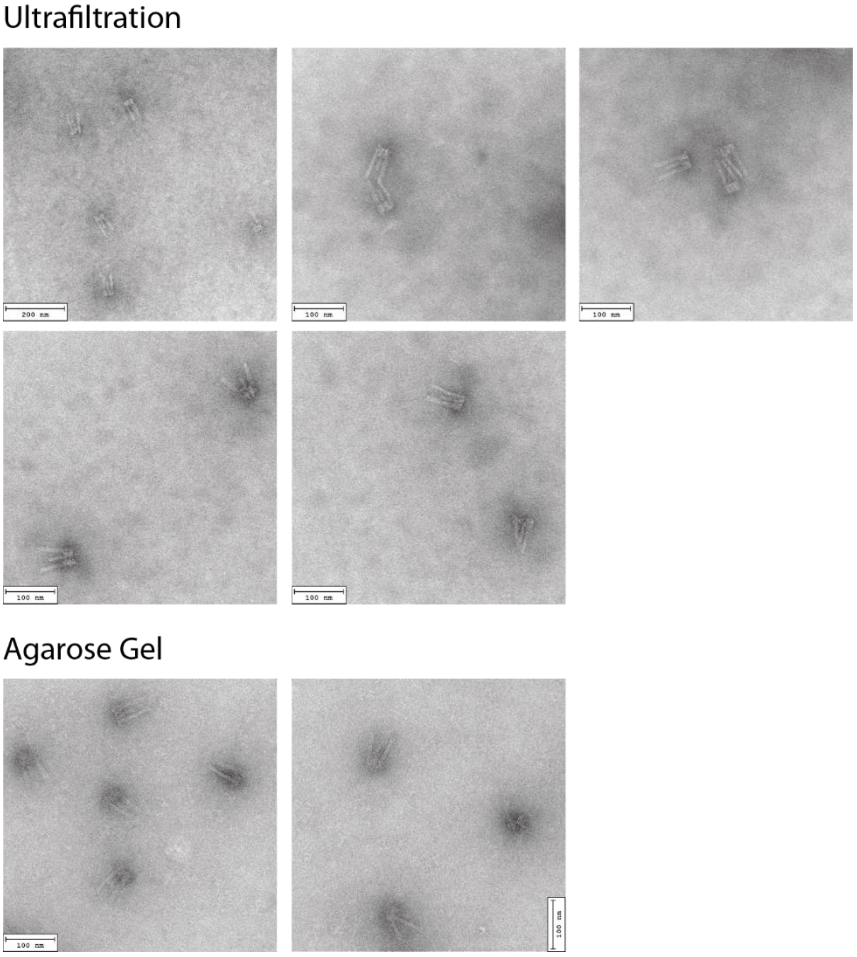

Figure S5. TEM images of Trident DNA origami, acquired after two different purification methods.

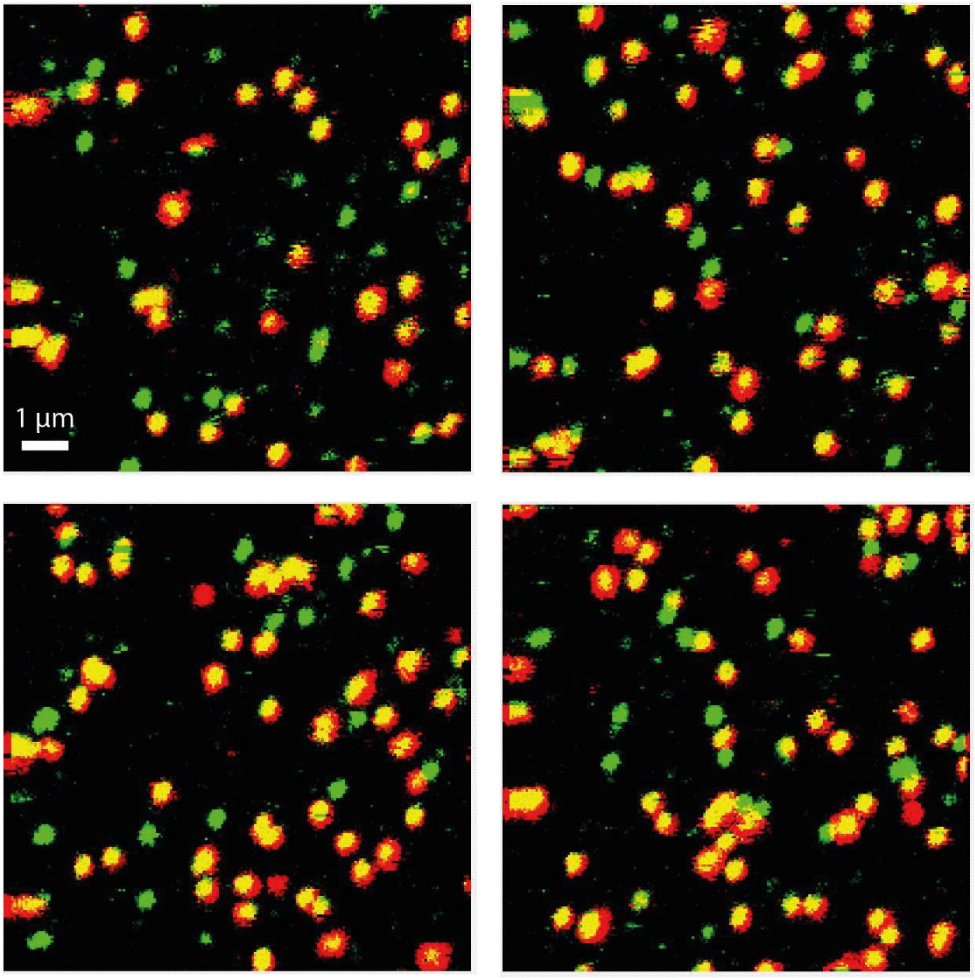

Figure S6. Incorporation efficiency of ATTO 647N (hotspot dye) in DNA origami Trident, localized via labelling with ATTO 542. Non colocalized red spots, explained e.g., by DNA Origami with photobleached or not incorporated green localization dye, were not taken into the calculation.

$$Colocalization\ [\%] = \frac{\#\ colocalized\ (yellow) spots}{\#\ green + \#\ yellow\ spots} \quad (1)$$

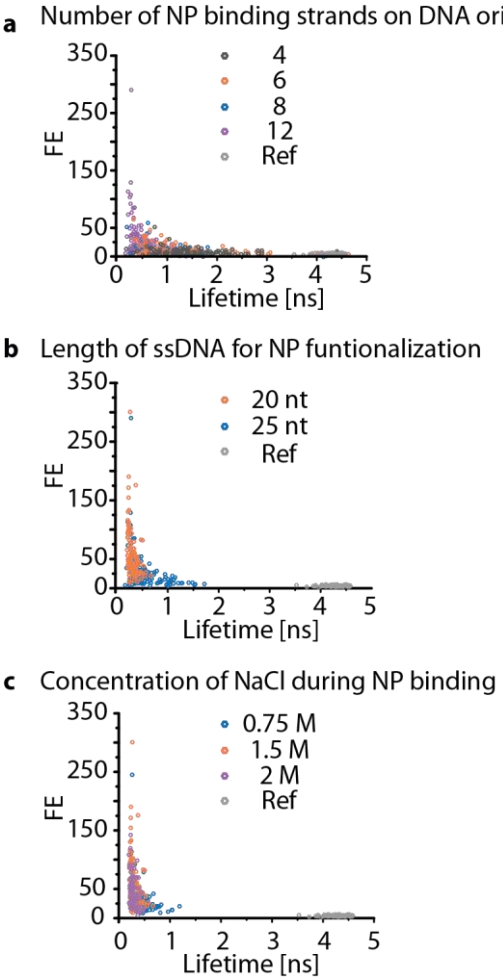

Figure S7. FE versus fluorescence lifetime scatter plots for the optimization of FE values in the Trident NA (ATTO 647N in the hotspot). (a) Comparing the FE values obtained for different the number of NP binding strands on the DNA origami. Incubation of 25 nt functionalized NPs in buffer containing 750 mM NaCl. (b) Comparing the FE values obtained for different lengths of strands used for NP functionalization. Comparison was made on Trident with twelve binding strands and buffer containing 750 mM NaCl. (c) Effect of NaCl concentration in the NP incubation buffer on FE values for Trident origami with twelve NP binding strands (20 nt). Ref stands for reference samples without NPs. Transients of more than 100 molecules per sample were analyzed.

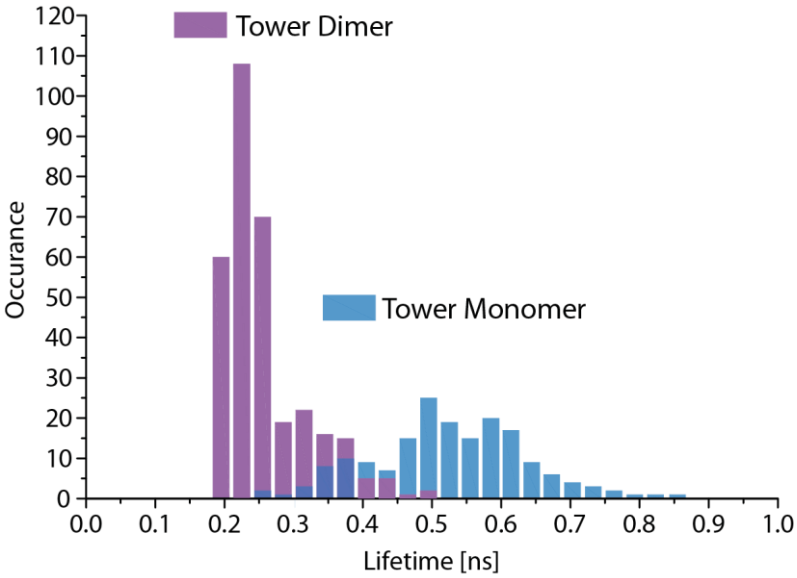

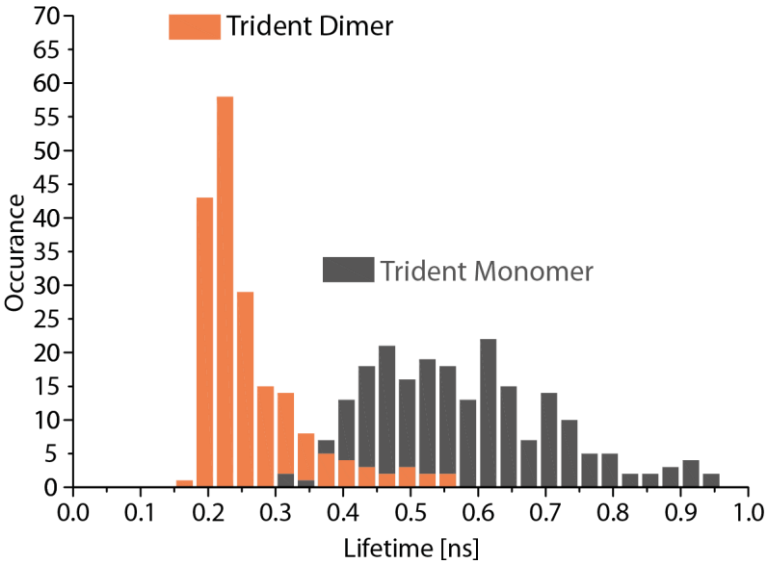

Figure S8. FE in Monomer Structures of NACHOS Tower and Trident origami with 100 nm Ag.

Supplementary notes to Figure 3a, S7 and S8:

Trident structures including four, eight and twelve polyadenine strand extensions (20A, distributed equally between four to eight helices on opposite sides of the two outer pillars, see Figure 2b and Figure S2, Supporting Information) were folded with ATTO647N in the hotspot and respective NA samples were prepared with 100 nm AgNPs.

To study formation of monomer subpopulations in detail we specifically designed a monomer DNA origami Trident nanostructure, that was equipped with six NP binding strands on only one side of the DNA origami towers (see Figure S2 and Figure S8). To compare the results with

the previous Tower NACHOS construct, we designed a monomer Tower structure in the same manner by including only six instead of twelve NP binding strands. As expected, we observed longer τ_{fl} and lower FE values for the monomer constructs of both Tower and Trident NACHOS. In the scatterplot for eight and twelve binding strands on Trident (Figure S7a), the larger fraction of values binding strands lies between 0.2 and 1.0 ns at accordingly higher FE of ATTO647N, representing a large fraction of dimer NAs in the sample. The variance in FE values for a population of molecules with similar τ_{fl} around a cut-off at 0.2 ns is explained by the fact that our fluorescence lifetime measurements are limited in time resolution by the instrument response function of our TCSPC system (see Methods for details).[4]

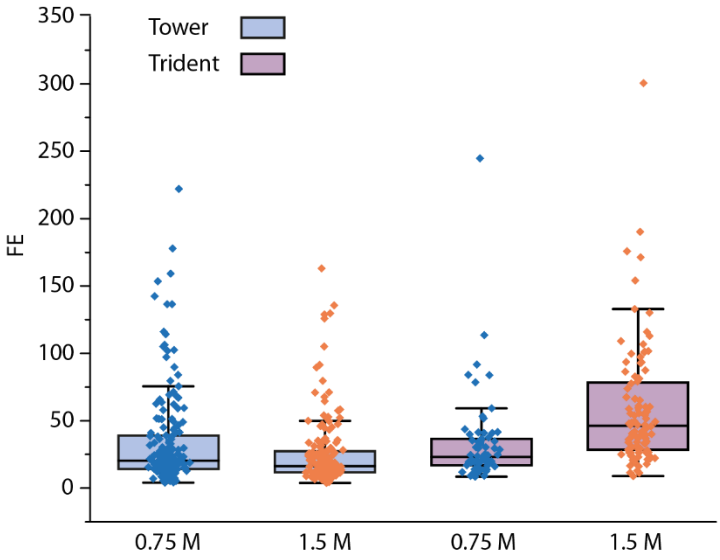

Figure S9. Effect of NaCl concentration in the NP incubation buffer on FE values for Tower and Trident origami with twelve NP binding strands (20 nt).

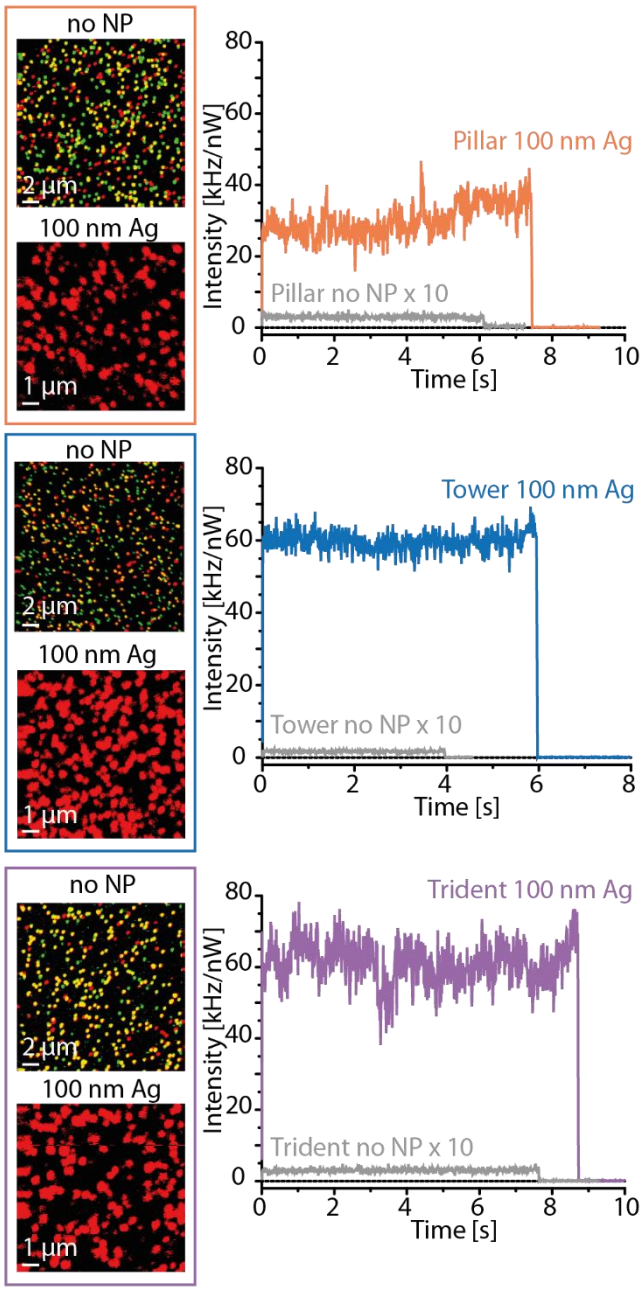

Figure S10. Exemplary confocal fluorescence scans and transients of all DNA origami NAs compared in this work. Reference image acquired at 2 µW excitation power (red and green channel, 20 x 20 µm) without NP to confirm colocalization. Scan of 100 nm Ag NAs (10 x 10 µm, red detection channel only) acquired at 50 nW. Fluorescence intensity/time traces acquired at 50 nW for 100 nm Ag, 200 nW for Reference without NP (multiplied 10x for visual purposes).

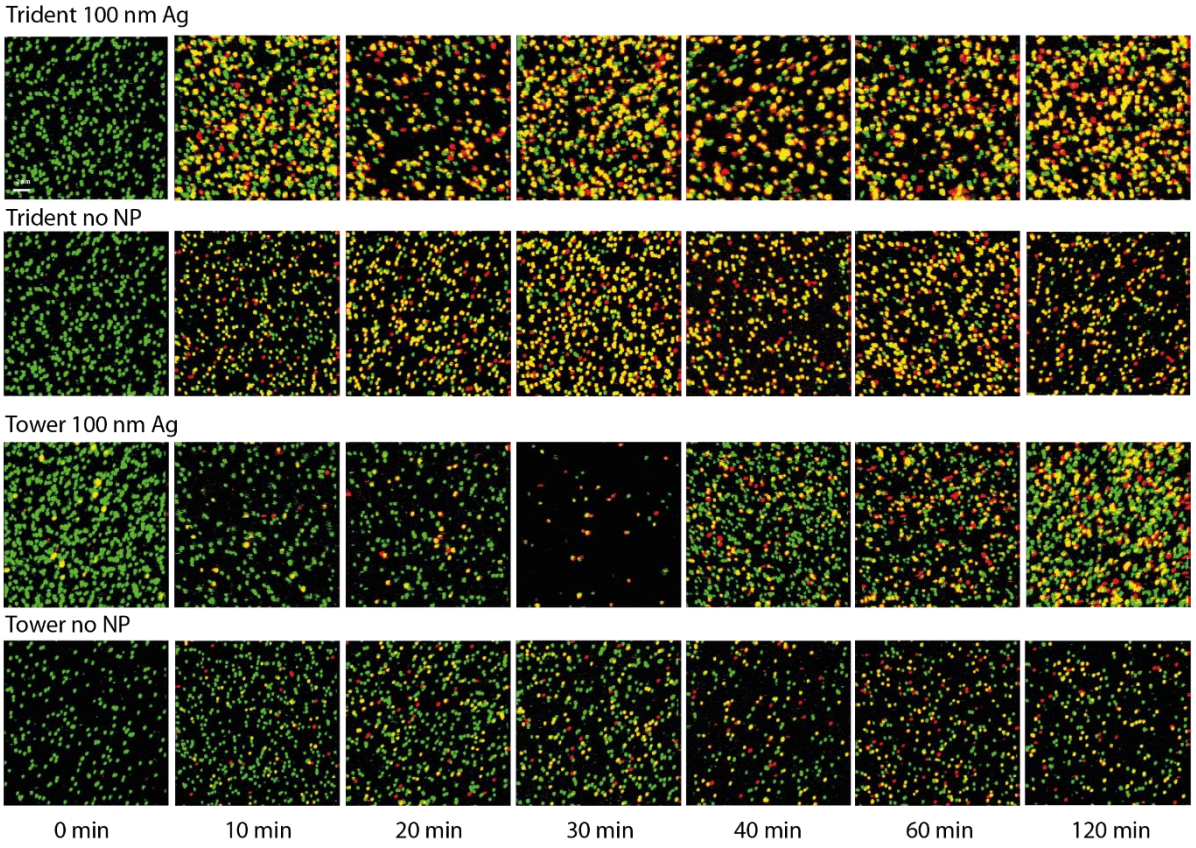

Figure S11. Exemplary confocal fluorescence scans for determining the kinetics of binding in the NA hotspot of two different NACHOS DNA origami structures (Figure 5). 20 x 20 µm scans were acquired at 2 µW excitation.

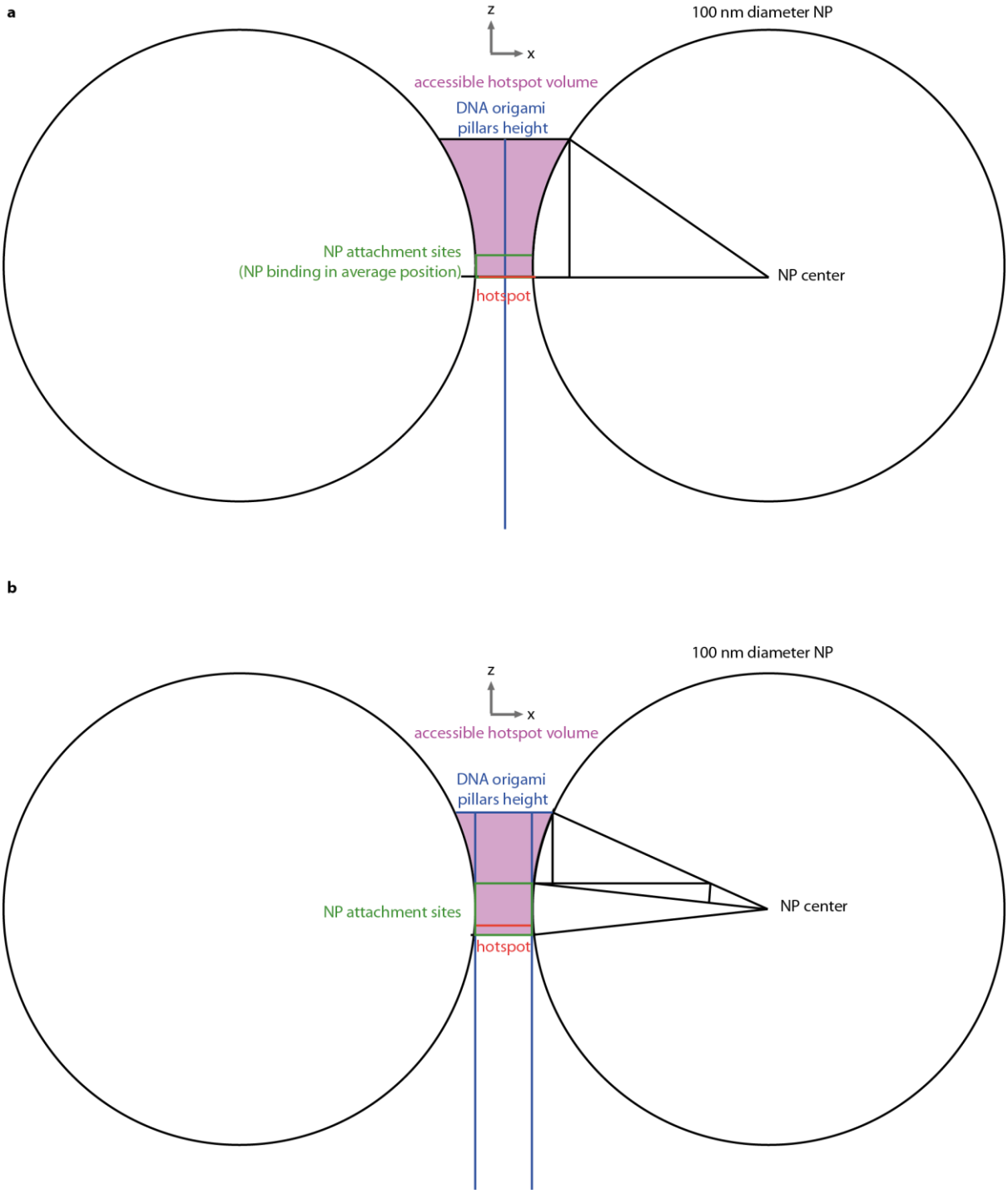

Figure S12. Simple geometrical approximations to estimate the accessible hotspot volume. (a) Tower. (b) Trident. Calculated by multiplying with the y dimension (Tower 728.9 nm^2 x 6.5 nm, Trident 368.9 nm^2 x 19 nm).

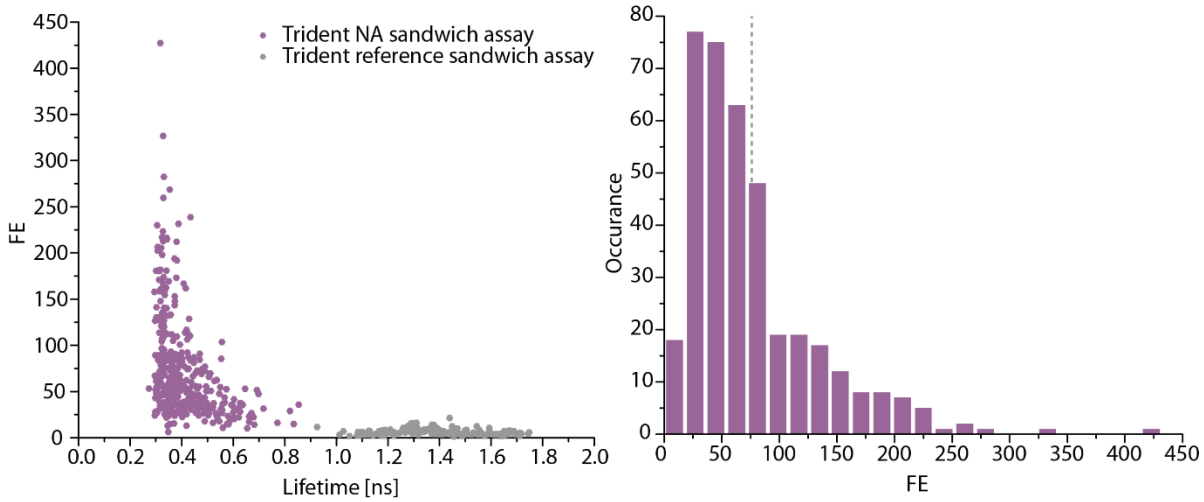

Figure S13. Enhancement of AF647 in Trident sandwich hybridization assay.

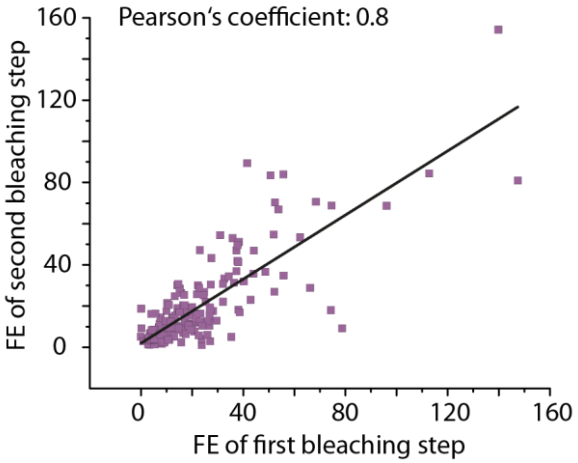

Figure S14. Correlation between FE from two individual AF647 molecules in Trident. FE values up to 160 were taken into consideration, representing majority population of molecules (Figure S14). Quantification using Pearson's correlation coefficient indicates a positive relationship between the FE of two individual AF647 within the structure.

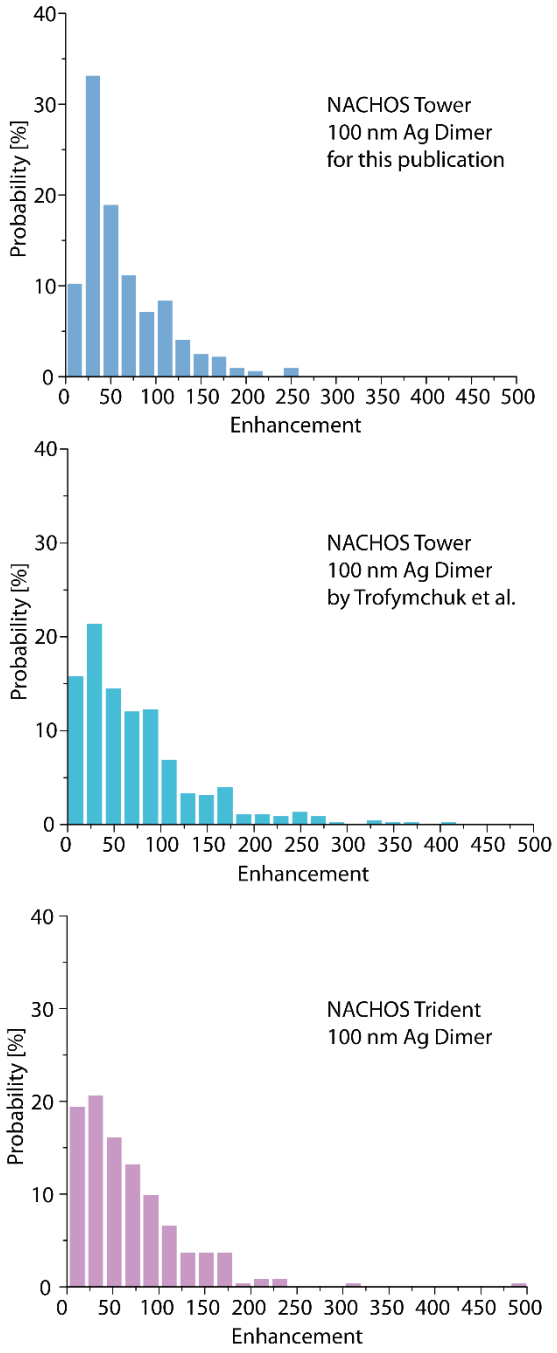

Figure S15. Fluorescence enhancement distributions acquired for this publication compared to previously published values for the identical DNA origami NACHOS and the new Trident DNA origami architecture.[5]

Table S1. Parameters for CanDo simulation

Parameter	**Value**
Axial rise per bp [nm]	0.34
Helix diameter [nm]	2.25
Crossover spacing [bp]	10.5
Axial stiffness [pN]	1100
Bending stiffness [pN x nm²]	230
Torsional stiffness [pN x nm²]	460
Nick stiffness factor	0.01

Table S2. Recipes for buffers.

10 x FoB20 (1 mL)	1 M Tris	50 µL
	0.5 M EDTA	20 µL
	1 M $MgCl_2$	200 µL 10
	5 M NaCl	µL
	Fill up with H_2O	
FoB5 (10 mL)	1 M Tris	50 µL
	0.5 M EDTA	20 µL
	1 M $MgCl_2$	50 µL 10 µL
	5 M NaCl	
	Fill up with H_2O	
TE 750 mM NaCl (40 mL)	1 M Tris	400 µL
	0.5 M EDTA	80 µL
	5 M NaCl	6 mL
	Tween20 10%	40 µL
	Fill up with H_2O	
TE 1.5 mM NaCl (40 mL)	1 M Tris	400 µL
	0.5 M EDTA	80 µL
	5 M NaCl	12 mL
	Tween20 10%	40 µL
	Fill up with H_2O	

TE 2 M NaCl (40 mL)	1 M Tris	400 µL
	0.5 M EDTA	80 µL
	5 M NaCl	16 mL
	Tween20 10%	40 µL
	Fill up with H_2O	
PBS 3300 (40 mL)	10 x PBS	4 mL
	5 M NaCl	26.4 mL
	Fill up with H_2O	
PBS 10 (40 mL)	10 x PBS	4 mL
	0.5 M EDTA	200 µL
	5 M NaCl	80 µL
	KH_2PO_4 (P8709)	84.4 µL
	K_2HPO_4 (P8584)	115.6 µL
	Tween20 10%	40 µL
	Fill up with H_2O	
ROXS:		
Buffer A (90%)	NaCl	750 mM
	Tris	50 mM
	Trolox/Troloxquinone	2 mM
	Glucose	1% w/v
Buffer B (10%)	Glucose oxidase	1mg/mL
	Catalase (50 µg/mL)	0.4% v/v
	Glycerol	30%
	KCl	12.5 mM

Table S3. Recipe for Tower and Pillar origami. Sequences of staple strands have been published previously.[6, 7]

DNA Origami structure	Pillar	Tower	Trident
Unmodified staples [µL]	35	18	18
Modified staples [µL]	4	2	2
MgCl2 [µL]	14	-	-
10 x TE [µL]	7	-	-
FoB5 [µL]	-	5	5
p8064 scaffold [µL]	10	25	25

Table S4. Staple strands used for folding DNA origami Trident. Values in first two columns refer to the helix number in CaDNAno design (height in bp along the axis of the helix in paranthesis). Colored sequences refer to modifications of the respective staples (green and red: dye labelling, orange: extension of capture strand by a sequence partially complementary with target strand, purple: complementary sequences in target and imager strands).

Start	**End**	**Sequence**
25[5]	68[2]	ATAAAGGTGGAATAAGTTTAT
73[5]	72[5]	TGAGAGTCTGTAAAACTA
53[5]	48[5]	AAAGTAAGCGAGGAAACG
69[2]	64[2]	GACATTCAACCGTTATTCATTAAA
59[9]	53[29]	AGGGTAATTGAGCGCTATATCTTACCCGAACAAAG
15[5]	70[5]	GAGAGGGTAGTCATTGCC
47[2]	46[2]	TTAATTTCATCTCCGTGTGATAAA
51[5]	22[2]	CAATAATAACTCCTTATTACG
45[2]	44[2]	TGCAAATCCAATAATATATTTTAG
64[18]	60[9]	GGAAAATTGAGGAGCAAGGCCGGA
75[5]	74[5]	GCATGTCAACCCAAAAAC
49[2]	16[2]	TAAGGCGTTAAAAAAAGCCTGTTT
33[58]	37[51]	AAATCGAACCACAGTTTCGTAGTACCGCCACCCTAG
20[151]	19[148]	CAGAACGCGCCTTAAGCAATA
14[136]	21[151]	ATTTACAACATGTTCAGCTAATG
14[151]	17[148]	TACCATATCAAAGCAAAAGAA
18[148]	20[134]	AAGCCTCAGAGCATAAGCAAAATGTTTAT
14[129]	15[151]	CGTATTCTGAATAATGGAAGGGTTAGAACC
16[148]	14[137]	GATGATGAAACAAACATACCTGAATT

8[220]	7[216]	CCCCCACAATATTACCGCGCCTGCAACCCCC
6[217]	8[193]	CCCCCCAGTGCCACGCTGAGATTAACACCCAGCCATTG
28[217]	29[219]	CCCCCTTTGCCAGATATATTCGGTCGCCCCC
32[192]	28[188]	AACGCGAGAGGATAGTAAA
6[178]	5[171]	AATCACAGAGGACGCTCATGGAAATCCTGAGTAAAATCCGTTC
2[159]	9[160]	AGCTGCGGGTGGTTGGTGGTAATAACA
5[161]	6[160]	GAGTGTTTGTTTGATTTTCTTTCACCTTG
7[150]	2[150]	GAACCTCAAATGGCGCCAATTA
32[143]	36[139]	GAATGGTAAAAAATTGTGT
36[185]	35[171]	GAAACAAAGTACGGTGTACAACGTAACAAAGCAGAA
28[150]	30[139]	TCATAAATATTTAAACAGGGAACGAG
29[164]	35[160]	CGCCTCAGCAGCGAAAGATGCCACTCATCAGTCTTATGC
29[150]	33[160]	GATACCGATAGTGCGGAACCTCGTT
8[150]	5[150]	CAATGATTAGTTCCGAAACCCG
9[161]	2[171]	TCACTTGACCTACACAGCAGAAGATAAATAAAGCATTCACCAGAAA
35[161]	36[171]	GATTTTATGCTCATAGAGGACAGATGAACAAC
21[1]	20[18]	CCCCCTGATATTCAACCGTTCCAA
20[17]	53[16]	ATCAAAGGGTGATTAAGACGGAATAGGAAACCAGA
1[144]	1[128]	CAAAATCGGCCAACGCGCGGGGTGGAA
2[58]	9[59]	CGCCTGTGCAGGTAATGGCATCAGCGGTGGTGCCA
34[24]	28[18]	CCTATAAATCCAGGTTGAAGCCCCCAATAGCGTCA
31[115]	35[119]	TTCATACATAAGCTTGAGA
32[198]	35[216]	CGAGTTGGGAAGAAAAATCCCCCC
23[0]	26[7]	CCCCCCAGTATGTTAGCAAACGAAAGCGCATTAGACCCCCC
32[71]	37[86]	CCTTCCAGTAAGCGTCTCAGTGCAGGCGGATAA
43[0]	40[0]	CCCCCAGGGCGATCGGTAAGGGGGATGTGCCCCC
79[1]	76[3]	CCCCCATTTCTGCTATCGACATACCCCC
29[73]	31[79]	AAAACAGGTCTCCAGAGCCACCACCCCACCCTTAC
31[1]	32[0]	CCCCCCTCATTTTCCAGACGATTGGCCCCCC
45[35]	45[58]	TCATAGGTCTGAGAGACTACCCCC
3[67]	5[73]	CTTGTGTCACCAGTTGAGGATCCCAAGCCGGCTTT
82[59]	43[36]	CCCCCCCGGAAACCAGGCAAAGCGCCATTCGTAAGCTTTC
4[198]	9[219]	CACCTTGCTGGTAATATCCAGACCCCC
34[66]	28[60]	AGTGTTTACCGGCCACCAACCGGAATTACCCTGAC
32[102]	34[87]	ACCGCCAGACAGAAGTATAGCCCGGACGTCGAGAAGTTTTAACG
0[24]	2[3]	CTAGGGCGCTGGGTTTCTGGGCCGTTTTCACGGTCCCCC
0[185]	4[179]	ATCAAAAGCCTCGCTTTCCAGTCGGGTGAGACGCA
54[56]	59[55]	CCCCCCGCTAACGAAAATAAACACCCCC
1[199]	5[216]	ATGAAGGGCGATAAAGAACGTGGACTCCCCCC

54[37]	57[55]	CTTTCCTGAATCTTACCAACCCCC
31[80]	34[67]	AACGTATCACCGTACTCACAGTACCCTTGAGTAAC
39[0]	10[0]	CCCCCACGACGGCCAGTACGGATAACCTCCCCCC
67[37]	65[55]	GCTTAAGAGGTCGTACCTTTAATTGCTCCCCCC
74[16]	15[17]	AGCTCATATGGGTAATCGGAGCAACTATCAGGCTA
55[1]	50[3]	CCCCCCAAGAAACATTTTTAAGACCCCC
9[32]	10[31]	GCCAACGGCATTTAAAAAATCCTTCCGTAATGGGA
16[106]	21[95]	AACAATTTCATTTGAACCAAGTTTTCAGGTCCGAC
19[115]	15[107]	AGGCCCTGAACAAGAAAAAGTAATTAAATTGCTCC
71[0]	66[0]	CCCCCTTTGTCACAATCAGACAAAAGGGCCCCCC
15[31]	18[32]	CCTTCCTGTAGCTTAATTATAAAGCCCCTCATATA
16[45]	11[69]	GAATGAGTAACAACCCGTCGGATTCTCCCCCC
64[59]	67[36]	CCCCCAATGCTGTAGCTCAACATGTTTTATATGGCTTAGA
9[46]	1[38]	CGTCGGGGTCCGCCGCTGGAAGAAAGCGAAACTGT
67[0]	64[19]	CCCCCGGTGAATTATCACCGTCACCGACTGAAATATTGAC
28[59]	32[53]	TATTCACGTTGCGTTAGTAAATGAAAACACTGCAC
8[108]	0[102]	TCACTCTGTCCGACAGGAGAATCAGCTAAAGGGAG
71[37]	29[38]	CCAATAAAGCGAAGGAAGCAGCGGATAATT
15[108]	17[122]	TGATTGTTTGGATTATACAAACAGATTAT
37[144]	29[149]	AACTGACCAACCTGATATACGTAACAGCATCCTT
0[93]	6[101]	TTATGCTTTCCTCGTTAACGGTACTGTGTTCGTTG
41[37]	47[34]	GACGATAGTGAATTTATCGAAAGCGA
6[100]	9[87]	AAAGGAATTGTGGCTATGTAATAAAAGGGACTGAG
4[178]	7[191]	GGCGAGAAGAACTCAAACAGGAAAATGAGGCGGTC
41[0]	38[0]	CCCCCCTGCAAGGCGATCGACGTTGTAAACCCCC
53[30]	53[51]	GGCGTTTTAGCGAACCTCCCCC
35[139]	37[143]	ATCATTGTTTGCCCTACCG
10[24]	1[23]	CCGCGACAACTTAATACATGAGCCGATGCGGCGCC
34[196]	32[193]	ATTCATTATCAGGACACT
6[51]	3[66]	TAAACTGAAAGCGTAAGAATACGTTTTAGGAGTTT
29[91]	33[95]	GAGCCTTGAATGACCCTCC
1[1]	0[0]	CCCCCCATACCGGGGCAAGTGTAGCGCCCCC
6[159]	8[151]	CTGAACGAACCACTTTTGACGCT
5[151]	1[143]	AGAGTTTTTTGGGGTCGCTCA
39[17]	41[23]	AAGCATACCGATCTGACCTAAATTTAGAAAACGGT
1[39]	9[31]	TCTGTGCTGCGGCCAGAGGTCACTGCGCTTTGAAT
18[101]	20[87]	CCCTGTAATACGCATTAACCCATCCTAAT
19[88]	16[86]	GTATTTTGCGTTGAATATTACC
9[88]	1[80]	GCCTCCTGAGTATAACGGAGCTTGACGGGGACGGG

21[75]	19[87]	AAGAGAATACGAGCATTACTAATAGTA
28[17]	30[3]	GACTATAGAAATTTCAACAGTTTCAGCCCCCC
31[122]	31[114]	GGAACTGCTCCATGTTACTTAGCATCCAAGACTTT
3[46]	5[52]	GCTCTCTGTGTCGCGTCCGTGAGCAAGGAAGACAG
20[133]	14[130]	CAACAATAACAATAAGCA
47[35]	47[58]	TAGCTTAGATTAAGACGCTCCCCC
27[5]	20[25]	CCCCCAGAATCAAGTTTGCCTTAAAGAACAAATAAAAGAGA
2[220]	4[199]	CCCCCACATTAATTGCGTTGCGCTTGCCCTTGGTC
62[56]	67[58]	CCCCCCTTTTGATAATTGCTGAATATCCCCC
49[35]	49[58]	TCGTCGCTATTAATTAATTCCCCC
35[172]	29[163]	CTGCAGGTAGCGACGATATAGCGTCCAATACTTG
37[52]	33[44]	GATTAAACAGTTAATGCCATGGAAAGCCGCCGCAT
71[24]	25[17]	TCATGCAAAGACACCACGGCAA
51[30]	51[51]	TATAGAAGGCTTATCCGCCCCC
76[52]	77[30]	CCCCCTGAAGGGTAAAGTTAAATTTTA
60[56]	69[58]	CCCCCCAACAGGTCAAGTACGGTGTCCCCCC
16[85]	21[74]	TTTTTTAATGGAAACATTCGCCTATATACAGTAAT
69[37]	63[55]	AACTAAGGATTAGACCGGAAGCAAACTCCCCCC
5[185]	6[179]	GAGTTGCCCCAGGGCAACGCAAATGAAA
42[59]	43[58]	CCCCCCCTTTTTAACCTCCGCTTCTGGTGCCCCC
40[59]	41[36]	CCCCCCCTCAGGAAGATCGCACTCCAGCCTTCCTTGAGGG
19[109]	16[107]	TCAAACATTACGCGCAGCATTT
12[63]	9[45]	CCCCCACAAAGAAACCACCAGATTATCATATTAATGCAC
15[18]	18[0]	TTTTGATAAAGTTATACATGCCTGAGTAATGTGTAGCCCCC
32[178]	37[191]	ATTAGCTCATTATACCAGCCCAAATCAGACCAGGC
52[52]	55[29]	CCCCCAGATTAGTTGCTATTTTGCACCCATAAGCAATAGC
19[24]	10[25]	AAGGAAATGCAAAATTCTTCATAATACGTACAGAG
19[130]	16[128]	TTAAGCTAAATTTCAATTCAAG
35[129]	29[121]	TTCATCAACTAGGCATAGTCCCCCTCAAATGCTTG
11[0]	12[3]	CCCCCACCGGAAACAATCCGGAATTTCCCCC
29[1]	28[0]	CCCCCGGAGTGAGAGTAGCGCGTTTTCCCCC
38[59]	39[36]	CCCCCCATCGTAACCGTGCATCTGCCAGTAGGGAGGTCAC
46[59]	39[58]	CCCCCTTCCCTTAGAATTGTAGATGGGCGCCCCC
29[31]	31[37]	AAGGTGCATCATTATTAGCGTTTGCCCAGCATAAC
18[31]	23[30]	TTTTCCAGCTATATTTTCAAGCAAATCAGAACTTA
72[52]	78[25]	CCCCCTCAGCTCATTTTTTAACTCGATGAACTACCCCGCAG
4[224]	3[223]	CCCCCGAGAGTTGCAGCAAGCCACCGCCTGGCCCTGACCCCC
65[5]	62[26]	CCCCCAGAGCCAGCAAAATCACCAGTAGCGAATTTTTGCG
53[17]	52[3]	TAGCGAAGCCCATGAAATAGCCCAATAATAAGAGCCCCC

7[192]	1[198]	AGTAGCCAGCAAGCTGATCACTGCCGGGGTGCCTA
4[94]	7[107]	AGAAACCGAGTAAAAGAGACGACCATAGTCTTTAA
43[25]	82[0]	CGCCCATTCAGGCTGCGCAACTGTTGGGACCCCC
39[37]	49[34]	GTTGGCCTTGAAAACATTGGGGTAAA
35[0]	34[7]	CCCCCCTTGATATTCACAAACAAATTATTCTGAAACCCCCC
24[63]	27[65]	CCCCCCGGGTATTAACTTCAAATATCCCCCC
6[72]	9[73]	ATCGGCACAGCCAACAGAGATAGACACGCAACCAG
4[136]	7[149]	CCCTAGCAATACTTCTTTCGTCTGATAAAAATACC
33[96]	29[102]	CTCAGAGCCGCCACCCAGTTCAGAAAACGATAATT
5[172]	2[160]	CAGGTGAACCATCACCCCGAGCCGGTCGTGCC
28[136]	32[144]	TGAATAAGAGCAACACTATAG
0[217]	1[219]	CCCCCCAACGTCAAGTGAGCTAACTCCCCCC
49[20]	41[17]	TAAACACCGTTTGAATTTCAGAGGTTTTCCCAGTCATAAG
18[50]	14[45]	TTGCGCGAGGCTGTCTTTCCTTCTAATTTAAGTA
37[101]	34[116]	GTTGATCGGAACGAGGCGTAG
36[162]	34[158]	GTATCATCGCTTTGAATCA
18[78]	20[66]	AGCCTTTATTCAATTCGTAGAAACCAA
43[37]	45[34]	CGGCACCGGCTTAGGTTGGCGCAAAA
9[74]	6[87]	CTATAATCAGATTCTGGACAATATTTTTGAAAGGA
17[0]	14[3]	CCCCCAGTATCATATGCTTAATGCCGCCCCC
17[32]	13[24]	AGTGAGAATCGCCATGCTTGAGAGCATGTTTAACG
4[65]	2[59]	GAGATGGTTGCGAACGTGGCGAGACTCCTCATGCG
5[0]	4[7]	CCCCCGTCACGCTGCGCGTAACCAAATCCGCCGGGCCCCCC
2[149]	5[160]	ATGTTCCACACAACATAAAATCAATAGGGTT
48[52]	29[30]	CCCCCGTATTCTAAGAACGCGATTAGAAACGCATAAAACTA
76[24]	83[51]	CGGTAAAGCCGCACAGGCGGCCTTTAGTGACCCCC
7[122]	4[137]	GCCCTAAAACACAATATCGAAGAGGCGGTTTGAAT
68[59]	71[36]	CCCCCTAGATTTAGTTTGACCATTAGATAACATTTGATTC
21[118]	19[129]	AGACGACGGATAAGTAAGGCAAAGAA
1[129]	4[144]	ATTGTTATCCGAGGTGCCAATCAAAAGAATAGTCG
80[24]	81[51]	ATCCAAAAAGAGATTTTTTCGTCTCGTCGCCCCCC
28[178]	36[186]	CTGGAAAAACCAAAATAGGAACAACGAAAGAGCGC
77[1]	74[17]	CCCCCAGGAAGATTGTATAAGGAAA
55[30]	55[51]	TTTGAAGCCTTAAATCACCCCC
50[52]	56[26]	CCCCCCCCGACTTGCGGGAGGTTAATTTGCCCAATCCAAA
70[52]	80[25]	CCCCCAAAATAATTCGCGTCTGCTACAAAGGACAAGAGCAC
44[59]	41[58]	CCCCCGAGAAGAGTCAACGACAGTATCGGCCCCC
36[44]	29[45]	AACGTACCGTTTTTCTGAATA
31[38]	34[25]	CCATCGCCACCCTCAGAAGAGACTCTATTTCGGAA

25[18]	24[3]	CATGCTAGAAAATACATACCCCCC
8[31]	0[25]	GGACTTGTAGAACCGCAACGCACTCCCACACCGCG
7[108]	1[114]	TGCGATCAACAAGCAAATGCCAGCGGGTCATAGCT
37[87]	29[90]	GTGCATAGGTGCCTGTAGCGATCTACCAAAAG
37[5]	30[25]	CCCCCATGAAAGTATTAAGAGGCTCCGCCACGCAAGCCAAA
20[31]	26[39]	TTGGAACATTTCGCAAATTACCGCACATCGTAAGA
20[86]	15[86]	TTATAAAGTATTAACGTGAT
20[24]	20[32]	CAGTTAATTTAACAACGCCAACATGAATAACCTGT
10[70]	10[45]	CCCCCCGTGGGAACAAACGGCGGAT
35[96]	32[103]	TGATGATACAGGAGGGCGCCTCAGA
10[44]	3[45]	TGATGCCCGATAGATTATGCG
5[74]	6[73]	GACGAGCACGAAGTGTTCATAAACTTATCTAAAAT
81[1]	78[3]	CCCCCGGGATAGCTCAAACTTAACCCCC
8[16]	39[16]	CAGACAATTCCACGGGAGCC
75[31]	75[51]	TTAAATTTTTGTTAAACCCCC
29[122]	29[114]	CTTTACAGAGGCTTTGAGGACTACTATCGGTTTAT
36[170]	28[179]	GGACACCAACGTCACCCGACAATGACAACAAAGA
58[66]	71[58]	CCCCCGCGTTTTAATTCGAGCTTCTCTGCGAACGAGCCCCC
23[31]	71[23]	TTTTCTCATCGGATTAAGACAGCAGCACCGTAAAT
26[66]	33[57]	CCCCCAATAGCAGCCTTATTTTTTATAGTCATCATAATCA
56[25]	56[7]	ACCCTGAACAAAGTCAGCCCCC
17[123]	19[114]	TCATCGGTTGTACCAAATAC
37[66]	29[72]	TGCTGGAGGTTTCACCAGTTCCAGAAAAATCTCCA
9[1]	8[17]	CCCCCGGTCTGGTCAGCAGCAACGT
7[0]	8[3]	CCCCCTAGACTTTACAACGTGGTGCTCCCCC
16[127]	21[117]	AAAACAAAATTAATTAAGGCGAAAATAAAGCTGTCC
83[1]	78[17]	CCCCCAAAAAATCCCGTAAAATGTGTACCATTTGCAGCG
29[46]	23[58]	ATATACAGAGGGAATCATTACCCCCCC
74[52]	76[25]	CCCCCATTTTGTTAAAATTCGCTGATAATCACAAATATGGG
22[59]	16[46]	CCCCCGCGCCCAATAGCATTTGGGTTTAGAACAACGCTAGT
37[124]	30[129]	GGTCAATCACCGCGACGTTTCCAAACG
4[38]	8[32]	GCAGGTTGCCCGAGCCGTCAATAGACGTATTAGTC
1[81]	4[66]	TACGACGATCCAGCGCATGCTCGTTTTTACGGCTG
32[217]	31[219]	CCCCCTACGTTAATTAAAACACTCATCCCCC
15[87]	18[102]	GGCAATTCATCAATATAAGTAGATTACAAAATTGA
19[61]	16[58]	AAGGTGGCATTCAACGTAACGGAGTACATAAATCA
21[96]	19[108]	AAAAGGTAAATAATATCATCCAATAAA
78[52]	75[30]	CCCCCCCGGCAAACGCGGTCCGCGGTA
14[44]	14[58]	GGGCCAGAAGGAGCGGAATTATCATACCT

1[115]	0[130]	GTTTCGGAACCAGCGGGAGCTAAACAGGAGTAGTA
57[5]	54[26]	CCCCCCACAAGAATTGAGTGCTACAATTTTATCCAGAGCC
36[138]	35[128]	CGAAATTAAGGGAGACGAGAAACACCAAAT
41[18]	43[24]	TTGTTTTTCACGCAAGACAAAGAAGTTATATTCTT
62[25]	62[7]	TGAGCCATTTGGGAATTCCCCC
37[192]	29[198]	GCATTACCAAGGCAAAAGAAAGGCCCCACGCATAA
1[24]	4[39]	AGCACGCGTGCGGAGCGGCGCCGCGCTTAATGATT
54[25]	54[7]	ATATCAGAGAGATAACCCCCCC
30[24]	19[23]	CAACGGAACAAACAGGGAGCCGTTTTGGCATGAGA
0[101]	4[95]	CCCCTAATCATGTGCCGGTGCCCCCACACTGGGCC
0[129]	3[114]	AAGCACTAAATCCTGTGTCCGGGTTACCTGCACGT
13[25]	73[51]	GAACGTGCTTGCCAGAGAACAATAGGAACGCCATCACCCCC
13[1]	49[19]	CCCCCGTGAGAGATAGACTATACCAGTCCGGCGAATACTAGATAAGAA
20[65]	15[67]	TCACGAGCCAGTAACAGTCATA
56[56]	61[65]	CCCCCGCCATATTAGTTTAACGTCAAAAATGAACCCCC
33[161]	36[163]	TACCAGAAAAGATTACGAAGGGATTT
77[31]	77[51]	AATTGTAAACGTTAATCCCCC
30[220]	32[199]	CCCCCCTGAGGCTTGCAGGGAGTTAATACACAAAA
28[78]	32[72]	ATAAAGGCTAAGTTTTGTCGTCTTACAAACCAGAG
10[30]	17[31]	TTGGCTTAAATGTGAGCAACCTTGCTTCTAATACC
3[122]	8[109]	ATCATGGTCAGTTGGCAACGAACTGGATTCACCAG
33[45]	24[45]	CTTTGAAGCAACCGAAAGAACC
63[5]	60[26]	CCCCCAACGTCACCAATGAAACCATCGATCAGAACCATTA
34[115]	37[100]	TAAATTTGTACTGGTAATAGG
8[136]	3[121]	GGATTATTTACCCGTTGTTAGCCGATTAAAGGGGC
41[24]	43[17]	AACGACGCCAGCTGGCGAGCGG
66[59]	69[36]	CCCCCTGGAAGTTTCATTCCATATAACAGGGGGAATATGC
26[38]	54[38]	ATAAATTTTTTTTTATCCAGTTACAGCGT
35[32]	36[45]	TAAAGCCAGACCCTGCCCTCAAGAGAAGGATTCAG
29[199]	33[216]	CCGAGGGGGTACTTTTGCAAAAGAAGTCCCCC
43[18]	42[0]	GCCAACTATATGTAAATGCTGACCCCC
33[0]	31[17]	CCCCCCATCGGCATTTTCGGTCATGGCAGGTAGGG
29[103]	35[95]	GTCATAGTTAGCGTAACATTCCACACCCTCGCTTT
24[44]	25[62]	AAGGGTATCATTCCAAGAACCCCC
4[143]	8[137]	GCAACGTATTGATCAAACCCTCAATTCGCCATAAT
14[57]	19[60]	TTTACATACGGCAGAGGCATTTTATAATCGCTGAA
16[57]	18[51]	ATATATGTGCACGGGAGAAACAACAAGGATAAAAA
28[187]	32[179]	ATGTTTCCATCGCGCTTTTGCGGGATCCTAAAACATT
5[53]	6[52]	GGCGCGTACTGTGTCCAGGTAAAGGCACTAACAAC

78[24]	79[51]	AAACCGCCAGCAGCGATGCTGATTGCCGTTCCCCC
80[52]	15[30]	CCCCCTGGCAGCCTCCGGAGTAACCTTTCATCAACAGCATG
30[128]	28[137]	GCTCGAGGTGAATTTCTCAT
60[25]	66[17]	CCATTGAGGGAATTTACCAGCGC
15[68]	18[79]	TTCCTGATTATCAGATCAGATGAGATTGCTGGAGA
36[220]	34[197]	CCCCCCTTTGACCCCCAGCGATTAAGGCTGGCCGGAT
3[115]	7[121]	TAACGATTTTAATCACGCAAATTAAATTGGCAATA
31[18]	36[3]	ATACCTCAGAGCCACCACCCCCCC
19[0]	20[3]	CCCCCGTAAAGATTCAACCATCAATACCCCC
34[86]	28[79]	GGGATACATGAGAGCCAGGAACCGCATAAATCAAAA
6[86]	0[94]	AGGATCCCTTTGCATCACGAGCTCGAATTCGCGAT
9[60]	13[62]	TCCACCCTTCTGACCGTTTTTGCGGACCCCC
66[16]	58[7]	CAAAATAGAAATCAGTAGCGACCCCCC
2[170]	5[184]	CCTGAAGCATAAAGTGTCCACTACTTTGGAACAA
35[120]	37[123]	TGGTTTGAACGAGCAGAC
3[5]	6[0]	CCCCCGCGGTTGCGGTATTTGAGGATTTAGAAGTATCCCCC
78[16]	80[3]	GATCTCACGGTCTTCTCCGTGGTGAACCCCC
34[157]	28[151]	GTGAATAAGGCGAATTACTGAGATTTCATAACTCG
8[192]	0[186]	CAACTATCGGCGCTGGTTCCACTATAAAACCGTCT
29[115]	31[121]	CAGCTTTAAACAAAAGGAATTACGAATGCAGATGA
32[52]	37[65]	CAGAGCGCAGTCTCTGAACCCGTATAGCGGGGTTT
61[5]	51[29]	CCCCCGGGAGAATTAACTGAACTAACCAGAACCCAAAAGA
30[138]	35[138]	GGTAGCTTAAACGACCACATACTTTA
29[39]	35[31]	GCGTATGGGATTTTGCTCAATAGGTGACAGGTCAT
34[224]	37[223]	CCCCCGTAATCTTGACAAGAACTGACCTTCATCAAGACCCCC
Start	**End**	**Sequence + Modification**
25[5]	68[2]	ATAAAGGTGGAATAAGTTTAT[Biotin]
73[5]	72[5]	TGAGAGTCTGTAAAACTA[Biotin]
53[5]	48[5]	AAAGTAAGCGAGGAAACG[Biotin]
69[2]	64[2]	GACATTCAACCGTTATTCATTAAA[Biotin]
59[9]	53[29]	[Biotin]AGGGTAATTGAGCGCTATATCTTACCCGAACAAAG
15[5]	70[5]	GAGAGGGTAGTCATTGCC[Biotin]
47[2]	46[2]	TTAATTTCATCTCCGTGTGATAAA[Biotin]
51[5]	22[2]	CAATAATAACTCCTTATTACG[Biotin]
45[2]	44[2]	TGCAAATCCAATAATATATTTTAG[Biotin]
64[18]	60[9]	GGAAAATTGAGGAGCAAGGCCGGA[Biotin]
75[5]	74[5]	GCATGTCAACCCAAAAAC[Biotin]
49[2]	16[2]	TAAGGCGTTAAAAAAAGCCTGTTT[Biotin]
6[178]	5[171]	AATCACAGAGGACGCTCATGGAAATCCTGAGTAAAATCCGTTC[25A]

2[159]	9[160]	AGCTGCGGGTGGTTGGTGGTAATAACA[25A]
5[161]	6[160]	GAGTGTTTGTTTGATTTTCTTTCACCTTG[25A]
7[150]	2[150]	GAACCTCAAATGGCGCCAATTA[25A]
32[143]	36[139]	GAATGGTAAAAAATTGTGT[25A]
36[185]	35[171]	GAAACAAAGTACGGTGTACAACGTAACAAAGCAGAA[25A]
28[150]	30[139]	TCATAAATATTTAAACAGGGAACGAG[25A]
29[164]	35[160]	CGCCTCAGCAGCGAAAGATGCCACTCATCAGTCTTATGC[25A]
29[150]	33[160]	GATACCGATAGTGCGGAACCTCGTT[25A]
8[150]	5[150]	CAATGATTAGTTCCGAAACCCG[25A]
9[161]	2[171]	TCACTTGACCTACACAGCAGAAGATAAATAAAGCATTCACCAGAAA[25A]
35[161]	36[171]	GATTTTATGCTCATAGAGGACAGATGAACAAC[25A]
33[58]	37[51]	AAATCGAACCACAGTTTCGTAGTACCGCCACCCTAG[ATTO542]
18[148]	20[134]	[ATTO647N]AAGCCTCAGAGCATAAGCAAAATGTTTAT or [Alexa647] AAGCCTCAGAGCATAAGCAAAATGTTTAT
18[148]	20[134]	TGT GCC TGT TTA TCA AGT TTA AGC CTC AGA GCA TAA GCA AAA TGT TTA T (Capture strand 1)
14[136]	21[151]	ATT TAC AAC ATG TTC AGC TAA TGT TTT GTG CCT GTT TAT CAA G (Capture strand 2)
20[151]	19[148]	CAG AAC GCG CCT TAA GCA ATA TTT TGT GCC TGT TTA TCA AG (Capture strand 3)
Target		TTCGAATACCACCGTCGAGCCAGAAACTGTCTACATTGCCC GAAATGTCCTCATTACCATAATCGAAAGCATGTAGCATCTTG CTCATACGTGCCTCGCCAATTTGGCGGGCAAATTCTTGATAA ACAGGCACAACTGAATATTTCATCGC
Imager		GCGATGAAATATTCAGT[Alexa647]

Table S5. Annealing ramp for DNA origami folding.

Temperature [°C]	**Cooling rate [s/°C]**
65	120
64 to 61	180
60 to 59	900
58	1800
57	2700
56	3600

55	4500
54 to 44	5400
43	3600
42	2700
41 to 39	1800
38	900
37 to 30	480
29 to 25	120

Table S6. Nanoparticle preparation protocol. Each step was followed by 2 minutes of stirring.

Step	**PBS 3300 added [µL]**
1	10
2	10
3	20
4	20
5	20
6	20
7	50
8	50
9	50
10	50
11	100
12	100
13	100

References

[1] Douglas, S. M.; Marblestone, A. H.; Teerapittayanon, S.; Vazquez, A.; Church, G. M.; Shih, W. M., *Nucleic Acids Res.* **2009,** *37* (15), 5001-6. DOI 10.1093/nar/gkp436.

[2] Kim, D.-N.; Kilchherr, F.; Dietz, H.; Bathe, M., *Nucleic Acids Res.* **2012,** *40* (7), 2862-2868. DOI 10.1093/nar/gkr1173.

[3] Castro, C. E.; Kilchherr, F.; Kim, D. N.; Shiao, E. L.; Wauer, T.; Wortmann, P.; Bathe, M.; Dietz, H., *Nat. Methods* **2011,** *8* (3), 221-9. DOI 10.1038/nmeth.1570.

[4] Schedlbauer, J.; Wilhelm, P.; Grabenhorst, L.; Federl, M. E.; Lalkens, B.; Hinderer, F.; Scherf, U.; Hoger, S.; Tinnefeld, P.; Bange, S.; Vogelsang, J.; Lupton, J. M., *Nano Lett.* **2020,** *20* (2), 1074-1079. DOI 10.1021/acs.nanolett.9b04354.

[5] Trofymchuk, K.; Glembockyte, V.; Grabenhorst, L.; Steiner, F.; Vietz, C.; Close, C.; Pfeiffer, M.; Richter, L.; Schutte, M. L.; Selbach, F.; Yaadav, R.; Zahringer, J.; Wei, Q.; Ozcan, A.; Lalkens, B.; Acuna, G. P.; Tinnefeld, P., *Nat Commun* **2021,** *12* (1), 950. DOI 10.1038/s41467-021-21238-9.

[6] Ochmann, S. E.; Vietz, C.; Trofymchuk, K.; Acuna, G. P.; Lalkens, B.; Tinnefeld, P., *Anal. Chem.* **2017,** *89* (23), 13000-13007. DOI 10.1021/acs.analchem.7b04082.

[7] Grabenhorst, L.; Trofymchuk, K.; Steiner, F.; Glembockyte, V.; Tinnefeld, P., *Methods Appl. Fluoresc.* **2020,** *8* (2), 024003. DOI 10.1088/2050-6120/ab6ac8.